# Personalization of human body models to simulate obese occupants in automotive safety

Tomáš Janák

N°d'ordre NNT : 2020LYSE1136

**THESE de DOCTORAT DE L'UNIVERSITE DE LYON**

opérée au sein de

**l'Université Claude Bernard Lyon 1**

**Ecole Doctorale** 162

**(Mécanique ; énergétique ; génie civil ; acoustique)**

**Spécialité de doctorat** : Mécanique

Soutenue publiquement le 26/08/2020, par :

**Tomáš Janák**

---

# Personalization of human body models to simulate obese occupants in automotive safety

---

Devant le jury composé de :

| | | |
|---|---|---|
| M. Sébastien LAPORTE | Professeur des Universités, ENSAM Paritech, Paris, France | Rapporteur |
| M. Steffen PELDSCHUS | Professeur des Universités, Ludwig Maximilians Universität München, Munich, Allemagne | Rapporteur |
| Mme Kristy ARBOGAST | Professeure des Universités, Children Hospital Philadelphia, Philadelphie, États-Unis | Examinatrice |
| Mme Isabelle BLOCH | Professeur des Universités, TELECOM Paris, Paris, France | Examinatrice |
| M. Stéphane BUFFAT | Directeur R&D, Renaut s.a.s, Nanterre, France | Examinateur |
| Mme Laurence CHÈZE | Professeure des Universités, Université Claude Bernard Lyon 1, Villeurbanne, France | Examinatrice |
| M. Philippe BEILLAS | Directeur de Recherche, Université Gustave Eiffel, Bron, France | Directeur de thèse |
| M. Yoann LAFON | Maître de Conférences, Université Claude Bernard Lyon 1, Villeurbanne, France | Co-Directeur de thèse |
| M. Philippe PETIT | Responsable Industriel, Renaut s.a.s, Nanterre, France | Invité |

# Université Claude Bernard – LYON 1

| | |
|---|---|
| Administrateur provisoire de l'Université | M. Frédéric FLEURY |
| Président du Conseil Académique | M. Hamda BEN HADID |
| Vice-Président du Conseil d'Administration | M. Didier REVEL |
| Vice-Président du Conseil des Etudes et de la Vie Universitaire | M. Philippe CHEVALLIER |
| Vice-Président de la Commission de Recherche | M. Jean-François MORNEX |
| Directeur Général des Services | M. Pierre ROLLAND |

## COMPOSANTES SANTE

| | |
|---|---|
| Département de Formation et Centre de Recherche en Biologie Humaine | Directrice : Mme Anne-Marie SCHOTT |
| Faculté d'Odontologie | Doyenne : Mme Dominique SEUX |
| Faculté de Médecine et Maïeutique Lyon Sud - Charles Mérieux | Doyenne : Mme Carole BURILLON |
| Faculté de Médecine Lyon-Est | Doyen : M. Gilles RODE |
| Institut des Sciences et Techniques de la Réadaptation (ISTR) | Directeur : M. Xavier PERROT |
| Institut des Sciences Pharmaceutiques et Biologiques (ISBP) | Directrice : Mme Christine VINCIGUERRA |

## COMPOSANTES & DEPARTEMENTS DE SCIENCES & TECHNOLOGIE

| | |
|---|---|
| Département Génie Electrique et des Procédés (GEP) | Directrice : Mme Rosaria FERRIGNO |
| Département Informatique | Directeur : M. Behzad SHARIAT |
| Département Mécanique | Directeur M. Marc BUFFAT |
| Ecole Supérieure de Chimie, Physique, Electronique (CPE Lyon) | Directeur : Gérard PIGNAULT |
| Institut de Science Financière et d'Assurances (ISFA) | Directeur : M. Nicolas LEBOISNE |
| Institut National du Professorat et de l'Education | Administrateur Provisoire : M. Pierre CHAREYRON |
| Institut Universitaire de Technologie de Lyon 1 | Directeur : M. Christophe VITON |
| Observatoire de Lyon | Directrice : Mme Isabelle DANIEL |
| Polytechnique Lyon | Directeur : Emmanuel PERRIN |
| UFR Biosciences | Administratrice provisoire : Mme Kathrin GIESELER |
| UFR des Sciences et Techniques des Activités Physiques et Sportives (STAPS) | Directeur : M. Yannick VANPOULLE |
| UFR Faculté des Sciences | Directeur : M. Bruno ANDRIOLETTI |

# Personalization of human body models to simulate obese occupants in automotive safety

# Personnalisation de modèles humains pour la simulation d'occupants obèses en sécurité automobile

The thesis was prepared at Laboratoire de Biomécanique et Mécanique des Chocs (LBMC), UMR_T9406, Université Gustave Eiffel – Université Claude Bernard Lyon 1
25 avenue François Mitterrand, Case 24, 69675 Bron Cedex, France

# Acknowledgments

First of all I would like to thank my supervisors Philippe Beillas, Yoann Lafon and Philippe Petit for their help, guidance and mainly patience. Since I did not come directly with a biomechanical background, many of the tasks required me to learn brand new skills and knowledge, so thank you for taking the time to teach me.

This work would also not be possible without Matthieu Lebarbé, Pascal and Catherine Potier and the rest of the CEESAR staff, who did a major portion of the work with PMHS for which I am grateful.

I would like to thank Sébastien Laporte and Steffen Peldschus for reviewing the thesis and for their insightful comments. The same thank you also goes to the rest of the defence committee: Kristy Arbogast, Isabelle Bloch, Stéphane Buffat and Laurence Chèze.

Furthermore I would like to thank Xavier Trosseille for additional help with Finite Element simulations and Marie-Christine Chevalier for providing some of the data for the initial morphing study. Cyrille Grébonval deserves a thank you not only for helping with setting up the sled simulations, but also for being a more than tolerable officemate.

I would like to thank all the people around me with whom I shared the years of this thesis: all the LBMC staff, fellow doctorands and friends. Lastly I need to thank to my parents and sisters for their support and for waiting for me back home.

Un résumé de la thèse en Français est proposé page 215.

# Table of contents

# 1. Introduction

The EU-wide road fatality rate has been stagnating for more than five years (European Commision 2020). Although safety systems in vehicles are steadily improving, their designs are mostly being evaluated for a population that is average in terms of anthropometry. The European Road Safety Observatory recommends to "better account needs of the variability of human beings", and encourages the use of physical and numerical simulations because "virtual testing (…) should take account of the natural bio-mechanical variations between individuals" (ERSO 2018). The obese are perhaps one of the largest group with increased vulnerability. In 2013, 40 out 53 World Health Organization European Regions member states reported that over 20% of adult population is obese (Galea et al. 2013) and the worldwide obesity rates continue to rise each year (World Health Organization 2020). At the same time, obese vehicle occupants have been found to be in increased risks of injuries related to incorrect restraint by the lap belt due to increased fat mass around abdomen (Kent et al. 2010; Thorbole 2015).

Human surrogates for vehicle crash are a valuable tool to help design restraint systems in vehicles. Crash test dummies have been used in industry for safety tests for decades and Finite element (FE) Human Body Models (HBM) are parts of the new ways "*to provide input for design guidance and for the assessment of future advanced protection systems*" (ERTRAC 2019). Their use is increasing as they provide more flexibility than testing scenarios with dummies and, in the case of state of the art HBMs, also higher biofidelity. However, most surrogates are created to represent only a limited part of the population, with the most common being $50^{th}$ percentile males and $5^{th}$ percentile females. As developing a new surrogate is costly and time consuming, morphing has lately been used in research to represent different population groups based on existing FE models. Notably, the PIPER Open Source project, initially funded by the European Union, provides tools to help with the positioning and the personalization of HBM for road safety (PIPER 2020).

This thesis aims to investigate how such morphing methodologies can be used to create Human Body Models that would realistically represent the obese population for road safety assessment. The investigation needs to cover several aspects, including the morphing method itself, the geometrical description of obese subjects, their mechanical characterization, and the use of morphed models to assess their relevance and study the interaction with the safety belt.

First is the morphing method itself. While morphing is a common practice with simple surface models, e.g. in the field of computer graphics, morphing finite element models brings specific challenges. The models consist of millions of elements formed into thousands of parts connected together that

describe the entire volume of a human body. The simulation stability of the model is, among others, affected by the shape of individual elements as well as contacts between individual parts. The morphing method therefore needs to maintain the element quality and contacts for the model to be usable after morphing.

Then, morphing "targets" have to be defined, i.e. the shape to which the model should be deformed. Obese-specific constraints include the spatial distribution of adipose tissues (intra abdominal vs. subcutaneous) as well as the presence of a "gap" between the thighs and the abdomen due to the abdomen protruding and folding. This gap might affect the interactions with the lap belt during a crash, but this was not investigated so far.

Lastly, once the models are morphed, their mechanical relevance can be evaluated by comparing their mechanical response from simulations to mechanical tests with Post Mortem Human Surrogates (PMHS). Only a small number of such tests with obese PMHS have been reported in literature. Additional tests focusing specifically on the abdominal fold are therefore sorely needed.

The second chapter reviews literature on obesity, its role in vehicle safety, FE models and their morphing. First, adipose tissues are defined and their mechanical properties are illustrated. Then obesity is briefly presented, mainly in how it relates to anthropometry, as the body shape is more relevant for the vehicle safety than health risks traditionally related to obesity (i.e. cardiometabolic issues). The impact of obesity on injury patterns in vehicles is then summarized, along with a review of mechanical tests done to study the behaviour of obese occupants in vehicles. Overall, while various injury mechanisms are discussed, no consensus seems to emerge from the studies

The next chapter presents PMHS experiments that were conducted. A complex imaging of the PMHS was acquired to be able to create detailed morphing targets to personalize existing HBM on each PMHS. In order to characterize the abdomen interaction with seat belt, several test under non-injuring belt loading were performed and finally, in two PMHS cases a crash scenario on a reverse sled was performed as well.

The fourth chapter present the efforts on improving the numerical methods for morphing FE models. Prior to the thesis, the author was involved in the PIPER project as a software developer. Although kriging was already implemented in in the PIPER open source software as a method for morphing the HBM, challenges still remained, including prohibitive computational costs when detailed targets are used. These challenges will be addressed in this chapter. In line with the open science approach of

PIPER, all methods developed within this study are generally applicable to any HBM and implemented as modules within the PIPER open source framework.

The developed methods were applied to create subject specific models of the PMHS using morphing targets from the collected imagining data. The fifth chapter describes in details workflows used at each step of this process. Targets with three levels of detail were created for each PMHS: one detailing both the subcutaneous fat as well as the abdominal fold, one with the abdominal fold but without the subcutaneous fat, and one without both (using only a simplified skin shape with the abdominal fold smoothed out). Aside from the created models themselves, the workflows and suggestions for their improvement are also an important result that could serve as a guidance for additional studies.

Finally, the sixth chapter describes the simulation of PMHS experiments with the morphed HBM. Material properties for the subcutaneous fat modelling were investigated. The importance of the abdominal fold and the personalized inside of the abdomen was assessed by comparing the mechanical behaviour of the three model types with differing level of details.

To summarize, the study will present several novel findings and methods:

- An efficient methodology for morphing FE human body models using detailed targets and its implementation as an open source software
- Workflows for creating detailed morphing targets from obese PMHS
- Characterization of interaction of obese abdomens with seat belts, with previously unreported details on the role of the abdominal fold and thickness of the subcutaneous fat

# 2. State of the art

## 2.1. Introduction

This chapter provides a brief overview of literature relevant to the topic of morphing and personalization of Finite Element (FE) Human Body Models (HBM) towards the obese population. The term “overweight” can be used to describe a person with “weight in excess of standard” while “obese” as a person with “excess body fatness” (Ogden and Flegal 2010). The World Health Organization (WHO) defines what this “excess” is in the following way: *Obesity can be defined simply as the disease in which excess body fat has accumulated to such an extent that health may be adversely affected* (World Health Organization 2000).

In this definition, the risks are assumed to be “direct” health risks, such as increased cardiometabolic risk. However, in the context of vehicle crashes, the health risks caused by Adipose Tissues (AT) are indirect: the excess mass and volume of the body fat is what affects the mechanical behaviour of the body, its interactions with the restraint systems of the vehicle, and possibly its tolerance to injury. These effects are purely geometrical and mechanical, not chemical or biological, which leads to some differences in how the problem needs to be formulated. For example, in the medical context, subcutaneous adipose tissue (SCAT) is considered less harmful than visceral adipose tissue (VAT, i.e. the fat layer around the viscera) (Ibrahim 2010), because of lower insulin resistance and many other factors. But in the context of vehicle crashes, the SCAT vs. VAT proportion may only be important because it could affect the belt interactions and the stress distribution on ribcage or liver for example.

Therefore, the term obesity will be used rather loosely in this thesis: when talking about “effects of obesity” in further text, it is in general a shorthand for “effects of large surplus of adipose tissues in the abdominal area”.

To be able to realistically model the tissues, it is necessary to understand where in the body is which type of tissue deposited and what are their mechanical properties. Section 2.2 will focus on these questions, first from the anatomical standpoint (Section 2.2.1) and then from the mechanical one (Section 2.2.2). Section 2.3 will introduce anthropometric measurements used for identifying obese population. Differences obesity makes in vehicle crashes will be discussed in Section 2.4. Section 2.5 will describe existing HBM, with a focus on the one used in the current study, and methods for their morphing. Finally, Section 2.6 focuses on data needed to create plausible target geometries.

Based on the review of these various points, the specific objectives of the thesis will be provided in Section 2.7.

## 2.2. Adipose tissues

### 2.2.1. Types and anatomical distribution of adipose tissues

Before further dissemination of obesity, it is important to understand what actually is body fat. Shen et al. (2003) provides the following definitions and observation: *fat is usually lipid in the form of triglycerides. In mammals, it is stored exclusively in depots of adipose tissue (AT), barring pathological conditions such as hepatic steatosis (fatty liver) and various forms of lipidosis. AT is a loose connective tissue that acts as an energy storage, thermal insulator and mechanical cushion. Although ATs contain only approximately 80% of fat, the remaining 20% being water, protein and minerals, the terms fat and AT are often used interchangeably*. Since this study is not concerned with the composition of the body on a molecular or chemical level, this simplification will be used as well in the following text.

AT in a human body is usually divided into several groups based on location of its compartments: subcutaneous (SCAT), visceral (VAT) and non-visceral adipose tissue (NVAT). SCAT refers to the layer of AT *found between the dermis and the aponeuroses and fasciae of the muscles,* VAT to *adipose tissue within the chest, abdomen and pelvis* and NVAT to remaining AT (AT within or between muscles and muscles and bones) (Shen et al. 2003). For illustration, Figure 1 shows the main AT compartments in the abdominal region on an axial section of the Visible Human Body Male subject taken approximately on the umbilicus level.

The different AT compartments differ not only by location, but also by their biological functions and chemical/cellular compositions. Because of these differences, it has been hypothesized that different types of AT have varying impacts on health. This has motivated a number of medical research studies that gathered data about differences in the composition, mainly between SCAT and VAT.

For example, Seidell et al. (1987) compared anthropometric measurements to Computed Tomography (CT) scans in a single slice at level of the fifth lumbar vertebra (L5). They reported, among other things, a VAT/SCAT ratio of 0.77 ± 0.39 for 71 men (mean ± standard deviation) and 0.38 ± 0.19 for 34 women. Kaess et al. (2012) repeated the study on a larger-scale, this time taking into account whole volume of SCAT and VAT. The volumes were obtained by semi-automatic segmentation of the CT scans: the abdominal wall manually traced and used as a separator between the two compartments. Intramuscular fat and possibly other tissues with similar intensity levels on the images were counted

as part of the VAT. The study describing the details of the image acquisition (Maurovich-Horvat et al. 2006) noted that measurement of the ratio based on areas tend to overestimate the SCAT volume, especially for high VAT/SCAT ratios (over 2.5). However, the reported volume-based ratios are similar to those of Seidell et al. (1987): mean VAT/SCAT ratios of 0.84 (0.64 – 1.10) for men and 0.43 (0.30 – 0.53) for women (based on VAT = 2 226 ± 1 020 $cm^3$ and SCAT = 2 633 ± 1 207 $cm^3$ for 1 680 men and VAT = 1 350 ± 829 $cm^3$ and SCAT = 3 136 ± 1 508 $cm^3$ for 1 543 women). The large differences between sexes should therefore be accounted for when creating (or morphing) human body models. Section 2.6.2 will focus on this problem in more details.

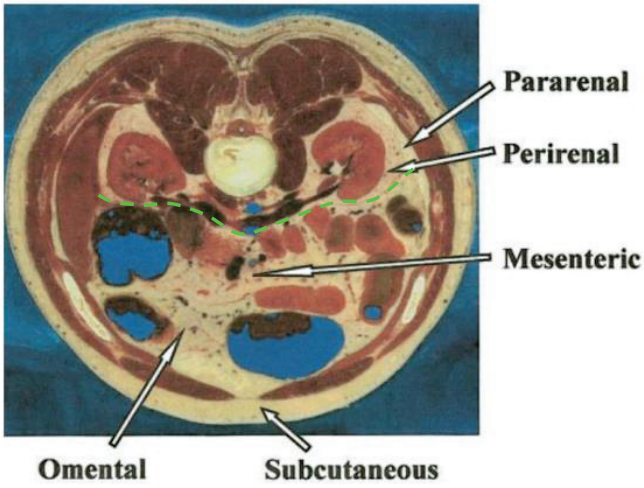


*Figure 1: Main adipose tissue compartments in the abdominal region shown on a slice from the Visible Man dataset. Front of the body is on the bottom of the image. Source of Figure: (Shen et al. 2003), adapted to show the approximate separation between the retro-peritoneal and the peritoneal fat compartments (green dashed line).*

### 2.2.2.Material properties of adipose tissues

This section will summarize recent studies that measured properties of AT in sample tests in tension and compression.

Comley and Fleck (2012) tested porcine fat samples at various strain rates. At lower strain rates, their results are overall consistent with those of Alkhouli et al. (2013) on human tissues, i.e. with a nonlinear behavior including an initial modulus in the order of magnitude of 1 kPa followed by a much higher final modulus . Based on an analysis on the elastin and collagen fibers in the sample Alkhouli et al. (2013) also suggested that, as in other tissues, these initial and final modus could be related to the loading of the elastin and collagen networks, respectively. The findings of Comley and Fleck (2012) included that tensile and compressive responses were similar and that the effects of strain rate were

limited below 10 $s^{-1}$, which may cover most of the relevant strain rate range for crash applications. Comley and Fleck (2012) also proposed a one term Ogden fit to describe the response. Some of these findings are illustrated in Figure 2. However, their study focused on sub-failure properties: the maximum strains remain within 0.3 to 0.4 range, and many stress results are limited to 1 kPa stress range (including for the Ogden fit). Much higher stresses and strains are likely in strenuous impact loading as encountered in automotive environments. Other studies provide experimental results of material fit for other loading modes (e.g. uniaxial shear as in Geerligs et al. (2010) or multiaxial loading as in Sommer et al. (2013), material fit in Naseri et al. (2018)). Some results of Alkhouli et al. (2013) and Sommer et al. (2013) are illustrated in Figure 3. Overall, while all these studies potentially provide useful and complementary information, they all focus on sub-failure properties and low stresses.

Lackey et al. (2014) proposed average tensile strengths of 34.7±4.2 kPa and 13.7±2.5 kPa for omental and subcutaneous fat in healthy obese, respectively. An illustration of the result of a test is provided in Figure 4. These strengths provide an upper bound for the stresses that can be transferred through the tissues in case of uniaxial tension.

In summary, most literature reports sub-failure properties and none include loading up to very large compressive levels that may occur in impact conditions. All experimental studies indicate a very soft initial behavior followed by a stiffening (prior to failure), the definition of the initial state (zero strain) in the tested tissues is not always clear. The experimental zero strain state may also differ from the in-situ initial strain/stress state: because of their material softness and large volume in presence, fat tissues are likely deformed due to their own weight in obese subjects. For all these reasons, these properties may not be sufficient to fully define material properties for the intended application. They can likely be used as a starting point but their usability in a FE model, where numerical implementation issues may also arise, will need to be assessed.

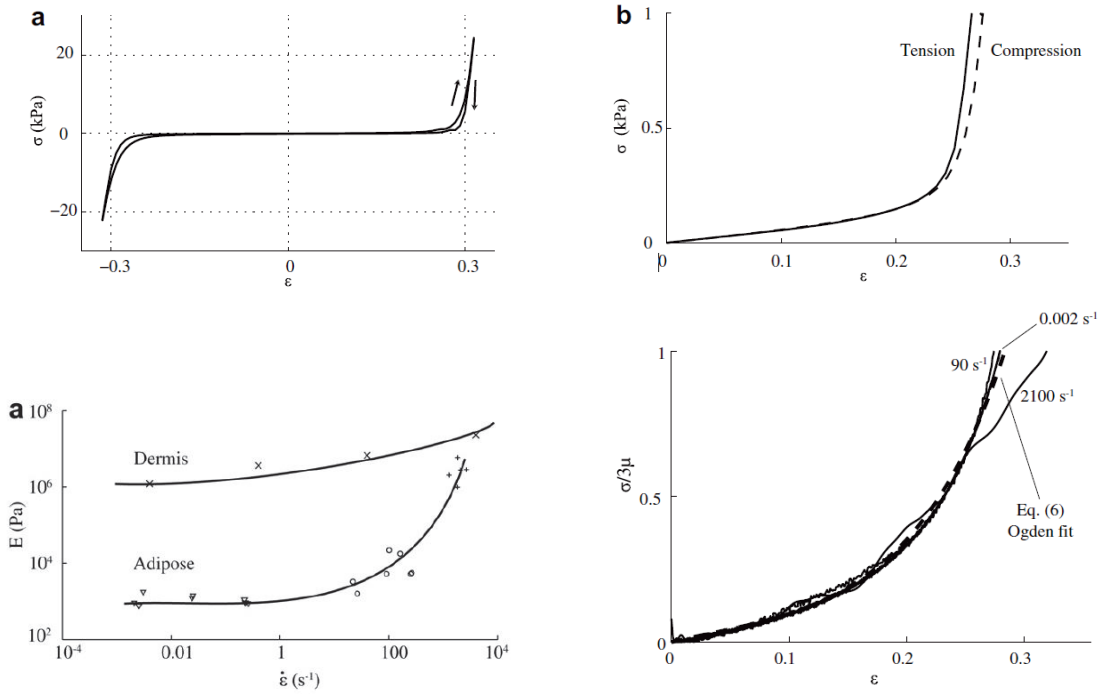


*Figure 2: Key results from Comley and Fleck (2012) porcine fat testing. See paper for exact test conditions and equations of the fit. Top: results from tensile and compressive tests are similar when the strain origin is selected between the sharp stress rise up to 1kPa (plot on the right is a magnification of the plot on the left). Bottom: linear compressive modulus variation with strain rates (left) and similarity of the response shapes at various strain rates vs a single order Ogden fit (normalized plot, right). The fit uses a linear coefficient (μ) and a power ($\alpha$) applied to the stretch ratio. The best fit is obtained with a power $\alpha = 23$ and values of 0.4 kPa and 1.7 kPa for the strain rate ranges of 0-10 and 20-260 $s^{-1}$, respectively. μ is used to normalize the plot on the right*

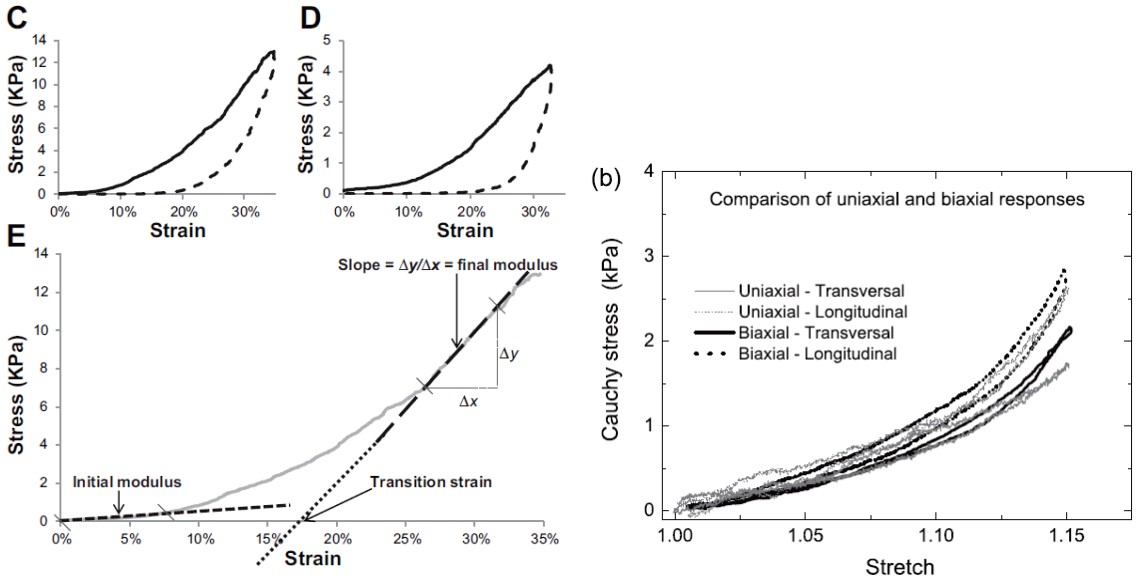


*Figure 3: Examples of results from Alkhouli et al. (2013) (left) and Sommer et al. (2013) (right). All studies observe a very soft and sharply nonlinear response.*

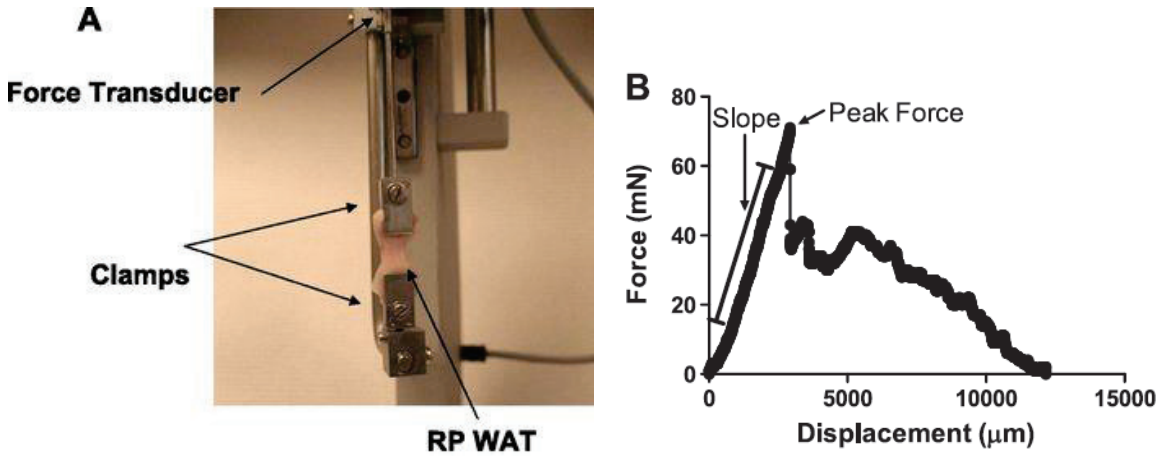


*Figure 4: Tests setup (left) and exemplar curve of fat testing until failure (right) from Lackey et al. (2014). An adipose tissue sample (RP WAT) from mice was used for the tests.*

## 2.3. Anthropometric descriptors of obesity

Assessing the "increased health risks" for a given patient is not trivial, but since large amount of body fat is apparent even to a naked eye, there is a presumption that obesity could be estimated by simple anthropometric measurements. Based on this presumption came one of the most common ways of assessing obesity: by using the body-mass index (BMI) which is the body mass (in kg) divided by the square of the body height (in m). The WHO suggested the following classification for adults (World Health Organization 2000):

- Underweight: BMI < 18.5
- Normal range: BMI 18.5 – 24.99
- Overweight: BMI 25 – 29.99
- Obese class I: BMI 30 – 34.99
- Obese class II: BMI 35 – 39.99
- Obese class III: BMI ≥ 40

Individuals with BMI over 35 (Obese class II and III) are the usual patients undergoing bariatric surgeries. In this field, the terms “severely” (BMI over 35), “morbidly” (over 40) and “super” (over 50) obese are often used, although this nomenclature is not standardized and the cut-off points may vary between individual surgical facilities. A few examples of external scans corresponding to different levels of obesity are provided in Figure 5.

Using the BMI as an obesity monitor might be misleading in some cases. There are significant differences between different ethnicities ages and sex. For example, increased health risks appear for much lower BMI (>25) for most Asian ethnic groups (Zimmet and Inoue 2000). Also, at ages above 60 the amount of adipose tissue tends to increase while weight tends to decrease due to loss of mineral, protein and water in muscles, bones and organs and this declining effect is appearing sooner for men than for women (Scafoglieri et al. 2014).

Even within the same ethnic, age and sex group, BMI can be misleading. BMI being simply the ratio between weight and the square of height means that for the same BMI, subjects of different heights will not have the same apparent shapes and circumferences. An example if provided in Figure 6. In addition, very muscular people will have large BMI due to muscles having higher density than fat, even though they will have very little adipose tissue (Figure 7).

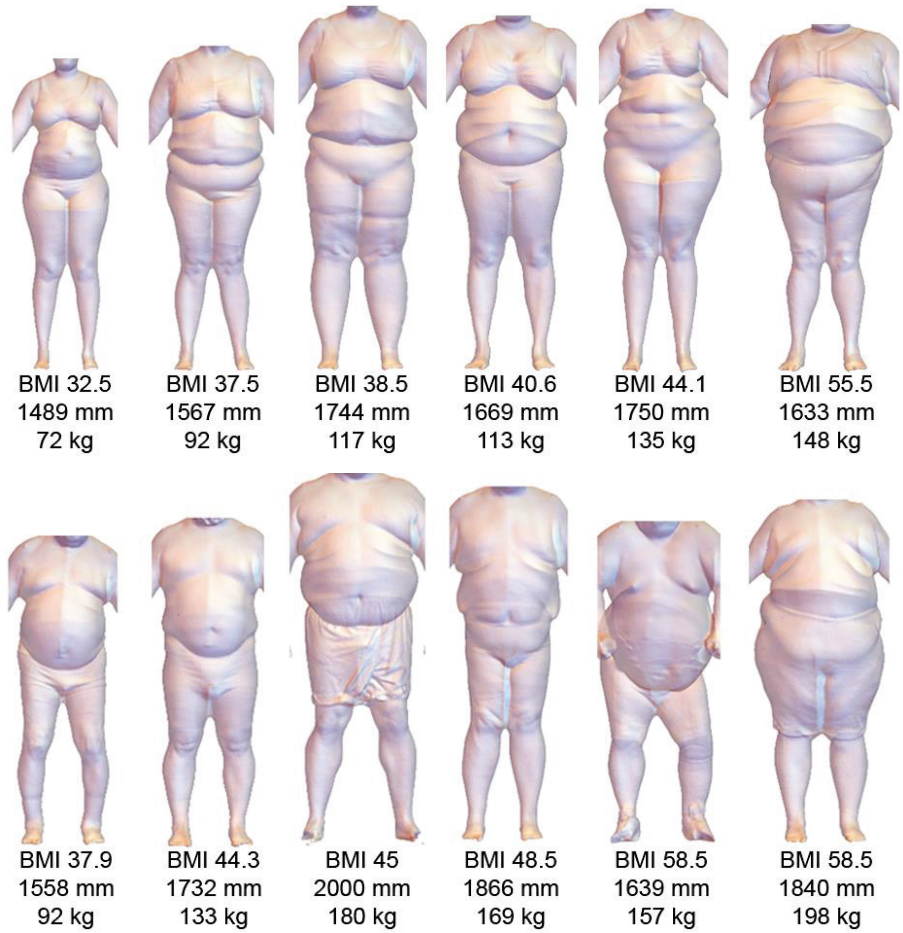


*Figure 5: Examples of external scans of overweight females (top) and males (bottom). Data provided by Jingwen Hu and Monica Jones (University of Michigan, Transportation Research Institute; personal communication).*

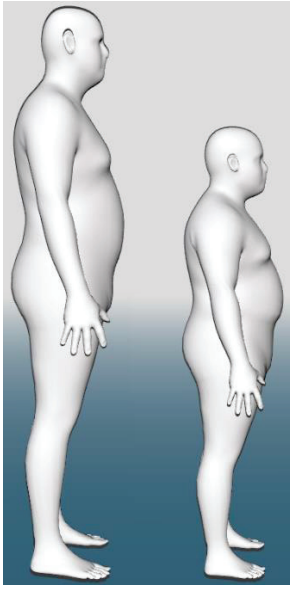

*Figure 6: Comparison of the body shapes of subjects presenting the same BMI 35 with two distinct heights, 1.95 m (left) and 1.55 m (right) statures. Source: http://adultshape.org/standingmale/, accessed Jan 2018.*

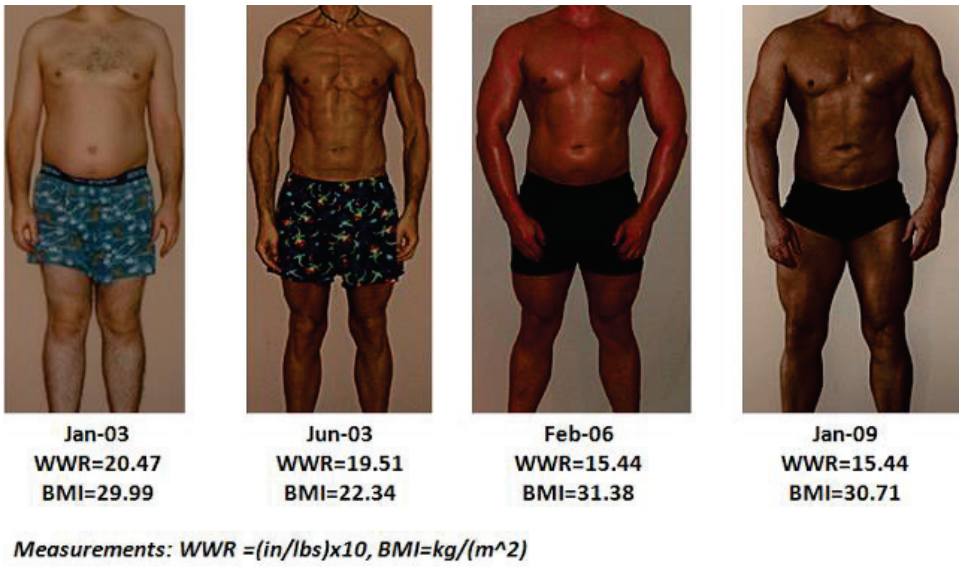


*Figure 7: Images of the same person at different stages of a bodybuilding transformation, with noted BMI and WWR (Waist to Weight Ratio). Notice that the BMI is similar in the first and the third and fourth images, yet the shape of the body is very different. Source of Figure: Ned Kock (http://healthcorrelator.blogspot.fr/2014/01/waist-to-weight-ratio-vs-body-max-index.html, accessed Jan 2018), based on data from John Stone Fitness (http://www.johnstonefitness.com/, accessed Jan 2018).*

Ideally, obesity would be determined based on direct measurements of the adipose (fat) tissue: skinfold measurement by a trained specialist with callipers (for subcutaneous fat, i.e. the fat layer immediately below skin), ultrasound, Computed Tomography (CT), MRI (Magnetic Resonance Imaging), dual energy X-ray absorptiometry or laser scans can be used to estimate the actual volume

of fat (Pepper et al. 2010; Schneider et al. 2010; Orphanidou et al. 1994; Stevens-Simon et al. 2001). However, this requires dedicated tools, expertise and time to take the measurement for each subject, making it often impractical. Therefore, BMI remains the standard monitor measure for obesity. To determine what measure is considered obese, a cross-check with epidemiology data needs to be made to determine at what point a significant increase of likelihood of obesity-induced diseases appears for the subjects. The WHO released the aforementioned recommended BMI cut-off values for diagnosing obesity. USA's National Institutes of Health suggests the same BMI thresholds in their guidelines (NIH 1998)[1].

Besides BMI, complementary measurements such as Waist Circumference (WC) and Waist-to-Hip Ratio (WHR) are also often mentioned as useful measurements for identifying obesity. Schneider et al. (2010) did a large study of over 9000 subjects aiming to measure obesity in terms of increased obesity-related cardiometabolic risk, comparing how accurate WC, WHR, BMI and WHtR (waist-to-height ratio) are in predicting it. The subjects were investigated twice in a span of several years. The WHtR was claimed as the best indicator while BMI as the worst. However, the average BMI was 27.2 (± 4.8), i.e. very obese subjects were not a large part of the subjects. A large-scale meta-analysis of publications such as this was performed by Ashwell, Gunn, and Gibson (2011). They aggregated 389 published papers based on the keywords WHR, BMI, WHtR etc. and of those, 31 contained studies of relation of the anthropometric factors to increased obesity-related cardiometabolic risk. This allowed analysing the combined results based on more than 300 000 subjects. The result was that WHtR is the most discriminative indicator, WC being the second and BMI third. WHtR of 0.5 was concluded as a good indicator of obesity. Similar conclusions were reached also by Swainson et al. (2017), who measured whole body fat percentage of 40 males and 40 females (using dual energy X-ray absorptiometry) and studied how well BMI, WHR, WHtR, WC and waist/height$^{0.5}$ predicted the amount of total fat mass and VAT mass. They propose WHtR as the best predictor, stating the values 0.53 and 0.54 for men and women, respectively, as the cut-off threshold signifying obesity.

Regarding the relationships between those anthropometrics measurements (BMI, WC and WHR) and AT distribution, Scafoglieri et al. (2014) sums up their literature review as such: *In summary, among the three adiposity indexes described here, the BMI seems to be the best correlate of total and subcutaneous AT in both genders. The WC is the anthropometric index that best correlates with*

[1]The guidelines are marked as out of date, but no updated version was found.

*absolute amounts of several abdominal AT compartments (e.g. intra-peritoneal, retro-peritoneal, and subcutaneous AT), while the WHR best relates to relative AT distribution.*

In summary, the WHtR seems to be the best indicators of obesity in the context of the medical definition. In the context of vehicle crashes, it is unknown if it can be used to provide an indication about the proper or improper restraint provided by the lap belt as used by the occupant. Given that the belt is positioned in the lower abdominal region, it is plausible that any metric based on waist or hip circumference will be more accurate than BMI at identifying occupants with potential problems with lap belt. However, to our knowledge there has not been a study focusing on differences between anthropometric measurements in the context of increased injury risks for obese occupants.

## 2.4. Obesity in vehicle crashes

### 2.4.1. Impact of obesity on fatality and injury patterns

Obese bodies have significantly different internal tissue distribution when compared to non-obese, which could result in different injury patterns and perhaps severity for the two groups in case of impact. This presumption was affirmed by many studies. Smith Choban et al. (1991) analysed data from 184 patients with blunt trauma and reported significant correlation of obesity and fatality rate: while there was 5% fatality rate for patients with BMI below 27 and 8% for patients with BMI between 27 and 31, patients with BMI over 31 had fatality rate of 42%, despite statistically insignificant correlations with other factors such as age or injury severity score between the three groups. The survivors from the obese cohort also had significantly longer stays in the hospital, signifying complications with treating the injuries.

In a more recent study, Rice and Zhu (2013) analysed results from “Fatality Analysis Reporting System” (NHTSA 2020), a census of fatal traffic collisions in the US. Data from years 1996 – 2008 were used, selecting only collisions during which impact between vehicles was the most harmful event. A “matched-pair cohort study” was conducted on the data: death risk ratio was estimated among driver pairs from the same collision and only if they were driving similar vehicles. This was done in order to remove a possible confounding of various unmeasured or unmeasurable qualities, such as arrival time of ambulance, quality of provided healthcare etc. This reduced the sample size to 3 403 pairs of drivers. The authors observed statistically significant increase of the fatality risk with increasing levels of obesity (see Figure 8). For “secondary” measures, sex was found to have meaningful impact on the results, with females being at higher risk than males, but no meaningful correlation was found between vehicle types, seat belt use or head-on collision status.

| | Female drivers | | | Male drivers | | | All drivers* | | |
|---|---|---|---|---|---|---|---|---|---|
| Body mass index category | RR | 95% CI | p | RR | 95% CI | p | RR | 95% CI | p |
| Underweight (<18.5) | 0.99 | 0.66 to 1.46 | 0.93 | 1.78 | 1.01 to 3.14 | 0.05 | 1.19 | 0.86 to 1.63 | 0.29 |
| Normal (18.5–24.9) | Ref. | – | – | Ref. | – | – | Ref. | – | – |
| Overweight (25–29.9) | 1.26 | 0.98 to 1.63 | 0.07 | 0.83 | 0.70 to 0.99 | 0.04 | 0.94 | 0.82 to 1.09 | 0.43 |
| Obese I (30–34.9) | 1.36 | 0.96 to 1.93 | 0.08 | 1.11 | 0.87 to 1.41 | 0.42 | 1.21 | 0.98 to 1.49 | 0.08 |
| Obese II (35–39.9) | 2.20 | 1.27 to 3.81 | 0.005 | 1.25 | 0.84 to 1.86 | 0.27 | 1.51 | 1.10 to 2.08 | 0.02 |
| Obese III (≥40) | 1.92 | 0.85 to 4.32 | 0.12 | 1.75 | 0.91 to 3.34 | 0.09 | 1.80 | 1.15 to 2.84 | 0.01 |

*Wald p for effect modification by sex, 0.02.

*Figure 8: Fatality risk ratios (RR) of obese drivers (probability of fatal incident of an obese driver divided by probability of fatal incident of non-obese driver), grouped by sex. CI stands for "confidence interval". Source of Figure: (Rice and Zhu 2013).*

More recently, Bellal et al. (2017) performed similar crash report, focusing on subjects suffering morbid obesity (BMI > 40) based on the National Trauma Data Bank (NTDB 2020). The retrospective analysis was conducted by analysing data of 214,306 drivers (included 10,260 with BMI > 40) involved in motor vehicle crash from the 2007-2010 collection of U.S. trauma data. The reported increase of fatalities for morbidly obese drivers was 52% when compared to occupants with non-morbid obesity (but obese nevertheless, with BMI between 30 and 40), especially for occupants without any restraint systems (increase by 84%). But the risk of death also increased among motorists with obesity who used restraint systems (morbidity of obese drivers with seat belt only by 48%, with both airbag deployment and seatbelt by 49%), except for airbag deployment only (no significant difference in the odds of death).

Looking more in details at injury patterns, Boulanger et al. (1992) collected data from 6 368 patients of which 12% had BMI over 30 and 63% were injured in a car accident. For the vehicle crash patients, the authors reported lower head injuries (7.1% of obese vs 12.6% of non-obese), lower liver injuries (1.9% vs. 3.9%), no other significantly different abdominal injuries among the two groups, but higher pelvic fractures (14.6% vs. 10.8%) and lower extremity fractures (23.4% vs 18.8%). The lower rate of liver injuries led the authors to a hypothesis that the adipose tissue acts as "*intrinsic air bag*" that protects the obese vehicle occupants. This hypothesis was later partially supported by the results of analysis of 189 car crashes by Arbabi et al. (2003), where overweight (not obese) subjects had less severe abdominal injuries than normal-BMI subjects.

Mock et al. (2002) performed a similar study but on a much larger dataset of 26 727 subjects that participated in a vehicle crash, of which 3 974 had BMI over 30. They observed similar results, mainly stressing more prevalent chest injuries, for which close correlations between weight and odds of injury to chest were found, namely increase by 0.9% per kg ($p = 0.004$) or 2.7% per point of BMI ($p = 0.029$). Correlations for extremity injuries were second most increasing with 0.6% per kg of weight or 2.9% per

point of BMI. However, the significance of those is smaller, with p-values at 0.17 for weight and 0.18 for BMI.

A study of over 1100 subjects with blunt traumas (25% of which were obese) with detailed injury data also reported higher fatality rate among obese (V. R. Brown et al. 2005) as in Rice and Zhu (2013) or Smith Choban et al. (1991). The study noted that the rate of complications (*multiple system organ failure, acute respiratory distress syndrome, myocardial infarction, and renal failure*) was higher for the obese population, probably contributing to the higher fatality rate and perhaps making up for the possible reduced risk of head impact. Figure 9 shows the observed injury patterns in the obese (BMI 29-41) and non-obese (BMI 22-28) groups together with the significance of the observation.

Only 40% of the traumas from the V. R. Brown et al. (2005) were caused by vehicle accidents, but as can be seen in the table in Figure 9, the injury patterns strongly correlated with obesity were lower severity of head injuries and higher of lower extremities. Regarding other body regions, the significance of the correlations provided in V. R. Brown et al. (2005) or Mock et al. (2002) are low. The lack of these correlations with obesity suggests that the overall higher morbidity of obese patients could be caused by the fact that the treatment of the injuries is more difficult.

| Injury | Obese (n = 283) %(n) | Non-obese (n = 870) %(n) | p value |
|---|---|---|---|
| Head injury | 42 (119) | 55 (480) | 0.0001 |
| Head AIS > 3 | 23 (65) | 30 (258) | 0.03 |
| Admission GCS | 12 ± 5 | 11 ± 5 | 0.004 |
| GCS < 8 | 26 (73) | 35 (303) | 0.004 |
| Chest injury | 45 (127) | 38 (332) | 0.05 |
| Chest AIS > 3 | 12 (33) | 12 (100) | 0.93 |
| Abdominal injury | 29 (82) | 25 (210) | 0.10 |
| Abdominal AIS > 3 | 14 (39) | 11 (91) | 0.12 |
| Pelvic fracture | 26 (74) | 22 (195) | 0.20 |
| Lower extremity fracture | 53 (150) | 38 (327) | <0.0001 |
| Upper extremity fracture | 20 (56) | 18 (155) | 0.45 |
| Extremity AIS > 3 | 5 (13) | 2 (18) | 0.03 |
| Spine fractures | 14 (41) | 16 (136) | 0.70 |
| Cervical | 8 (22) | 9 (75) | 0.66 |
| Thoracic | 5 (15) | 4 (38) | 0.51 |
| Lumbar | 4 (12) | 6 (48) | 0.40 |

*Figure 9: Injury patterns in obese and non-obese patients. AIS stands for Abbreviated Injury Score (https://www.aaam.org/abbreviated-injury-scale-ais/), GCS for Glasgow Coma Scale (http://www.glasgowcomascale.org). Source of Figure: V. R. Brown et al. (2005).*

In summary, the morbidity could be higher for obese occupants but when looking at injury distribution, the effects of obesity vary between studies and are not always significant except for lower extremity (higher risk), head (lower risk) and perhaps chest (higher risk, albeit the significance is slightly lower). Another observation is that these studies typically use BMI and sex as descriptive parameters, but, as seen in Section 2.3, many variations on the fat distribution, the body shape, etc. are not captured by these parameters and could affect the risk of injury.

## 2.4.2.Restraint system interactions with obese occupants

The increased weight (for a given height) and the geometrical changes of obese vehicle occupants may lead to different interactions with the restraint systems, when compared to the standardized geometries used to design the vehicles. This section will focus on laboratory based observations and how they may explain the injury patterns.

Kent et al. (2010) performed several sled crash tests with post mortem human subjects (PMHS) using both obese and non-obese test subjects (Kent et al. 2010), (Forman et al. 2009). Their study was partially motivated by the opinion that the "cushion effect", as Arbabi et al. (2003) named it, was not proven in a sufficient way as conclusions based on epidemiology are not always consistent, and that it is difficult to have paired populations.

The conclusion of their PMHS study was that obese subjects tend to have more serious injuries, because their increased mass causes significantly larger excursion of the pelvic region before the lap belt can hook the pelvis and stop the motion (as can be seen in Figure 10). The large hip motion observed in the tests was similar to those observed in submarining conditions, i.e. "*the lap belt sliding over the iliac crest with lap belt forces affecting the internal abdominal organs during the forward displacement of the lower torso"* (Adomeit and Heger 1975). Forman et al. (2009) also documented that higher mass of the occupant is an additional factor contributing to more likely occurrence of submarining: the shoulder belt is likely to engage sooner than lap belt, causing to accentuate the pelvis forward motion, which in turn leads to increasing the angle between legs and torso. As a result, the lap belt is even more likely to slip over the pelvis. However, the phenomenon finally observed by Kent et al. (2010) may not be submarining as it was attributed to the belt compressing the tissues in front of the pelvis (subcutaneous fat and perhaps hollow organs) but the belt did not necessarily pass over the anterior superior iliac spine (ASIS). In fact, it is unclear from the illustration in Figure 10 if the large excursion could not be due to the belt motion below the abdomen, i.e. within the abdominal fold.

The compression of the soft tissues in front of the ASIS can be better understood looking at belt fitting tests. The effect of BMI on seat belt fitting was tested in laboratory conditions (a single car seat model, 54 volunteers, men and women) by Reed et al. (2012). The authors observed that increasing BMI shifts the lap belt "forward and upward", which can be considered as a poorer fit. Figure 11 shows the differences of belt placement between obese and non-obese vehicle occupants. The large amount of tissues in front the ASIS would likely delay the engagement of the pelvis in frontal impact and allow large excursions as in Kent et al. (2010). The shoulder belt is not affected too much by these changes. Reed et al. (2012) further noted that poor lap belt fit is "*associated with foot position restriction",*

which "*suggests that obese occupants will experience particularly poor lap belt fit in rear-seat conditions where lack of legroom causes elevated-knee postures*".

In the context of seat-belt use, it is also worth noting that several crash analysis studies report that obese drivers are less likely to use seat belt altogether. Jehle et al. (2014) analysed data from the FARS database (NHTSA 2020) from years 2003 to 2009, yielding 194 120 drivers (after excluding samples with incomplete information), focusing on the comparison of seat belt use of morbidly obese drivers compared to other groups based on BMI. They report that morbidly obese drivers are 67% less likely to use seat belt when compared to normal weight (BMI 18.5-25), 60% when compared to overweight (BMI 25-30), 40% when compared with obese class I (BMI 30-35) and 24% when compared to obese class II (BMI 35-40). Bhatti, Nathens, and Redelmeier (2016) analysed data from FARS between 1999 and 2012 and reported that although overall non-use of seat belts decreased over this time period significantly (from 42% in 1999 to 29% in 2012), it remains higher for obese drivers. Jehle et al. (2014) hypothesized that this phenomena could be caused by increased discomfort of using seat belts unadjusted to the higher abdominal mass. However, so far there has not been any study focusing on the comfort aspect of seat belt use for obese occupants.

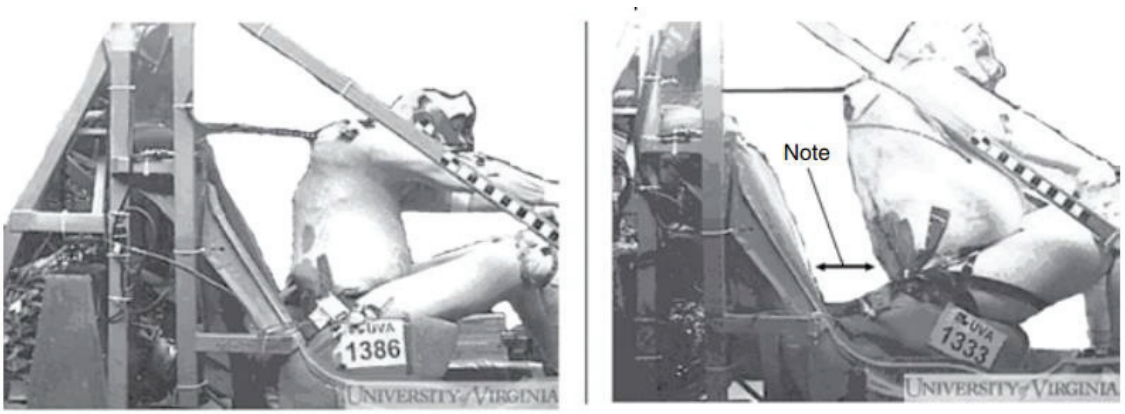


*Figure 10: Maximum forwards pelvic excursion of a non-obese (left, BMI 23.2) and obese (right, BMI 34.7) PMHS during a sled test. Source of Figure: (Kent et al. 2010).*

*Figure 11: A side view of non obese (left, BMI 23) and obese (right, BMI 31) vehicle occupants illustrating the different conditions for placing the lap belt. The bottom row shows mesh obtained from surface scans of the volunteers shown on the top row. Images provided by Jingwen Hu, Jonathan D. Rupp, Matthew P. Reed (University of Michigan, Transportation Research Institute).*

Considering possible relationships between loading to the various body regions (based on kinematic data) and injury, Kent et al. (2010) suggest that "*the increased hip excursion and concomitant decreased torso pitch in the obese cadavers may reduce the risk of the head striking some component of the vehicle interior in frontal or near-frontal impacts".* This could be in line with the lower occurrence of head injuries and higher occurrence of lower extremity injuries described in Section 3.1. For lower extremities, the risk could be associated with the larger forward excursion and the higher mass. However, severe lower extremity injuries are rarely fatal when treated, hence they do not explain the correlation between obesity and higher crash morbidity.

For the chest, Kent et al. (2010) also suggest that for obese, the "*load on the chest is concentrated on the more compliant and vulnerable lower thorax and less on the stiff upper ribs and clavicle",* which could cause rib fractures and pulmonary trauma. This could be in line with the finding of some of the studies reported in Section 2.4.1. The loading to the abdomen in Kent et al. (2010) is more difficult to interpret as the belt does not necessarily go over the ASIS, and the loading of the abdominal organs is unknown as the belt may go into the abdominal fold. For these two regions, one important difference to consider when comparing trends from Kent et al. (2010) to the field data is that the sled testing introduces a certain simplification, namely that the absence of airbag and knee bolster, which would tend to reduce the thorax and pelvis excursions, respectively, and thus might affect the injury risk to the upper and lower abdomen.

Overall, no consensus can be derived from these observations (or from the studies presented in Section 2.4.1) for thorax and abdomen. A higher tendency to abdominal loading or even submarining has been suggested (which would lead to more frequent and severe abdominal injuries), but (1) it was not observed in the PMHS tests, (2) it could be mitigated in the real world by the knee bolsters (and the presence of lower extremity injuries) and (3), without speaking of a "cushion effect", the loading of the internal organs (vs. subcutaneous tissues) is difficult to assess.

The use of a simulation approach able to describe the interactions between the belt and the thoraco-abdominal region in obese subject may help investigating some of these issues by allowing to study both the kinematics as well as the loading paths in a reproducible way and without limitations in terms of instrumentation.

## 2.5. Human body modelling, morphing and obese models

This section aims to review existing human body models, focusing mainly on FE models (Section 2.5.1) and more specifically on the model that will be used in the study. After a general description, more details about the abdomen will be provided. Finally, methods used for morphing such a model will be shown. Other models than FE will be briefly shown as well (Section 2.5.3).

### 2.5.1.FE models for impact

Although several full human body models can be found, two commercial model families are mainly used in the car industry: the Total Human Model for Safety (THUMS) (Shigeta, Kitagawa, and Yasuki 2009) and models from the Global Human Body Model Consortium (GHBMC) (Combest 2018). Both families have models of an adult 5$^{th}$ percentile female and adult 50$^{th}$ and 95$^{th}$ percentile males. Furthermore, the THUMS have a three, six and ten year old child, while the GHBMC has a six year old child model. Both models are actively developed and have been used and validated in many situations. However, since the GHBMC 50$^{th}$ percentile male occupant model (called M50-O) was used for this thesis, it will be described in more details.

The GHBMC is a private consortium including most major automotive manufacturers (www.ghbmc.com) also receiving funding from the National Highway Traffic Safety Administration and Canada. It supervises and fund the development of the models since 2008 by five academic "Centres Of Expertise" (COE) selected by the consortium body. These COEs are in charge of the full body assembly and geometry (Wake Forest University), head (Wayne State University), neck (University of Waterloo), thorax and lower extremities (University of Virginia) and abdomen (LBMC, University Gustave Eiffel). The M50-O model was the first available in the family. It stands for a detailed HBM

representing a 50th percentile male occupant based on a number of anthropometric characteristics (Gayzik, Moreno, Vavalle, et al. 2011). The geometry of the model is based on CT scan and MRI of a 50th percentile male volunteer (26-year-old, weight: 78 kg, size: 174.9 cm), (Gayzik, Moreno, Geer, et al. 2011; Gayzik et al. 2012).

In its current version, the model has over 1300 parts describing the main anatomical structures from head to shoes using over 2.5 million elements. It is mostly deformable (only 32000 elements are rigid) for both bones and soft tissues (brain, internal organs, fat, muscles, ligaments, etc). The parts are either connected directly though continuous mesh or through contacts to represent anatomical relationships.

For the abdomen, which is of particular interest for the study, the solid abdominal organs (liver, spleen, kidneys, pancreas) are meshed with tetrahedral solids and capsule shells. Hollow organs and some of the major vessels are represented using a simplified modelling approach: their walls are represented using shells while their contents is simulated using a simple volume pressure relationship (AIRBAG_LINEAR_FLUID). While the stomach, colon, and bladder are described individually with their actual boundaries, the small intestines are lumped together along with some of the mesentery in a large “bag”. Organs relationships are represented using actual representations of some of their attachments (e.g. falciform ligament, vessels) as well as different contacts to represent the sliding or tied interactions (e.g. bare area of liver). The space between organs is filled with fat meshed using tetrahedral elements. A sliding contact with a large thickness and no separation allowed is used to prevent gap opening between structures and to improve the coupling in compression (Beillas and Berthet 2018). The abdomen is surrounded by bones (deformables), muscles, subcutaneous fat and skin. Material laws are non-linear for the solid mesh (e.g. tabular MAT_SIMPLIFIED_RUBBER for the liver or fat, linear viscoelastic for the muscles), linear elastic for the capsules and fascia, and viscoelastic for the hollow organs and skin. Material failure of soft tissues is not described explicitly.

Tissues called fat, adipose or flesh in the model all use a tabular MAT_SIMPLIFIED_RUBBER material law, with the uniaxial tensile and compressive behaviour described by a curve. Different properties were selected by different COE and they differ between anatomical regions. These tissues sometimes include a mix of fat and muscles. Most properties were selected prior to the publication of the recent studies presented in Section 2.2.2. An illustration of the full body model and abdomen region is provided in Figure 12.

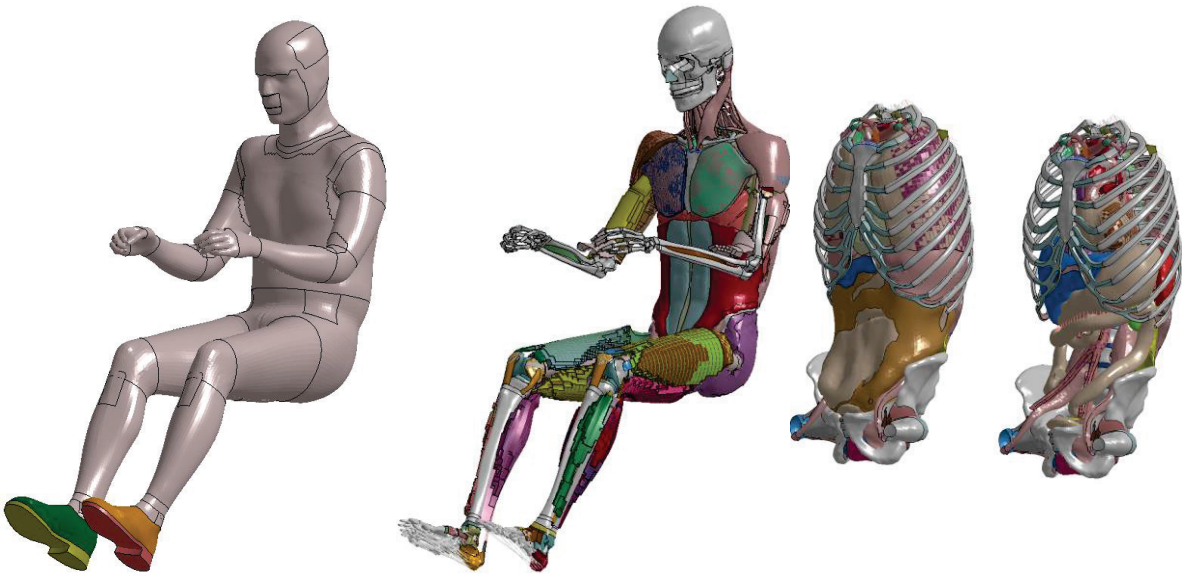

Figure 12: Illustration of the GHBMC M50-O v5.1. From left to right: complete; after removing the superficial tissues (fat essentially) to show the muscle; after removing the limbs, some muscles and organs.

The M50-O has been extensively locally and globally validated against experimental data mostly gathered on PMHS and volunteers, e.g. head (Mao et al. 2013; Takhounts et al. 2013; Yanaoka and Dokko 2013), neck (Barker, Cronin, and Nightingale 2017; DeWit and Cronin 2012; Fice, Cronin, and Panzer 2011; Mattucci et al. 2012; 2013), thorax (Z. Li, Kindig, Kerrigan, et al. 2010; Z. Li, Kindig, Subit, et al. 2010; Poulard et al. 2015), abdomen (Beillas and Berthet 2017), and pelvis (Kim, Kim, and Eberhardt 2012) and lower extremity (Shin and Untaroiu 2013; Untaroiu, Yue, and Shin 2013; Yue and Untaroiu 2014) in rear (Hassan and Meguid 2018), frontal (Arun et al. 2015; Gayzik, Moreno, Vavalle, et al. 2011), and lateral impact (Katagiri et al. 2016; G. Park et al. 2013). Between local, regional and full body setups, the model has been checked against well over 200 loading scenarios.

For the abdomen, besides some loading cases at the isolated organ or spine level, the loading cases are all full body setups in frontal or side impact (over 20 configurations in total (Beillas and Berthet 2017; 2018)). They include loading using bars, flat impactors, belts, airbags or padded surfaces applied to a fixed (typically on a seat, called fixed back) or a free body (free back or body seated on a sled seat) at velocities from 1 to over 10m/s.

Free or fixed back bar and belt loading are commonly used to assess the external response of the abdomen. Examples of typical loading cases are provided in Figure 13. While such loading cases are common in the literature, they do not seem available for very obese PMHS for which a gap seems to be present between tissue and full body sled tests (both already presented).

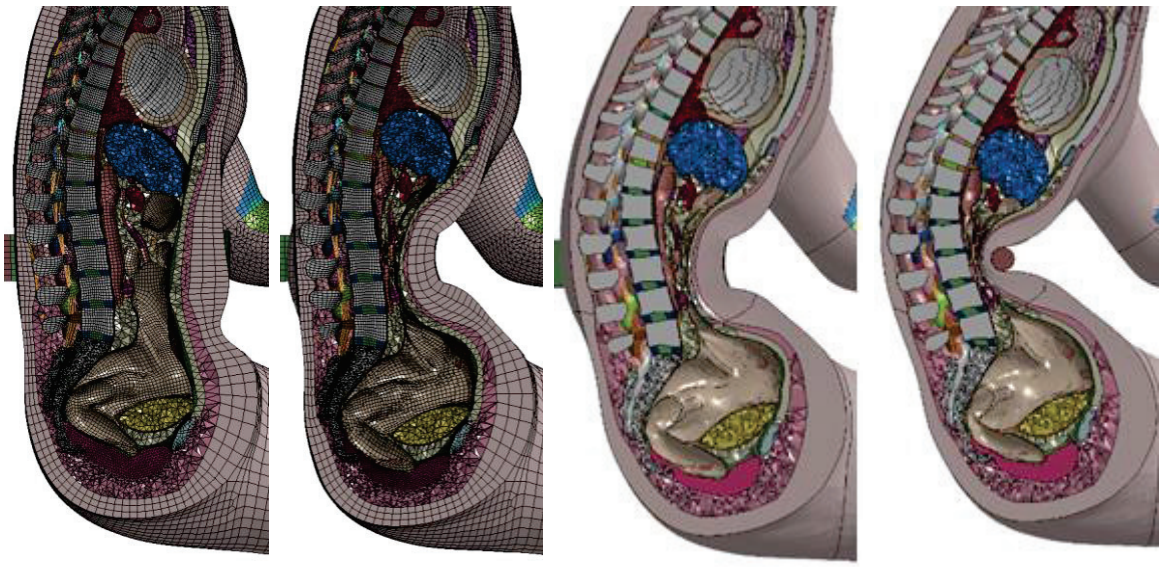

Figure 13: Example of typical loading cases used for the validation of the abdomen. Left: Fixed back mid abdomen belt loading (Lamielle et al. 2008). Centre: free back mid abdomen belt loading (Hardy et al. 2001). Right: mid abdomen rigid bar impact at 6m/s (Cavanaugh et al. 1986).

### 2.5.2.FE models morphing

The University of Michigan has been one of the more active organizations in this area. Their preferred transformation method is Radial Basis Functions (RBF) interpolation, which they used successfully to scale both the GHBMC and THUMS occupant models occupant models (Shi et al. 2015), (Hu et al. 2016), (Hwang et al. 2016). The target geometries are obtained from Statistical Shape Models (SSM) for anatomical structure for which there are a large number of available medical scans (ribcage, pelvis, femur, tibia) or external surface scans (Reed et al. 2014). There is no target for the internal abdominal organs – they are morphed directly from the baseline model based on surrounding structures. Figure 14 provides an overview of the workflow.

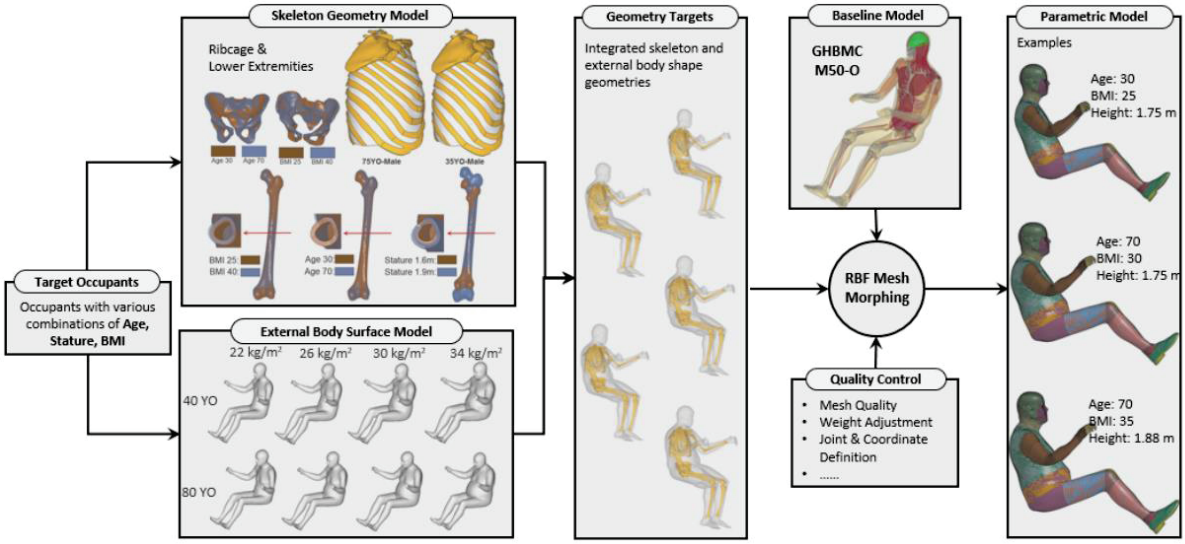


*Figure 14: Overview of the morphing workflow used in Hu et al. (2016). Source of Figure: Hu et al. (2016).*

Shi et al. (2015) reported that using these targets, the weight of the transformed model was within 3% from the weight of the subject the targets were based on. The additional mass was distributed equally on all nodes of the HBM. They further list as limitations*: "the external body contour model only focused on the torso geometry with limited lower extremity geometry information. As a result, the lower extremity geometry difference between obese and non-obese individuals is not as accurate as that in the torso region. Furthermore, the abdomen organ geometry model is not yet available, thus the organ shapes were not specially controlled and only morphed along with the ribcage surface and abdominal wall".* Their approach also does not take into account differences between adipose and muscle or other tissue. The authors used the workflow to create obese models and performed frontal crash simulations with them. The results were compared to the PMHS experiments of Kent et al. (2010) and were found to be matching the response corridors well. The authors also performed a parametric study, using several settings of BMIs, airbag inflation rates and seatbelt force limiters for the tests. They came to the same conclusions already stated in Section 2.4.2, i.e. that obese occupants are more prone to lower extremities and thorax injuries due to higher mass and worse belt fit. Hu et al. (2016) morphed the GHBMC M50-O to twelve different targets by increasing height, weight and age. The transformed models were tested in a frontal crash scenario used by NCAP crash tests (35 mph speed). The findings about obese occupants were again consistent with the ones presented in Section 2.4. However, in both cases, the analysis of the abdominal response and submarining tendencies were limited.

Vavalle et al. (2014) used the same method to scale the GHBM 50$^{th}$ (M50) percentile model towards a 95$^{th}$ (M95) percentile (not obese). The target geometry was obtained from a CT scan of a 95$^{th}$ percentile male volunteer. The authors used two sets of landmarks to register the target and source. The first set

was a set of homogenously distributed points inside and on the surface of the source model (GHBM M50). They were registered to the target geometry through the CT images that were used to generate the GHBM M50 model using the 3D Slicer[2] software. A second set of 2995 landmarks was placed on liver, spleen and kidneys. The total number of landmarks was 11 631. A validation by simulation and comparison to PMHS tests was performed on the transformed model. Seven simulation scenarios were successfully performed – a lateral sled test and six impact tests on various body parts. The model response, scaled to the 50$^{th}$ percentile, was within the corridors defined by the PMHS experiments. The continuous nature of the interpolation and the choice of control points only on the skin and solid organs lead to multiple approximations on the resulting model: bone geometry was only scaled based on the skin and the solid organs in the M95 model differed very significantly from those on the 95$^{th}$ subject scan (the spleen volume of the model was 363 ml, while for the subject it was 519 ml).

Jolivet et al. (2015) compared the Moving Least Square (MLS) and Kriging methods for morphing FE models. The Kriging, which is equivalent to the RBF under the conditions used in HBM morphing, was evaluated as more practical as it could lead to acceptable solutions (using approximations coming from the nugget effect) similar to the ones obtained by MLS, but without the prohibitive cost of MLS. Several parameters (interpolation kernel function) for Kriging were compared, but no significant differences were found. As stated by Jolivet et al. (2015), the RBF and Kriging methods have, for the purpose of HBM morphing, identical formulations. Kriging was used in Beillas and Berthet (2017) to scale the GHBMC M50 and F05 (5$^{th}$ percentile female) detailed models to the anthropometries of over 50 PMHS of various BMI that were tested in impact studies from the literature focusing on the abdomen. They found that morphing generally improved the response of the models (especially for abdominal penetration) but that the effect was more limited on force metrics. They also found large differences in terms of solid organ loading (strain energy density) due to the anatomical specificities of organ locations of the M50 and F05 geometry. However, the morphing was only based on estimated external anthropometry and did not include internal constraints on the ribcage or internal organs or subcutaneous fat thickness.

Mayer et al. (2017) scaled the THUMS v4 model's limbs and torso separately towards a BMI 38 target surface obtained from the RAMSIS CAD tool[3]. During the process, the elements around joints had to be manually deleted and then re-created after appending the limbs back. The authors used the model in an accident reconstruction of a far side case involving an obese occupant contacting the central

[2] https://www.slicer.org/

[3] https://www.intrinsys.com/software/ramsis

console and they found that the model kinematics and internal response were consistent with the kidney injury observed in the field.

In summary, morphing methods based on Kriging / RBF have already been successfully used by several independent groups on various HBM. The scaled models generally show good match of mechanical response characteristics with those of PMHS tests. However, the targets used in most published studies do not account for all internal structure changes between non-obese and obese individuals. As a result, the fidelity of shapes and sizes of those structures is limited, especially for the internal organs and adipose tissue distribution. In addition, while the lap belt interaction with the lower abdomen has been suggested to be important (Section 2.4.2), none of the studies addressed possible realism issues in that region, namely modelling of the abdominal fold and its interactions with the belt.

In all cases, more detailed morphing targets accounting for both internal structures and more local skin surface (fold) would be needed to check and/or address the realism of the scaled models. However, using detailed targets will make morphing more challenging. First, the use of continuous interpolation functions to scale both internal and external structures using independent targets may require either violating the target (as illustrated by Vavalle et al. (2014)) or performing manual adjustments (as in Mayer et al. (2017)). Then, the current morphing methods will need to be improved to facilitate the use of large numbers of control points.

The study of Jolivet et al. (2015) was one of the basis for the PIPER project, which focused on positioning and personalization of HBM. One of the outcomes of the project was a software tool, which among others contains a module for morphing HBM by Kriging. While the aforementioned HBM morphing studies used Matlab or other scripting languages to implement the morphing procedures, the Kriging code is compiled in PIPER, therefore suited for higher performance. In addition, the software provides other features that are tailored specifically for FE models, which can simplify the workflow. Figure 15 shows the user interface of the software. PIPER has not yet been applied to obese morphing in literature. The software is open source and since the author of this thesis was also one of the lead developers of it, it makes for an ideal platform for implementing the needed improvements of the morphing methods.

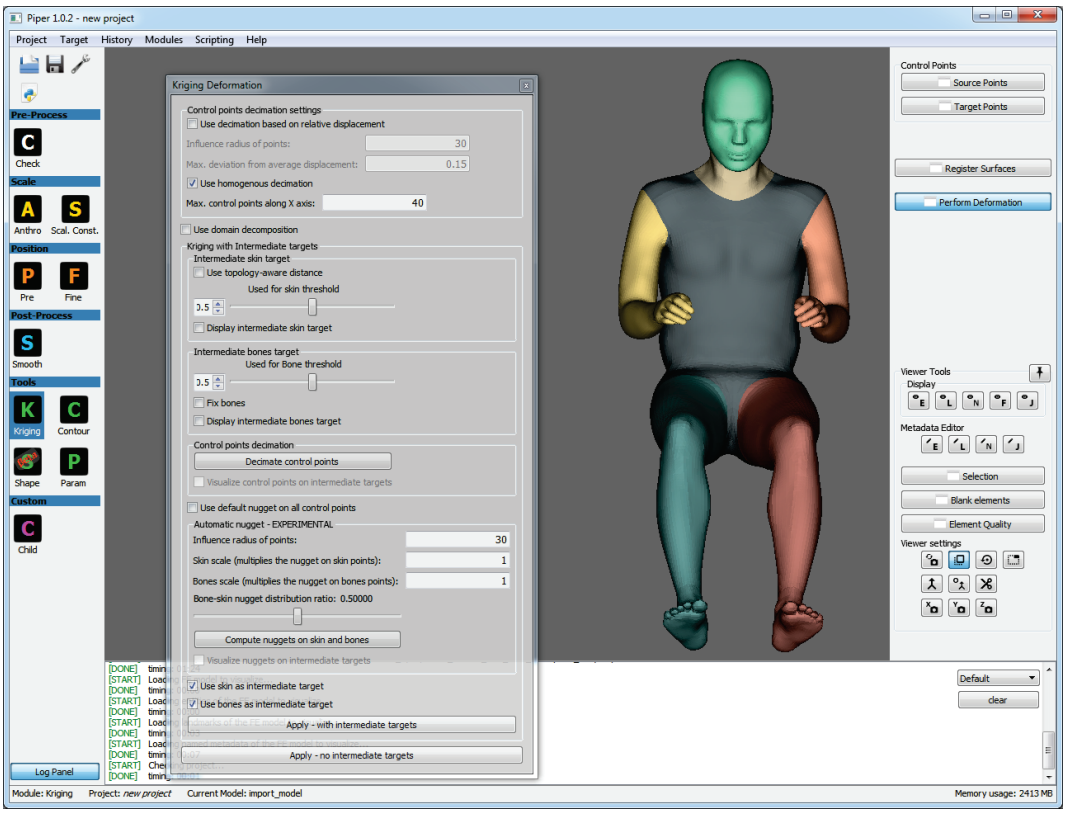


*Figure 15: User interface of the Kriging module in the PIPER software.*

### 2.5.3.Other models

There has also been other activities in morphing and scaling parts of human body, often for medical purposes such as Sigal et al. (2010), Park et al. (2014) etc.

Saito et al. (2015) reported a framework to personalize the external shape of deformable human body models dedicated to computer graphics applications. In their approach, a baseline mesh is first adjusted to a resized skeleton by classic skinning. Then the musculature and the fat are adjusted iteratively by a growth model (based on a solid elastic and a semi-fluid formulation, respectively). To achieve non-uniform fat growing, a scalar function is defined on each vertex of the skin, acting as a factor for increasing or decreasing the amount of fat growing around that vertex. The numerical approach for growth is simplified to achieve near-interactive user experience. “Envelopes” were used to assure smooth interface between anatomical structures and thus avoid “aliasing effects” due to a non-conforming tetrahedron continuous mesh. The final mesh, after creating obese or over muscular shapes, is suitable for computer graphics related simulation. But the method leads to a very large volume ratio between elements, and does “*not guarantee non-inverted tetrahedron*”. Also, only subcutaneous fat is represented (not visceral one).

More recently, Lloyd et al. (2016) simplified the previous approach to deal with the BMI variability (from 29 to 49) of the Virtual Population IT'IS models (https://www.itis.ethz.ch/virtual-population/, accessed January 2018). Thickness of the subcutaneous fat layer and organs (like the heart, the lungs etc.) was adjusted by modelling the tissues as a hyperelastic material and expanding the tissue through initial strain to control the final volume. At this stage, they assumed isotropic homogenous strains (thermal expansion analogy), and also considered only subcutaneous fat. They considered the bones as rigid, so the increase of the lungs' volume tends to push other organs and tissues down due to the rib cage confinement. The Virtual Population models are used as phantoms for exposure field simulation, without strong constraints on the final mesh quality and model runability as for models dedicated to mechanical simulation leading to large deformations, making them unsuitable to be used directly as surrogates for crash testing. However, they could serve to generate the target geometry for fat and internal organs, provided a validation study is performed first, confirming that the shape and size of fat compartments predicted by the growth algorithms is in accordance with the clinical data.

Anthropometric test devices (ATD, dummies) for representing obese occupants are being developed as well (Joodaki et al. 2015). An existing Thor ATD was resized and equipped with a silicone "flesh jacket" to represent the surplus soft tissue on the chest and a polyurethane mixture around thighs and pelvis. The authors showed comparison of the ATD's sled test response compared to the same test performed with PMHS (Kent et al. 2010). The ATD exhibited increased lower body motion, similarly to the behaviour of obese PMHS. The authors conclude that while further refinement is necessary, the created dummy might be a helpful research tool.

## 2.6. Building a detailed obese morphing target

In order to scale a HBM, a target geometry must be defined and associated to the HBM. The external shape on itself may not fully encompass the differences of interaction with restraint system in vehicles between obese and non-obese occupants. Therefore, the following subsections will describe the possibilities for creating a morphing target that include other structures and tissues such as the adipose tissue, the abdominal viscera and the skeleton.

As there is to our knowledge no database including all these structures of interest for morphing in a seated posture, each one will be described and discussed separately.

### 2.6.1. External shape

External body shape targets are the easiest to acquire. For example using rotary laser scanners (e.g. Pepper et al. (2010)) or cameras (e.g. four pairs of cameras in Xu et al. (2009)). There are numerous

similar surface acquisitions solutions, routinely used in academia and industry, so acquisition is not problematic. But in order to have a target that describes a certain population (e.g. obese), a significant amount of subjects descriptive of that given population is needed, ideally acquired using the same acquisition protocol to facilitate data analyses and the generation of a statistical shape model (SSM).

One such processed and free shape model can be found on *http://humanshape.org* (Reed et al. 2014). It is based on scans of several hundreds of subjects that were processed for SSM. More specifically, a template was registered onto each scan (using landmark definition) and Principal Component Analysis (PCA) was computed on the coordinates of the registered template. The main modes of the PCA were correlated with global descriptors such as age, BMI, sex or height, allowing predicting a likely shape for these descriptors. However, the regression are linear and the database does not have many subjects with BMI over 35, leading to lower fidelity of the generated model for very obese targets (source: personal communication with the authors). Still, it is probably the best freely available statistical shape model (SSM) of the human body external shape for automotive environment as the model is available in a seated posture. The authors have allegedly started efforts on collecting data from new, obese subjects. There are models available for standing male, seated male, standing female, standing child, seated child and seated toddler. Figure 16 shows the interface of tool and an example of a mesh exported from it.

Robinette, Daanen, and Paquet (1999) acquired surface scans of over 4500 American and European volunteers along with detailed anthropometric measurements to create the CAESAR database (Civilian American and European Surface Anthropometry Resource). Pishchulin et al. (2017) processed the CAESAR database by fitting a template mesh on the body scans available in the CAESAR database in order to create a more consistent set of meshes. The results are available for free on http://humanshape.mpi-inf.mpg.de/. However, the models are in the standing position making them less usable than the ones form Humanshape.org for the current application.

In summary, external shape data are available but are not yet focused on obese subjects, and, for the seated posture, the descriptions are not detailed near the abdomen fold. Dedicated acquisition may therefore be required.

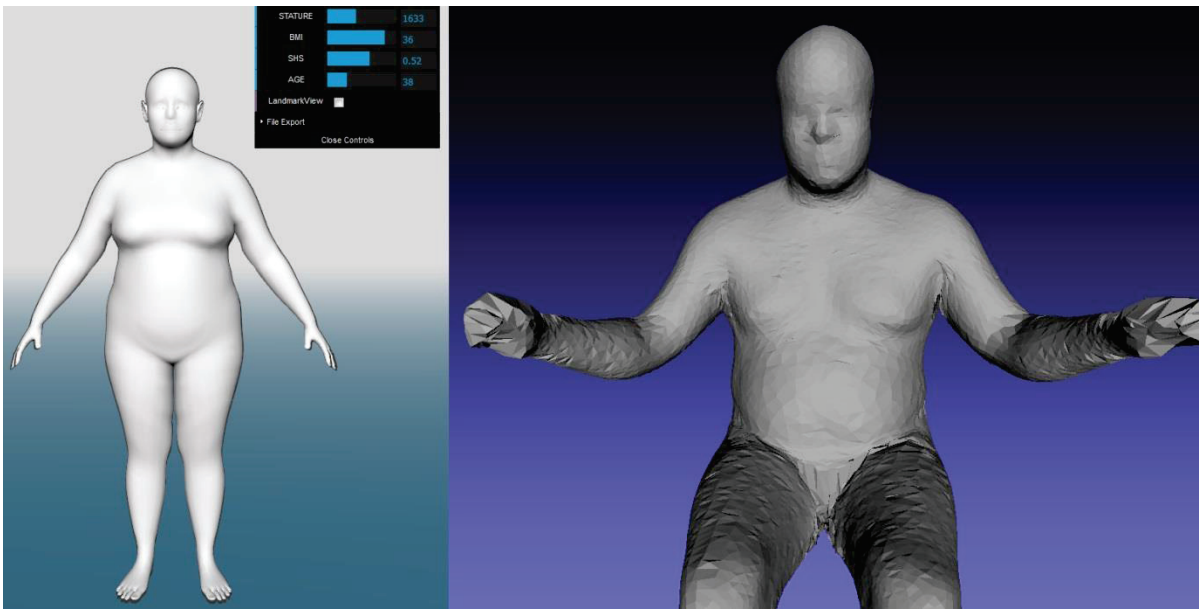


*Figure 16: Left: interface of the humanshape.org web application (showing a standing female model). Right: example of an exported mesh of a seated male – notice that the mesh is very rugged and in some areas even has holes and similar artefacts, thus requiring pre-processing before it can be used as a morphing target.*

### 2.6.2.Adipose tissue

As was already mentioned in Section 2.2.1, there is a number of medical studies measuring the amount of SCAT and VAT in patients. Typically, the studies segment CT images of patients and measure the volume in individual compartments (Seidell et al. 1987; Maurovich-Horvat et al. 2006; Kaess et al. 2012). Kullberg et al. (2017) reported algorithms for automated segmentation of AT from 3 CT scan slices covering liver, abdomen and thighs. The method was evaluated on 1089 subjects, who underwent CT imaging for determination of body composition. The study concluded that the automated segmentation correlated strongly with manual segmentation, although it tends to overestimate the amount of VAT and SCAT. The data were obtained by a high quality low-dose CT scanner; it is unclear if similar results are achievable with lower quality scans.

A recent survey (Scafoglieri et al. 2014) aggregated the results of studies regarding statistical modelling of adipose tissues based on anthropometry, similar to the two mentioned in the previous paragraph. Apart from the general assessment of impact of anthropometric measurements on AT distribution, the authors also presented formulas to compute the area or volume of VAT (Figure 17) and SCAT (Figure 18) as presented in the surveyed papers. The formulas are functions of anthropometric measurements such as WHtR, WC etc., but in some cases also include the impact of age, ethnicity and sex.

Practical utilization of these formulas for building a geometrical target, however, is not straightforward. The datasets as well as protocols for their acquisition differs between individual studies: they capture different anthropometric measurements, the tested population can lack certain groups of subjects (e.g. obese), the measurements are taken in supine posture, some measured area, other volume of AT etc. Even if a particular study was chosen, the information about exact spatial distribution of the AT is not covered by any of the studies. The information about area or volume could however be used to derive some constraints. For example, Machann et al. (2005) performed full body MRI scans on 80 overweight and obese subjects and captured SCAT and VAT per imaging slice. Such data could be used to attempt adjusting AT contents along the cranial caudal direction.

Perhaps the only processed dataset that describes the distribution of AT in three dimensions comes from the work of Holcombe and Wang (2014). They created SCAT maps of the torso based on over 17000 CT scans. Each map is a texture in which the y-coordinate corresponds to position along the spine, x-coordinate is perpendicular to spine. Each texel (texture element) denotes the width in mm of the SCAT. This is measured based on the boundary contours of the skin and "fascial envelope", i.e. the boundary between abdominal and paraspinous musculature; or the boundary of bony pelvis and gluteal musculature in the pelvic region; or the chest wall including the bony ribcage, costal cartilage, intercostal musculature and sternum in the chest region. The SCAT width for any given point on the skin is then defined as the distance from this point to the nearest point on the fascial envelope.

The data from Holcombe and Wang (2014) also contain information about BMI. Therefore, it could be used to create a geometrical constraint of SCAT based on a changing BMI. But a major complication is the fact that all the data comes from CT scans taken in a supine posture. It is expected that the AT compartments move significantly with a change of posture due to effects of gravity, especially for obese subjects, whose AT compartments have high mass.

Morphing approaches have so far not used VAT and SCAT as targets, the size of those compartments was morphed only implicitly through external shape targets. This does not necessarily discredit the results of impact tests with such models, as even though they may have wrong ratios of SCAT and VAT, the overall mechanical response may be the same since the material properties for both AT are likely similar in currently used HBMs. However, having realistic VAT/SCAT targets would enable to study in more details the impact of the different fat types, particularly the subcutaneous one, on the load seen by internal structures (e.g. organs, ribcage). Also, for very obese subjects, it would help with the realism of abdominal folds.

| Author | Method | VAT area equations | $R^2$ (%) | Age range (y) | Cross-validation |
|---|---|---|---|---|---|
| **Seidell et al. [91]** | CT | = (0.35*BMI) + (1.48*∑ umbiliusSF and suprailiacSF) + (34.122*WHR) + (0.06*age) – 37.322 *(M)* | 81.9 | 19-85 | no |
| | | = (0.367*BMI) + (WTR*10.911) + (0.994*menopausal state[a]) – 15.083 *(F)* | 79.5 | | |
| **Kvist et al. [94]** | CT | VAT ($cm^3$) = (0.731*sagittal diameter[b]) – 11.5 *(M)* | 81.0 | 24-64 | yes |
| | | VAT ($cm^3$) = (0.370*sagittal diameter[b]) – 4.85 *(F)* | 79.6 | | |
| **Weits et al. [99]** | CT | = (3.27071*WC) + (3.74794*HC) – 558.25696 *(M)* | 74.0 | 16-81 | yes |
| | | = (2.00558*WC) + (2.32435*HC) – 319.21927 *(F)* | 56.0 | | |
| **Ferland et al. [98]** | CT | = (1.0652*weight) + (1.6649*abdominalSF) + (1.6934*subscapularSF) + (200.9726*WHR) + (1.7137*age) – 292.1026 *(F)* | 73.7 | 23-50 | no |
| **Despés et al. [102]** | CT | = (2.843*WC) + (2.125*age) – 225.39 *(M)* | 74.0 | 18-42 | no |
| **Koester et al. [103]** | CT | = (3.4838*WC) – (67.0158*log chest ratio[c]) – 157.7378 *(M)* | 67.0 | 18-30 | yes |
| **Kekes-Szabo et al. [95]** | CT | = (4.37*WC) +(0.75*age) + (1.26*abdominalSF) – (1.55*∑legCC[d]) – 202.04 *(M)* | 73.0 | 18-71 | yes |
| **Bonora et al. [76]** | MRI | = (6.37*WC) – 453.7 *(M)* | 56.0 | 22-70 | no |
| | | = (4.04*WC) + (2.62*age) – 370.5 *(F)* | 68.0 | | |
| **Kekes-Szabo et al. [96]** | CT | = (2.57*umbilicusCC) + (0.69*suprailiacSF) + (0.92*age) – 188.61 *(F)* | 75.0 | 17-76 | yes |
| **Schreiner et al. [97]** | MRI | [c] WHR, age *(M)* | 32.9 | 48-68 | no |
| | | [c] WC *(F)* | 42.8 | | |
| **Stanforth et al. [107]** | CT | Ln (VAT) = (0.05*BMI) + (3.2*WHR) + (0.02*age) + (0.36*race[f]) – 0.70 *(M)* | 78.0 | 17-65 | yes |
| | | Ln (VAT) = (0.05*BMI) + (1.85*WHR) + (0.02*age) + (0.22*race[f]) + 0.33 *(F)* | 73.0 | | |
| **Brundavani et al. [104]** | CT | = (1.09*weight) – (2.29*BMI) + (6.04*WC) – 382.9 *(M)* | 74.2 | 40-79 | no |
| | | = (5.19*WC) – (0.86*weight) – 278 *(F)* | 62.6 | | |
| **Bouza et al. [105]** | CT | = (3.413*WC) – (2.281*HC) + (3.306*age) – 27.765 *(M+F)* | 62.0 | 18-78 | no |
| **Goel et al. [106]** | MRI | = (16.9*age) + (934.18*sex[g]) + (578.09*BMI) – (441.06*HC) + (434.2*WC) – 238.7 *(M+F)* | 52.1 | 15-50 | no |
| **Eastwood et al. [108]** | CT | = [h] (1.87*age) + (2.80*weight) – (1.79*height) + (7.57*WC) – (4.91*HC) – (2.85*TC) + 67.88 *(M)* | 69.0 | 58-85 | yes |
| | | = [h] (0.90*age) + (2.71*weight) + (2.62*WC) – (1.75*TC) – 250.86 *(F)* | 62.0 | | |
| | | = [i] (0.94*age) + (8.63*WC) + (1.47*TC) – (3.86*HC) – 422.31 *(M)* | 73.0 | | |
| | | = [i] (2.20*age) + (3.20*weight) – (2.42*height) + (3.35*WC) – (4.93*HC) + 323.39 *(F)* | 56.0 | | |
| | | = [j] (1.18*age) + (2.16*weight) – (2.35*height) + (6.56*WC) – (2.15*HC) – (1.81*TC) + 39.24 *(M)* | 61.0 | | |
| | | = [j] (1.13*age) + (6.28*weight) – (2.47*height) + (1.85*WC) – (3.71*HC) – (4.35*TC) + 475.69 *(F)* | 55.0 | | |

AT=adipose tissue; BMI = body mass index ($kg/m^2$); WC = waist circumference (cm); HC = hip circumference (cm); TC = thigh circumference (cm); CC= circumference (cm); WHR = waist-to-hip ratio; WTR = waist-to-thigh ratio; VAT = visceral adipose tissue ($cm^2$); CT = computed tomography; MRI = magnetic resonance imaging; M = for men, F = for women; [a] 1 = postmenopausal, 0 = premenopausal; [b] obtained by CT (cm); [c] logarithm of the chest circumference divided by the chest skinfold thickness; [d] ∑legCC = sum of the mid-thigh and lower thigh circumference (cm); [e] exact equation not given; [f] black = 0, white = 1; [g] male = 1, female = 2; [h] white European; [i] African Caribbean; [j] South Asian; sagittal diameter (cm); age (years).

*Figure 17: Equations for computing VAT area at umbilical level. Source of figure: (Scafoglieri et al. 2014).*

| Author | Method | SAT area equations | $R^2$ (%) | Age range (y) | Cross-validation |
|---|---|---|---|---|---|
| Seidell et al. [91] | CT | = (0.157*BMI) + (1.63*∑ umbiliusSF and suprailiacSF) + (29.159*WHR) + (0.051*age*) – (10.694*WTR) – 18.798 *(M)* | 79.4 | 19-85 | no |
| | | = (0.373*BMI) + (1.301*∑ umbiliusSF and suprailiacSF) – 3.327 *(F)* | 84.2 | | |
| Weits et al. [99] | CT | = (10.58479*BMI) + (3.20392*HC) – 430.0784 *(M)* | 71.0 | 16-81 | yes |
| | | = (12.47853*BMI) + (4.43236*HC) – 505.06653 *(F)* | 77.0 | | |
| Koester et al. [103] | CT | = (3.9545*WC) + (1.0041*∑ abdominalSF and suprailiac SF) – 297.2438 *(M)* | 78.0 | 18-30 | yes |
| Kekes-Szabo et al. [95] | CT | = (3.98*umbilicusCC) + (2.31*chestSF) + (3.41*suprailiacSF) + (1.84*age) – 398.78 *(M)* | 77.0 | 18-71 | yes |
| Bonora et al. [76] | MRI | = (9.37*BMI) + (5.51*HC) – 621.0 *(M)* | 87.0 | 22-70 | no |
| | | = (24.5*BMI) + (2.26*age) – 332.9 *(F)* | 87.0 | | |
| Kekes-Szabo et al. [96] | CT | = (11.86*BMI) + (3.12*umbilicusCC) + (2.22*suprailiacSF) + (1.32*horizontal abdominalSF) – (2.63*shoulderCC) – 155.85 *(F)* | 81.0 | 17-76 | yes |
| Schreiner et al. [97] | MRI | [a] $WC^2$, tricepsSF, HC, height, $age^2$ *(M)* | 74.1 | 48-68 | no |
| | | [a] WC, HC *(F)* | 75.5 | | |
| Bouza et al. [105] | CT | = (7.245*BMI) + (8.653*HC) – (78.262*$sex^b$) – (1.765*age) – 683.11 *(M+F)* | 76.0 | 18-78 | no |
| Goel et al. [106] | MRI | = (783.3*BMI) + (466*HC) – (17.15*age) + (1016.5*$sex^c$) – 49376.4 *(M+F)* | 67.1 | 15-50 | no |
| Eastwood et al. [108] | CT | = [d] (2.29*weight) + (2.34*WC) + (2.49*HC) – (1.19*age) – (2.00*height) – 28.95 *(M)* | 72.0 | 58-85 | yes |
| | | = [d] (3.76*weight) + (7.01*HC) – (0.99*age) – (3.07*height) – (3.03*TC) + 24.98 *(F)* | 80.0 | | |
| | | = [e] (3.83*WC) + (6.52*HC) – (0.08*age) – (2.09*height) – (1.23*TC) – 373.61 *(M)* | 81.0 | | |
| | | = [e] (0.23*age) + (2.24*WC) + (9.48*HC) – 896.27 *(F)* | 86.0 | | |
| | | = [f] (0.63*age) + (3.88*weight) – (3.21*height) + (1.43*WC) + (2.54*HC) + 48.58 *(M)* | 75.0 | | |
| | | = [f] (3.94*weight) + (5.63*HC) – (1.72*age) – (5.21*height) + 404.25 | 81.0 | | |

AT = adipose tissue; BMI = body mass index ($kg/m^2$); WC = waist circumference (cm); HC = hip circumference (cm); TC = thigh circumference (cm); CC= circumference (cm); WHR = waist-to-hip ratio; WTR = waist-to-thigh ratio; SF = skinfold (mm); SAT = abdominal subcutaneous adipose tissue ($cm^2$); CT = computed tomography; MRI = magnetic resonance imaging; M = for men, F = for women; [a] exact equation not given; [b] male = 1, female = 0; [c] male = 1, female = 2; ; [d] white European; [e] African Caribbean; [f] South Asian; age (years).

*Figure 18: Equations for computing SCAT area at umbilical level. Source of figure: (Scafoglieri et al. 2014).*

### 2.6.3.Abdominal organs

There are numerous studies that document how correlated is the weight of organs with some basic anthropometric measurements like weight, height or BMI. For instance, de la Grandmaison, Clairand, and Durigon (2001) gathered data from 684 autopsies performed in France on Caucasian subjects and reported positive correlation of weights of heart, liver, spleen and kidneys to the BMI. Linear interpolation results $R^2$ were significant but small in most cases (less than 0.5), with the exception of the liver and heart, plus the kidneys for females (Figure 19). However, the population characteristics (average BMI and range) also suggest a limited representation for high BMI subjects, correlations between variables (e.g. age and BMI) could skew the analysis, and some regressions could be nonlinear. This could be checked if the original data were available.

Vadgama et al. (2014) performed similar study in India, arriving to the same conclusion except for spleen, for which no significant correlation was found. Bhoi et al. (2017) did another study based on Indian subjects and confirmed correlation of organ weights with the subject weights, but did not measure the height, therefore correlation to BMI could not be computed. Chirachariyavej et al. (2006) did a study based on Thailand population, Garby et al. (1993) in Denmark etc. While the exact values

obviously differ based on other factors such as age, sex and ethnicity, it is clear that organ weights increase with BMI, at least for the solid abdominal organs.

Weight or volume may not be an easily enforceable geometrical constraint in many numerical transformation methods, but it could be checked at the end of a transformation based on a shape target. Then the shape could be adapted based on the weight difference and simple geometrical assumptions after a first transformation.

| | Males | | | Females | | |
|---|---|---|---|---|---|---|
| | Height | BMI | Age | Height | BMI | Age |
| Heart | 0.64 | 0.77 | 0.87 | 0.01 (ns) | 0.61 | 0.78 |
| Right lung | 0.41 | 0.01 (ns) | 0.05 (ns) | 0.43 | 0.18 | 0.03 (ns) |
| Left lung | 0.49 | 0.06 (ns) | 0.04 (ns) | 0.4 | 0.13 | 0.02 (ns) |
| Liver | 0.88 | 0.61 | 0.33 | 0.8 | 0.57 | 0.62 |
| Spleen | 0.7 | 0.11 | 0.17 | 0.42 | 0.21 | 0.11 |
| Pancreas | 0.08 (ns) | 0.28 | 0.05 (ns) | 0.69 | 0.07 (ns) | 0.04 (ns) |
| Right kidney | 0.4 | 0.39 | 0.3 | 0.72 | 0.66 | 0.21 |
| Left kidney | 0.45 | 0.36 | 0.32 | 0.68 | 0.62 | 0.28 |
| Thyroid | 0.26 | 0.21 | 0.22 | 0.01 (ns) | 0.08 (ns) | 0.08 (ns) |

[a] ns: Non significant.

*Figure 19: Linear interpolation results ($R^2$ values) of organ weights with height, BMI and age for males and females. Source of figure: (de la Grandmaison, Clairand, and Durigon 2001).*

Creating SSM of abdominal organs has been of interest for predicting organ locations for automated segmentation of CT/MRI images. For example, Gauriau et al. (2015) uses machine learning techniques for predicting organ positions using a set of manually segmented images as the database for learning. Okada et al. (2015) uses a similar approach, but apart from the learning database also requires at least one organ's shape to be specified as an input. Based on this input and the regression created in the learning phase the algorithm predicts the shapes of other organs. The authors claim that the shape prediction of other organs becomes more precise when such additional input shape of at least one organ is provided. Other similar approaches include Cuingnet et al. (2012) or Criminisi et al. (2011). The issue of variability of the organ shape based on anthropometric or BMI differences is not addressed in those publications and the authors do not state the anthropometric measurements of the subjects used in their tests. Therefore, it does not allow determining if the organ weights changes with BMI (e.g. liver) are associated with growth in specific regions.

(Lu et al. 2013) focused on the liver as the organ most often injured during car crashes. The authors created a SSM of liver using PCA based on liver samples from 15 adult subjects in a seated posture. Their results demonstrated that the changes of shape between different subjects are irregular, stressing the need for non-linear morphing method.

Apart from the assumed differences based on anthropometric measurements, position and shape of organs are also affected by the postural differences (Lafon et al. 2010; Hayes et al. 2013). The results of these studies should be taken into account when processing data acquired from CT or MRI supine scans. However, none of the subjects were obese, and no information is provided about the distribution of fat. No studies were found on the correlation between organ location (e.g. ribcage coverage of the liver) and BMI either.

### 2.6.4.Skeleton

While there has been some effort on creating morphing targets for bones, it is usually performed in the context of personalizing individual bones for the purpose of personalized prosthetic design, e.g. for hip replacement (B.-K. Park et al. 2014) or knee arthroplasty (Zhu and Li 2011, 3). As the survey of Sarkalkan, Weinans, and Zadpoor (2014) states: *not many statistical models of shape and appearance are currently available. Statistical models are only available for a limited number of bones such as femur, acetabulum, tibia, and scapula. Even when the models are created for a specific bone, they are often not publicly or commercially available, meaning that the access of the bone research community to statistical models is currently limited.*

Wang et al. (2016) created a statistical model of ribcage, including all ribs, sternum and thoracic spine, that correlate the size and shape of the ribcage to various parameters such as BMI, age, sex or height. The authors have found height and age-sex interaction to be dominant parameters for determining the size of the ribcage and age, sex, height and BMI for the shape. Figure 20 shows the impact of those parameters on the ribcage. A BMI increase was found to affect the lower ribcage dimension more than the upper ribcage, and to make the ribs more horizontal. The model was based on 101 adult subjects and used the THUMS model as the baseline geometry model. However, these models are not currently publicly available.

Fréchède et al. (2013) disseminated efforts on creating statistical models of individual bones in more details. The publication contains references to several SSMs of ribcage, spine, pelvis, femur, knees, femur etc. However, majority of the models are based on variation of sex, age and/or height. Therefore it is not directly possible to assess whether the subjects used for creating the models were obese or not, which limits their utility for the purposes of morphing towards obese subjects.

The morphing studies done at UMTRI use SSMs of pelvis, ribcage and femur collected on different subjects (Shi et al. 2015), not an entire skeleton per subject. Such a whole body skeletal SSM would be useful to use in conjunction with an external statistical shape model to ensure a realistic bony shape

in other regions (thickness of long bones, etc.). However, many of the datasets seem derived from clinical imaging of specific regions for which anthropometric measurement and even sometimes the subject height and weight are not available. Indirect correlations could possibly be derived based on external measurement and soft tissue thickness.

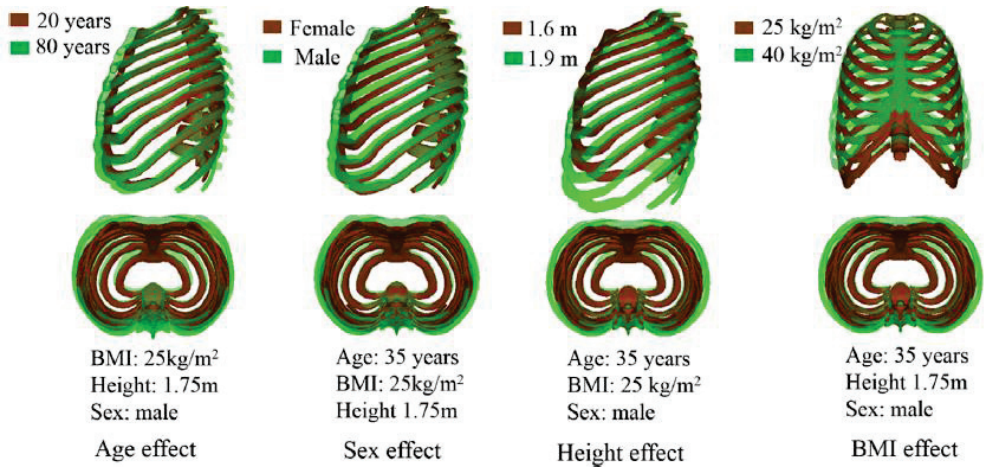


*Figure 20: Effect of age, sex, height and BMI on ribcage size and shape. Source of figure: (Wang et al. 2016).*

### 2.6.5.Target assembly

As the data reviewed in this section were all collected in different studies, using different samples, assembling them could be considered. The data are of different nature: some could be constraints (e.g. fat contents ratio) while others are shape models which could be more directly applicable.

As statistic shape models are only available on specific structure, assembling them would be required. That is likely to be challenging, since shape targets created based on the separate SSMs (e.g. external shape, bone, solid organs) are likely to be inconsistent with each other.

A constrained method similar to the one described by Okada et al. (2015) may be usable. Okada et al. (2015) used an initial shape of liver and/or kidneys as constraints to predict the shape of other organs. However, this requires having overlap between statistical shape models. For making a coherent bone-organ-fat target, it would be beneficial if one could be an input constrained for the other, allowing for a hierarchical construction of the target. For example, if organ shapes could be predicted based on the amount of SCAT, the fat could be (one of) the initial constraints. The relationships between organ and skeletal shapes could be used, etc. However, such relations are currently not available.

Other ways of assembling the targets might be more pragmatic, albeit requiring more assumptions. For example, starting from the ribcage, enforcing non-penetration through a soft-body physics

simulation of the organs and relationships regarding organ weight might be sufficient conditions to add the solid organs to the skeleton. Fat contents could then be adjusted by deforming abdominal sections using hypotheses on the transformation, etc. The final target would then result from an optimization of the various constraints.

## 2.7. Conclusions and specific objectives of the work

Obesity is defined for health, and its definition may not be the relevant one for crash. BMI is used as main descriptor but it does not capture necessarily well fat distribution differences (among sexes, etc.) which may be relevant for crash. BMI is also sensitive to height and fitness, and should therefore be considered with caution.

Effects of obesity on abdomen response and injury, as well as local belt interactions (e.g. lap belt to abdomen) are not well described yet. It is unclear if the lap belt loading could lead to an increased risk which could be hidden in real world data due to lower extremity loading for example. Simulation studies could help answering such questions but models do not account for details such as internal organ weight, fat spatial distribution, and abdomen fold. Their realism for internal response or external interactions has not been verified.

One aim of the thesis is to develop a morphing methodology that could account for fat distribution and abdomen fold, and see how they affect the belt interaction and internal organ loading. Besides the numerical challenges it will create for morphing, such as number of control points and compatibility of internal constraints, building a plausible target including internal (e.g. fat spatial distribution) and external surfaces in seated position is needed.

Assembling different sources of information reviewed in this document (e.g. statistical shape models for various structures, constraints on fat distribution or organ weight, etc.) could already help building a more detailed target than was used up to now. However, ensuring the compatibility of these sources and the realism of their combination will be a challenge. Also, a majority of the information about internal structures and soft tissues are collected in a supine position, performing the changes from supine to seated may be problematic in the absence of reference data. This is also true for the abdomen fold which is not currently described seated in external shape scans.

Therefore, as the concept of an average obese seems irrelevant considering the variability and that the interactions between the belt and the abdomen is still poorly understood, it was decided to develop and validate a few subject specific models to attempt observing the main mechanisms involved. More specifically:

- develop a few subject specific models with relevant details (especially for the abdominal fold) rather than average models lacking details
    - Work on the geometrical data collection and PMHS testing required for the validation are presented in Chapter 3. Four PMHS were used.
    - The focus of the study was set on the geometrical personalization. Material properties characterization was left out of the main scope as other studies on this topic are currently ongoing (e.g. at University of Virginia (Gepner et al. 2018)).
- use a morphing approach: it was decided to use a morphing approach based on an existing model to save on development time and allow generating multiple models with different characteristics
    - Work on the methodology will be needed to assess and improve upon the performance of current morphing approaches. This will be detailed in Chapter 4.
    - The actual morphing and the target building is provided in Chapter 5. Three models were generated with varying levels of detail on the targets: one using skin target without the abdominal fold, one using skin target with the abdominal fold and one with using the skin target with abdominal fold and also target for subcutaneous fat.
- Exercise the morphed models against the experimental data collected to assess their ability to explain the test data and discuss the deformation patterns
    - Comparisons with belt loading tests and one sled test are provided in Chapter 6.

The interactions mechanisms will be discussed as part of Chapter 6 and the general conclusions.

# 3. Experimental data collection and processing

## 3.1. Introduction – Context and objectives

Data are required to construct a model of an obese person from a non-obese model, and then to calibrate it using impact testing. First, a geometrical target has to be defined to morph a HBM. There are numerous ways to obtain the external surface of the human body, but as Section 2.6 described, options become more limited when additional details are needed. Specifically, the geometry of the abdominal fold and subcutaneous fat in seated posture are not available from the published studies. Volumetric scans (CT, MRI) of Post Mortem Human Surrogates (PMHS) are plausible sources for such data as the use of volunteers would not be compatible with subsequent impact testing. An alternative could be a slicing approach as in the Visible Human project after testing but this would be much more complex than imaging and would only allow collecting information about one posture. One challenge with imaging is that it is typically obtained in a supine posture. In this posture, the shape of the abdomen differs significantly from the one in a seated posture, even for non-obese (Lafon et al. 2010). Therefore, collecting new imaging data of obese PMHS in a seated posture was specified as a necessary task for this study.

Furthermore, this study also aims to assess the relevance of the morphed models for safety simulation, with a focus on the abdomen and its fold. As very few obese PMHS tests are available in the literature and as these are essentially sleds (cf. Section 2.4.2), the PMHS used in the imaging task will also be considered for belt testing and sled testing. Using matched imaging and testing along with subject specific modelling is expected to help with the calibration and evaluation of the obese models by removing the specimen geometrical variability from the problem. Therefore, testing of the PMHS used in imaging was specified as another necessary task for the study.

These two tasks related to PMHS (imaging and testing) were mostly performed by CEESAR[4] with LBMC and LAB[5] defining the requirements and specifications. Detailed protocols were proposed by CEESAR, and then discussed, collectively improved and agreed upon. The PMHS collection, imaging and testing were all performed by CEESAR, either in their facilities or through other collaborations (imaging

[4] Centre Européen d'Etude de Sécurité et d'Analyse des Risques // European Centre for Security Studies and Risk Analysis

[5] Laboratoire d'accidentologie, de biomécanique et d'études du comportement humain // Laboratory of Accident Analysis, Biomechanics and Human Behaviour

centres, sled facility). LBMC participated to the positional imaging onsite and processed the imaging data. Test results were processed by CEESAR.

Independently of the primary contributor of each task, it is essential to summarize the process and results to understand the present study. Section 3.2 describes the protocols and methods used to process the PMHS: first the collection and preparation is described in Section 3.2.1, then the imaging protocols in Section 3.2.2 and finally the setup of the mechanical tests in Section 3.2.3 how the PMHS were obtained and provides their characteristics. Section 3.2.1 also contains an anthropometric description of the PMHS. Section 3.3 then describes results of the mechanical tests.

The imaging results were used in the generation of the morphed models as described in Chapter 5. The test protocols were modelled and the tests simulated as described in Chapter 6.

## 3.2. Methods

### 3.2.1. PMHS collection and preparation

Four PMHS were requested, based on the following specification defined in collaboration with CEESAR:

- Sex: 2 males, 2 females, to perform comparisons related to the internal fat distribution
- No hip replacements (to avoid imaging issues near the abdomen)
- Height between 1.6 and 1.8 m
- Waist to Height Ratio over 0.65 or BMI over 35 kg / $m^2$, i.e. well above the obesity threshold (Section 2.3). Those criteria were selected to ensure that the PMHS would have significant abdominal mass with a likely fold.

PMHS were procured by the “Centre du Don des Corps de l’Université René Descartes, Paris V” (Centre of Body Donation of University René Descartes, Paris V) according to the procedures and convention in place between CEESAR and the donation centre. As two suitable male PMHS were not found in due time, a third female PMHS was acquired. The height requirement was also slightly relaxed as suitable PMHS were difficult to find. The following identification codes were assigned to the PMHS: MS730 for the male PMHS and MS731, MS742 and MS743 for the three female PMHS. As will be reported below, the processing protocol for the first two PMHS was too long, which lead to increased deterioration of the bodies making them unsuitable for sled testing. Given this combined with the fact that the MS731 was just at the limit of obesity, it was not used for the simulation study. For this reason, the experimental results for MS731 will not be reported in this study.

After collection, the PMHS were instrumented. A temperature probe (inserted through the neck) was used to measure the internal temperature. Teflon and aluminium markers were stitched to the skin to be used as landmarks for the abdomen: these markers, visible on both the CT and laser scans (see Section 3.2.2), can therefore be used for aligning the geometrical data. Figure 21 shows one of the PMHS with these markers.

Two methods were used to position and maintain the bodies in an upright seated position: (1) a belt passing under the clavicles for MS730 or (2) an adjustable metal sliding rod mechanism mounted between the seat back and the skull for MS742 and MS743 (Figure 22).

A mix of antibiotics was applied to the PMHS to slow down the decay of the bodies (Potier 2010). Then the PMHS were frozen in a desired posture. Since different postures were initially required (seated, supine, standing), the PMHS had to be thawed several times. The protocol was designed to minimize the time the PMHS is not frozen. Nevertheless, changes were observed due to the freezing cycles, notably some weight loss. The following Table 1 shows the characteristics of the collected PMHS and documents the weight changes.

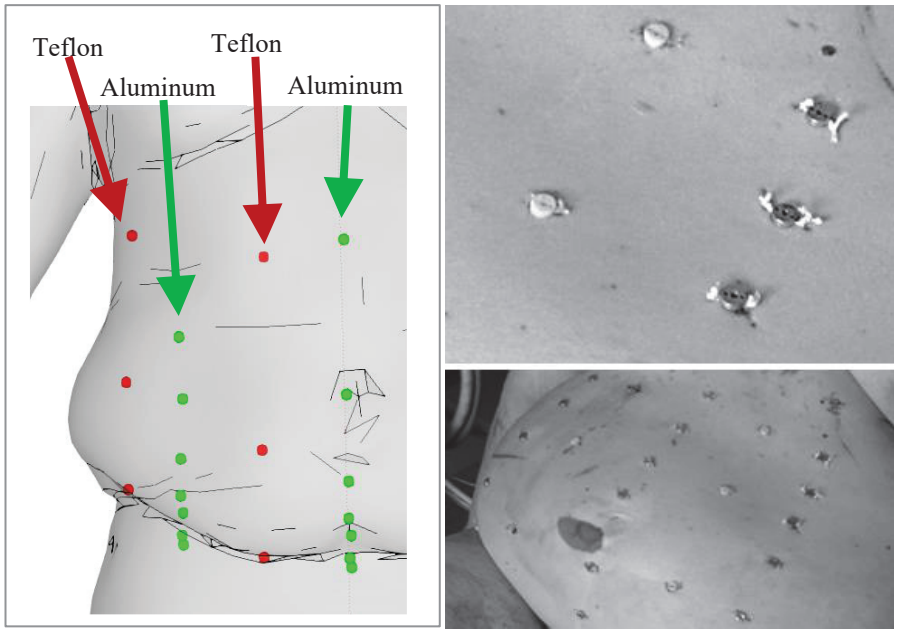


*Figure 21: Skin markers implanted onto the PMHS. Left: schematic view. Two different materials were used to be easier to distinguish on a side view of an X-ray. Right: detail and overview of one of the PMHS with markers.*

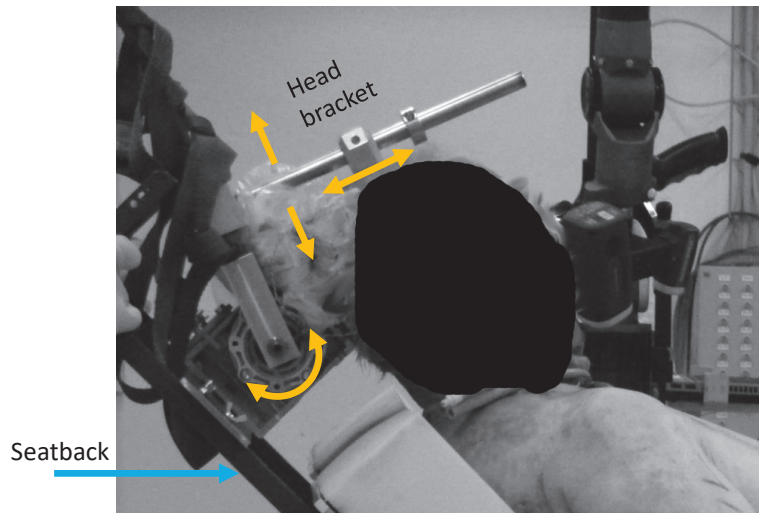


*Figure 22: A profile view of the sliding rod attached to the skull to facilitate head positioning. Adjustments are shown in orange. The head of the PMHS is edited out of the picture (painter over in black) for anonymity.*

*Table 1: Characteristics of the collected PMHS.*

| ***Parameter*** | ***Units*** | ***MS730*** | ***MS742*** | ***MS743*** |
|---|---|---|---|---|
| *Age* | *Years* | *66* | *89* | *87* |
| *Gender* | *Male/Female* | *M* | *F* | *F* |
| *Initial weight* | *kg* | *113* | *100* | *105* |
| *Stature* | *cm* | *176* | *161* | *153* |
| *Weight with antibiotics* | *kg* | *115* | *102* | *107* |
| *Weight after freezing/defrosting cycle* | *kg* | *93* | *100* | *101* |
| *Loss of weight after freezing/ defrosting* | *kg* | *22* | *2* | *6* |
| *BMI when collecting the PMHS* | *kg / m²* | *37.1* | *39.4* | *45.7* |
| *BMI after defrosting* | *kg / m²* | *30.0* | *38.6* | *43.1* |
| *Abdomen circumference (umbilicus level)* | *cm* | *118* | *129* | *135* |
| *Waist to Height Ratio* | *-* | *0.67* | *0.8* | *0.88* |

The MS730 was first to be processed. Based on that experience and the large weight loss, the protocol was shortened. Specifically, the standing posture was removed to focus on the essential position for the thesis application (seated for belt interaction). Table 2 summarizes the actions and their order that were done with each PMHS after it was acquired. The laser scan imaging and the belt tests (Sections 3.2.2.3 and 3.2.3) were planned to be performed within one and a half day (starting day 1 7:00, finishing day 2 12:00). The sled test, described in Section 3.2.3.2, was not performed with MS730 since the PMHS was too deteriorated. Improving the protocol allowed to keep the later PMHS (MS742 and MS743) in a condition deemed acceptable for the sled tests. Additional details about the PMHS handling, instrumentation and conservation will be published separately from this thesis in a paper led by CEESAR.

*Table 2: Sequence of experimental steps for each PMHS. The MS730 was the first processed PMHS, MS742 and MS743 last. The table documents how the protocol evolved to minimize exposure of the PMHS to room temperature. "CT", "MRI" and "Surface scan" are imaging techniques that will be described in Section 3.2.2. "MHA belt tests" and "Sled test" will be described in Section 3.2.3.2. *For MS743, the MRI scan was not performed due to malfunction of the scanner.*

| ***MS730*** | ***MS742 and MS743*** |
|---|---|
| ***Freezing in supine position*** | *MRI** |
| *CT supine (arms crossed)* | *CT supine (arms crossed)* |
| *Defrosting* | *MHA belt tests* |
| *MRI* | *Implanting abdomen markers* |
| *Implanting abdomen markers* | *Surface scan* |
| ***Freezing in seated position*** | ***Freezing in seated position*** |
| *CT seated* | *CT seated* |
| *Defrosting* | *Defrosting* |
| *Surface scan* | *Sled test* |
| ***Freezing in supine position*** | *Necropsy* |
| *CT supine (arms along body)* | |
| *Defrosting* | |
| *MHA belt tests* | |

## 3.2.2.Imaging protocols

### 3.2.2.1. Computed Tomography

The CT scans were acquired using the Siemens Somatom Definition AS scanner at "Radiology Service B" of the Cochin Hospital, Paris. In order to get realistic pulmonary volumes, the lungs were inflated with approximately two litres of air through a tracheotomy tube, which was held closed during the scan. The PMHS were frozen in a seated position on the adjustable seat that was used in the positioning study.

The seating posture selected for the study is close to the one of the GHBMC M50-O model. The seatback was set at an angle of 22.5 degree with respect to the vertical and seat pan at a 14-degree angle with respect to the horizontal. The seatback was covered with foam. For the MS730, the seatback angle may differ by 2 to 3 degrees from the 22.5-degree target. In order to be able to put the body in the body container, the head and the lower legs were moved rearward (neck extension and feet plantarflexion). For each PMHS, one CT scan of the whole the body was performed at a resolution of 1 by 1 by 0.5 mm per voxel).

As the field of view could not be enlarged beyond 50 cm in diameter, the knees, elbows and parts of soft tissues on arms were always missing from the scan. For MS730 (which was taller than the others), the anterior part of thorax and the face were also missing. This is shown in Figure 23.

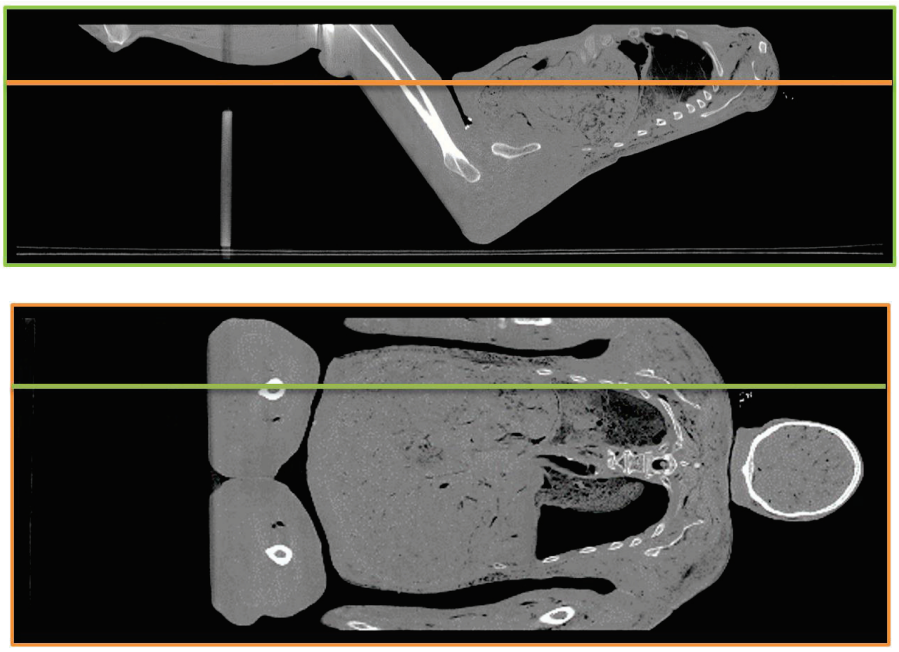

*Figure 23: CT scan of the MS730 in a seated posture. Upper: sagittal view, note the missing knees, feet, and part of the chest. Lower: coronal view, note the missing elbows and soft tissues on arms. Orange and green lines denotes the lower and the upper slice, respectively.*

Two containers were used for the PMHS: one smaller for the supine posture (easier to handle and used for all PMHS at CEESAR) and a larger one custom built for the seated posture and the space available in the CT scanner. Figure 24 shows photos of both next to including the CT scanner. Two supine postures differing in the placement of arms were tested: arms along the body, or arms in front of the abdomen (i.e. wrists were joining at the lower abdomen level). The position with arms across saves space and was used by CEESAR in their previous experiments. The larger container was used for the configuration with arms along the body. Placing the arms along the body has the benefit of not interfering with the shape of the abdomen, which was the main aim of the study. On the other hand, placing the arms over the body has the benefit of capturing the bones in arms in their entirety, which is not true for the other configuration due to limitations in terms of field of view (as for the seated posture, illustrated by Figure 23. This meant that the supine posture with arms across, the only configuration capturing the entire skeleton, was used to create the skeletal target. Therefore, the supine posture with arms along the body was not performed for MS742 and MS743 (as can be seen in Table 2) due to constraints associated to body conservation.

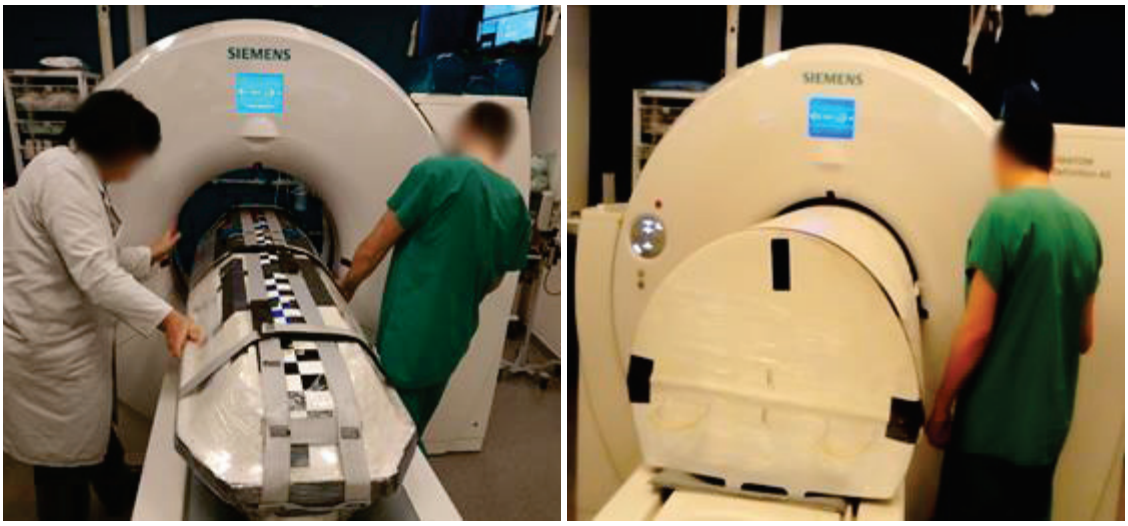


*Figure 24: CT scanning of the PMHS. Left: smaller container for supine posture with arms crossed. Right: larger container for the other postures.*

#### 3.2.2.2. Magnetic Resonance Imaging

MRI scans of the PMHS were acquired using a Philips scanner with a magnetic induction 1.5 Tesla in the Service Hospitalier Frederic Joliot (Orsay). They were intended to complement the CT-scans with a better view of the soft tissues: as Figure 25 illustrates, MRI makes it easier to distinguish different layers of tissues when compared to the CT scans in Figure 23.

However, there were also some practical limitations. The axial field of view being limited to 30 cm of length, the PMHS were imaged in several parts and then assembled to capture the entire PMHS. More importantly, the diameter of the machine (55.9 cm) only allows using the smaller container and therefore a supine posture (see Section 3.2.2.1).

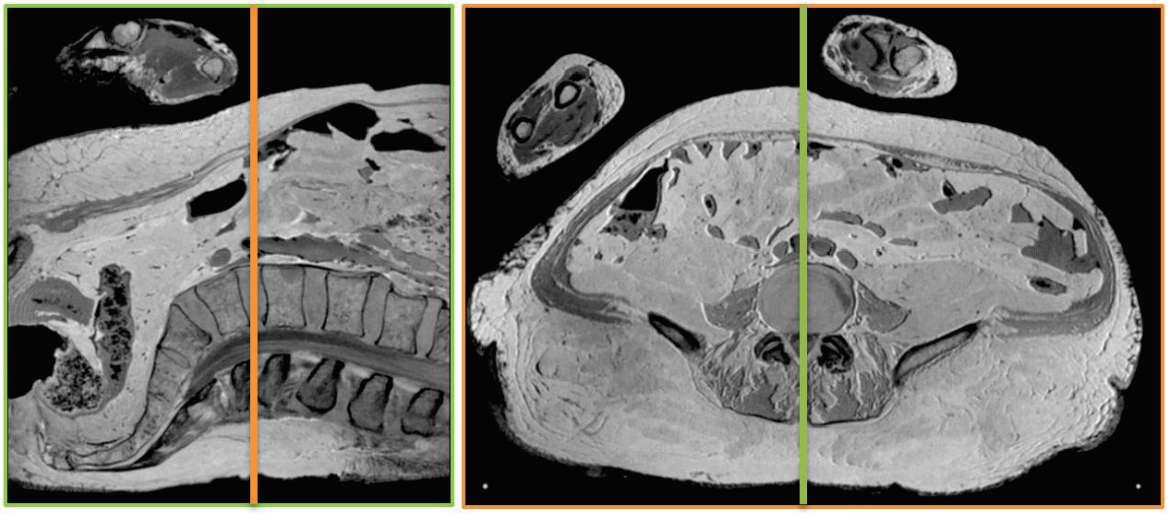

*Figure 25: MRI scan of the MS730. Left (green): sagittal view in the area of the lumbar spine. Right (orange): axial view at the lowest lumbar vertebra (L5). Orange and green lines denotes the right and the left slice, respectively.*

#### 3.2.2.3. Laser surface scan

A handheld laser scanner Nikon ModelMaker MMDx200 mounted onto a seven axes MCA II measuring arm was used to capture the surfaces of the PMHS (Figure 26). This setup allowed capturing almost the entire PMHS without having to reposition the scanner and thus changing the coordinate system.

The scans were performed in the seated posture with the same seatback and seat pan angles as the ones used for belt tests (Section 3.2.3). Additional scans were also performed in a supine posture and in several intermediate postures with a progressively more reclined seatback to quantify the changes of shape of soft tissues in these postures. While the data from these postures were not used for this study, they could be helpful for future projects studying different seating positions that might become available with automated vehicles (Grébonval et al. 2019).

Post-processing was performed using the Nikon Focus software. The seat and other support structures captured during the scanning process were separated from the body. The head was deleted to anonymize the data. The remaining points were decimated and, after using the built-in reconstruction functions, exported as a triangular surface for target building (Section 5.2.3).

The limitations of the laser scan, compared to the CT, is that only visible surfaces can be scanned and only if the scanner positioning is possible: the back and the backside of legs and difficult to reach areas between the trunk and arms cannot be scanned. As the main focus was on the shape of the abdomen, the arms were moved away when necessary to facilitate abdomen scanning and so the arms were only partially captured. Figure 27 contains an overview of the full body scans of the PMHS.


*Figure 26: The laser scanner (left) and measuring arm (right) used for surface scanning. Image source: www.nikonmetrology.com (left), metrisusa.wordpress.com (right), accessed May 2020.*

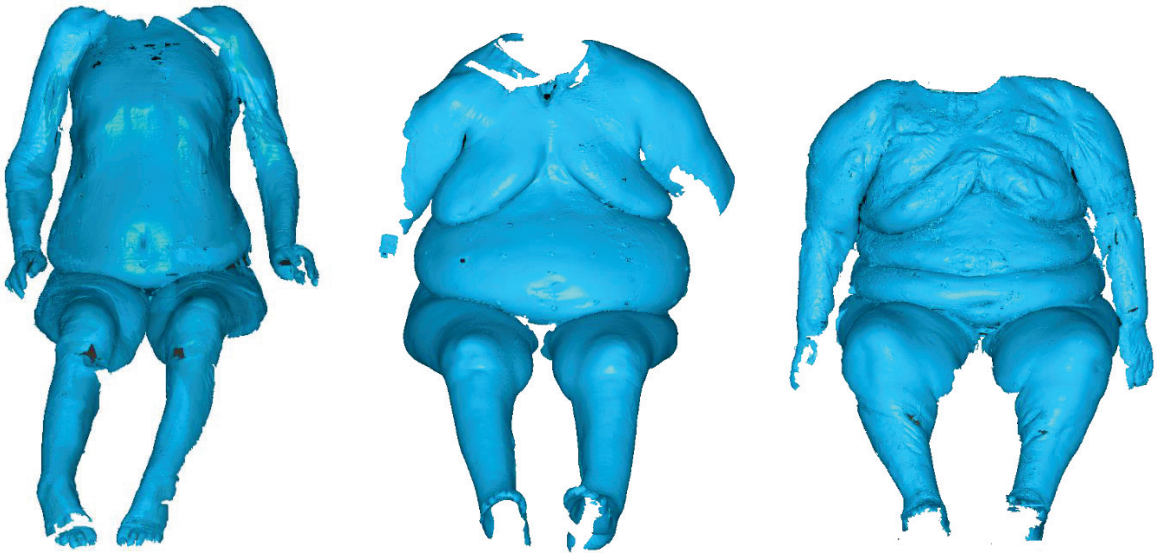

*Figure 27: Laser scans of the three PMHS. Left: MS730, middle: MS742, right: MS743.*

## 3.2.3.Setup of mechanical tests

### 3.2.3.1. Belt tests

Modelling the abdomen and its fold is the primary aim of this study. As seen in the literature review, experimental data are available regarding material properties and the full body kinematics was observed in sled tests (Section 2.4.2). However, at the intermediate level, the interaction of the belt with the abdominal fold and surrounding tissues, which seems essential to ensure the relevance of the model response, has never been reported. A series of experiments quantifying the mechanical behaviour of the abdomen and its interaction with a seatbelt was designed and then performed by CEESAR for each of the PMHS.

The PMHS was positioned in a rigid seat equipped with a lap belt connected to a hydraulic pulling servo controlled piston (more details can be found in Lamielle et al. (2008), who used the same equipment). For each PMHS, three belt positions (illustrated in Figure 28) were tested:

- Belt inside the abdominal fold ("belt inside"): this configuration is targeting the response of the tissues around the pelvis to represent the case where the belt is on it (initially or after moving inside the fold).
- Belt parallel to the seat placed just above the legs ("belt parallel"): this configuration aims to exercise the tissues of the fold.
- Belt just above the umbilicus, such that it passes over the pelvis ("belt high"): this configuration aims to compress the tissues of the abdomen while reducing the involvement of the fold.

In all cases, in order to limit the risk of injury, force and stroke limits were set.

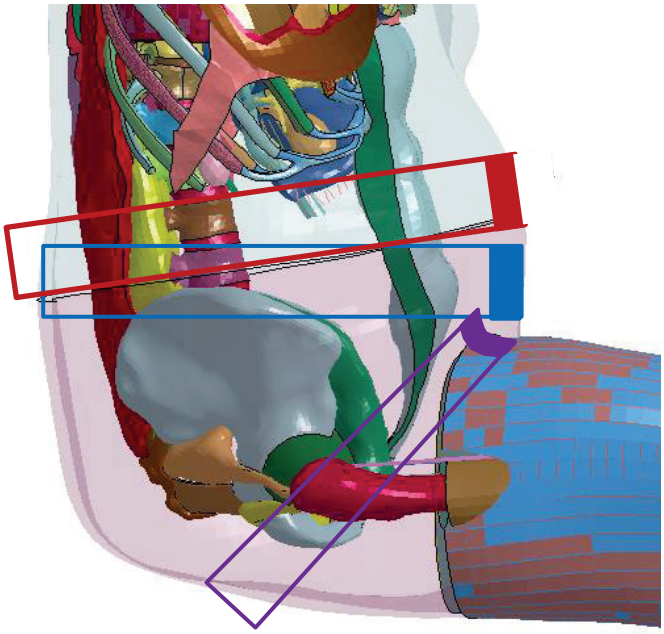

*Figure 28: Belt configurations for the Belt tests. Red: belt high over the umbilicus; blue: belt parallel to the seat; purple: belt inside the abdominal fold. The configurations are shown on the GHBMC BMI 35 without fold developed to check numerical approaches (see Chapter 4).*

Before each test, a Faro Arm[6] was used to capture the position of the abdominal markers on the PMHS, the belt markers, and also several notable points on the seat, to model the conditions of the experiment as closely as possible. Furthermore, a lateral X-ray of the pelvic area was performed in

[6] https://www.faro.com/products/3d-manufacturing/faroarm/

position to document the position of the belt (onto which radio opaque markers were attached) in relation to the pelvis.

The angles of the seat were kept the same for each configuration: 14 degrees for the seat pan relative to the horizontal plane, and 22.5 degrees for the seatback relative to the vertical plane. The lower legs were not constrained, but a strap just above the knees was used to hold the thighs in position. Arms were tied above the PMHS to prevent them from interfering with the abdomen or masking the belt. Figure 29 illustrate this positioning using photos from one of the tests.


*Figure 29: Illustration of the belt test setup for the parallel configuration. A custom device (called MP2D) used to measure the displacement on the centre of the abdomen can be seen on the right side of the right photo.*

The belt was pulled through buckles and cables attached to its ends. This motion is generated by a hydraulic piston. The motion is transmitted to the belt cables through an articulated bar system with a 3.5 multiplication factor, i.e. each 1 mm displacement of the piston results in 3.5 mm cable displacement. Table 3 contains the numbers assigned to each test and used in the rest of the text along with the cable displacements for each test. Note that the belt does not unload after the target displacement is reached.

*Table 3: Test numbers used to denote the individual belt tests. The stroke profile is provided for each test.*

| ***PMHS:*** <br> ***Belt configuration:*** | ***MS730*** | ***MS742*** | ***MS743*** |
|---|---|---|---|
| *High* | *MHA387* <br> *100 mm / 100 ms* | *MHA418* <br> *142 mm / 110 ms* | *MHA422* <br> *142 mm / 110 ms* |
| *Parallel* | *MHA388* <br> *100 mm / 100 ms* | *MHA420* <br> *142 mm / 110 ms* | *MHA423* <br> *148.5 mm / 110 ms* |
| *Under* | *MHA389* <br> *76 mm / 90 ms* | *MHA421* <br> *76 mm / 90 ms* | *MHA424* <br> *76 mm / 90 ms* |

Four cameras set at 2 000 frames per second were used to capture each experiment. One was positioned in front of the PMHS, one to the left side of the PMHS, and one between the first two cameras. The fourth camera was used to monitor the relative displacement between the back of the PMHS and the seat back. For this, a marker at the end of a short rod implanted in the spine was tracked. The footage from the cameras was used to track the trajectories of markers on the belt. The tracking is in the X-Z plane (medio lateral motion is assumed negligible). Other measurements included:

- The displacement and rotation of the hydraulic piston controlling the pulling mechanism, which is linked to the displacement of the cable pulling the belt (through a mechanism with lever arms).
- The pull time history of the cable attached to the belt. Measured by a string potentiometer attached to the cable.
- The displacement of the centre of the belt (mid abdomen). Measured by a custom sensor (MP2D) consisting of a mechanical arm with two joints attached to the centre of the belt (see Figure 29). The rotation of the arms is measured and used to compute the displacement of the endpoint in the X (posterior-anterior) and Z (superior-inferior) axes.
- Belt force. Measured by sensors on the left and right side. Total belt force is computed by adding the two measurements.

Note that due to equipment malfunctions, the following data is not available:

- For MS742 the X-rays are not available.
- For MS742, test MHA418, the cable displacement is not available. The displacement of the belt is therefore estimated using the camera footage as a replacement.
- For MS730, test MHA388, the MP2D sensor failed, therefore the displacement of the centre of the abdomen is not available.

#### 3.2.3.2. Sled tests

The sled test aims to recreate restraint conditions a car occupant could face during a frontal crash. Unlike the belt tests in Section 3.2.3, the PMHS may sustain injuries. Therefore, these tests were always scheduled as the last action with the PMHS. As already mentioned in Section 3.2.1, the MS730 was not subjected to sled testing as it deteriorated too much during the previous processing.

The tests were performed by CEESAR and Faurecia at Faurecia facility in Brières-les-scellés. The seat used for the test had a foam on the back to prevent potential injuries during the rebound (unlike the rigid seat used for the belt tests). It is a so called semi-rigid seat (Uriot et al. 2015) for which the model is available. The seat pan and anti-submarining guards are mounted on springs whose stiffness can be adjusted. The feet are fixed to a plate in front of the model. A three-point belt with pre-tensioners on both lap and shoulder belts was used (Renault: Espace V – n°878176089R). The time to fire (TTF) of these two pre-tensioners were 18ms and 25ms, respectively. In addition, a 4kN load limiter was used at the shoulder belt. The seat is placed on a reverse sled (i.e. the sled is immobile initially and accelerated up to the equivalent impact speed) as shown in Figure 30.

Different acceleration pulses were used for the two PMHS. For MS742, a velocity of 50km/h with a peak acceleration of 32g was used (Figure 31). Post-test autopsy showed that the pelvis sustained 28 fractures, including six disjunctions of the pelvic ring (Figure 32). This may be attributed in part to low mineralization of the bones, which could be observed on the CT. However, this casted some doubt on the usability of the response for modelling after the fracture is initiated unless the fracture can be simulated with the HBM, which would seem difficult considering the little information available on the fracture process and timing. Therefore, for MS743, the sled velocity was lowered to 30km/h and the peak acceleration to 8g in order to reduce the risk of injury (Figure 31). No fractures were found after the test.

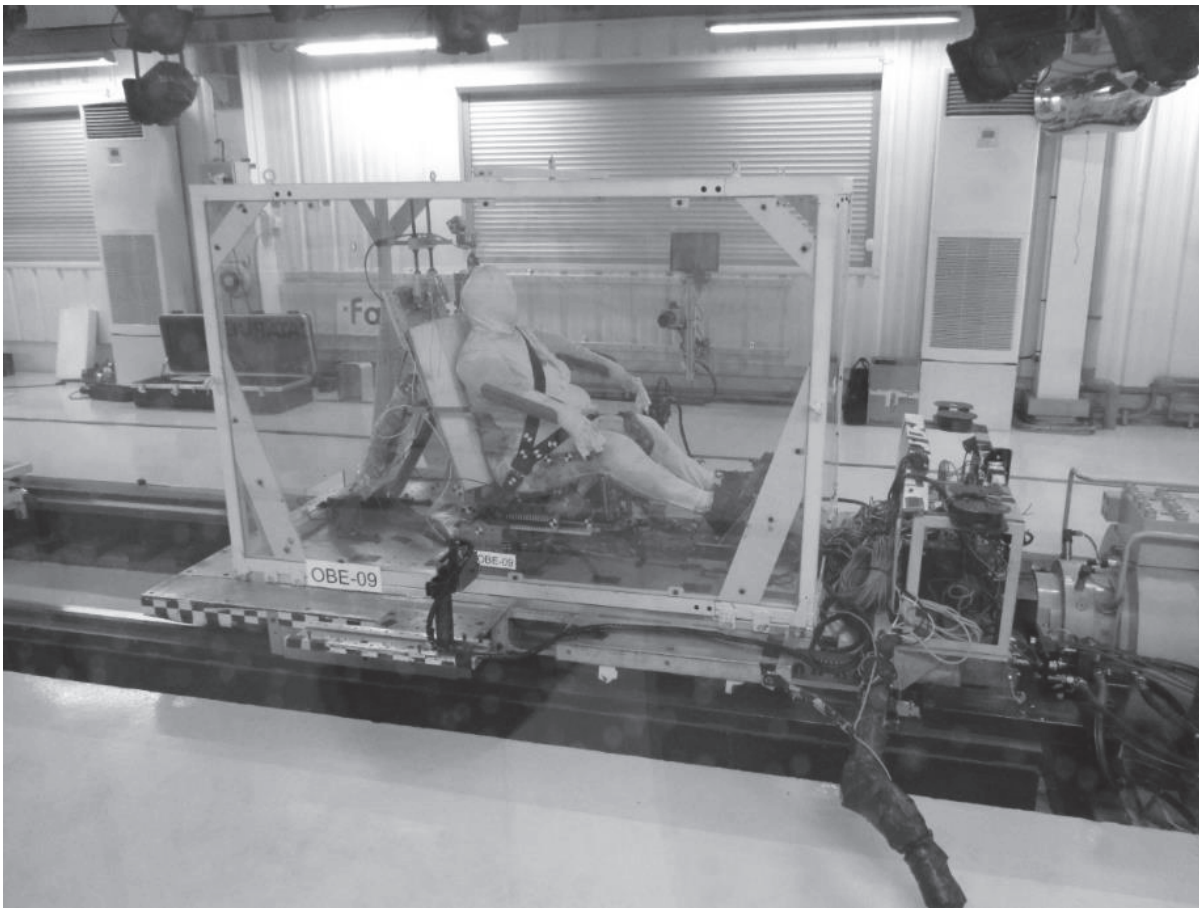


*Figure 30: Overview of the Sled test setup prior to the test.*

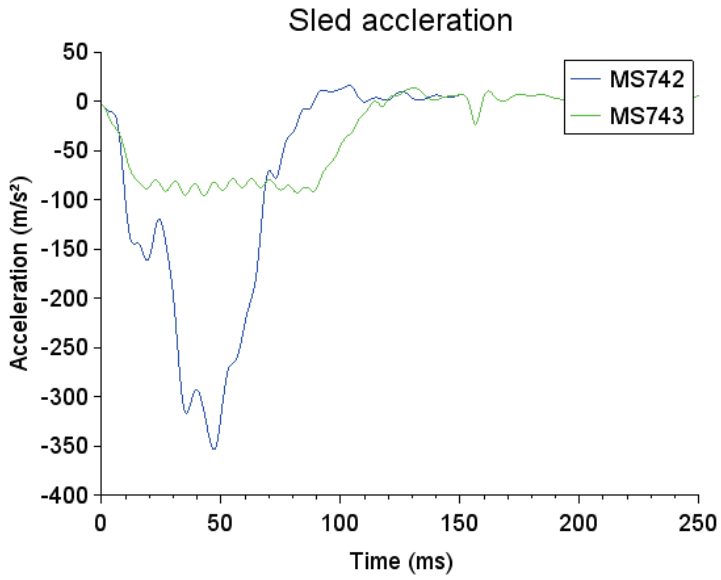


*Figure 31: Acceleration of the sled for each of the sled experiments.*

*Figure 32: Fractured pelvis of the MS742 PMHS after the sled test.*

## 3.3. Results

This section will present the kinematic behaviour of the PMHS during the belt and sled tests. The coordinate system is oriented based on the body orientation: X is the posterior to anterior axis, Y the lateral left to right axis and Z the superior to inferior axis. See Figure 33 for illustration.

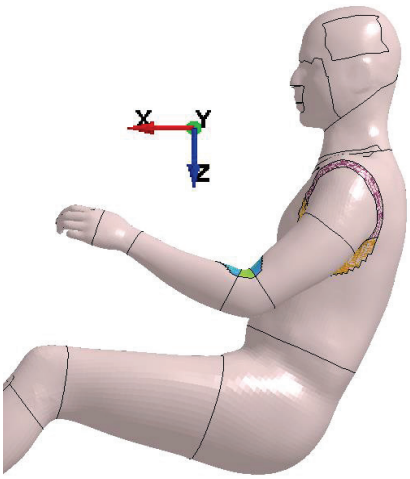


*Figure 33: Coordinate system used for measurements in relation to the body position. The GHBMC M50-O model is used for illustration as the body.*

### 3.3.1. Belt tests results

All tests were performed successfully with no obvious signs of injury. The belt did not slip in any of the tests. Figure 34 to Figure 36 show video captures from the “high belt” configurations for MHA389, MHA418 and MHA422 tests, respectively and Figure 37 to Figure 39 show the “parallel belt”

configurations for MHA388, MHA420 and MHA423, respectively. Aside from the initial position, two points of interest are shown in these captures: the time when maximum belt force was achieved and the time when the maximum centre resultant displacement was achieved. For the MHA388, the centre displacement was approximated by video tracking of the end of the MP2D (MP2D sensor failed). This is inaccurate since the end of the sensor is not visible at each frame of the video, but it is enough to reveal behaviour similar to other tests.

The peak centre displacement was in general reached significantly later than the peak force for all the tests, except for the MHA420. While the other tests shown monotonous rise of belt force until a single global peak, the MHA420 shows two distinct peaks separated by a saddle rather than a single one (c.f. Figure 41). The peak centre displacement is reached at a similar time as the second, larger, peak force. For this reason, the two points of interest shown on Figure 38 are captures of the two separate force peaks.

Lastly, Figure 40 shows video footage from the “belt inside” configurations. Only side view is provided, since minimal motion can be observed on the frontal view. This configuration is challenging to evaluate, since there is less control over the position of the middle part of the belt that is inside the fold. For example, a lot of initial slack can be observed at the beginning of the video of the MHA389, causing the belt to engage the body after the pulling starts (delay of approximately 30 ms). This did not occur in the other tests.

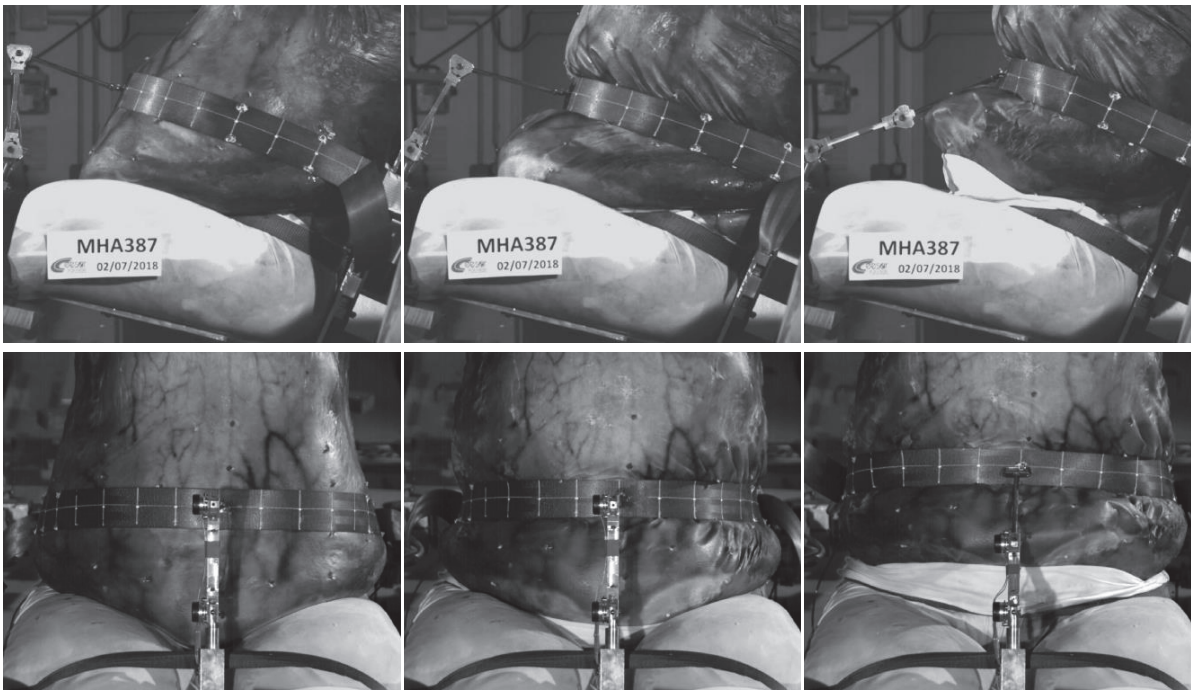


*Figure 34: Side and frontal view of the MHA387 experiment at three points of interest. Left: initial position (time 0 ms). Middle: maximum belt force (67 ms). Right: maximum centre resultant displacement (140.5 ms)*

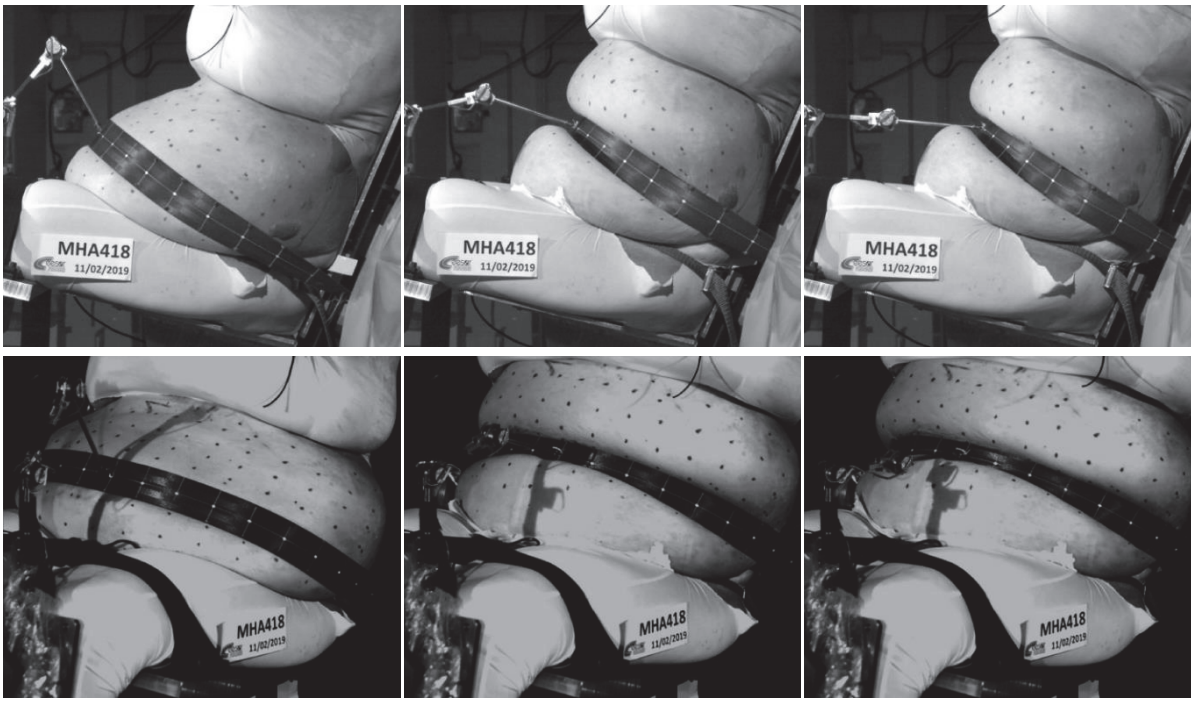


*Figure 35: Side and corner view (front camera data were corrupted) of the MHA418 experiment at three points of interest. Left: initial position (time 0 ms). Middle: maximum belt force. (120.5 ms). Right: maximum centre resultant displacement (146.5 ms).*

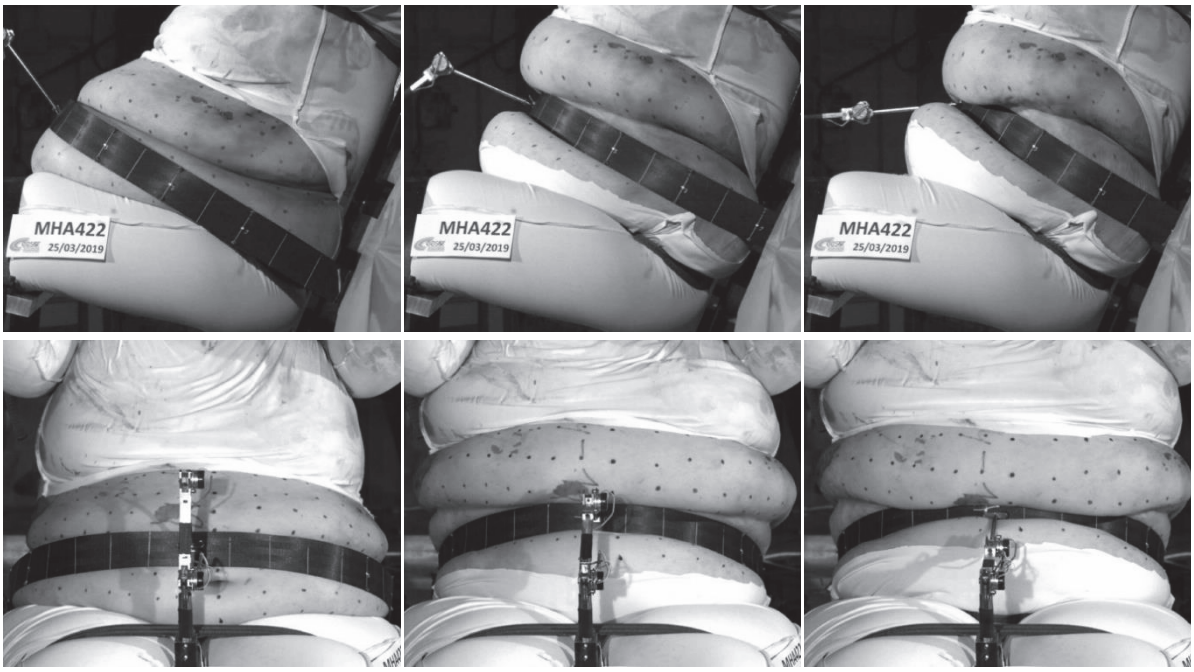


*Figure 36: Side and frontal view of the MHA422 experiment at three points of interest. Left: initial position (time 0 ms). Middle: maximum belt force. (96.5 ms). Right: maximum centre resultant displacement (130.5 ms).*

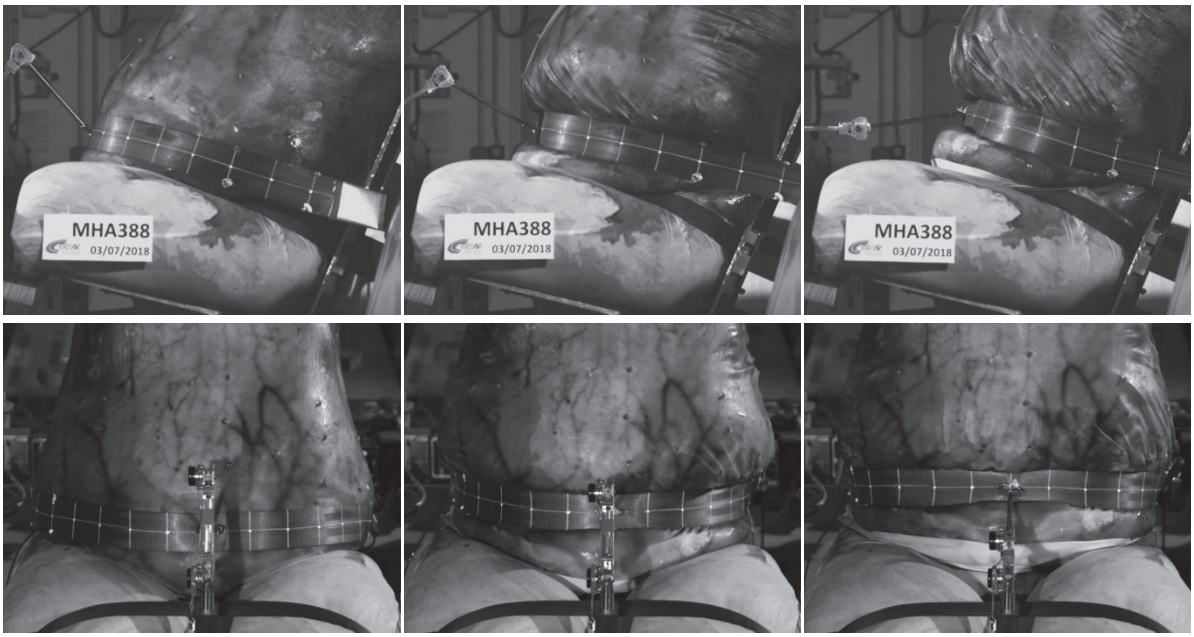


*Figure 37: Side and frontal view of the MHA388 experiment at three points of interest. Left: initial position (time 0 ms). Middle: maximum belt force (time 67 ms). Right: approximate maximum centre displacement (106 ms) – based on video tracking.*

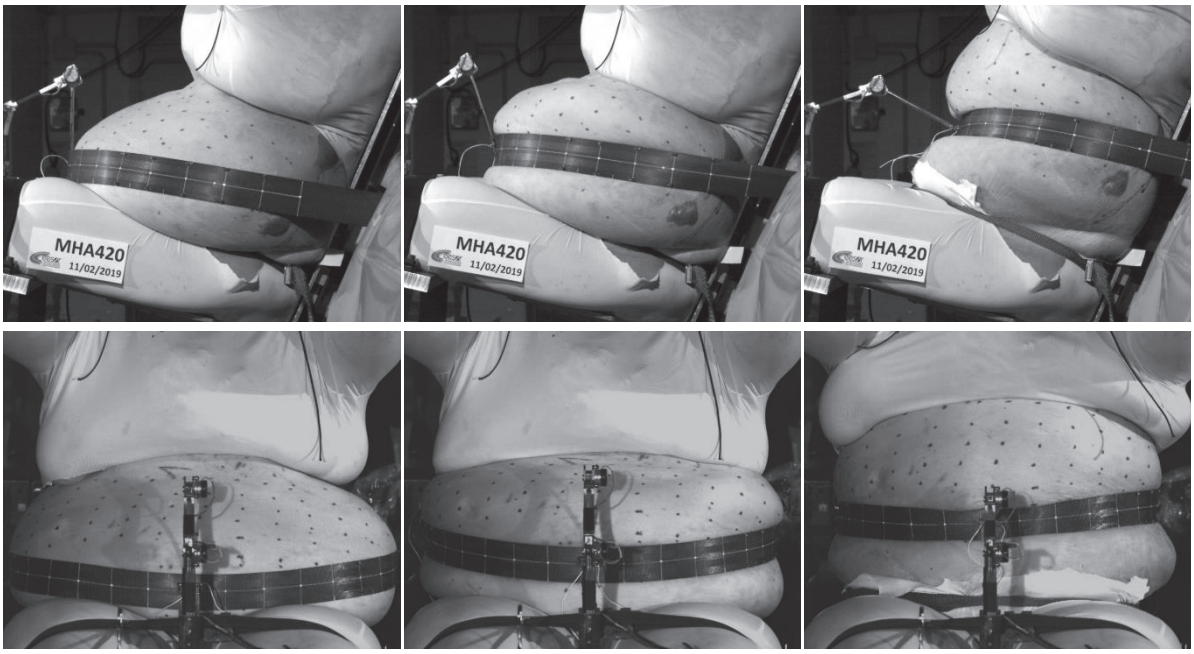


*Figure 38: Side and frontal view of the MHA420 experiment at three points of interest. Left: initial position (time 0 ms). Middle: first belt force peak (time 49 ms). Right: second belt force peak (time 118 ms).*

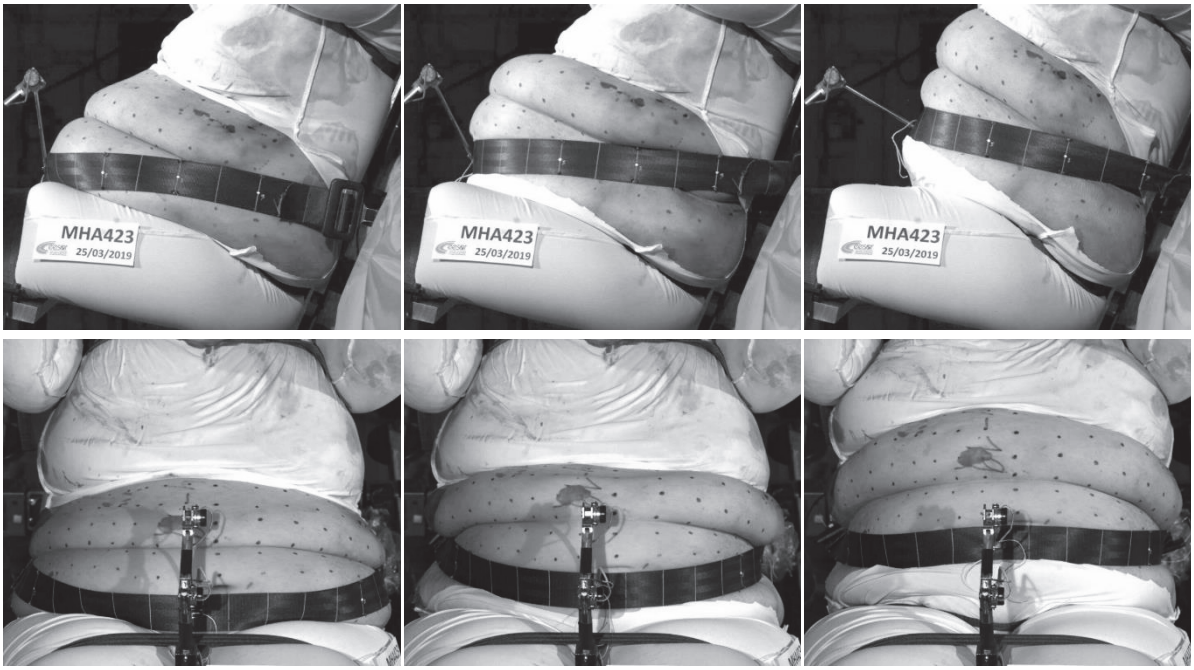


*Figure 39: Side and frontal view of the MHA423 experiment at three points of interest. Left: initial position (time 0 ms). Middle: maximum belt force (time 48 ms). Right: maximum centre resultant displacement (124 ms).*


*Figure 40: Side view of the "belt inside" experiments. Left: MHA389. Middle: MHA421. Right: MHA424. Top: initial position (time 0 ms). Bottom: maximum belt force. (97.5 ms for MHA389, 81 ms for MHA421, 50 ms for MHA424).*

In all the high and parallel belt tests the belt can be seen travelling upwards. The abdominal fold "opens" as the abdomen is being pulled up. This behaviour seems to be most pronounced for MS743 (Figure 39 and Figure 36), although MS730 also shows large opening in the high belt configuration (Figure 34). The abdomen is moving only minimally in the belt inside configuration.

Figure 41 shows the total belt force as a function of belt displacement for each test configuration and PMHS. While similarities can be observed in terms of magnitude on many of the responses especially at the beginning of the loading (e.g. high belt, centre displacement plot), significant differences are also visible. Despite MS742 and MS743 being subjected to almost the same loading input and having similar waist circumference, MS742 shows higher peak force and displacements than MS743 for the "belt inside" and "belt parallel" configurations. In addition, the side belt displacement seems to increase with limited force increase for MS730 compared to the other PMHS or the centre displacement. It is unknown if differences in belt slack could have affected these responses.

Figure 42 compares the belt X-Z trajectories (in a coordinate system with origin in the initial position of the tracked point). The initial angle under which the belt is being pulled on is also shown in the same figure as dashed lines for each test.

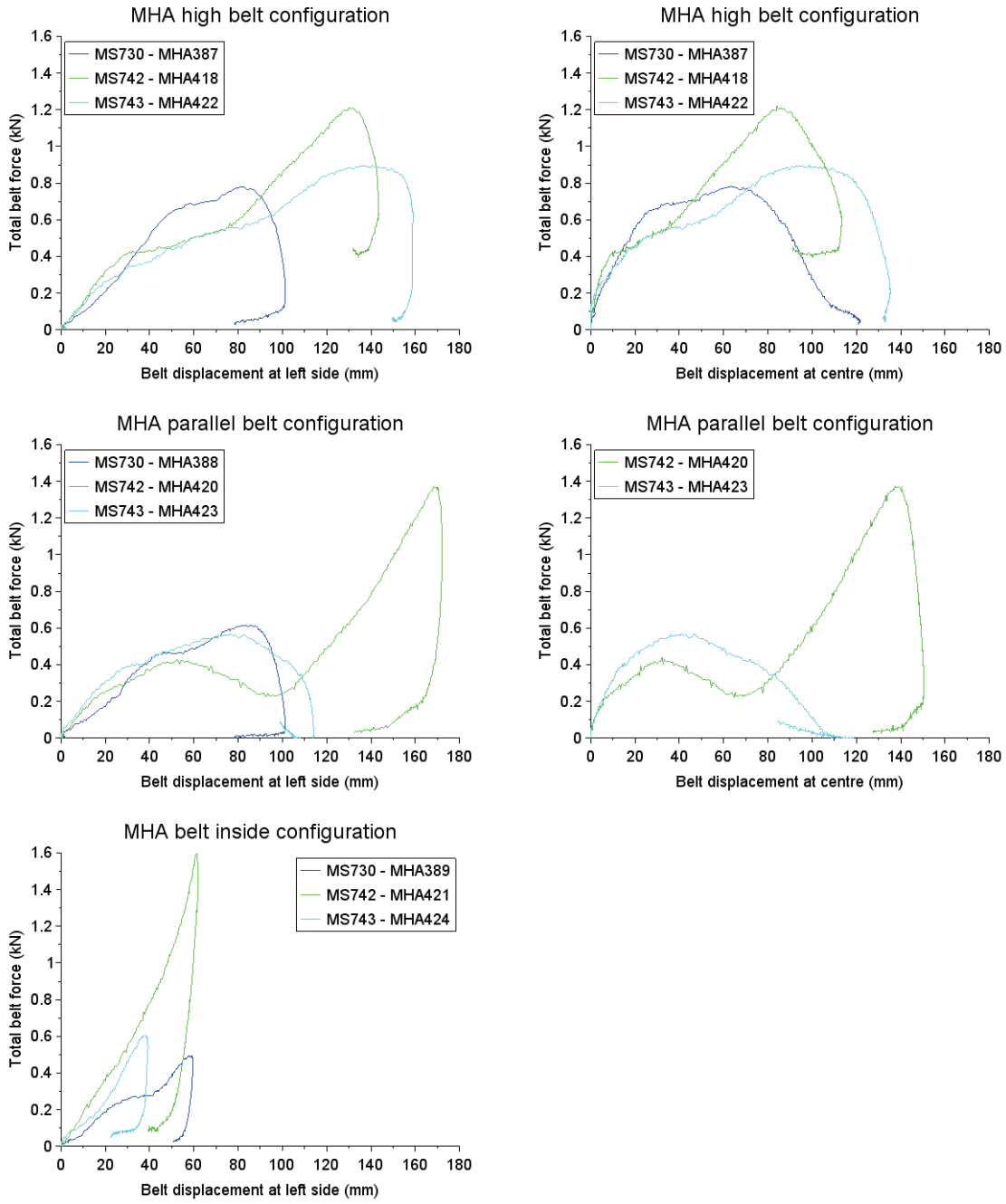


*Figure 41: Comparison of total belt force as a function of belt displacement of MHA tests between the different PMHS. Top: configuration "belt high". Middle: "belt parallel". Bottom: "belt inside". Charts in the left column use displacement of the side of the belt measured on the video footage, i.e. resultant displacement computed from the X and Z displacements of a selected point on the belt. Charts in the right column use displacement of the centre of abdomen measured by the MP2D sensor. This is not available for the configuration with belt inside the fold and also for test MHA388 (sensor malfunction).*

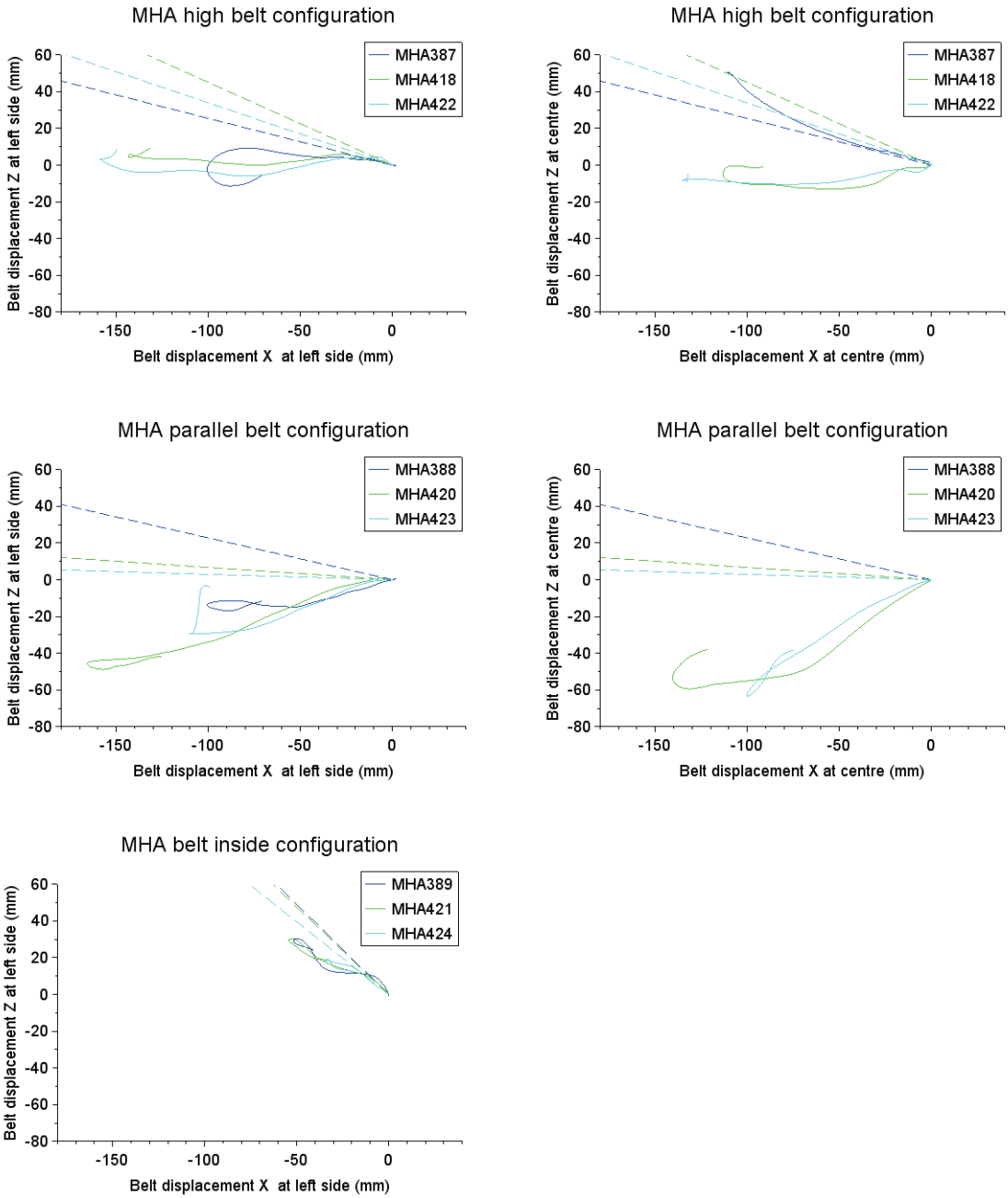


*Figure 42: Belt trajectories. Top: configuration "belt high". Middle: "belt parallel". Bottom: "belt inside". Charts in the left column use displacement of the side of the belt, charts in the right column use displacement of the centre of abdomen. This is not available for the configuration with belt inside the fold and also for test MHA388 (sensor malfunction). Dashed lines show the angle of the belt pull, i.e. direction of the pulling cable in the initial position. Note that the belt is not pulled on the same point as the one used for tracking, i.e. the point (0,0) in the charts; the dashed line therefore represent only the angle of the pull, not its trajectory.*

According to Figure 42, the configuration with belt inside the fold shows almost identical trajectories for all PMHS, since they all use the same loading with the belt being guided below the fold: the belt

moves down (Z increases) and back (X decreases) in an almost straight line. Greater differences between PMHS can be observed on the configurations “belt high” and “belt parallel”, particularly the MS730 which is less obese than MS742 and MS743 and also uses different cable loading input. Also compared to MS742, the more obese MS743 showed slightly higher belt penetration for the “high belt” configuration but a much smaller one (by 50 mm) for the “belt parallel”. This smaller penetration cannot be explained by input differences as MS743 had a larger cable displacement for the “belt parallel” configuration (MHA423, 148.5 mm in 110 ms instead of 142 mm). Here again, belt slack could be a possible cause. The response seen in the belt trajectory between the configurations regardless of PMHS can be partially explained by the cable trajectory. For the “belt parallel” configuration, the cable orientation is almost straight, i.e. with only minimal Z displacement and the belt travels upwards, i.e. in an opposite direction than in the “belt inside” configurations, which has the cable oriented under a much larger angle relative to the horizontal. In the “belt high” configuration the belt travels neither upwards nor downwards, and coincidentally, the cable is oriented at an angle intermediate between the other two configurations.

### 3.3.2.Sled results

Figure 46 and Figure 47 show an overview of the MS742 kinematics as seen from the right and left cameras, respectively. The six lines correspond to: the initial position, a time after both pre-tensioners were triggered but before the belt force sharp rise, the times of peak force at the buckle (and coincidentally the shoulder belt anchor as well) and the lap belt and finally two times during the unloading phase. The front view in Figure 48 provides a more detailed view of the behaviour of the belts during the pre-tensioning phase, with two additional times (2 ms after each of the two pre-tensioners triggered). Similar figures are provided for the MS743 (Figure 46 to Figure 48), except the time of peak shoulder force is shown rather than peak lap belt force as unlike with MS742, it occurs at a different time than the peak buckle force. Finally, for some more details, Figure 49 and Figure 50 are from cameras placed on the sled for the MS743 test, focused on the belt buckle and the left side of the lap belt, respectively. Glare appears on the footage at several parts because of the buckle camera being positioned behind safety glass.

Overall, significant compression of the abdomen is visible near the fold. When looking in detail at MS743, belt does not seem to slip into it but rather to compress the area. This is not unlike the MHA belt parallel configuration although the angle of the belt pull is different. The behaviour is slightly different for MS742. In that case, the belt compresses only a small portion of the abdomen in the centre, but can be seen slipping inside the fold on the sides. In both cases, the large compression of

the fold region was associated with an apparent forward excursion of the abdomen above, perhaps resulting from a combination of the compression itself (like in the MHA tests) and the deceleration of the sled. Submarining did not occur and it is not certain if that abdominal mass above the belt may prevent it.


*Figure 43: Right camera footage from sled tests with MS742. Top left: initial position (time 0 ms). Top right: end of pretension phase (40 ms). Middle left: peak buckle force (87.5 ms). Middle right: peak lap belt anchor force (99 ms). Bottom left: unloading, 120 ms. Bottom right: unloading, 140 ms.*


*Figure 44: Left camera footage from sled tests with MS742. Top left: initial position (time 0 ms). Top right: end of pretension phase (40 ms). Middle left: peak buckle force (87.5 ms). Middle right: peak lap belt anchor force (99 ms). Bottom left: unloading, 120 ms. Bottom right: unloading, 140 ms.*

*Figure 45: Front camera footage from sled tests with MS742. Top left: initial position (time 0 ms). Top right: 2 ms after PT1 was triggered (20 ms). Middle left: 2 ms after PT2 was triggered (27 ms). Middle right: end of pretension phase (40 ms). Bottom left: peak buckle force (87.5 ms). Bottom right: peak lap belt anchor force (99 ms).*


*Figure 46: Right camera footage from sled tests with MS743. Top left: initial position (time 0 ms). Top right: end of pretension phase (40 ms). Middle left: peak buckle force (96.5 ms). Middle right: peak lap belt anchor force (111.5 ms). Bottom left: unloading, 130 ms. Bottom right: unloading, 160 ms.*

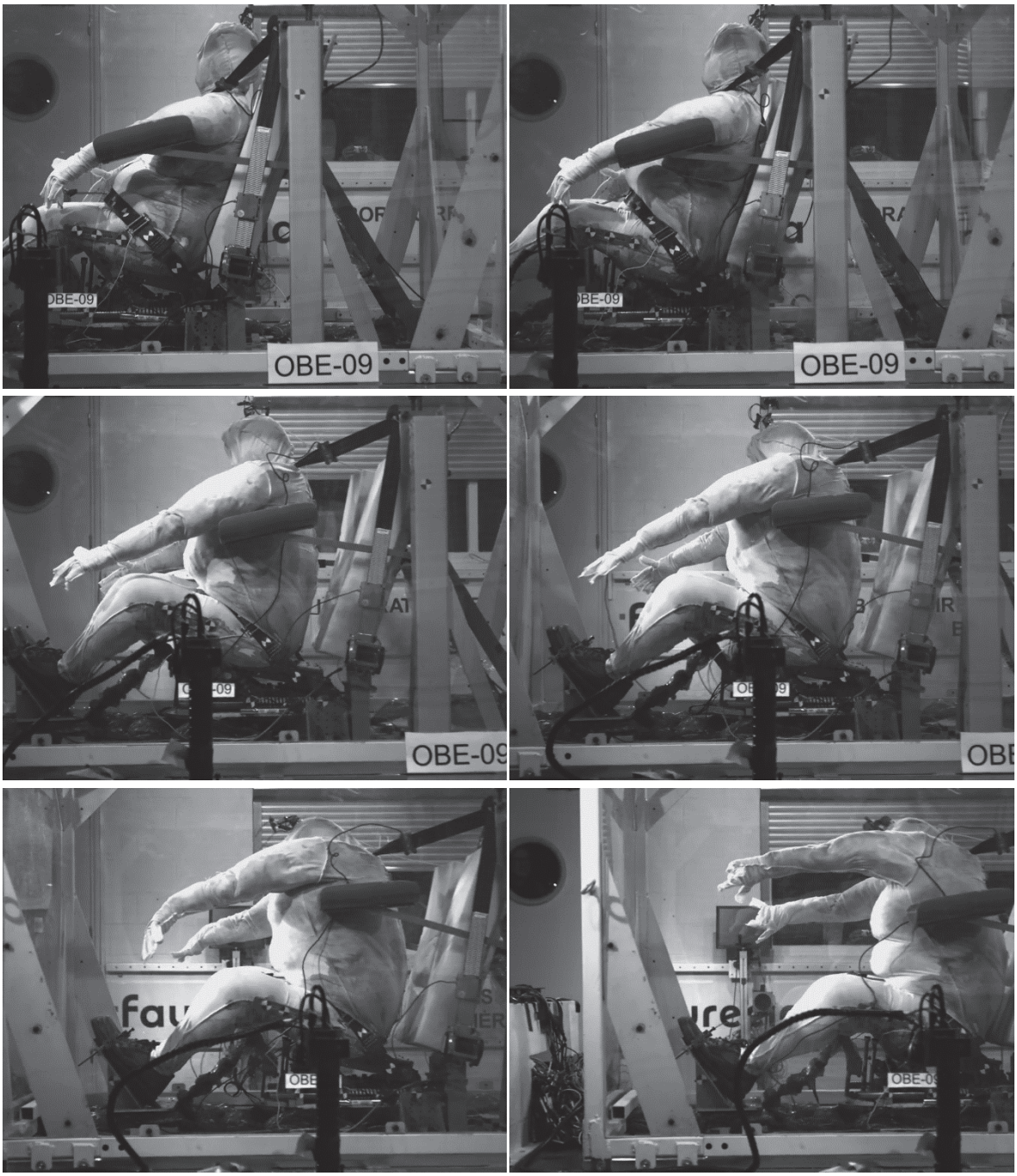


*Figure 47: Left camera footage from sled tests with MS743. Top left: initial position (time 0 ms). Top right: end of pretension phase (40 ms). Middle left: peak buckle force (96.5 ms). Middle right: peak lap belt anchor force (111.5 ms). Bottom left: unloading, 130 ms. Bottom right: unloading, 160 ms.*


*Figure 48: Front camera footage from sled tests with MS743. Top left: initial position (time 0 ms). Top right: 2 ms after PT1 was triggered (20 ms). Middle left: 2 ms after PT2 was triggered (27 ms). Middle right: end of pretension phase (40 ms). Bottom left: peak buckle force (96.5 ms). Bottom right: peak lap belt anchor force (111.5 ms).*

*Figure 49: Buckle camera footage from sled tests with MS743. Images are in chronological order from left to right, top to bottom: initial position (time 0 ms), PT1 triggers (18 ms), 2 ms after PT1 was triggered (20 ms), PT2 triggers (25 ms), 2 ms after PT2 was triggered (27 ms), end of pretension phase (40 ms), start of main loading phase (50 ms), peak buckle force (96.5 ms), peak lap belt anchor force (111.5 ms), unloading (130 ms), unloading (160 ms).*

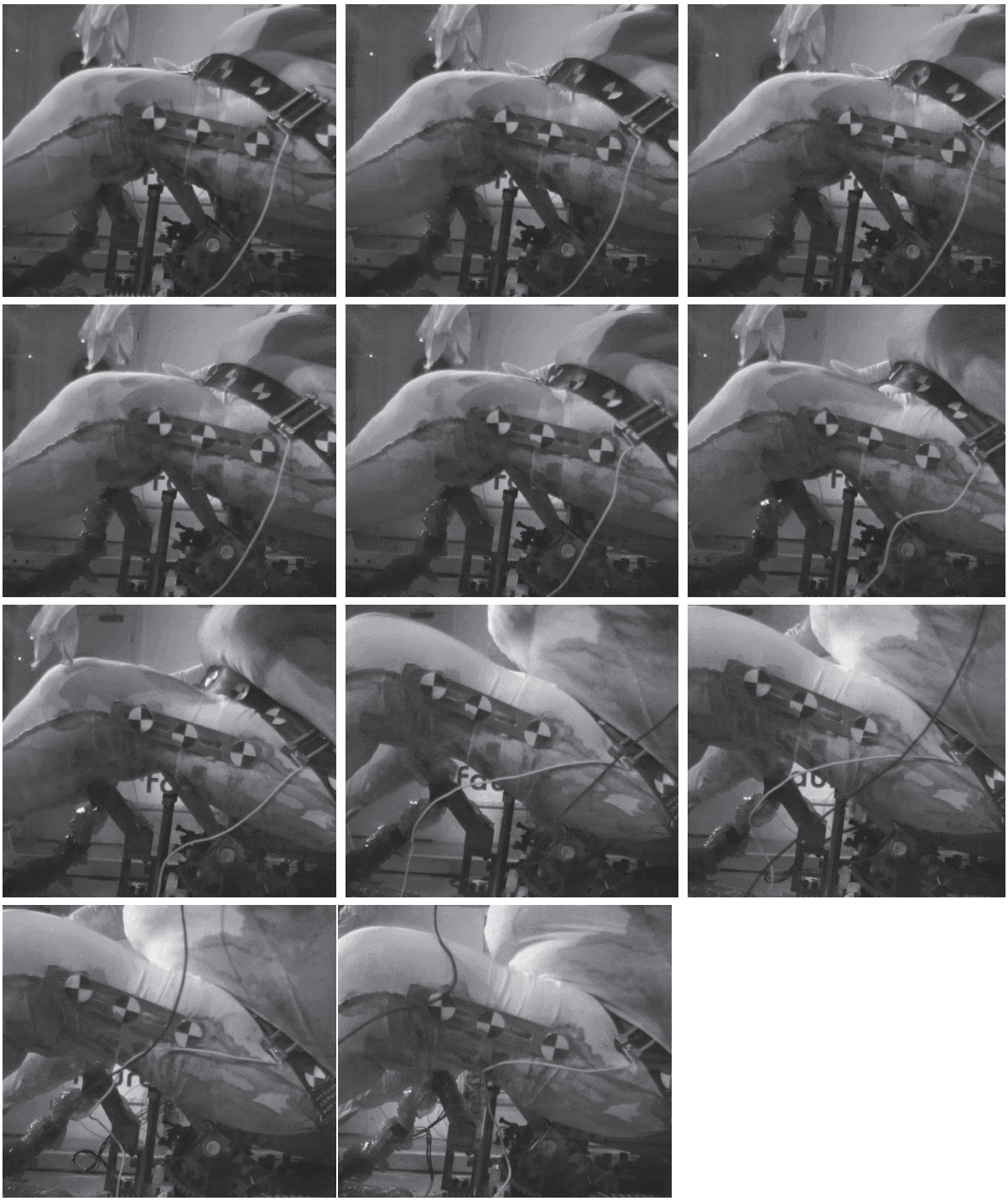

*Figure 50: Lap belt camera footage from sled tests with MS743. Images are in chronological order from left to right, top to bottom: initial position (time 0 ms), PT1 triggers (18 ms), 2 ms after PT1 was triggered (20 ms), PT2 triggers (25 ms), 2 ms after PT2 was triggered (27 ms), end of pretension phase (40 ms), start of main loading phase (50 ms), peak buckle force (96.5 ms), peak lap belt anchor force (111.5 ms), unloading (130 ms), unloading (160 ms).*

Figure 51 shows the belt force measured during the experiments for both PMHS. Three sensors were used: one measuring the tension of the lap belt at its anchor point, one measuring the tension in the

shoulder belt at the upper pulley block, and one measuring the force acting on the buckle. The effects of the pre-tensioners (with their TTF of 18 ms for shoulder and 25ms for lap belt) are visible on the force time histories. The force magnitudes are much higher for MS742 on both shoulder and lap belt. For the shoulder, the 4kN load limit is only reached for MS742. The lap belt force reached 6kN for MS742, which is similar to the maximum force observed in Uriot et al. (2015), for which fractures were observed (although less severe).

A small delay before the main loading can be seen on the MS742 between 40 and 60 ms, particularly on the lap belt. This coincides with the time period during which the belt can be seen slipping into the abdominal fold as noted above. Afterwards, it engages the pelvis and force starts to rise rapidly.

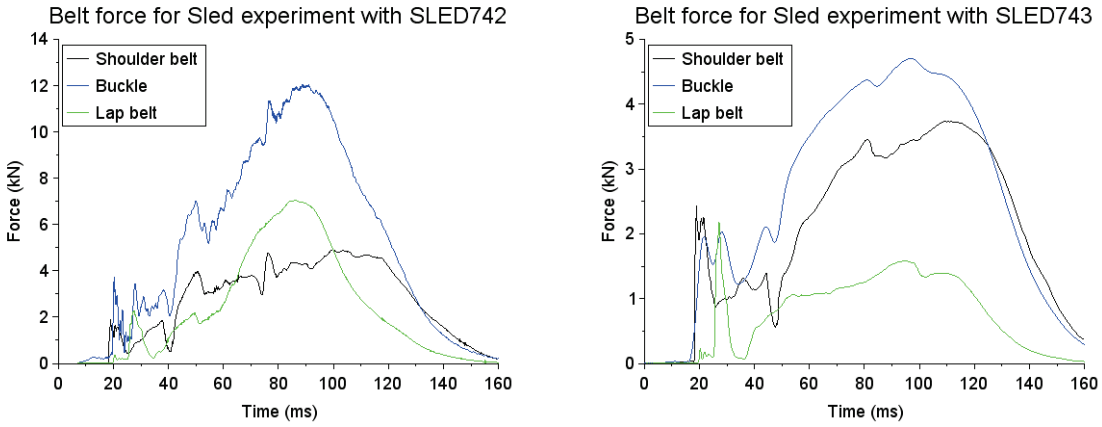


*Figure 51: Belt force-time history for the sled experiments. Left: MS742. Right: MS743.*

## 3.4. Discussion and Conclusions

This chapter reports on the imaging and testing protocols developed to characterize obese PMHS. For imaging, it includes full body seated imaging of obese PMHS, which was not performed before to our knowledge, that allowed observing the abdominal fold and internal fat distribution in an occupant position. For testing, new experiments dedicated to the characterization of the mechanical response of the abdominal fold in case of belt loading were conducted, along with two sled tests. The geometrical data will be processed and exploited in Chapter 5 to create morphing targets and the detailed results will be discussed in that section. The belt tests have shown very different responses depending on the belt configuration, with a large fold opening in the case of the belt parallel loading. Despite the limited force levels reached (which was selected to minimize the risk of injury), the compression levels are significant and it is hoped this will help evaluating the morphed model and the assumptions for the soft tissue modelling before their use in sled (Section 6.3.2). The fact that the loading modes in the region near the abdominal fold appear to be similar in the belt parallel pull and

sled seems encouraging. This will be further discussed in Chapter 6 when comparing with simulation results.

Regarding the protocol itself, the work with obese PMHS created significant and sometimes specific challenges. Obese PMHS were difficult to procure for, which limited the number of male specimens as well as required to include different obese profiles (large range of BMI, abdominal shape, proportion of fat, bone quality etc.). Basic comparisons on the effect of the amount of subcutaneous fat – which differs between sexes – on the response cannot be assessed based on the limited number of specimen and will have to be tested numerically. Also, the PMHS dimensions make the medical imaging particularly difficult and prevents in-position imaging of the whole body (unless physically cutting the specimen as in the Visual Human Project, which would prevent testing). Such dimensional constraints led to develop solutions to match several imaging modalities. The option used for the last two PMHS represents a reasonable compromise for the collection of full body information while limiting the number of thawing cycles. As the effect of these cycles on the mechanical response of soft tissue (especially for adipose ones) is uncertain at this time, future work should investigate further reduction of the acquisition period before testing.

# 4. Numerical methods

## 4.1. Introduction

One of the main goals of this study was to design a methodology for morphing an HBM to different shapes. Based on literature and previous experience (Section 2.5.2), the Kriging method was chosen for the morphing. It is a meshless technique using pairs of source and target vertices ("control points") to define a continuous interpolation function applicable to any vertex in the space, i.e. including those that are not part of the source-target set. First correspondence between the source and target has to be established: a matching target control point is required for each source control point. For example, the target surface can be the skin extracted from CT images of a particular PMHS, the source can be the skin surface of the FE model to be morphed, and the deformation field will be then applied to the nodes of the mesh. Two main challenges that need to be addressed are the registration, i.e. the process that establishes the matching between the source and target, and dealing with high computational costs when large sets of control points are used.

Section 4.2 will first focus on the problem of registration. Registration provides a deformation of a given source mesh towards the shape of the target mesh – it can be understood as a specific type of morphing. Vertices of the undeformed source mesh can then be used as the source control points for Kriging, while the deformed (registered) one can then be used as the target. Based on these constraints, Kriging (Section 4.3) then provides a deformation not only for the parts used as source and target, but also for all other parts of the HBM. The methods implemented to facilitate its use with many control points are described along with a test case using skin targets from a statistical model and fixed (i.e. not morphed) skeleton. Application of these techniques for morphing towards the PMHS from Section 3.2.1 is detailed in Chapter 5.

Only limited effort has been devoted to the registration challenge: an implementation of a registration algorithm has been created in PIPER, based on available literature (summary included in Section 4.2.1) with only small tweaks to fit the application to HBM. The challenge of using many control points with Kriging has been studied more thoroughly, resulting in novel methodology that has been submitted as a separate scientific journal paper. The Section 4.3 is therefore longer as it contains the entire text of said paper along with additional details.

## 4.2. Geometric Registration

### 4.2.1.Definition

In general, registration is an optimization problem under constraints: search for correspondence between source and target to deform the source to the target by penalizing shapes dissimilar to the target. To implement such a concept, the key parts that need to be defined are how to create the matching, what is the transformation to be used and how is the similarity measured. To narrow down the options, only methods relevant for the intended application in this study will be discussed, i.e. assuming the following:

- **Registered objects**: the registered objects are surface meshes, e.g. skin extracted from CT images of PMHS, as target and skin parts of an FE HBM as source. Therefore, only methods for geometric mesh-to-mesh registration will be investigated.
- **Transformation**: the aim is to use the established correspondence as an input for morphing. This means it is expected that the source object will be deformed, i.e. non-rigid transformation can be allowed for the registration to achieve closer similarity between source and targets.
- **Correspondence and similarity**: the transformation is driven by the established correspondence between source and target meshes. It will minimize the relative motion of neighbouring vertices in order to prevent shearing of elements once the resulting matching is applied to morphing of FE model. This among others implies that each specific anatomical part of the source should be matched with that same anatomical part on the target mesh.

Additionally, since the surfaces used in this study have thousands of vertices, it would not be practical to register each of those vertices manually: the registration needs to be automatic or at least with minimal input (not a significant proportion of the number of vertices of the mesh). To summarize the goals, Figure 52 shows the desired output of the registration: the source mesh in the shape of the target surface.

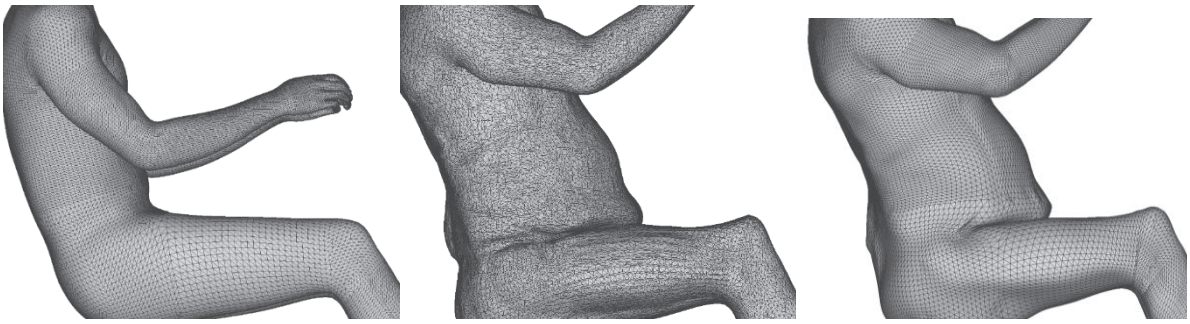

*Figure 52: Example of the desired results of registration. Left: source mesh (skin of GHBMC M50-O). Middle: target mesh (CT scan of MS730, see Section 3.2). Right: output of registration, i.e. source mesh in the shape of the target mesh with the same parts of the mesh representing the same anatomical structures on both the source and the output.*

Most mesh registration methods are derived from the Iterative Closest Point (ICP) algorithm. A single iteration of the algorithm consists of two steps: finding point correspondence and aligning the model based on the found correspondence. These two steps are repeated until a minimum of a specified error metric is reached.

One of the simplest algorithm to assign correspondence is to match pairs of points that are closest in terms of their Euclidean distance. For example, Besl and McKay (1992) assumes the meshes to be already aligned and simply finds the closest points. Local surface descriptors can be used to avoid such assumptions. They are vectors that express distinct geometrical characteristics of a given vertex, e.g. the position of the vertex as well as the curvature of the surface in the neighbourhood, valence, distance to neighbours etc. Many authors use this approach, with various choices for the descriptors (Huang et al. 2008; Gelfand et al. 2005; Yang et al. 2016). Han et al. (2018) provides a comprehensive review of such descriptors. Landmarks can also be used to specify key points of the surfaces that are known to be matching because of a priori knowledge by the operator (Allen, Curless, and Popovic 2003). Placing the landmarks is often time consuming and tedious task, so using more than tens of them is usually not practical. However, even in small numbers they can be useful when combined with the surface descriptors.

In the case of non-rigid ICP, the alignment step consists of deforming the mesh. A deformation model then specifies rules and assumptions on this deformation. Differential representation is useful for describing the deformation model as it provides information about the shape of local features: for surface meshes, the Laplacian is most often used (Sorkine 2006). How the deformation treats the shape of local features is one of the key properties of a deformation model. For registration purposes, it is in general desirable for local features to retain their shape as much as possible. This can be expressed as an energy minimization problem using the Laplacian formulation. Various ways of constructing the

energy function to achieve the “local rigidity” have been proposed in literature (Zhou et al. 2005; Sorkine and Alexa 2007; Yamazaki et al. 2013).

### 4.2.2.Implemented solution

Based on elements from the literature and previous internal works conducted at LBMC, a non-rigid ICP registration using local surface descriptors was implemented in a pragmatic manner, accounting for issues observed with the registration of the fold as they arose. A fast and rotationally invariant descriptor was sought. A descriptor inspired by (Fehr et al. 2014) was chosen for its low computational and storage requirements. Figure 53 illustrates geometrical features used to construct the descriptor. For a particular vertex *V*, it consists of:

- The position of the vertex *V*
- The normal of the vertex $N_v$
- The histogram of scalar products of the normal $N_v$ with normals $N_{nei}$ of vertices *Nei* in the (4-ring) neighbourhood of *V* (i.e. all vertices that can be reached by traversing at most four edges from *V*)
- The histogram of scalar products of the normal $N_v$ with directional vectors $D_{nei}$ from *V* to each of the (4-ring) neighbouring vertices *Nei*.

The number of buckets of both histograms was set to 5 for all experiments. In total, the descriptor for each vertex therefore is a vector with 16 dimensions: 3 for position, 3 for normal, and 5 + 5 for the two histograms. The correspondence is then established by matching pairs of vertices on source and target that have minimal Euclidean (in all 16 dimensions) distance between their descriptors.

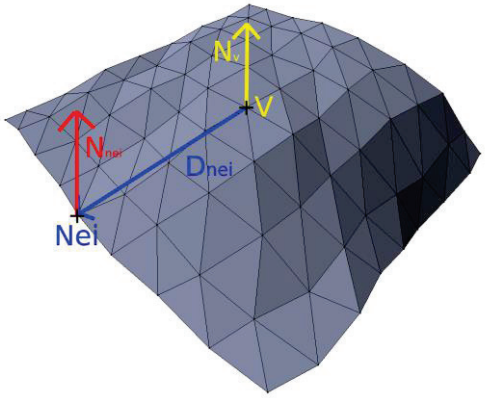


*Figure 53: Illustration of vectors used to create feature descriptors for registration for a particular vertex V: the normal of the vertex $N_v$ (yellow), the normal $N_{nei}$ (red) of a neighbouring vertex and a directional vector to a neighbour $D_{nei}$ (blue). Only one of the neighbour (in the fourth ring of V) is shown for illustration, but all neighbours in all four rings are used for the descriptors.*

The displacement field from the source toward the corresponding target is smoothed by averaging displacements in a 2-ring neighbourhood and then used for deforming the source model directly. The stopping criterion is designed to favour minimal shearing of the registration: for each vertex of the registered mesh, its matching vertex on the target is found. The angle between the displacement towards this vertex and the normal is measured and averaged over all the vertices. If the latest average is larger than one achieved by the registration from previous iteration, the process ends and the registration with lower mean angle is output.

The curvature part of the surface descriptors is progressively assigned a lower weight with each iteration, while the positional part gets a larger weight. This helps the algorithm to converge in areas with small curvature changes. However, in areas with large changes, such as the abdominal fold and armpits, self-penetrations often occur, as vertices on both sides of the fold are very close to each other which makes them difficult to distinguish based only on position (example in Figure 54). An algorithm for avoiding self-penetrations was also implemented and is executed at the end of each iteration. Occasional self-penetrations remained after the registration and required manually post-processing (Figure 54): perhaps more localized changes to the weights of the surface descriptors could help alleviate these problems, but it was not investigated further.

A mechanism was also implemented for enforcing correspondence between a particular pair of vertices, for example anatomical landmarks or points easily identifiable on both the source and target meshes, which can help achieve faster and more precise convergence.

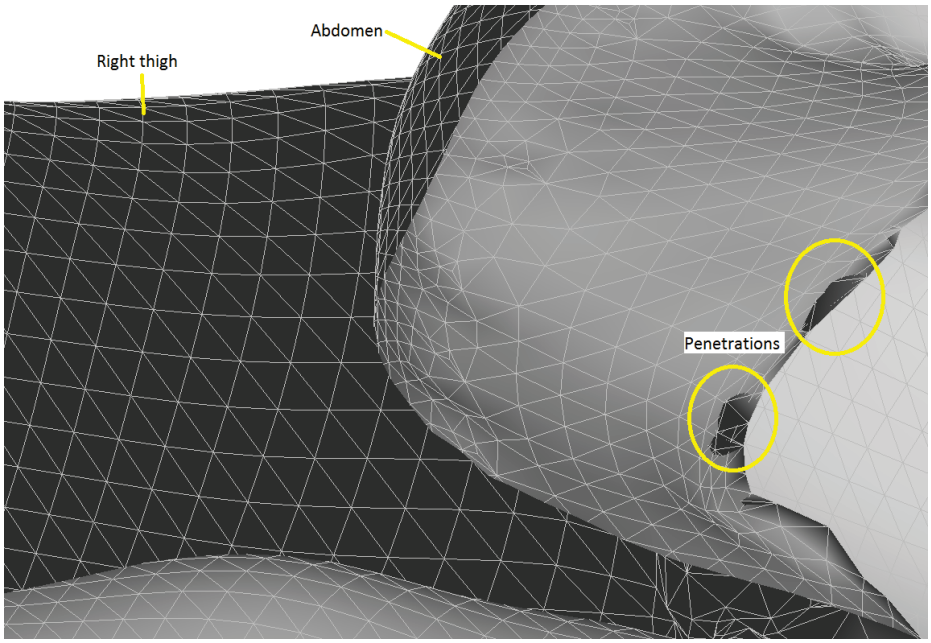


*Figure 54: Illustration of penetrations appearing after registration in the abdominal fold (PMHS MS742).*

## 4.3. Kriging

### 4.3.1. Definition

Kriging is a stochastic numerical method for linear unbiased estimation of a random function (Trochu 1993). The estimation is based on a set of samples of that function in known locations, which will be called Control Points (CPs) in further text. A similar method is the Radial Basis Functions interpolation (RBF), which estimates the values as a superposition of basis functions (Baxter 1992). In the context of estimating positions or displacements of 3D points, both definitions end up formulating the same function. Since Kriging provides perhaps a more easy to understand insight on the foundations of the interpolation function, it will be used in the following text.

The stochastic approach to interpolation sees the known values $u(X_i)$ as realizations of an unknown random function $u^*(X_i)$. To find the values of this function for other points (i.e. not CPs), statistical analysis of the known dataset is employed to find the "most likely" positions for the new points. The criterion to achieve the "most likely" interpolation values is realized by minimizing the variance of the estimation, while assuming there is no bias between the interpolation function and the actual function, which is formulated as Equation (4.1) (*E* signifies the expected value)*:*

$$Min(E[u(X) - u^*(X)]^2), while\ E[u(X)] = E[u^*(X)] \qquad (4.1)$$

Furthermore, Kriging is based on the assumption that the interpolated function $u(X)$ can be expressed as a sum of two terms – drift $a(X)$ and fluctuation $b(X)$. The drift represents the linear part of the transformation, while the fluctuation represents the local differences around each CP. In terms of the statistical description, this can be expressed by assuming that $E[u(X)] = a(X)$ and $E[b(X)] = 0$.

The two aforementioned conditions lead to a construction of the following interpolation function (4.2). Please refer to the appendix in Trochu (1993) for a detailed derivation.

$$u(X) = \sum_{j=1}^{M} a_j D_j + \sum_{i=1}^{N} cov(X_i, X) \cdot b_i \qquad (4.2)$$

By solving equation (4.2), the obtained coefficients *a* and *b* can be used to interpolate the function *u* at arbitrary location. This function can be formalized in a matrix form as shown in equation (4.3):

$$\begin{bmatrix} F_{N,N} & D_N \\ D_N^T & 0 \end{bmatrix} \begin{bmatrix} b \\ a \end{bmatrix} = \begin{bmatrix} U \\ 0 \end{bmatrix} \qquad (4.3)$$

The product of the $F_{N,N}$ submatrix and the coefficients *b* describes the fluctuation part $b(X)$. As Trochu (1993) shows, it is equal to the covariance between the CPs, i.e. $F_{i,j} = E[u(X_i)u(X_j)]$. The product of the $D_N$ submatrix and the coefficients *a* describe the drift part, usually realized by a linear polynomial $p(X)$ that describes the affine part of the transformation, i.e. $p(X) = a_1 + a_2 x + a_3 y + a_4 z$, where *x, y, z* are the coordinates of *X*. Again, see Trochu (1993) for an evaluation and discussion of several different choices of the drift part formulation.

This form is called the dual form of kriging, or simply Dual Kriging. The advantage of this formulation is that after the equation (4.3) is solved, which is the most costly operation as it requires inverting the left side matrix, any number of points in space can be interpolated using the transformation – it is a global interpolation method.

Note that the definition of the submatrix $F_{N,N}$ implies that the diagonal elements are equal to the variance of $u(X_i)$, which is zero, since the values in CPs are known exactly. However, by assigning a non-zero negative value as the variance in CPs, one can express an uncertainty of the sampled values. The interpolation then effectively changes into a regression. This technique is usually called the "nugget effect", based on its first application in mining planning (Krige 1951).

The assumption used for choosing the covariance function is that there is a spatial correlation between the measured values of function $u(X)$, i.e. functions that have increasing values with increasing distance (the higher the value, the lower is the correlation). The functions usually used as covariance

functions are various spline functions ($cov_{ij} = \|X_i - X_j\|^d$), mainly thin-plate spline ($cov_{ij} = \|X_i - X_j\|^2 \cdot \ln(\|X_i - X_j\| + \varepsilon), \varepsilon \ll \min_{i \neq j}(cov_{ij})$ ). However, as Jolivet et al. (2015) showed, there are no significant differences in the output quality when the interpolation is applied to HBM. The biharmonic 3D transformation resulting from the Euclidean distance as the covariance function ($cov_{ij} = \|X_i - X_j\|$) is usually sufficient.

### 4.3.2.Dealing with large amounts of control points

Using the Dual Kriging directly with a large number of control points is not practical with personal computers due to large memory and computing time cost. The numerical solution of these interpolation problems requires an LU (lower-upper) factorization of a dense *n* by *n* matrix (the covariance matrix), which is an operation with $O(n^3)$ complexity that requires $O(n^2)$ memory (Golub and Van Loan 1996).

One simple and often efficient method for cost reduction is to directly remove CPs, i.e. to "subsample" or "decimate" them. This is a relevant technique for applications with a very dense mesh of CPs carrying very similar information in a neighbourhood. However, while this could provide a good approximation of the target in such cases, it would not allow respecting the exact target with all its details (e.g. maintaining the exact bone shape).

Other methods to reduce the cost were proposed in the literature. Haas (1990) used a "moving window" approach for Kriging, where the estimation at each point of interest is computed based on only a local neighbourhood. The results are often discontinuous for dense (lot of CPs) problems, as CPs are added and removed abruptly as the window moves. This can be mitigated by applying additional weights to the covariances based on the distance from the boundary of the window – the closer they are to the boundary, the lower their weight is, which results in smoother transitions as the window moves (Gribov and Krivoruchko 2004; Rivoirard and Romary 2011). However, there is also an issue of large computation demands, as it requires building and solving the covariance matrix for each point, making it inefficient for large number of such points of interest. In the case of HBM morphing, those are the nodes of the FE mesh, which is in the order of millions for the most detailed models.

Another approach is to transform the system to solve into a sparse linear system as such systems can be solved more efficiently with $O(t \cdot n)$ memory and $O(t \cdot n^2)$ time, where *t* is the expected number of non-zero elements per column. Each element *(i, j)* in the covariance matrix represents the covariance of CP *i* with the CP *j.* Since CPs far away from each other are expected to have small correlation, the corresponding elements can be zeroed out. Furrer et al. (2006) introduced a "tapering" approach

based on covariance functions with compact, limited support, which are limited in such a way to preserve the asymptotic optimality of minimal square error of prediction provided by the resulting Kriging system. Hartman and Hössjer (2008) approximate the interpolation field by a Gauss Markov Random Field and then construct a Kriging predictor for that field, where the Markov property of the field ensures that covariances are non-zero only for CPs in "neighbourhood" of a given CP. The authors show that even for small neighbourhood, and hence significant sparsity of the matrix, the prediction obtained this way is similar to the one obtained by full model. However, the tests are made on 2D soil data (geochemical measurements of magnesium oxide concentration) and the authors themselves note that not all data fields are suitable for fitting by the Gaussian fields. Cressie and Johannesson (2008) proposed a "fixed rank Kriging" method that formulates the Kriging predictor using a fixed, small amount of nonstationary basis functions constructed in a way to represent the input data. It leads to an alternative formulation of the system, namely as a sum of a diagonal matrix of rank $n$ and an $r \times r$ covariance matrix, where $r << n$ is the number of basis functions. The authors demonstrated the method on "total column ozone" data measured at 173 405 locations (i.e. CPs) and used 396 basis functions (wavelets) in a total time below 2 minutes (including pre-processing). Recent reviews contain other similar "low rank Kriging" methods and their comparisons (Sun et al. 2012; Bradley, Cressie, and Shi 2016).

However, Stein (2014) argues that the low rank methods are unsuitable for a large class of problems. Specifically, when the correlation of neighbouring CPs is strong, the influence of other CPs is virtually ignored, despite still being significant. Stein (2014) proposed a solution where the CPs are split into blocks under the assumption of independenct blocks. This results in a block, sparse covariance matrix and similar computational demands as the low rank methods, but better results for the mentioned class of problems. Nevertheless, the obviously flawed assumption of block independence is noted by the author, suggesting that it is not perfect solution.

The aim of this study is to develop and implement as an Open Source solution a methodology that allows using arbitrary amount of control points for interpolation of HBM, while maintaining the continuity of the transformation across the whole model. To deal with the large computational load, this study investigated a spatial subdivision approach, which divides the CPs into multiple separate Kriging systems and solves them separately. This is to a certain extent similar to the method of Stein (2014), except that instead of solving a single, sparse system, the problem is solved as multiple dense ones. The "block independence" assumption mentioned earlier can lead to continuity artefacts on the boundaries of the blocks. Methods to address these artefacts are presented as well.

### 4.3.3.Spatial subdivision

The basic principle of spatial subdivision is to divide the space into “cells”, assign CPs and nodes of the HBM to those cells and perform kriging in each cell separately. The core idea of this approach is that the global transformation can be approximated within a cell precisely enough by using only the CPs present in that cell. This is based on the property of kriging that the influence of CPs on the transformation of a node diminishes with the CP-to-node distance (Jolivet et al. 2015). The following subdivision scheme was implemented to generate the cells: the bounding box of the model is recursively divided into equal, axis aligned halves until there is no cell containing more than a specified amount of CPs. Cells are always split by the midpoint of their longest axis.

As the CPs near a cell boundary will still have similarly impactful effects on the nodes on both sides, spatial subdivision may create discontinuities in the transformation near the boundaries when such CPs are ignored on one side of the boundary, as illustrated in Figure 55b. The discontinuities near the boundaries could degrade the element quality of the transformed mesh, which is a critical issue for finite element simulation. A way to mitigate these discontinuities is to include CPs from neighbouring cells when defining the cell transformation. Two strategies used to mitigate discontinuities between cells created this way were implemented: “overlapping” (Figure 55c) and “neighbourhood extension” (Figure 55d).

In the overlapping strategy, each cell size is increased by a constant percentage after all cells are generated. This makes neighboring cells overlap each other. The transformation of nodes within a region overlapped by multiple cells are computed by averaging the transformation predicted by each overlapping cell.

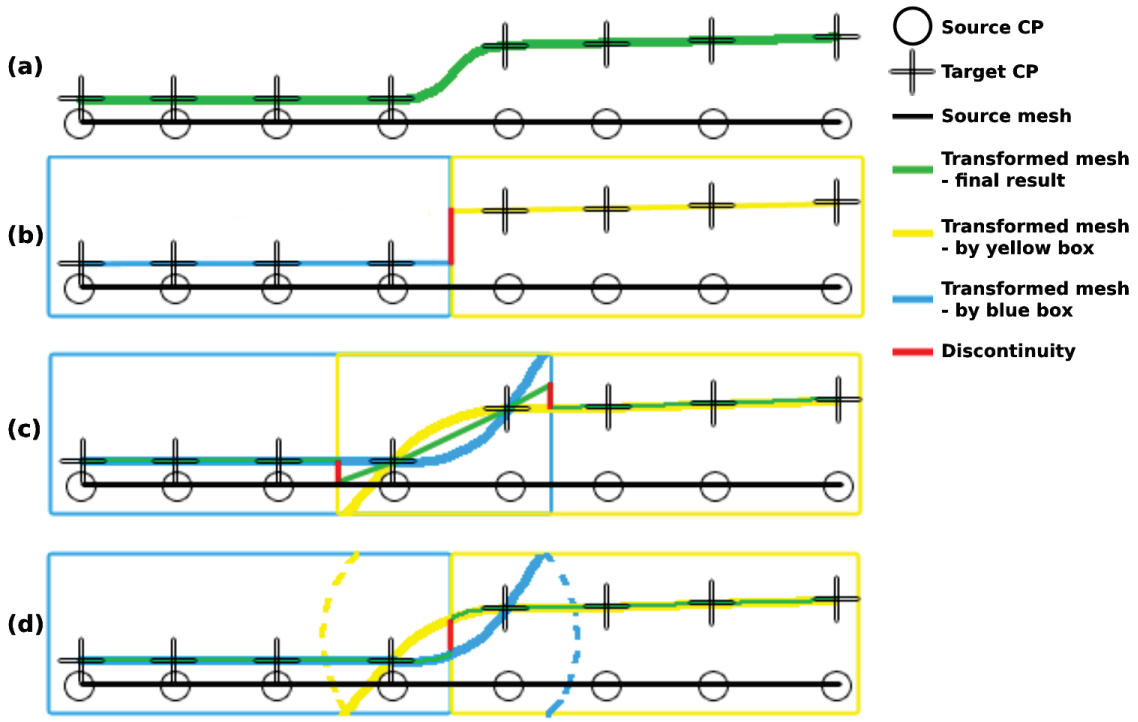


*Figure 55: Illustration of the effect of spatial subdivision. The top image (a) shows the transformation when no spatial subdivision is done. In the middle image (b), spatial subdivision by two cells (blue and yellow) is visualized. The blue and yellow lines show the results after applying only transformation defined by CPs in the blue or yellow cells, respectively. These lines represent the final concatenated result (yellow transformation applied only within the yellow cell, blue only in blue cell), including the red steep discontinuity. The bottom images (c,d) visualize the two strategies to mitigate discontinuities: overlapping (c) and neighbourhood extension (d), which results in smoother transformation, although some discontinuities (red) might still appear if the overlap is not large enough (here only two CPs in both cases (c,d)). The dashed lines in (d) signify the neighbourhood of the blue and yellow cell.*

As an alternative, a heuristic approach to obtain a finite set of CPs closed to each face of the cell was implemented: the neighborhood extension (Figure 55d). First, for each face of the cell, starting from a corner, the N-nearest CPs are found (N being a user parameter). Then, a square with edge length equal to the distance to the farthest of those N CPs is considered as “covered”. The remainder of the face is subdivided into three quadrilaterals as shown in Figure 56. These are recursively processed the same way until the entire area of the original face is covered. All the CPs collected are used with the ones inside the cell to compute the transformation field inside the cell. The final positions for transformed nodes are then always computed within a single cell, but as Figure 55d shows, the transformation is expected to behave more similarly to the global one near the boundaries of the cells, possibly leading to smaller discontinuities.

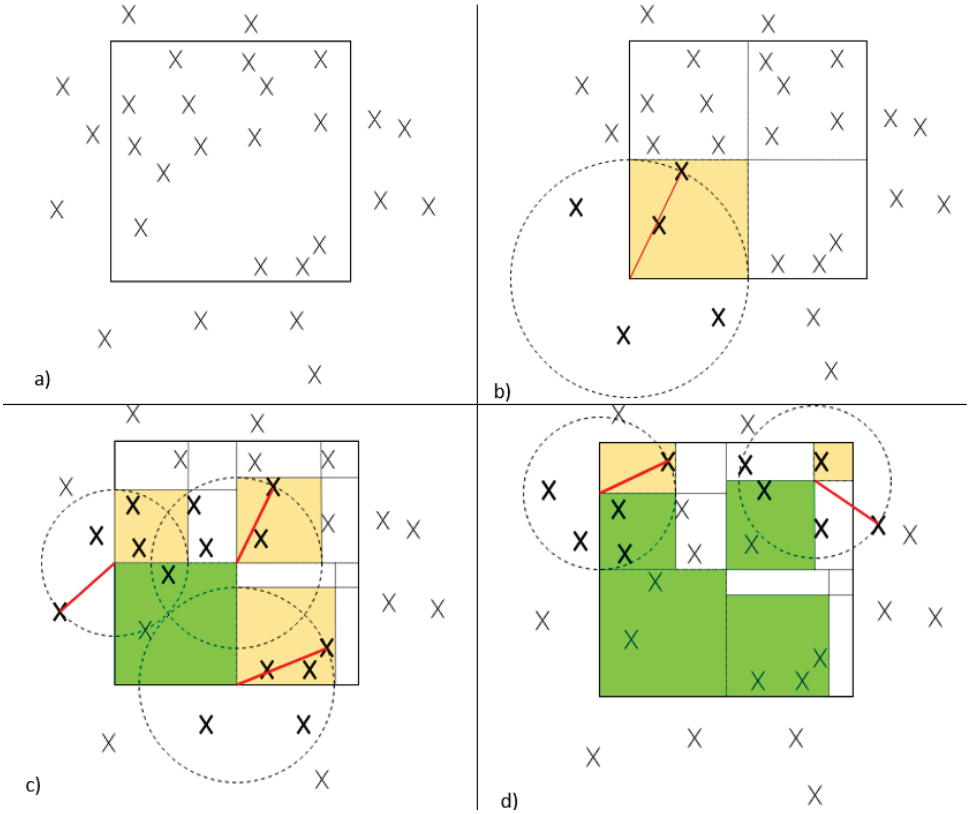


*Figure 56: Three iterations of the algorithm for finding closest CPs to a face of a cell. First (a), only the face (black rectangle) and the CPs in its vicinity (crosses) are shown. Then (b) the algorithm starts from bottom left corner, finding 5 nearest CPs. The red line shows the distance to the farthest one, which becomes the diameter of the circle (dashed) that lays out the "covered" part of the face (shaded in yellow). Then (c) three remaining parts of the face (beyond the dotted line) are processed recursively. The part covered in the previous iteration is shaded in green. The last image (d) shows only a part of a next iteration – 2 out of the 9 rectangles that need to be processed – for better clarity. It shows that for those two parts, the algorithm will reach the end of the face and will terminate (for that direction).*

### 4.3.4.Subsampling

Decimating the CPs reduces the size of the correlation matrix by directly removing some of the CPs, which reduces the computational cost. The subsampling algorithm implemented here subdivides the CP space in a regular cubical grid and then assigns CPs to its cells. One CP per cell is kept at most (the one closest to the centre of the cell) and the rest is discarded. A large numbers of CPs and a fine grid will lead to a homogenous distribution of the remaining CPs across the HBM, distributing the loss of details across the model evenly.

### 4.3.5.Workflow combining subdivision and subsampling

As Figure 55 illustrated, discontinuities may still occur at cell boundaries even when overlapping or neighbourhood extension are used. To reduce them further, an approach similar to (Sang, Jun, and Huang 2011) was designed, with first a low-detail transformation capturing the global features and then block transformation to deal with local features. This is implemented by employing both subsampling and spatial subdivision techniques using the following iterative Subsampling + Spatial Subdivision workflow (abbreviated as "3S"):

1. Subsample the CPs down to such an amount that allows kriging without the need for subdivision.

2. Transform the model using the subsampled CPs to generate an "intermediate" morphed mesh. The source position of all CPs (not just the subsampled) are transformed as well.

3. Re-iterate steps 1 and 2, progressively decreasing the number of CPs discarded in step 1. The intermediate mesh and CPs obtained by transformations in previous iterations are used as input.

4. Compute the final transformation from all the CPs (transformed in the previous steps) using the spatial subdivision and apply it to the last intermediate morphed mesh.

### 4.3.6.Kriging evaluation – weight-change study

The workflow described in Section 4.3.5 was tested on the GHBMC M50-O HBM in a weight change scenario. Four skin surfaces were generated using publicly available statistical shape model (SSM) ((Reed et al. 2014), available at *http://humanshape.org)*. One skin surface was generated for anthropometric parameters similar to those of the GHBMC M50-O (BMI 25.34 kg/m²) and it was defined as the baseline mesh (source). Three other surfaces were generated with the same anthropometric parameters except the BMI to be used as targets: one of an obese model (BMI 35) and two with a lower weight (BMI 20 and 22.7). Details about the preparation can be found in Appendix 1.

These skin targets were then used to morph the model using Kriging. The PIPER software (PIPER 2020) was used to perform the kriging-based morphing. The implementation of kriging in PIPER is written in the C++ language, is optimized for multithreaded processors and uses the Eigen library ("Eigen" 2018) for linear algebra calculations. Tests were performed on a PC with Intel Xeon E5-1650 CPU (3.5 GHz, 6 cores), 32 GB RAM and Windows 7 64-bit operating system. The subsampling and spatial subdivision implementation was incorporated into PIPER.

In order to be able to use a model in a finite element simulation, there must not be elements with negative volume. Only solid (3D) elements were concerned by the negative volume criteria, which represents 1 663 647 tetrahedral and hexahedral elements in the GHBMC M50-O. The Scaled Jacobian metric of the solid elements was also measured to assess general quality of the model. The morphed models without negative volume elements were subjected to a FE simulation of abdomen impact by solid bar corresponding to the test conditions in (Hardy, Schneider, and Rouhana 2001) using LS-Dyna (LSTC, CA). The models were considered as "runnable" if the simulation started. Regarding the time step of the models, mass scaling is used with the original model with a time step target of 0.3 µs, leading to an added mass of about 140 g. Using the same target, added masses for the morphed models were found to be similar, i.e. between 149 and 127 g, decreasing with increasing BMI. Since the presented methodology aims to be used on personal computers for fast HBM morphing, the computation time required for the transformation was also evaluated. The following subsections will describe the results observed.

#### 4.3.6.1. BMI 35: Spatial subdivision only

Morphing towards the BMI 35 target using all CPs and spatial subdivision only, i.e. without overlapping or neighbourhood extension, led to 3 449 negative volume elements. The neighbourhood extension reduced that number to 80. Figure 57 illustrates some of the artefacts near the boundary of subdivision cells with and without neighbourhood extension. Neighbourhood extension quadrupled the computation time (from 207 s to 830 s). The 6% overlap strategy led to slightly lower computation time (753 s), but a larger number of negative volume elements, 372.

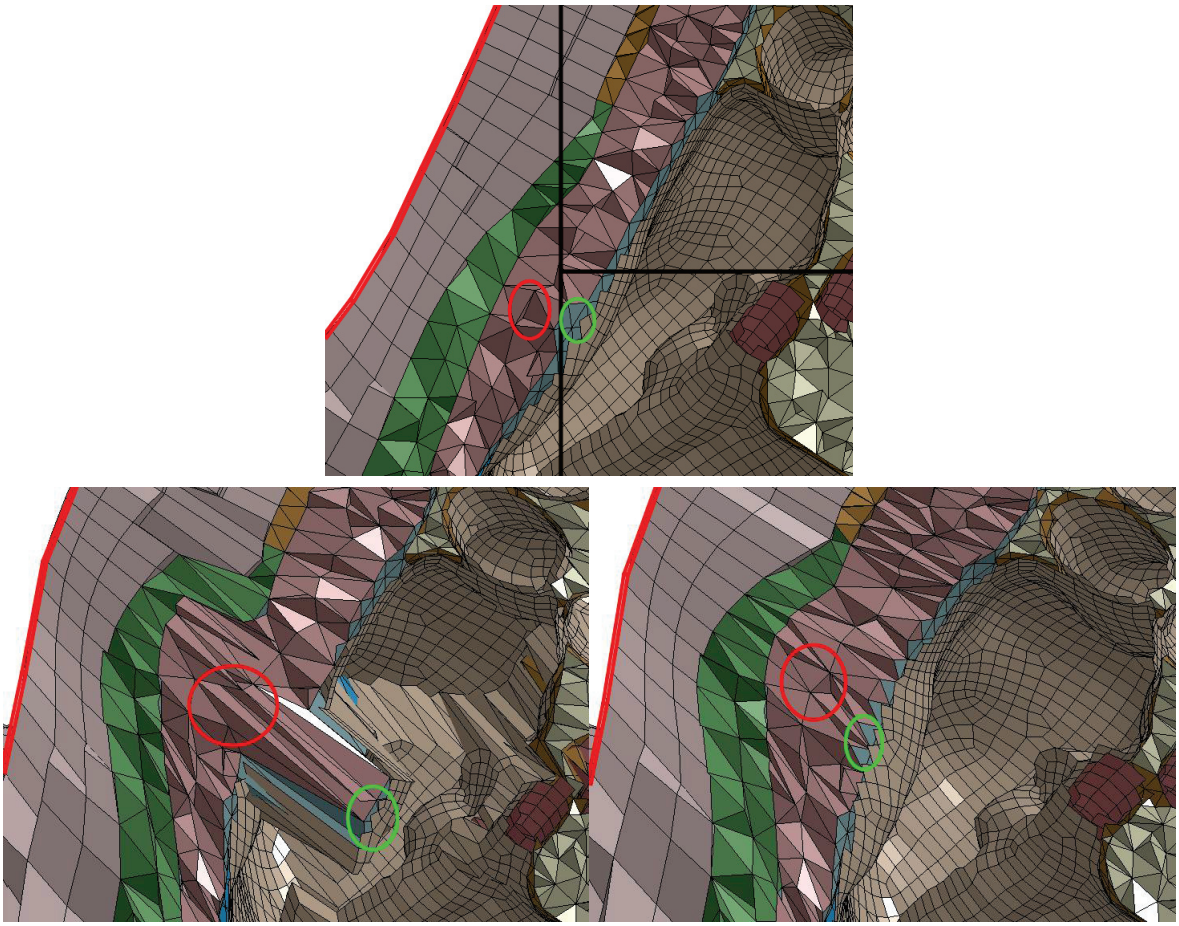

*Figure 57: Example of artefacts near cell boundaries when morphing towards the BMI 35. Detail of sagittal section through the abdomen. The top image shows the baseline model before morphing, including the cell boundaries, marked by thick black lines. The skin outline is marked by a thick red line. The green and red circles highlight the groups of nodes that share elements but fell into different cells. After transformation, without any measure for continuity (bottom left), the red nodes follow the skin while the green nodes stay with the abdomen, resulting in a large distortion of elements. With neighbourhood extension (bottom right), the green nodes are influenced by neighbouring cell, resulting in a smoother mesh. Other discontinuity artefacts near the box boundary can also be observed in the bottom left image.*

#### 4.3.6.2. BMI 35: Combination of subsampling and spatial subdivision (3S)

The 3S workflow with neither overlapping nor neighbourhood extension resulted in a mesh with 5 negative volume elements. The total computation time was 310 s, of which 227 s was spent on the last step.

A runnable model without negative volume elements was obtained by using the 3S workflow with neighbourhood extension. The resulting model was tested in the FE simulation of abdomen impact, and the simulation terminated successfully.

The bone shape was conserved, as there was a CP for each node of the bone surfaces to constrain it. The mean distance between the bone shapes before and after morphing was $9.48 \cdot 10^{-7}$ mm, with a maximum of $9.65 \cdot 10^{-5}$ mm. It was attributed to rounding errors.

Visually, the model skin surface also matched closely the skin target. There was not a one-to-one correspondence between the CPs and skin nodes as for bones. The distances between the BMI 35 skin surface and the target surface were computed using the Hausdorff distance function in Meshlab (ISTI – CNR, Italy). The mean distance was 0.72 mm (Root Mean Square (RMS) of 3.28). This is slightly higher than the initial distance between the shape of the $GHMBC_{25.3}$ model and the baseline (BMI 25.34) target (mean 0.44 mm, RMS of 1.50, maximum 39.45 mm in the armpits). The largest differences for the BMI 35 shapes were observed on the feet (maximum 19.59 mm) and armpits (maximum 69.75 mm). As Figure 58 illustrates, these differences are caused by details of the GHBMC M50-O model not captured by the shape of the skin target. The actual weight of the resulting model was 115.36 kg, i.e. BMI 37.7.

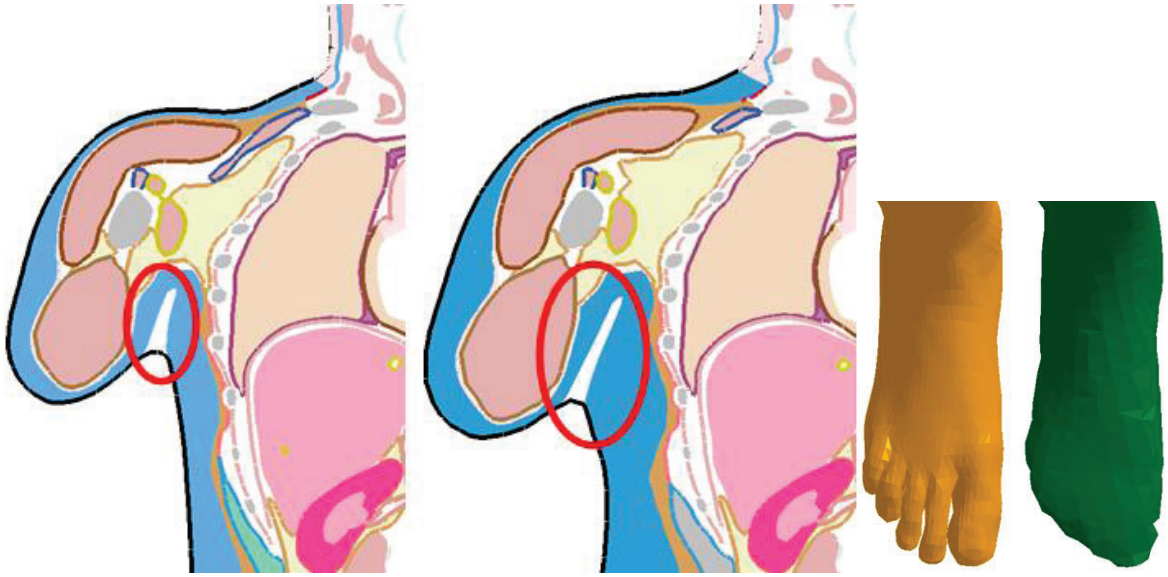

*Figure 58: Regions with the highest differences between the skin target and the model. Left: section near the right shoulder of the model (superficial flesh in blue) and the skin target (thick black line). Left is the baseline BMI 25.3 and right the BMI 35. The armpit fold (marked by red ellipse) is not present on the target surface, which explains the high maximum distance between target skin and model. Right: the level of details of the GHBMC M50-O foot (in orange) also differs from the target mesh (in green).*

Figure 59 shows the Scaled Jacobian for elements, comparing the baseline model with the BMI 35 model morphed using the 3S workflow with neighbourhood extension and 6% overlap. The neighbourhood extension produces slightly less elements with negative Jacobian than the overlap (140 vs 172, the baseline model having 43), otherwise the performance is very similar – the number of

elements in each bucket varied by less than 0.5% between the two methods. The added mass due to mass scaling was 127 g, i.e. similar to the baseline, which had 128 g added.

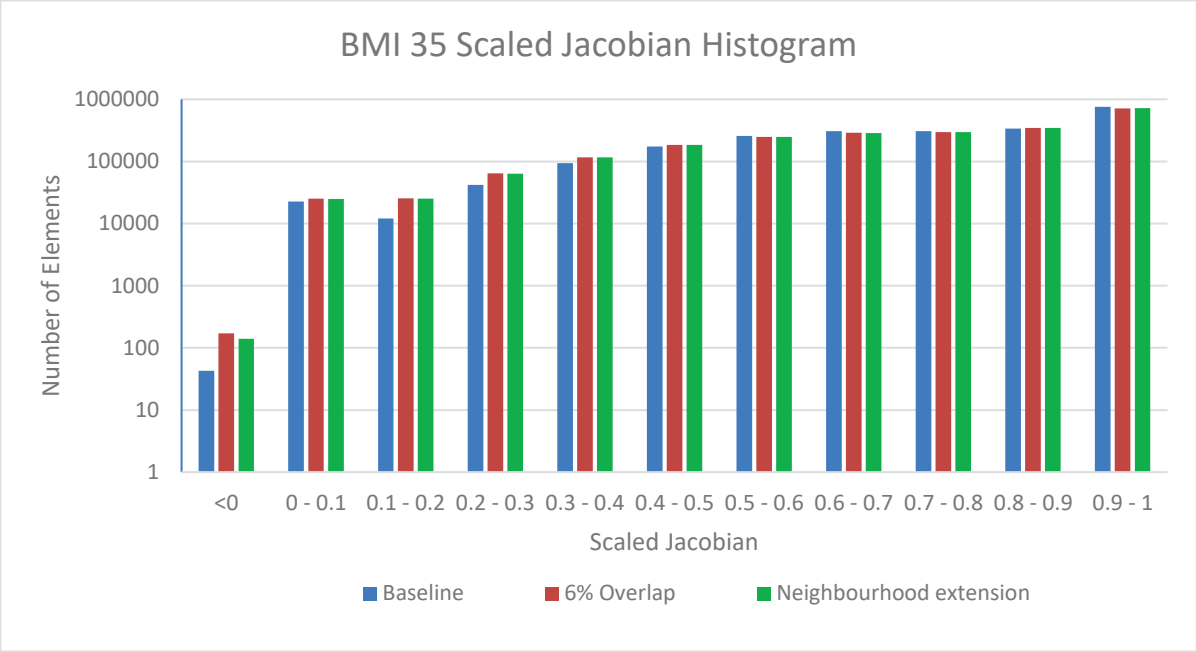


*Figure 59: Histogram of the Scaled Jacobian metric (solid elements) for the BMI 35 test case in logarithmic scale. The Baseline value shows value for the model before morphing.*

Table 4 shows a detailed breakdown of computation times corresponding to the BMI 35 test case when the 3S workflow is used with neighbourhood extension. For the steps performed with subsampling, the time to solve the kriging system is lower than the time needed to apply the transformation to the mesh. This is due to the low number of CPs used in these steps relatively to the total number of nodes to transform (1 255 225). However, in the last step, the higher algorithmic complexity of solving the system manifests itself, leading to a total transformation time of 914 s. The average number of iterations the nearest neighbour algorithm needs to "cover" one face of a cell (as described in Section 4.3.3) was 3.82, with a median 3 and a maximum 18. This led to an additional 3.7 s of pre-processing time when spatial subdivision was employed (Step 4) and also additional 0.69 s for creating the subdivision grid. Thus the total pre-processing time rose to 5.02 s, which is still relatively small compared to the total computation time of the process (831.32 s).

*Table 4: Computation times of the 3S process for the BMI 35 case and neighbourhood extension. Legend: "Subsampling" is the time spent on the homogenous decimation of CPs. "Pre-processing, Subdivision" time is mainly spent on creating the subdivision grid and assigning CPs to its cells. "Kriging solve" time is spent to create the covariance matrix, including memory allocation, and to solve the system. "Kriging apply" is spent applying the transformation to the nodes. "Total" is the total time needed for the whole process, including post-processing operations done by the PIPER framework (writing output etc.). It is therefore slightly longer than the sum of the other times.*

| **3S step** | **Steps 1-3** | | **Step 4** |
|---|---|---|---|
| **Time (s) for BMI 35** | **2 008 CPs (Iteration 1)** | **9 912 CPs (Iteration 2)** | **234 777 CP** |
| **Subsampling** | 0.01 | 0.02 | n/a |
| **Pre-processing** | 0.59 | 0.63 | 5.02 |
| **Subdivision** | n/a | n/a | |
| **Kriging solve** | 0.50 | 16.96 | 772.14 |
| **Kriging apply** | 10.15 | 52.84 | 52.73 |
| **Total per step** | 13 | 69.94 | 831.32 |
| **Total (cumulative)** | 13 | 83 | 914 |

These results are to compare with results without subsampling, i.e. 207 s without overlapping or neighbourhood extension and 830 s with it. This means that the subsampling contributed to additional 84 s of computation time, while the neighbourhood extension added 623 s.

As for the neighbourhood extension, the overlapping also led to a runnable BMI 35 model. The bone target was respected, with a maximum shape-to-shape distance equal to $1.26 \cdot 10^{-4}$ mm and a mean of $2.61 \cdot 10^{-6}$ mm, also attributed to rounding errors. The mean shape-to-shape distance metrics for the skin target were almost the same as for the neighbourhood extension with a 0.73 mm average, a 3.28 mm RMS and a 69.75 mm maximum. The "Kriging solve" time (see Table 1) of the overlapping strategy was 728.77 s, i.e. almost identical to the neighbourhood extension. However, the "Kriging apply" time rose to 119.09 s, since there are in total more nodes being updated as they are shared by multiple cells. As a result, the overall time of the third step rose to 872 s for the overlapping.

#### 4.3.6.3. Thinning test cases

Applying the iterative 3S workflow with neighbourhood extension to the BMI 22.7 also led to a runnable model with no negative volume elements. The distance to the skin target of the resulting mesh of the BMI 22.7 case was at maximum 31.39 mm, with mean 0.40 mm (RMS of 1.21) for skin, and

maximum $1.23 \cdot 10^{-4}$ mm and mean $9.43 \cdot 10^{-7}$ mm for the skeleton. Weight of the resulting model was 72.91 kg, hence the actual achieved BMI of the model was 23.8. Similarly to the BMI 35 test case, the neighbourhood extension produced less elements with negative Scaled Jacobian than the overlapping (52 vs 85), otherwise the number of elements varied by less 0.2% in each histogram bucket between the two methods. The added mass due to mass scaling was 131 g (baseline model had 128 g added).

However, the application of the same approach to the BMI 20 led to 90 negative volume elements after the final step, although no negative volume elements appeared in the intermediate meshes. The negative volume elements were located in areas where the skin and bones get very close to each other, namely around ribcage and wrists. As Figure 60 shows, reducing the distance between bones and skin in such areas causes compression of the elements in between them, and inversions in extreme cases. After adjusting the target surface in the problematic regions, i.e. increasing the distance between bones and skin, a model with only four negative volume tetrahedral elements was produced. Those were removed in Ls-Prepost by the "reorder nodes" function. After that, the model successfully completed the same FE simulation of abdomen impact used for the BMI 35 test case. The BMI of the resulting model was 21.3 (weight 65.18 kg) instead of the targeted BMI 20. This may be caused either by the skin target adjustments to avoid bone penetration and to mitigate negative volumes or from difference in body composition not captured by the transformation. For the distance between resulting mesh and target, the mean was 0.42 mm for skin (RMS 1.24, maximum 26.82 mm) and $8.89 \cdot 10^{-7}$ mm for bones ($9.31 \cdot 10^{-5}$ mm maximum). Unlike the BMI 35 case, negative volume elements appeared when omitting the first iteration (30x30x30 subsampling) of the BMI 20. There were 162 elements with negative Scaled Jacobian with the neighbourhood extension and 354 with overlapping. The added mass due to mass scaling was 149 g (baseline model had 128 g added).

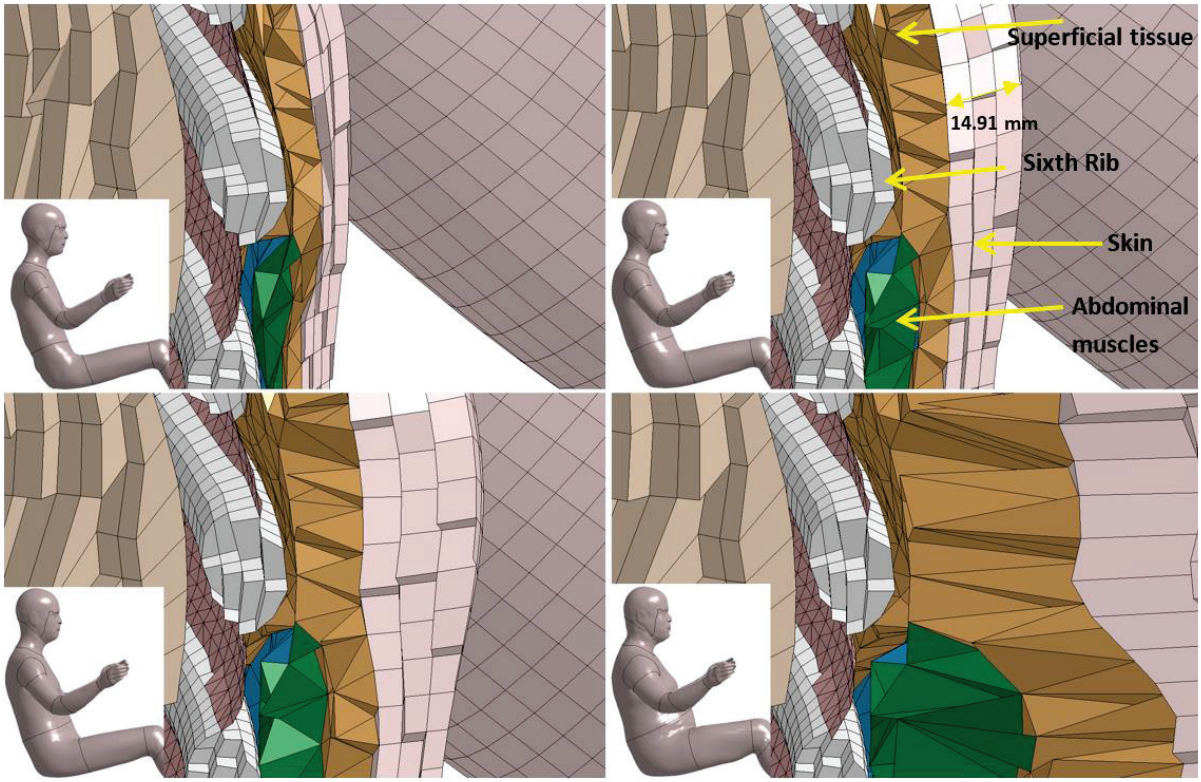


*Figure 60: A slice through the ribcage of the four created models: BMI 20 (top left), BMI 22.7 (top right), the baseline BMI 25.3 (bottom left) and BMI 35 (bottom right). The white cylinder-shaped parts are ribs, namely the sixth left rib in the middle of the image. The image illustrates the important changes in soft tissues thickness around the ribs. The full models corresponding to this image can be seen in the bottom left corners of each image.*

#### 4.3.6.4. Discussion

By applying the proposed methodology, the initial HBM was successfully morphed to BMI 20, 22.7 and 35 with a large number of CPs. Since the decimation and subdivision parameters were the same for the BMI 35, BMI 22.7 and BMI 20 test cases, the computation times to perform the transformation were almost identical. All models (from BMI 20 to 35) could be run in simulations at the end, although the BMI 20 required correction for a few negative volume elements. Such issue was not present for BMI increase. This observation was previously made by Zhang et al. (2017), who also had to locally violate the target shape for targets with BMI lower than the BMI of their baseline model.

This BMI 20 case showed that large reductions of the thickness of superficial tissues becomes difficult with the current method without inverting elements. In the current study, exact targets were required, but without this requirement, the “nugget” parameter of kriging could be used. The nugget allows for smoother transformation in exchange of violating the target CPs position by a specified margin (Jolivet

et al. 2015). Using it for the skin could be considered to mitigate some of the transformation issues in thin regions.

In all test cases, the morphed models ended with higher BMIs than the target. Different reasons could affect this discrepancy including (1) the density and tissue distribution could be affected by the BMI, (2) the material properties were not adjusted in the morphed model, (3) the targets were defined using a humanshape.org shape close to the GHBMC that was then adjusted for posture and depenetrated in the case of the smaller BMIs and (4) there is a small violation of the target due to the morphing itself. Overall, this was considered satisfactory for a methodological test case where the skeleton was assumed to be fixed but should be further refined if the aim is to generate representative models.

Two approaches, overlapping and neighbourhood extension, were presented to mitigate the degradation of element quality on the boundaries of cells of the spatial subdivision. Both are based on sharing CPs with neighbouring grid cells. The overlap approach does not guarantee that control points will be present in the overlap zone while the neighbourhood extension does. However, this had limited effect in the test case, perhaps due to the even distribution and large density of CPs. Neighbourhood extension performed marginally better, which is best evidenced in the non-iterative morphing using all the CPs (80 negative volume elements vs. 372). With the 3S workflow, both approaches produced acceptable results, i.e. runnable models and identical distances. The major drawback is that this was achieved while almost quadrupling the computational time compared to subdivision without additional measures. Without additional measure, a model with only 5 negative volume elements was produced for the BMI 35 test case, but 68 for the BMI 22.7. This suggests that the need for such costly strategies may be dependent on the transformation scenario.

To optimize the number and location of CPs added from outside the current cell, further analysis of the deformation function near the boundaries could help. For example, Heaton et al. (2017) did a hierarchical clustering based on a measure of spatial dissimilarity (applied for temperature data).The CPs subdivision may also be enhanced by some knowledge about the model. For example, Zhang et al. (2017) manually divided their model by anatomical regions (arms, head, torso, hips and legs), which allow limiting the effects disjoints regions of the body (e.g. torso vs. hands) but still requires ensuring the continuity near the region boundaries. Also, Auñón and Gómez-Hernández (2000) derived blending functions for overlapping 2D Kriging regions that ensure C1 continuity of the final transformation function and it may be possible to extend their work to 3D. In any case, both approaches could be combined with the proposed methodology, although likely requiring some adjustments to the method.

The distance to the target surface for the second intermediate mesh using 60x60x60 subsampling was already less than 1 mm (mean value). This raises the question of the number of control points really needed to capture the transformation of a human model. In the current test case, the respect of the bone target was assumed. Other scenarios for which an exact bone shape is expected could include the use of kriging for model positioning (Janak et al. 2018) or subject specific modelling based on high resolution imaging. However, for cases that allow some target violation, a subset of CPs might be sufficient. What magnitude of deviation from the target can be considered acceptable depends on individual applications. For example, Hu et al. (2017) placed a particular emphasis on respecting the target weight of the morphed BMI instead of focusing on shape error. Zhang et al. (2017) underlined the need to balance shape accuracy and mesh quality. In any case, it would be useful to have an automatic mechanism that would compare the distance to the target with a user-specified threshold and perform additional iterations only when needed. Also, evaluating automatically the mesh quality after each step (e.g. negative volume elements) could help automating the subsampling approach (e.g. revert the transformation and do a coarser pass first).

## 4.4. Conclusions

A geometric registration scheme was implemented using local surface descriptors for finding vertex correspondence. Deformation model chosen for the registration consists of simply applying the displacement between matched pair, albeit after smoothing it. When used to register the skin surface towards the PMHS targets, the registered meshes required manual post-processing in order to remove occasional penetrations, despite that an algorithm to avoid penetrations was implemented as well. As such the registration process was deemed satisfactory for the intended application and was used (as it will be described in Chapter 5). A deformation model based on (Yamazaki et al. 2013) using the Laplacian representation was implemented as well. While the deformation by applying the displacement field has negligible computation time, the Laplacian-based deformation adds 3-10 s per iteration when used to register a mesh with 57 000 vertices. The exact time added depends on chosen parameters of the model, as it is itself based on an iterative algorithm (energy minimization). Since the results obtained by the direct deformation were sufficient for this application, the Laplacian based deformation model was not investigated further.

One limitation of the method is that it is creating a vertex-to-vertex correspondence rather than vertex to surface correspondence. I.e. the expectation is that for every vertex on the source mesh there is one specific vertex on the target surface that is the best match for said vertex. This requires the target surface to have at least as many vertices as the source, otherwise multiple source vertices will be

matched with the same target vertex. This is not a problematic requirement, as the target surface can be decimated or subdivided as needed. However, even if the number of the vertices is the same for both meshes, their distributions might not be. In other words, the source mesh can have some parts meshed very densely, i.e. with many vertices per $mm^2$, while other parts might be less detailed. If the target mesh does not match the same distribution patterns, some details will be lost in the parts where the source has less vertices than the target. While this did not seem to be a large issue with the model used in this thesis, it could be for other models. To alleviate this problem and make the method more robust, the matching point for a particular source vertex should be searched for as any point on the target surface rather than only among the mesh vertices.

Spatial subdivision was described by many authors as an efficient way to process Kriging on many CPs. The main challenge of such approach is maintaining continuity of the transformation on the boundaries of the subdivision grid, as large deformations tend to cause local artefacts on the boundaries that can be especially critical for three-dimensional elements used in FE model. The BMI-change study showed that subsampling in conjunction with a heuristic spatial subdivision seemed efficient to mitigate such discontinuities: using an iterative approach, it was successfully applied to change the BMI of the GHBMC M50-O detailed model without changing the geometry of its entire skeleton. This proved the viability of the process and its potential for the intended application.

# 5. Morphing the midsize male GHBM model

## 5.1. Introduction

This chapter will present how the methods described in Chapter 4 were used to create obese FE model matching as closely as possible the PMHS geometry. The GHBMC 50$^{th}$ percentile male occupant model (M50-O) was used in versions 4.1 and 4.5 for preliminary work, and version 5.0 for the final models. They are very similar in the abdominal region, except some differences regarding the lumbar spine, internal contacts, and material properties.

The only available female version is a 5$^{th}$ percentile female, thus further away from the targeted subjects than the 50$^{th}$ percentile male in terms of shape of the soft tissues: using the 50$^{th}$ percentile model therefore limits the amount of deformation imposed on the model during morphing. Therefore, although two PMHS are female, the GHBMC M50-O was used as a baseline for all PMHS.

Morphing a model with a large difference between the source and target can be a complex process. The need to avoid creating elements with poor quality at each step (as those will not be improved by further morphing steps) creates strong requirements on the target definition and the application of the Kriging itself. The upcoming methods sections attempts to summarize this process.

Three targets were selected for the morphing: skeleton, skin and the subcutaneous fat. Two different approaches were used to obtain the skeleton target. The first one (Section 5.2.1), based mainly on the PIPER software, was tested on the MS730. However, since the results were not satisfactory, a different approach (Section 5.2.2) was used for the other two PMHS. The same approaches were used for all PMHS for obtaining the skin (Section 5.2.3) and subcutaneous fat (Section 5.2.4) targets.

Section 5.3 then described how the created targets were used for morphing and mainly challenges specific to the obese morphing that were encountered. Section 5.4 presents the models obtained by morphing and Section 5.5 provides a discussion of the results.

## 5.2. Methods: Target building

The data used for building the morphing targets include the CT, laser and X-ray scans (see Section 3.2.2 for additional details). However, data from each source are expressed in their own coordinate system, which is also different from the one of the FE model. The coordinate system of the GHBM-M50-O was chosen as the reference frame to stay consistent between subjects. Therefore, all scan data are transformed at some point during the process.

Skeletons of the PMHS are captured from the CT scans. The seated CT captures the desired trunk position into which the FE model should be morphed: it is used as a basis for creating the target. It usually does not contain the limbs in their entirety due to the field of view, and the limbs and neck positions of the PMHS were adjusted to fit the PMHS in the box (cf. Section 3.2.2). A general workflow for creating the skeleton target is then:

1. Extract skeleton from seated CT
2. Transform it to the coordinate system of the GHBM-M50-O
3. Position the GHBM-M50-O to match the subject posture
4. Morph the GHBM-M50-O skeleton to match the subject size and shape (using measurements from supine CT to morph the limbs)

An initial realization of this workflow relied mostly on PIPER and is reported in the following Section, 5.2.1. This workflow was tested using the MS730 subject first. Based on that experience, a more refined workflow was created and used for the remaining subjects (described in the Section 5.2.2).

The skin target was built from the CT scans, the laser scans and partially also using the skin of the GHBMC M50-O for parts that were not captures by either of the scans. The process was predominantly manual. It is described in Section 5.2.3, along with the choices made when assembling the surfaces from different sources. Finally, Section 5.2.4 describes how the subcutaneous fat geometry was extracted from the CT scans.

### 5.2.1.Skeleton target: PIPER-based workflow – PMHS MS730

The initial workflow was predominantly based on the positioning and Kriging modules of PIPER. The following is a summary of how was the target for skeleton created and tools used for it:

1. Extract the skeleton geometry from CT using 3D Slicer.
2. PIPER (Pre-positioning module):
    a) Manual rigid alignment of the seated CT skeleton with the GHBM-M50-O, using mainly the pelvis as reference.
    b) Spine positioning using the “spine controller”.
3. PIPER (Kriging module):
    a) Pelvis morphing by kriging with manually placed landmarks.
    b) Ribcage morphing by kriging with manually placed landmarks.

The subsequent text will describe these steps in more details. The 3D Slicer software was first used to extract the geometry of the skeleton from the seated CT selecting bone tissue according to the grey level (Figure 61). Since the density slightly varies for each bone, using a single threshold value gives only approximate segmentation in the form of a rugged surface: adjacent tissues with similar grey level might be considered as bones, and vice versa, some regions of bones with low mineralization might be excluded. Nevertheless, it seemed sufficient to capture the general size and shape of the skeleton.

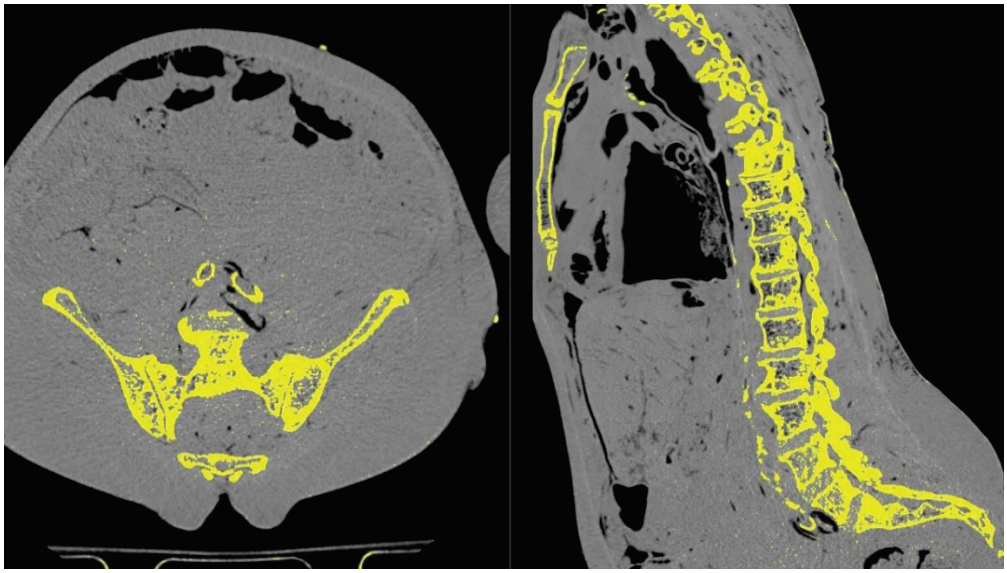

*Figure 61: Example of bone segmentation from a CT scan using a single threshold value. Left: axial view. Right: sagittal view. Part of the image in yellow are tissues that will be segmented based on the chosen threshold. It can be seen that for example some parts of some vertebra will not be extracted this way.*

The CT seated skeleton was aligned using manual rigid transformations in such a way that the CT pelvis position roughly matches the GHBM-M50-O pelvis position (Figure 62, left). Then, the spine of the GHBM-M50-O was aligned manually to the CT spine in PIPER's pre-positioning module using the spine controller, paying more attention to the lumbar spine. A small rotation of the pelvis along the lateral axis helped to refine the spine position. The spine controller drives the spinal shape by a Bezier curve with two control nodes per vertebra (inferior and superior anterior points of each vertebral body). While that allows detailed control over the overall curvature of the spine, individual vertebra can rotate into unnatural positions along their local axes. Although local artefacts could still be present as shown on Figure 63 (right), the process was stopped when the overall curvature was captured (Figure 63, middle) as this was considered sufficient for the current application. Further improvement would be possible but time consuming due to limited ergonomics of the user interface.

After positioning, 47 landmarks were manually chosen on the pelvis of both M50-O and subject (cf. Figure 62, right). These were used as Kriging control points to morph the pelvis. In order to fix the other

bones during the morphing, 49 landmarks already defined in the M50-O metadata on the spine, skull, limbs and pelvis were used as fixed points in the Kriging.

The M50-O ribcage was then morphed to the global shape of the PMHS ribcage, i.e. without considering the exact shape of each rib. Landmarks were selected manually to define the morphing: three on sacrum, three on each side of the ribcage, nine along the spine. To fix the rest of the skeleton, two landmarks were placed on skull and eight on pelvis and legs. As Figure 63 (left) shows, this was sufficient to capture the global shape of the ribcage.

The limbs and head were not morphed, since their dimensions were not notably different between the PMHS (measured on CT scan) and the M50-O (measured on a voxel image of the M50-O skeleton):

- Humerus length (centre of elbow to centre of surface of humeral head): 324 mm (MS730) vs 326 mm (M50-O)
- Forearm (centre of elbow to centre of wrist): 250 mm (MS730) vs 256 mm (M50-O)
- Femur (centre of knee to the base of the femur neck): 425 mm (MS730) vs 435 mm (M50-O)
- Lower leg (centre of knee to ankle): 398 mm (MS730) vs 408 mm (M50-O)
- Head: width: 140 mm (MS730) vs 144 mm (GHBM-M50-O); depth (top of eye socket to the most protruded part of occipital bone) 184 mm (MS730) vs 179mm (M50-O)

This workflow, mainly based on PIPER, had two weaknesses: first, individual vertebrae are hard to distinguish on the surface extracted from the CT scan, which prevents more precise positioning of the vertebrae using the spine positioning module of PIPER (cf. Figure 62, right). With a more refined target (i.e. with more CPs), Kriging could be used instead to enforce both the shape and the position for each vertebra. Second, manual landmark placement is both time consuming and limiting for the accuracy after morphing due to a small amount of landmarks.

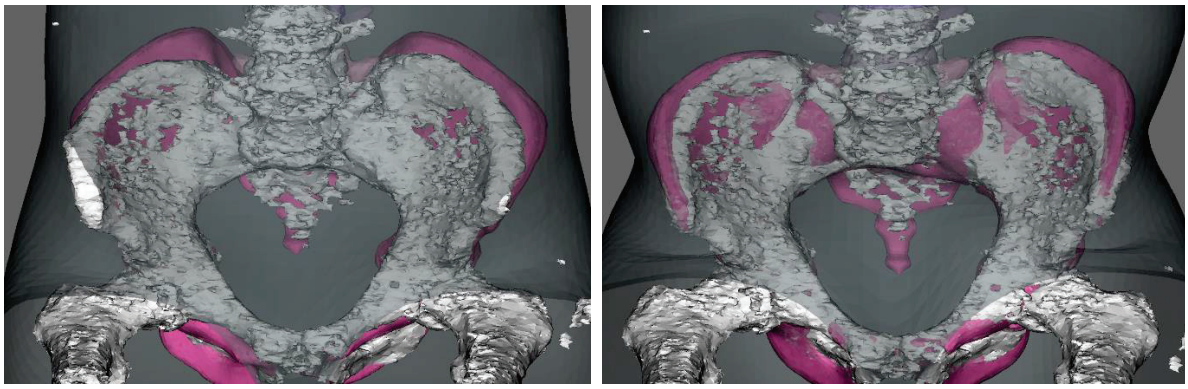

*Figure 62: Alignment of the mesh reconstructed from the CT using 3D Slicer (white surface) to the GHBM-M50-O (pink surface). Left: before pelvis morphing. Right: after pelvis morphing.*

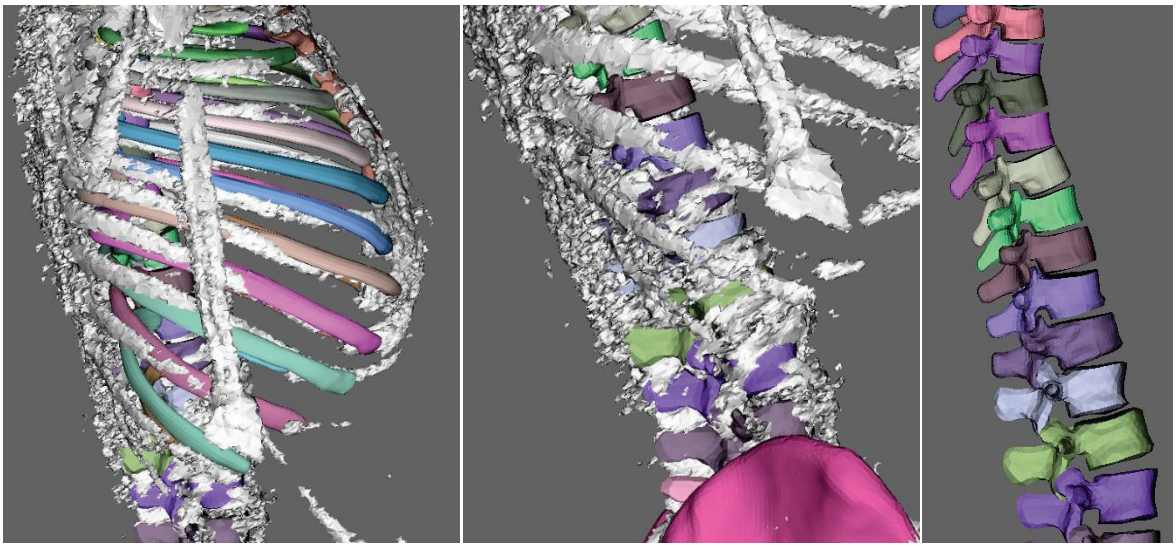

*Figure 63: Details of the M50-O skeleton after morphing in PIPER towards coarse skeleton extracted from CT of MS730 (white surface in left and middle images). Left: ribcage. Middle: lumbar spine. Right: lumbar and thoracic spine. Inconsistent sagittal rotation of some vertebra can be observed.*

### 5.2.2.Skeleton target: Anatoreg based workflow – PMHS MS742 and MS743

Segmentation by registration of a specific (source) surface model onto imaging data (mesh-to-image registration) has the advantage of providing a fast reconstruction of the surface of interest from imaging data that is topologically coherent with the source model. This intrinsically provides a correspondence between vertices that makes them usable as control points. Segmentation of various surfaces of interest from volumetric images such CT is a well-researched problem in medical application. However, image-to-image registration is more commonly used to identify the surfaces of interest (Viergever et al. 2016), mesh-to-image registration has been only rarely used. Baiker et al. ( 2007) registered an articulated full body surface model to a CT scan, but that of mice, not humans. Li

et al. (2015) registered a human CT image to an FE model of trunk, but the model was greatly simplified and not articulated. One reason that is likely the cause of lesser utilization of full body mesh-to-image methods is the higher complexity due to a large number of articulated structures to manage along with nonlinear deformation fields for bone and organ shapes.

The French "National Institute for Research in Digital Science and Technology" (INRIA) has been working on such issues (Gilles et al. 2010), leading to the *Anatoreg* software from *Anatoscope* (startup coming out of INRIA, *www.anatoscope.com*). LAB commissioned *Anatoscope* on improvements of the software for tasks such as the one considered in this thesis. *Anatoreg* has tools for both rigid and non-rigid registration of a geometrical surface mesh directly to a CT image. It was successfully used at LAB to build statistical shape models of ribcages, and it was provided to LBMC by Anatoscope to support this project.

A reference skeleton mesh is provided with Anatoreg. The aim is to use all of its vertices as control points for the morphing. To achieve that, the following workflow to build the target and source based on mesh registration was developed. It produces two outputs: the reference mesh morphed to the shape of the PMHS (target) and the reference mesh morphed to the shape of the GHBMC M50-O (source). The distal extremities and cervical spine are an exception, which were kept from the M50-O (see Section 5.2.2.3 for detailed explanation). Figure 64 summarizes main steps of the workflow, which will be explained and described in the following subsections.

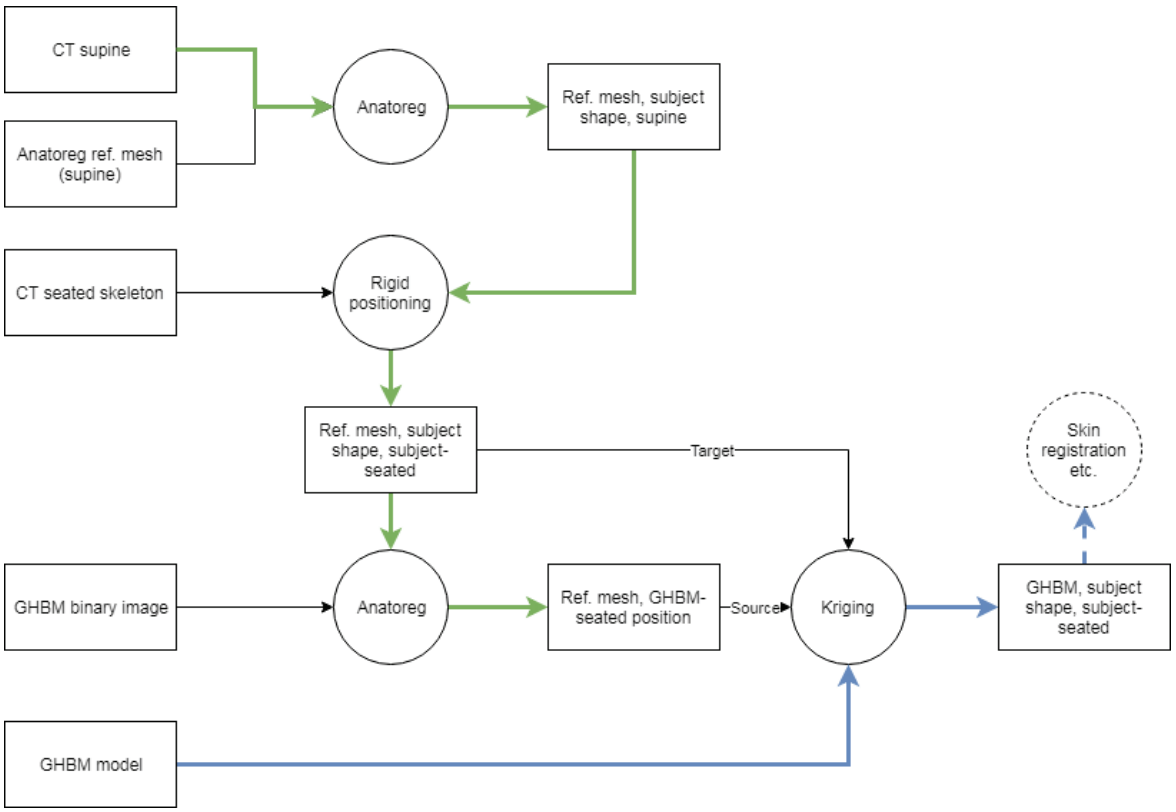


*Figure 64: Final workflow for skeleton registration using* Anatoreg. *"Ref. mesh" stand for the reference surface mesh. Rectangular nodes denote the state of the data, mainly their posture and shape. At the end of the process, the GHBM-M50-O skeleton mesh (denoted simply as "GHBM" in the figure) is in the subject shape and position, ready to be used for subsequent operations.*

#### 5.2.2.1. Registration to the PMHS in Anatoreg

First, the articulated reference surface mesh of the full skeleton (provided with *Anatoreg*) was registered to the supine CT image (including limbs) (cf. Figure 65). Then this registered mesh was positioned to the seated posture.

To detail the procedure, the reference mesh was first aligned by rigid transformation to the CT image according to the pelvis. Then two non-rigid registrations were performed, based on landmarks and on image information.

The landmark-based registration of the reference mesh is driven by a set of anatomical landmarks (already defined with the reference mesh), manually extendable to refine the deformation, notably for ribs (Figure 65, right). Each landmark has a "stiffness" to manage the importance of respecting its target position.

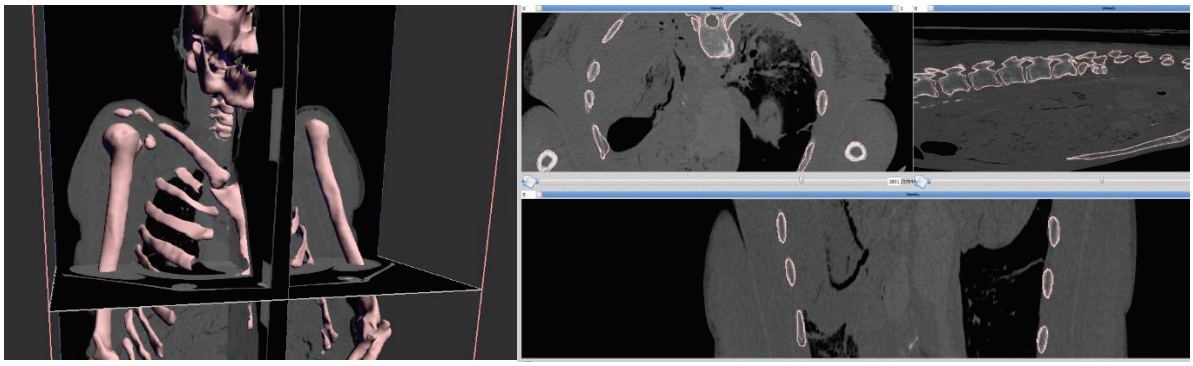

*Figure 65: User interface of* Anatoreg*. Left: 3D view, showing overlapping surface mesh (pink) and the CT images. Right: image view, showing three slices through the CT data with the reference surface highlighted in pink.*

The actual landmark-based registration is performed by a "*simplified constraints-based*" simulation (Tournier et al. 2015): this non-rigid mesh deformation tends to respect the target position of landmarks while minimizing the deformation of the initial shape, similarly to the Kriging step in the previous workflow in Section 5.2.1. The added benefit of *Anatoreg* is the user interface allowing placing interactively the targets directly on the CT image, both on image and surface mesh, to correct the deformation in quasi-real time and also that the skeleton is articulated.

Image-based registration was then used for finer matching. Each vertex on the surface of a specified bone is probing the image voxels in its proximity (a user parameter) and looks for voxels with large gradient, as that signifies a boundary between anatomical structures. Such a vertex-to-voxel correspondence drives a similar non-rigid mesh deformation as for the previous registration approach. The downside of this image-based registration is that it will occasionally find a false high gradient due to the large set of surrounding anatomical structures.

Therefore, both the landmark and image-based registration are best used together: first, anatomical landmarks are used to anchor the bones at distinct points. Then, mesh landmarks are used for higher precision in regions without distinct anatomical landmarks. Lastly, image-based registration is turned on. A low "stiffness" of the vertex-to-voxel correspondence is used to lock deformation into the correct gradient; this stiffness is progressively increased (while simultaneously decreasing the stiffness of the landmarks) to accomplish the transformation according to bone boundaries visible on the image. The advantage of this approach is that landmarks do not have be placed accurately.

In initial attempts, the image registration used at once for all bones lead to inconsistent results, due to incorrect vertex-to-voxel correspondence related to a soup of gradients for neighbouring bones. Adapting the registration stiffness per bone helped to fix such errors, leading to a bone-by-bone

registration: once the registration of a particular bone seemed acceptable, the stiffness of its image registration was set to maximum to fix it before applying the same process to another bone.

In practice, the registration was divided by anatomical regions: pelvis and spine first, then upper body, lower body, hands, and finally feet.

**The registration of the pelvis and spine** started with the pelvis, continuing by the lumbar and then thoracic spine. The mandible and skull were registered to the CT scan in order to constrain the cervical spine during the registration, but the cervical spine was left to deform freely. The cervical spine is not a region of interest for the current application. Its geometry is complex and its curvature on the seated CT scan to be used later is far from a normal seated posture (see Section 3.2.2.1, scanning box constraints and Figure 66, left). Therefore, the cervical spine was later replaced by the M50-O geometry (described below). While MS743 was shorter and therefore its head did not require to be reclined (cf. Figure 66, right), the same procedure was applied to both PMHS.

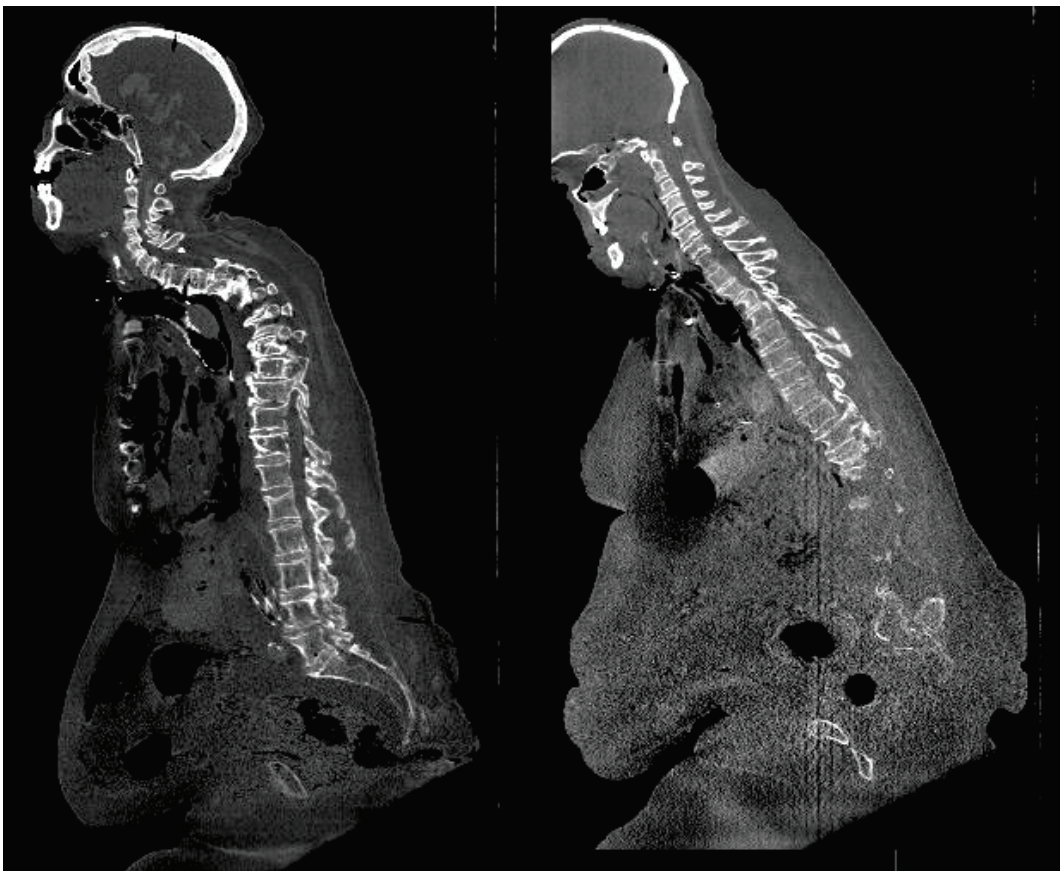

*Figure 66: Mid sagittal seated CT scan view of PMHS MS742 (left) and MS743 (right).*

The remaining **upper body** bones were registered in this order: sternum (using the xyphoid process and sternoclavicular joints as anatomical landmarks), clavicle and glenohumeral joint (using the greater tubercle of the humerus and the sternoclavicular and acromioclavicular joints), humerus, rest of the

arms. For the **lower body**, the process was generally easier than for the upper body since all the bones are relatively large and easily distinguishable. The order was femur first, followed by fibula, tibia and patella. Registering the **hands and feet** was problematic and tedious since they contain many small bones and that their cadaveric positions are very different from the model. Registration efforts were stopped because these extremities are not a region of interest of the current study and, similarly to the cervical spine, and they will be replaced entirely the M50-O ones.

For the first PMHS, the processed described above took two full days, but with increased experience the processing was faster. Approximately five hours could be estimated as time requirements for an experienced operator to process one full body skeleton registration.

Once the full reference skeleton is registered on the supine CT-scan, the last step was to position it to the seated CT image using *Anatoreg* but without non-rigid deformation. This process was generally fast (less than 30 minutes) since the shape of the bones is unchanged. An exception was the ribcage: its shape can slightly change between the two postures due to gravity. Therefore, once positioned, the non-rigid registration was used to refine the rib shape. Despite these efforts, the surface of some ribs exhibited some visible warping. This was attributed to an occasional confusion between the inner and outer boundary of the rib's thin cortical shell by the matching algorithm (Figure 67).

*Figure 67: Detail of a CT scan illustrating the cortical shell of ribs marked by red arrows.*

#### 5.2.2.2. Registration to the M50-O

The reference mesh registered to the PMHS in a seated posture was used as a target for Kriging the M50-O (after a rigid alignment to the M50-O coordinate system by Iterative Closest Point in Meshlab). For the matching source, the reference mesh was easily registered to a binary image of the M50-O using the image-based registration tool of *Anatoreg*. Such a binary image with sharp and distinct gradients was created by voxelizing the space occupied by the M50-O bones and assigning the value "1" to voxels inside bones (cf. Figure 68).

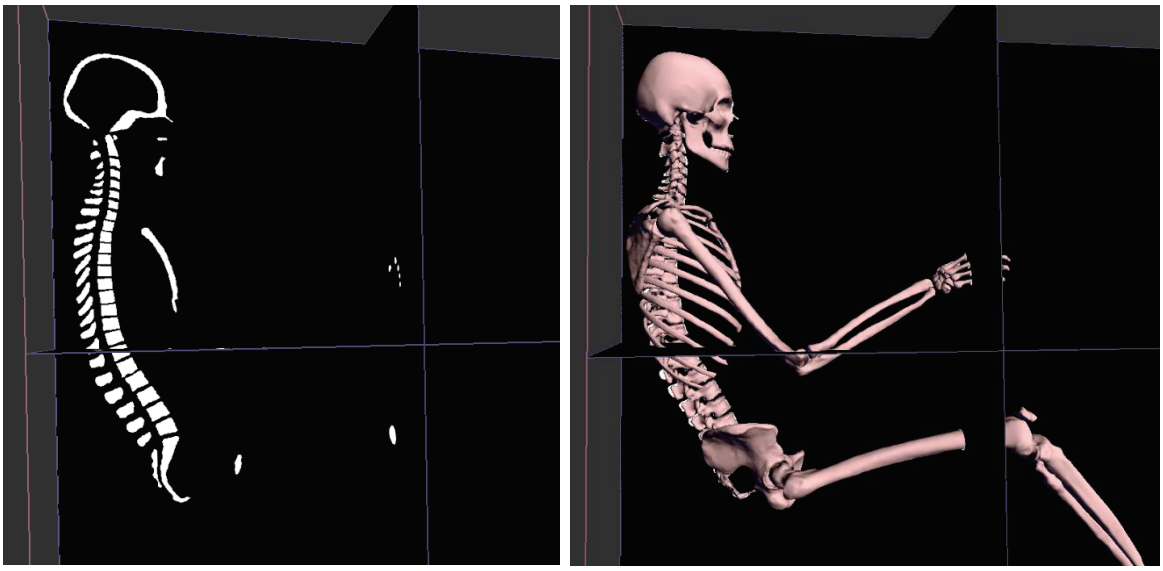

*Figure 68: GHBM-M50-O registration in* Anatoreg*. Left: binary image only, right: reference mesh after registration.*

#### 5.2.2.3. Corrections for extremities and skull

As previously mentioned, the feet and hands were replaced by those of the M50-O. In addition, for MS742 and MS743, the entire forearms (radius, ulna, hands) and lower legs (tibia, fibula, feet) were also replaced because they are not of primary interest for the study and their shapes would have prevented a proper connection with the M50-O extremities without further adjustments. For the replacement, the surface meshes of the M50-O humeri and femurs were manually aligned by rigid transformations with the ones of the registered skeleton, with a focus on the elbow and knee joints. The M50-O distal regions were then kept. The length of the forearms and lower legs was corrected later (Section 5.2.2.4) to match the PMHS lengths.

The cervical spine was replaced as well to have the head in an appropriate seated posture and the skull was replaced along with it. The GHBM-M50-O skull was scaled to the PMHS size along the three principal axes: distance between the temples, between the top of the skull and attachment of the C1 vertebra, and between the eye sockets and its projection to the back of the head along the horizontal axis. The highest change in one axis this way was 0.95 (MS743), i.e. 5% decrease in size.

All the vertices of the bone meshes obtained this way were then used as control points to morph by Kriging (in PIPER) the M50-O to skeleton data from the seated CT scan.

#### 5.2.2.4. Skeleton morphing process

The control points were separated into six sets with different nuggets: legs, pelvis and lumbar spine, thoracic spine, skull and cervical spine, arms and finally ribcage. The Kriging was performed in an

iterative way (see Section 4.3), with progressively decreasing nuggets. The ribcage was always assigned non-zero nuggets (-30) to smooth the warping created by the previous Anatoreg registration, while not changing the circumference of the ribcage. Note that for the MS742 subject the scapulae of the M50-O were left unconstrained to be deformed by the surrounding bones during morphing step, since they were in a posture deemed unnatural (perhaps due to fixtures used to maintain the position of the PMHS).

After the last morphing, the length of the forearm and lower leg were corrected using the "Scaling Constraints" module of PIPER. It defines a sparse and fast kriging system based on several anthropometric measurements (forearm, radius and tibia length), which can be used to change the limb lengths within seconds.

As a last step, the arms were rotated at the glenohumeral joint (in PIPER) to increase the gap between the skin of the arms and the skin of the trunk and thus facilitate the next skin morphing process.

The result is a M50-O with skeleton morphed to the subjects shape in the CT-related posture. Figure 69 shows the two skeletons created for PMHS MS742 and MS743 alongside the M50-O skeleton for comparison. As visible on this figure, the resulting meshes are asymmetric as the PMHS are. These models served as starting point for skin morphing, fixing all vertices of the bones to lock the skeleton shape. Figure 64 shows a summary of the workflow as a flowchart.

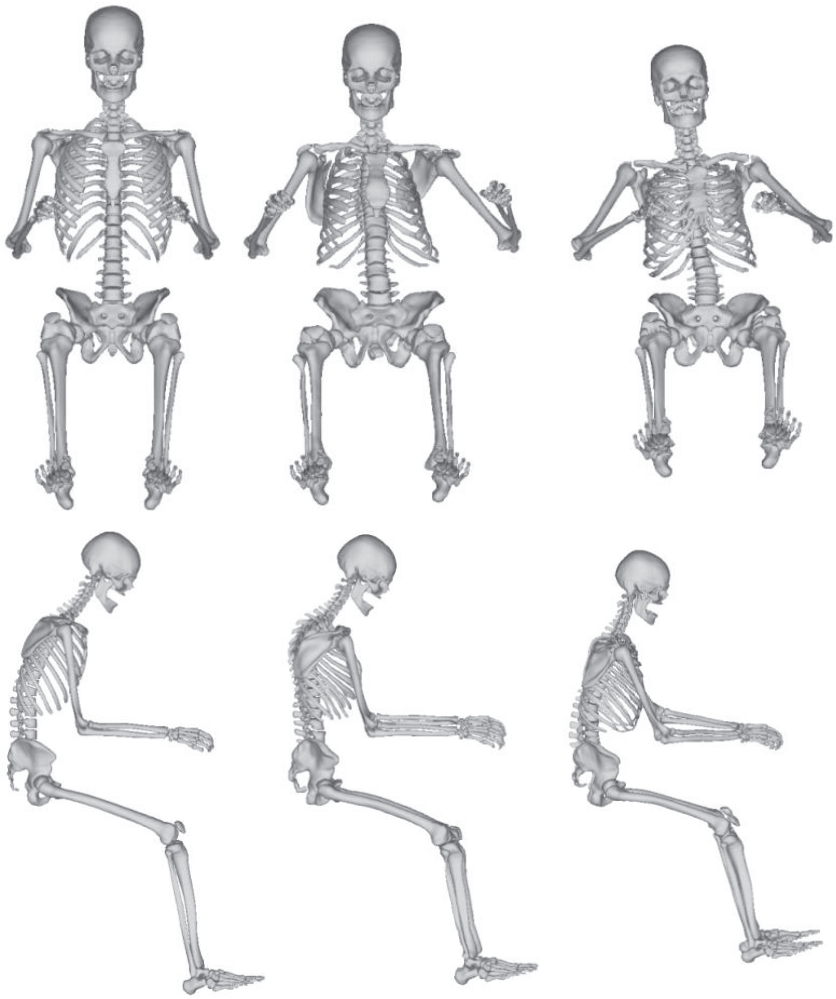

*Figure 69: Overview of the skeletons created with Anatoreg compared with the baseline M50-O. Left: M50-O. Centre: MS742. Left: MS743.*

### 5.2.3.Skin target

The PMHS skin surface is defined on both the laser and the seated CT scan. The CT scan does not contain the complete chest, arms and legs due to the size constraints of the scanner (see Section 3.2.2.1 for details). The laser scan is limited by the seat: the parts of the body that are in contact with the seat were not recorded, i.e. the back, the backside of legs and some parts of the arms. Section 5.2.3.1 first describes how the surfaces from different sources were assembled into a single skin surface. Sections 5.2.3.2 and 5.2.3.3 then describe how they were registered in order to obtain the skin target with and without abdominal fold, respectively.

#### 5.2.3.1. Surface assembly

As both scans are performed in positions that aim to be identical for the trunk, they can be combined to create a skin surface as complete as possible. Their coordinate systems were first aligned using an

Iterative Closest Point registration in Meshlab. For MS730 and MS742, the markers using the marker sewn onto the skin matched very closely after registration, with a maximal difference of 1.4 cm between one pair of markers. For MS743, the differences were larger, up to 4.5 cm. Differences were attributed to small manipulations of the PMHS after the surface scan to prepare for freezing for the CT scan (e.g. foam was inserted in the abdominal fold to make it more distinguishable on the CT scan, the abdomen was moved to insert the foam and then put back). For the MS743, only a small portion of the laser scan was used to complete the skin surface mainly visible on the CT scan.

After combining the laser and CT skin surfaces, parts of the thighs and upper arms skin surfaces were still not fully defined. Also, the skin surface of the head was not extracted from the CT to preserve PMHS anonymity. These missing parts of the skin were completed with corresponding parts of the M50-O skin after skeleton morphing. Combining the three data sources (CT, laser scan and M50-O limbs and head) into a single surface was done in Blender. Apart from minor manual corrections of vertex position, the main tools used for this were the “Shrinkwrap”, “Mesh Deform”, “Remesh” and “Decimate” modifiers. The “Shrinkwrap” was used for patching the surfaces together by projecting vertices onto a target surface and then smoothing out the transitions, artefacts of the scanned surfaces and the markers on the abdomen. The area around neck had to be partially remeshed and heavily smoothed, as it was cut open to insert temperature probe inside the PMHS. “Mesh Deform” was used to shape the mesh (taken from the M50-O) for the bottom of the thighs such that it respects the width of the thigs as seen on the CT scan. It deforms a specified geometry by deforming an arbitrary control mesh (a rectangular grid enclosing the legs was used). “Remesh” was used to smooth out the surface, homogenize node distribution.

#### 5.2.3.2. Target with abdominal fold

The assembled surfaces were then registered to the skin of the M50-O model using the developed registration method (Section 4.2.2). Note that the source surface was not selected from the baseline M50-O, but from the intermediate one already morphed by the skeleton target (Section 5.2.1 and 5.2.2). This is because the morphing was performed first by only the skeletal target and only then the skin target (see Section 5.3 for details).

The surfaces were decimated prior to the registration in order to match the number of vertices to the number of vertices of the M50-O skin to facilitate registration, i.e. 57 805. As mentioned in Section 4.2.2, minor manual editing of the fold was also required to remove small self-penetrations inside the fold and armpits caused by imprecise registration.

Since the skeleton of head, hands, forearms and feet were not personalized (registered to the PMHS), the corresponding skin parts were not either to avoid potential incompatibilities. For the PMHS MS743, the skin leg target was cut just below the knee for the same reason. It is believed that the soft tissues of these regions would only have a marginal effect on the abdomen response. To reduce the amount of CPs, only bone vertices were used as control points in these regions. Figure 70 shows the final surfaces used as skin targets that were created for the three subjects.

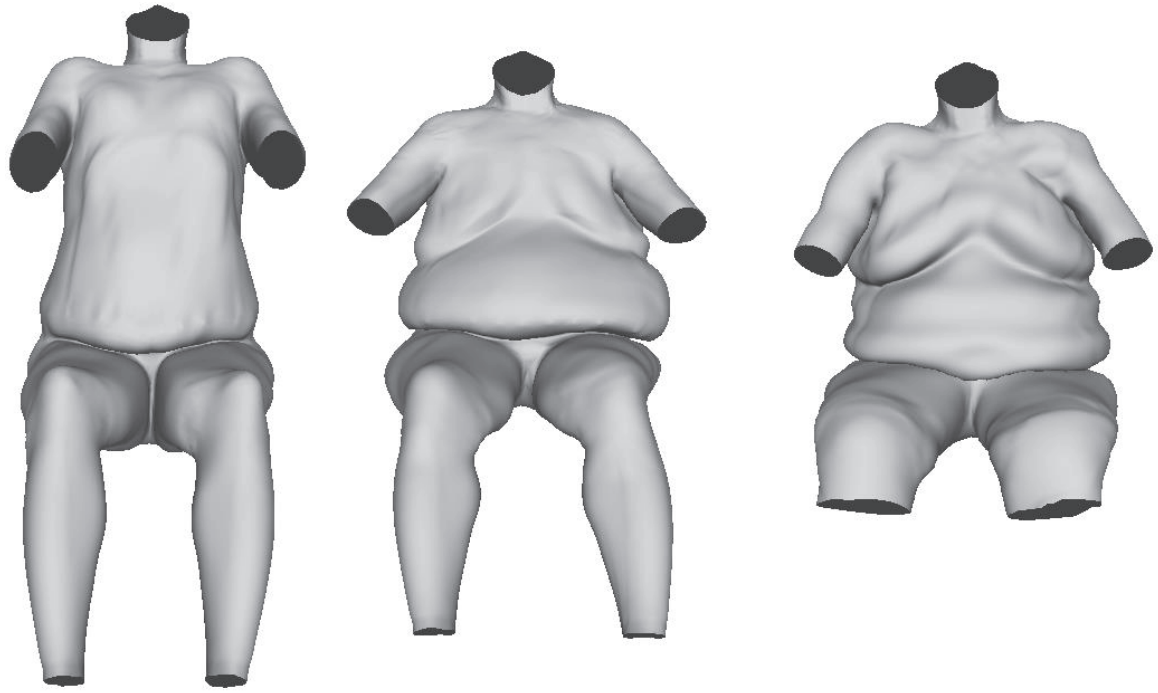

*Figure 70: Final skin targets for Kriging. From left to right: MS730, MS742 and MS743*

#### 5.2.3.3. Target without abdominal fold

The skin surfaces described in the previous section were also used to create a version of the target without the abdominal fold. This was done by selecting vertices of the most protruded portion of the abdomen and projecting them directly down (along Z) onto the skin surface to create a vertical surface connecting the abdomen to the thighs. Vertices that became hidden by this surface, i.e. those inside the abdominal fold, were deleted. Figure 71 shows the vertices selected as boundaries for the new vertical surface (left) and the resulting surface itself (right).

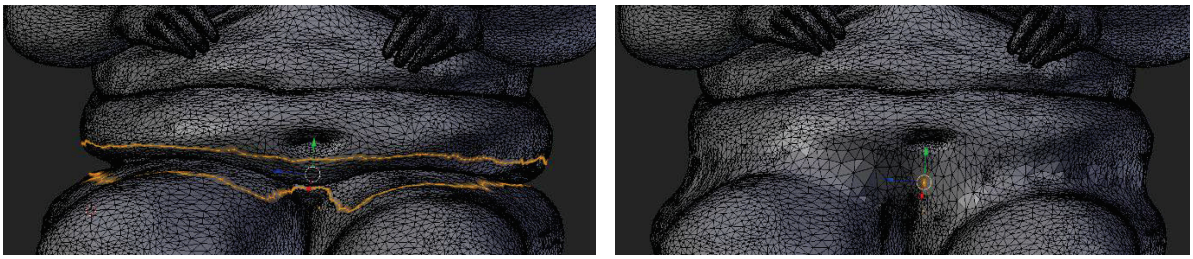

*Figure 71: Creation of a skin target without abdominal fold. Left: the yellow line shows the boundary of the portion of the mesh that was deleted: the top line corresponds to the most protruded portion of abdomen and the bottom line to a vertical projection of the top line. Right: final result (smoothed) after connecting the abdomen and thigs.*

### 5.2.4.Subcutaneous fat

The internal surface of the subcutaneous fat layer around the abdomen was used to drive the personalization of the interior shape of the abdomen. In subsequent text, this surface will be referred to simply as "subcutaneous fat target". Although the fat tissues are easily distinguishable on a MRI scan, the MRI scanner that was used had a limited field of view making it impossible to scan the PMHS in a seated posture (as mentioned in Section 3.2.2.2). Therefore, the subcutaneous fat target had to be built using the seated CT scan, although the MRI scan was occasionally used to as a visual aid.

The 3Dmod interactive tool (*bio3d.colorado.edu/imod*) was used to segment the subcutaneous fat from the CT between waist and the bottom of ribcage. The subcutaneous fat was manually contoured on individual images of the CT scan (every four images, leading to a 2 mm gap between contours). The triangular surface interpolating these contours was smoothed in Meshlab using the Taubin Smooth filter (to preserve the dimensions of the surface as it does not cause shrinking). Figure 72 shows the contours as well as the final surface.

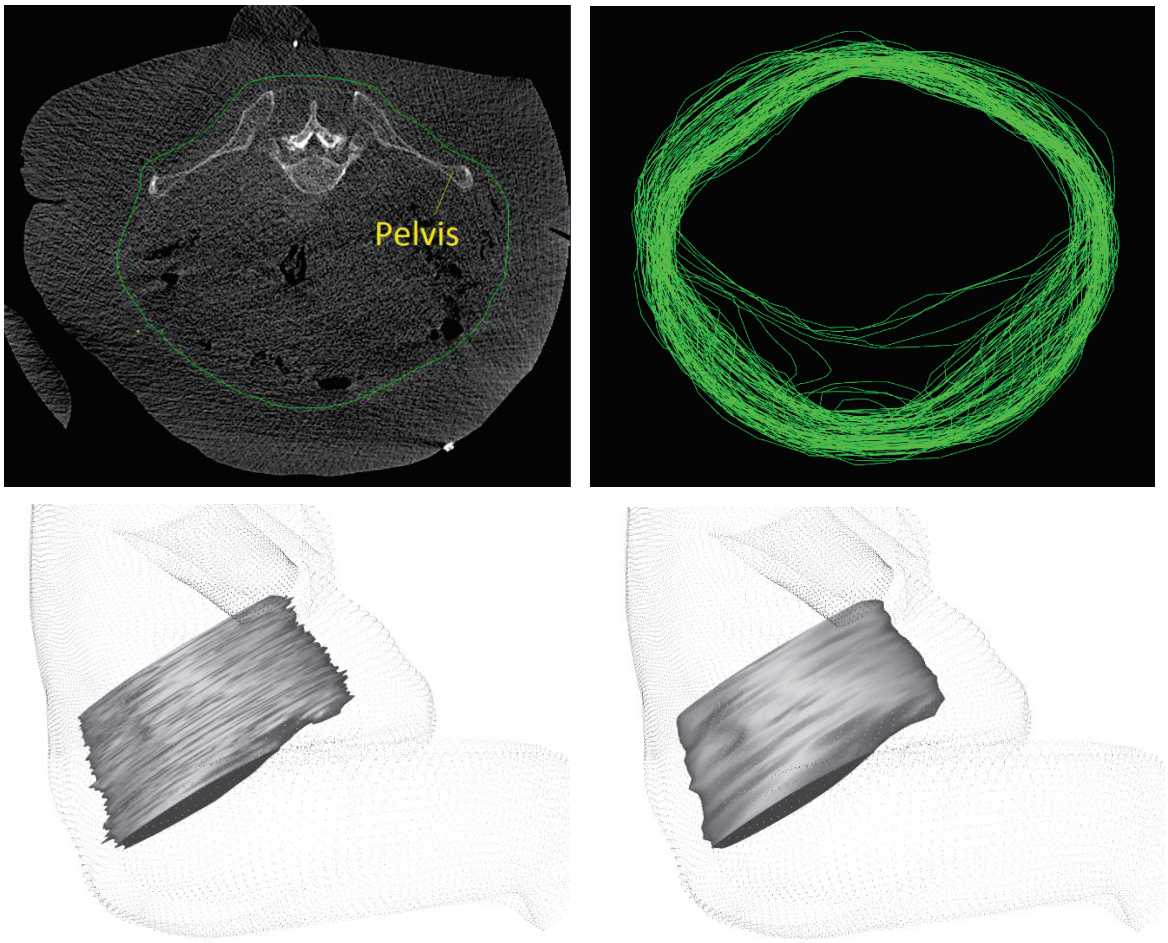


*Figure 72: Extraction of subcutaneous fat target for the MS742 using IMOD. Top: contour model of the subcutaneous fat target – single CT image with the contour marked in green (left) and the whole model viewed from the top (right). Bottom: triangular surface created by interpolation of the contour model, before (left) and after (right) smoothing. The vertices of the MS742 skin are shown for reference. Notice the limited contrast on the CT image.*

A corresponding surface then had to be defined on the M50-O to prepare for the morphing. However, the thickness of the abdominal wall muscles (rectus and oblique) is considerably higher on the M50-O than on the PMHS: 21 mm for the M50-O at the rectus (umbilicus level) vs less than 6 mm for the PMHS (measured on the MRI of MS730 and MS742, MRI for MS743 is not available). In fact, the PMHS abdominal muscle thickness is so small that it is difficult to distinguish at all in most locations. Morphing the abdomen using the muscle-fat boundary would therefore result in an even larger muscle thickness in the morphed model, and a misrepresentation of the thickness of the abdomen wall. Therefore, in the anterior part of the abdomen, the subcutaneous fat target was associated with the interior surface of the abdominal muscles, i.e. the boundary of the abdominal cavity. This will lead to considering the mesh of the abdominal wall muscles as fat in the morphed model. The subcutaneous fat target on the

back of the model was not personalized because there is no continuous surface to register to in the M50-O as Figure 73 shows. It was expected to have limited impact on the behaviour of the abdomen.

The same registration procedure used for the skin (Section 5.2.3) was tried with the subcutaneous fat target. However, the registration algorithms performed poorly on the boundary of the open surface (perhaps due to only one face per edge). On the other hand, the simplicity of the surface made it relatively easy and fast (about 20 minutes) to register it manually, specifically by using the "Shrinkwrap" tool in Blender used previously for creating the skin target. It projects the vertices of the source mesh to the closest vertex of the target mesh. Minor manual editing was required to ensure that the closest point projection leads to an even distribution of the vertices. The result is shown in Figure 74. Note that the subcutaneous fat target was applied only after morphing by the skeleton and skin targets (Section 5.3). Therefore, the source surface does not come from the baseline model, but rather from one already morphed by the skeleton and skin targets.

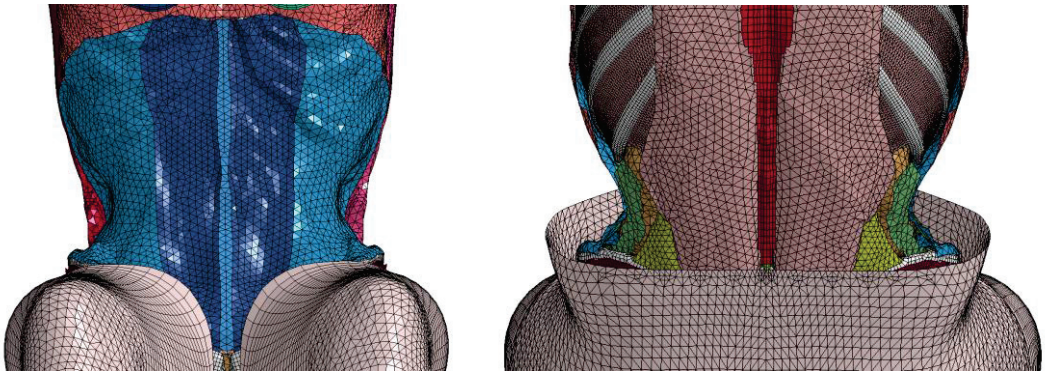

*Figure 73: The baseline GHBM-M50-O model. Left: front of the model, three surfaces (different shades of blue) that can be used as boundaries of the abdominal cavity. Right: back of the model, lack of a smooth continuous surface makes it complicated to match to a subcutaneous fat target.*

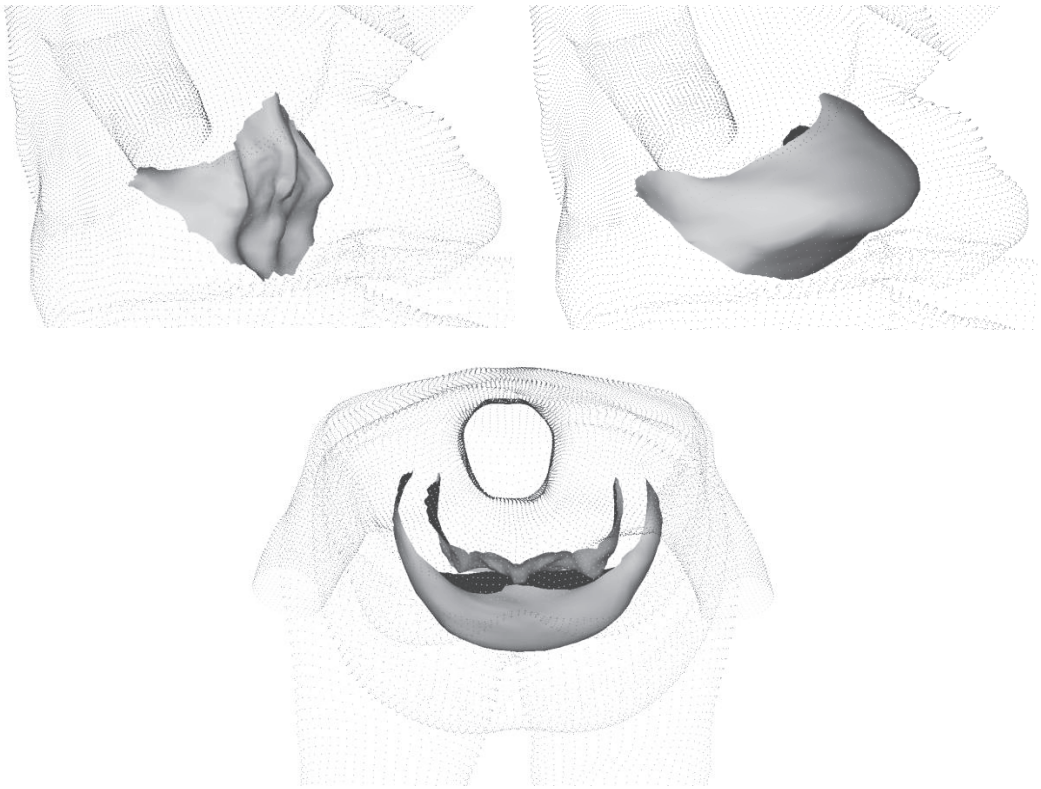

*Figure 74: The subcutaneous fat target for the MS743. The skin vertices are shown for reference. Top left: source surface. Top right: target surface. Bottom: top view with both the source and target surfaces.*

## 5.3. Methods: Morphing towards obese targets

PIPER was used to morph by Kriging applying the iterative workflow described in Section 4.3 in two steps. First, a model was created using only the skeleton target, then this model was morphed using the skin target and fixing the skeleton (same source and target CPs). For both steps, three iterations of Kriging were performed: first with large decimation (less than 8000 CPs), then low decimation but without spatial subdivision (up to 50000 CPs), and lastly with no decimation (all CPs) using the spatial subdivision. The nugget was decreased with increasing amount of CPs: the final iteration was performed without nugget on the skeleton and a small nugget on the skin (-30).

The costal cartilage was not part of the skeleton target. Therefore, after the skeleton target based morphing, the shape of the costal cartilage was fixed by adding its vertices as additional CPs to avoid unnatural shape (Figure 75, left). These new CPs were always associated with a nugget of -100 since in the absence of target the shape was unknown. The resulting shape seemed plausible for all subjects when following this approach (Figure 75, right).

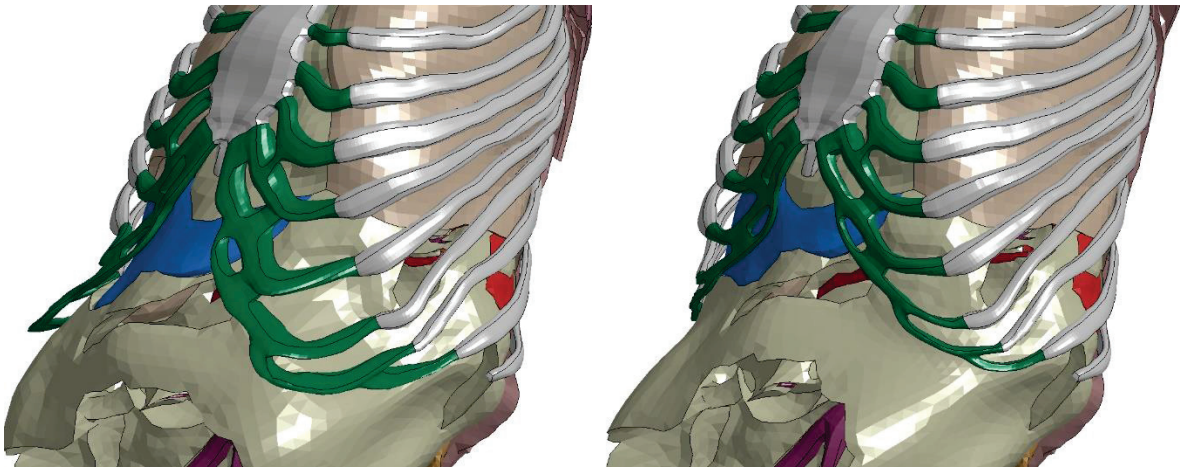

*Figure 75: The costal cartilage (green) of the M50-O after morphing towards the MS742 PMHS. Left: unconstrained during the entire morphing process. Right: fixed after morphing by skeleton only (setting fixed CPs on its nodes and using a nugget -100 for the morphing with skin target).*

However, there were several challenges specific to the obese targets that prevented obtaining runnable models reliably. Specifically, it was correct representation of the abdominal fold and the subcutaneous fat target. Sections 5.3.1 and 5.3.2 will describe those two issues in detail and present the chosen solutions.

### 5.3.1.Abdominal fold

For a non-obese person as the M50-O used as source model, the abdomen is modelled as a convex and mostly flat surface without fold. Accounting for the abdominal fold in the target geometry results in large deformations of this surface during the morphing. As illustrated Figure 76 with a possible source/target relationship, a few solid finite elements have to describe a surface that changes its normal by 180 degrees. This deformation needs to be propagated through all the inner layers of elements that are connected to the outermost layer, making the problem even more challenging.

**In a first trial,** the iterative workflow reported in Section 4.3 for the kriging test cases was used. A runnable model (i.e. without initially inverted elements) was generated when morphing towards the MS730 target. However, MS742 and 743 have considerably larger folds (Figure 77) and the Kriging resulted in tens to hundreds of inverted elements around the fold area, regardless of Kriging parameters.

Figure 78 shows details of the mesh distortion at the fold following the morphing process. A solution could be to use many small elements for the fold to better discretize the curvature, reduce the angles between neighbouring elements and avoid penetrations and large distortion. However, this would require remeshing the model in the area.

An **alternative** would be to represent the fold as a sharp angle between the thighs and the abdomen (Figure 79 left). With this idealization, the hexahedral elements of the subcutaneous soft tissues can then be distributed on either side of the sharp angle, with an edge line prolonging it (Figure 79 right). This can be realized by adding control points in Kriging to enforce this line on the skin and internal elements (red dots).

This was tested using the MS742 target. The source control points materializing the folding line were manually defined on the skin and subcutaneous tissues (i.e. 35 nodes times four layers). Their target was set by connecting the fold edge boundary on the skin to the subcutaneous fat target with 35 lines and cutting the lines in four. Figure 80 shows two sections of the resulting model. The model was not runnable due to negative volumes: some areas had good element quality (as intended) but many others had large distortion issues.

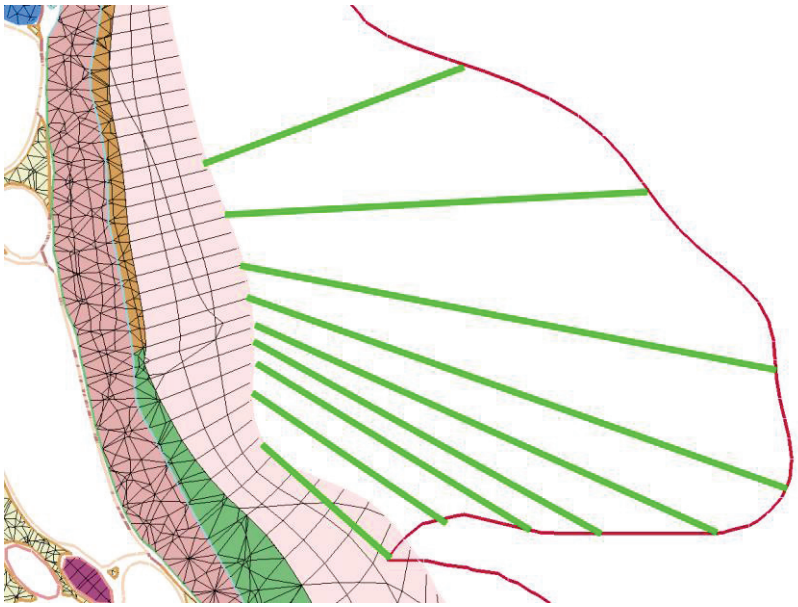

*Figure 76: Illustration of possible deformation imposed on the model by the abdominal fold target (side view from right to left, cut through the mid sagittal plane of the model; red line on the right side of the image is a contour of the skin target, geometry on the left the baseline model). Green lines represent a possible correspondence between the source and target skin surfaces. Such registration will clearly introduce large shearing particularly in the fold area (bottom of the image).*

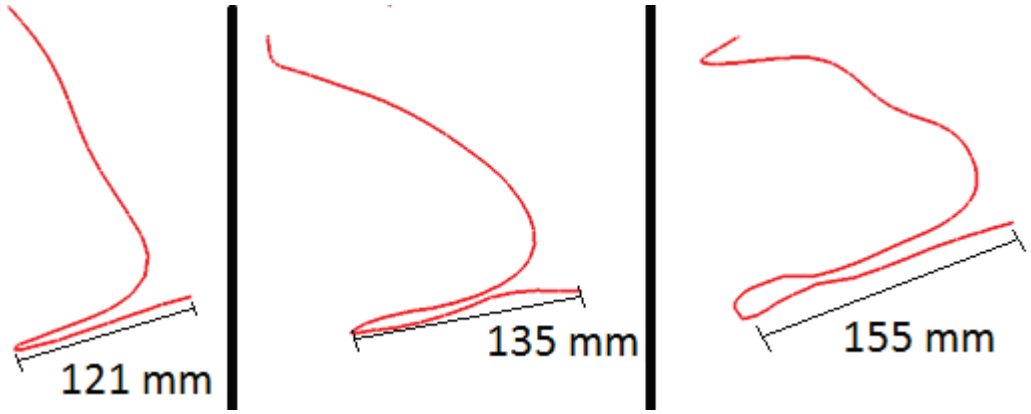


*Figure 77: Contours of the abdominal fold as a section perpendicular to the lateral axis at midpoint of the right thigh, view from the right side. From left to right: MS730, MS742 and MS743 (all shown at the same scale).*

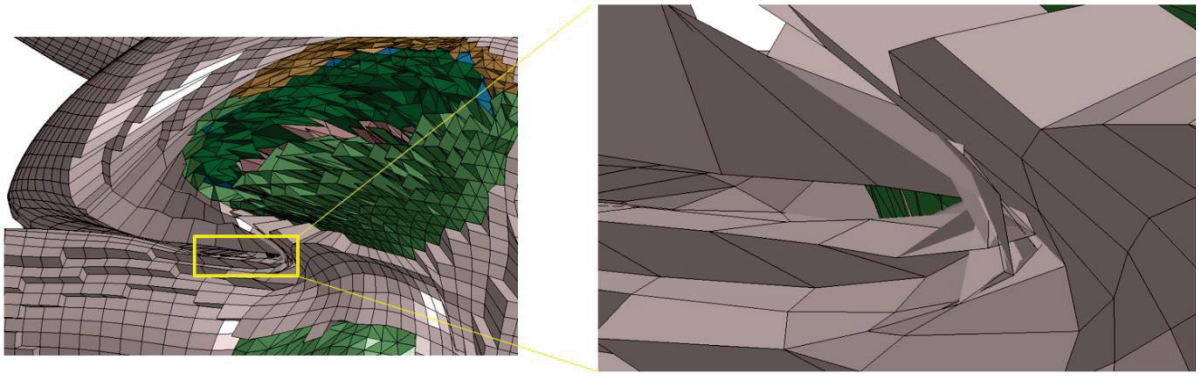

*Figure 78: Typical artefacts appearing inside the fold after morphing using the method from chapter 4 on the M50-O. Hexahedral elements penetrate each other as they follow a steep change of curvature. Subject MS742.*

*Figure 79: Schematic representation of the fold as a sharp angle (Skin in blue, inner soft tissues elements in green and red). Left: penetrations resulting from Kriging without controlling for the sharp angle. Right: the folding line is enforced by additional control points (red dots) on the skin and inside the tissues.*

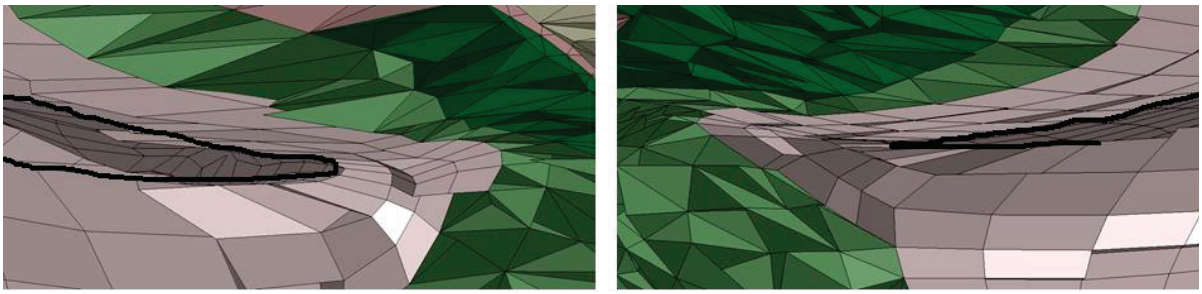

*Figure 80: Results of morphing enforcing the folding line (subject MS742). Boundary of the skin is marked in black. Right: area with desirable results (view from left side). Left: large distortion of elements directly above and below the enforced line (view from right side).*

Additional layers of CPs would probably be needed above and below the folding line to better control for the element distortion. However, choosing the target positions for these points would be challenging unless a general optimization scheme could be formulated. The whole approach is also very mesh specific: while it may work with the M50-O where the subcutaneous tissues are represented by a few layers of hexahedral elements, it would be difficult to constrain such a folding line with the subcutaneous layer meshed using tetrahedral elements.

**Since these attempts without mesh changes failed** in creating a runnable model, remeshing was introduced in the morphing approach. The subcutaneous fat around the fold and the muscles of the abdominal wall were merged into a single part and meshed with tetrahedral elements using LS-PrePost (Figure 81). This part can be easily remeshed after morphing to limit 3D element distortion.

*Figure 81: Subcutaneous fat and abdominal muscles of the GHBM-M50-O combined to a single tetrahedral part (in green). The fascia of the abdominal muscles were kept on their posterior aspect and their thickness doubled to account for the muscle removal.*

### 5.3.2.Subcutaneous fat

Directly using the subcutaneous fat target (Section 5.2.4) did not lead to runnable models, whether the target was used from the beginning or after morphing for the skeleton and skin. Negative volume elements and penetrations were always created around the iliac wings, regardless of the kriging parameters (nuggets etc.). Figure 82 provides an insight into the cause of the problem: after skeleton and skin morphing, the part of the subcutaneous fat target close to the pelvis prescribes a large deformation gradient in the outward direction (the pelvis is already final), which almost always leads to element inversion and other problems as was shown in Section 4.3.6.

To go around the issue, the subcutaneous fat target was only partially respected near the iliac wings. The partial target (Figure 82) was created by applying a percentage of the source to target displacement near the iliac wing and increasing it to 100% in the mid sagittal plane (linear morphing). In addition, a nugget was used in the Kriging transformation. The percentage and nugget were adjusted by subject to get as close to the full target as possible (cf. Table 5).

*Table 5: Details of subcutaneous fat morphing for each PMHS.*

| Subcutaneous fat | MS742 | MS743 | MS730 |
|---|---|---|---|
| **Percentage of the target** | 40% | 50% | 100% |
| **Nugget** | -30 | -30 | -50 |
| **Hausdorff distance between the target and the surface reached (mean [max])** | 2.7 [19.2] mm | 0.5 [12.9] mm | 0.4 [5.9] mm |

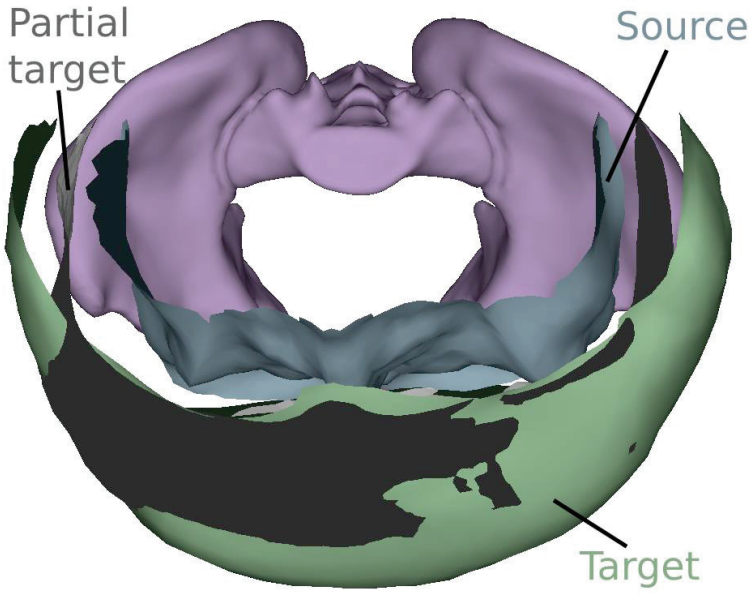


*Figure 82: Top view over the source and target of subcutaneous fat for MS743. The pelvis has its final shape. Morphing according to the subcutaneous fat target would result in a conflict (excessive deformation) for the elements near the pelvis. The partial target was created by linearly morphing the vertices on the side by only 50% towards the target, while the front was morphed fully.*

## 5.4. Results: morphed models

### 5.4.1. Model overview

In the end, three runnable models were created per PMHS. The first one (complete) uses all available information and matches the subject as closely as possible (complete). The other two use partial information to study the effect of the subcutaneous fat (with fold but not fat target, foldOnly) or the effect of the fold (no fold, no fat target, nofold). The last one corresponds to the current practice in the literature.

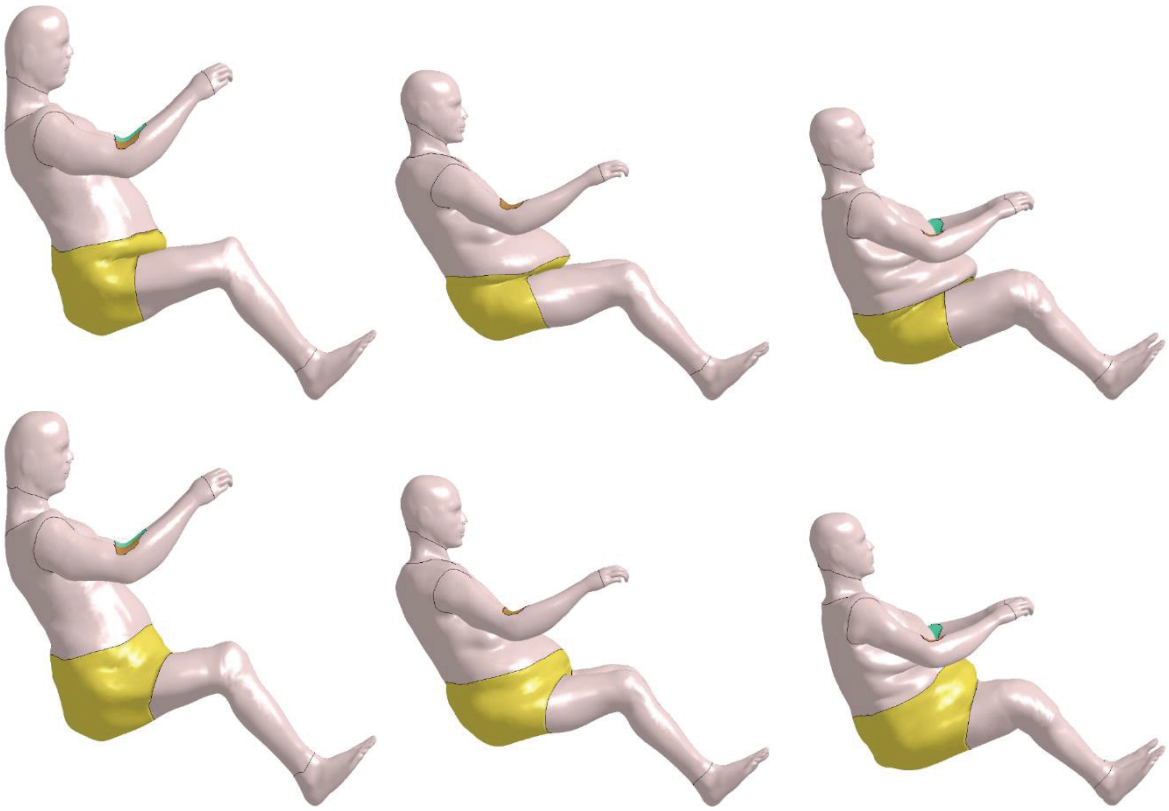

*Figure 83: External view of the morphed models with abdominal fold (top) or without (bottom). Left: MS730. Middle: MS742. Right: MS743.*

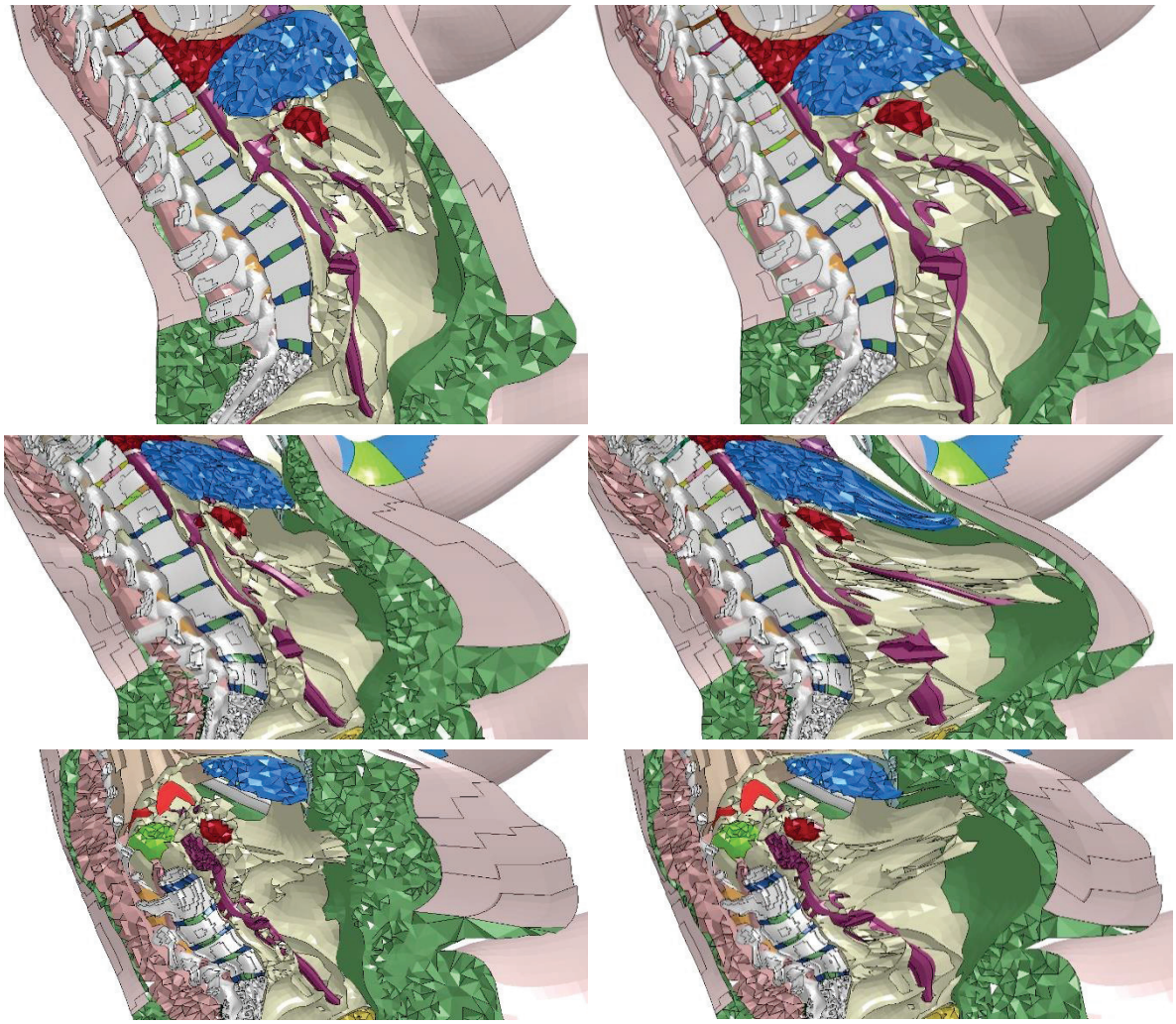

*Figure 84: Internal view of models with abdominal fat target (left) or without (right). The green and pink tissues parts represent subcutaneous fat. The blue organ is the liver. Left: models without the subcutaneous fat target. Top: MS730. Centre: MS742. Bottom: MS743.*

Table 6 summarizes the masses of each created model, along with the PMHS before and after freezing for comparison. Two different material properties (denoted C315 and NH-X1) for adipose tissues were tested in the simulation study that will be presented in Chapter 6. The mass differed by up to 2 kg based on which material was used. Please refer to Section 6.2.1 for more details about the materials.

The mean [maximum] Hausdorff distance between the target and the morphed skin surface was 0.1 [6.3] mm for the MS730, 0.1 [5.2] mm for the MS742 and 0.2 [5.7] mm for MS743. The maxima (Figure 85) were achieved inside the abdominal fold and, for the MS742 and MS743, on the knees (for which registration is challenging due to close proximity to bones). Since the bones were morphed without nugget, only minimal deviations from the target were observed (less than $10^{-5}$ mm, which can be attributed to rounding errors).

*Table 6: Mass of each created model, along with each PMHS before and after freezing. For the models, it is the mass reported by LS-Dyna during simulation, i.e. including the mass added to enforce a 0.3 µs minimum time step (between 0.14 and 0.16 kg, depending on the simulation).*

| Mass | MS730 | MS742 | MS743 |
|---|---|---|---|
| **Complete (C315)** | 107.46 kg | 102.96 kg | 102.26 kg |
| **Complete (NH-X1)** | 105.59 kg | 101.26 kg | 100.32 kg |
| **Fold only (C315)** | 108.65 kg | 103.48 kg | 102.98 kg |
| **Fold only (NH-X1)** | 106.78 kg | 101.78 kg | 101.04 kg |
| **No fold (C315)** | 108.77 kg | 104.06 kg | 102.8 kg |
| **No fold (NH-X1)** | 107.25 kg | 102.67 kg | 101.29 kg |
| **PMHS (initial)** | 113 kg | 100 kg | 105 kg |
| **PMHS (after defrosting)** | 93 kg | 100 kg | 101 kg |

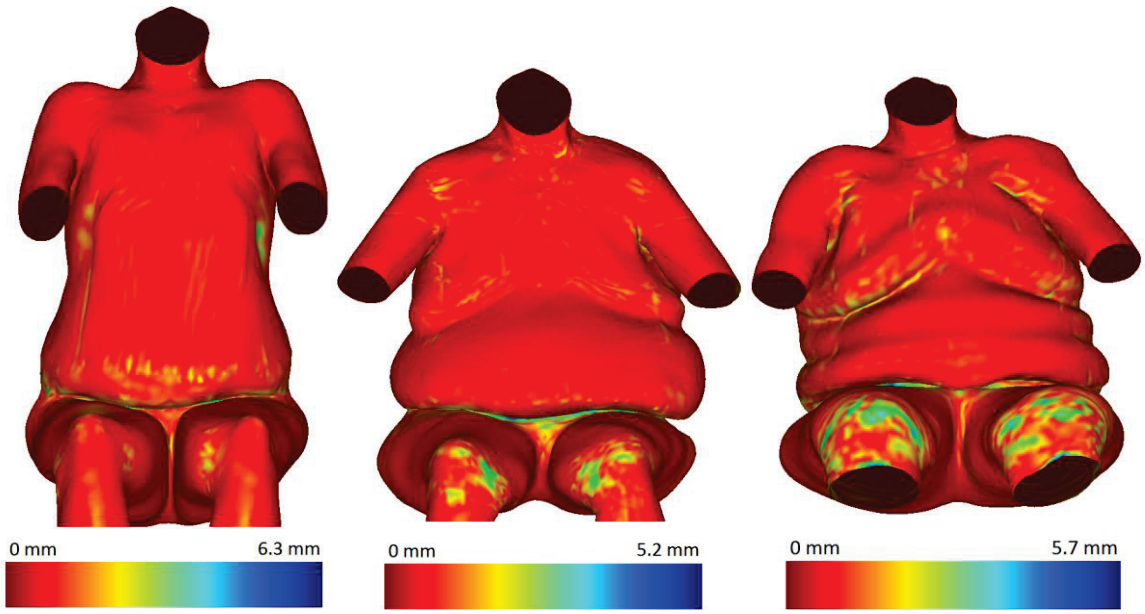


*Figure 85: Skin surface for each PMHS with Hausdorff distance visualization between the target and the surface achieved after morphing by Kriging with nugget. Left: MS730. Centre: MS742. Right: MS743.*

### 5.4.2.Element quality

Figure 86, Figure 87 and Figure 88 report the Scaled Jacobian (SJ) of the morphed models as computed in PIPER (VTK library based on Verdict library (Stimpson et al. 2007)) and plotted with histograms. SJ of an ideal element is 1 (regular tetrahedrons or cubes for hexahedrons). Elements with low or negative SJ are very degraded (distorted faces, etc.). Inverted elements (self-penetrating) that prevent the model from running in LS-Dyna have a negative SJ. The amount of elements per class of SJ was

expressed as a percentage of the total number of elements since it varied between models after remeshing (varies between 2 989 133 and 3 039 997 elements). The elements with negative SJ are listed in Table 7). They were omitted from the histograms since they would not be visible due to their low percentage (between 0.0004% and 0.0137%).

For each case, there is one histogram before remeshing the combined fat part (i.e. after the last step of morphing) and one histogram for the model after remeshing. As it could be expected, the morphing resulted in an overall reduction of element quality, with more low quality element (e.g. SJ < 0.3 increasing from 2.6% to 4.3-6.0%, depending on the test case) and less highest quality elements (SJ > 0.8 decreasing from 46.3% to 37.4-39.9%). Remeshing transformed elements from the 0-0.4 class into the 0.6-0.9 class, bringing the quality closer to the baseline model.

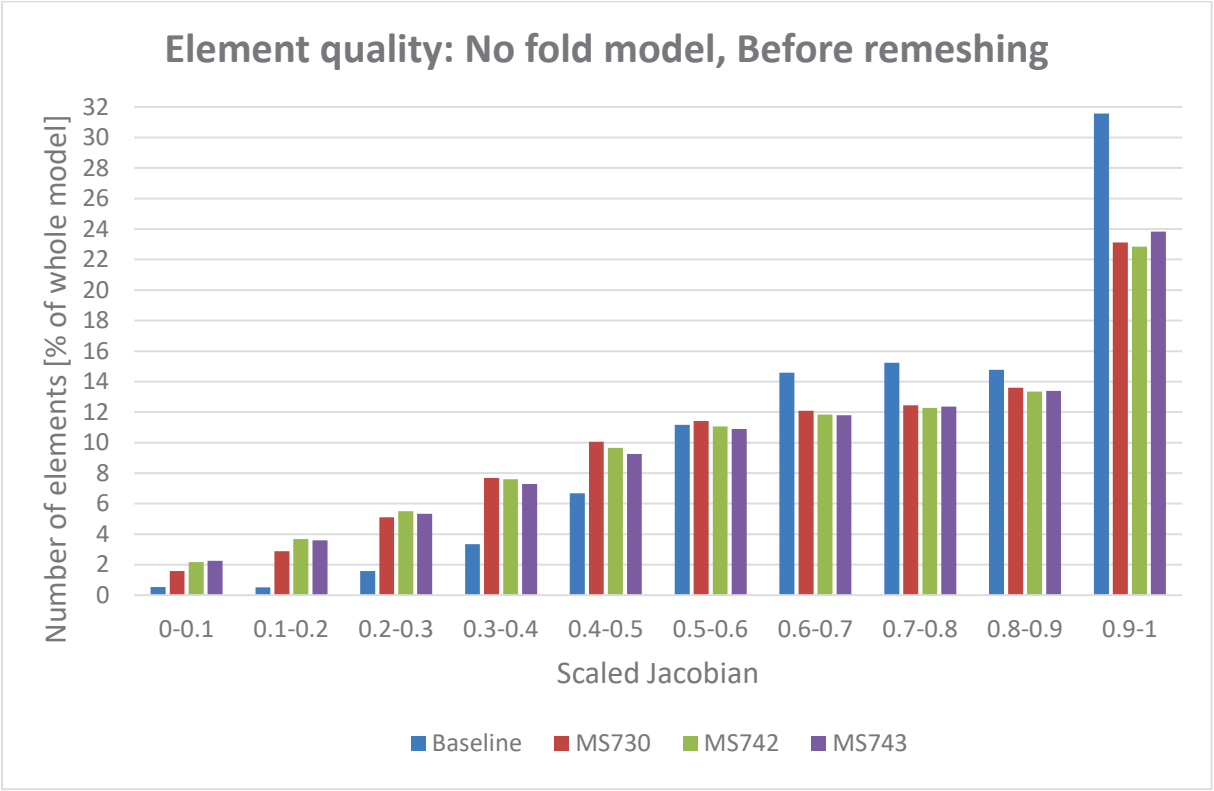


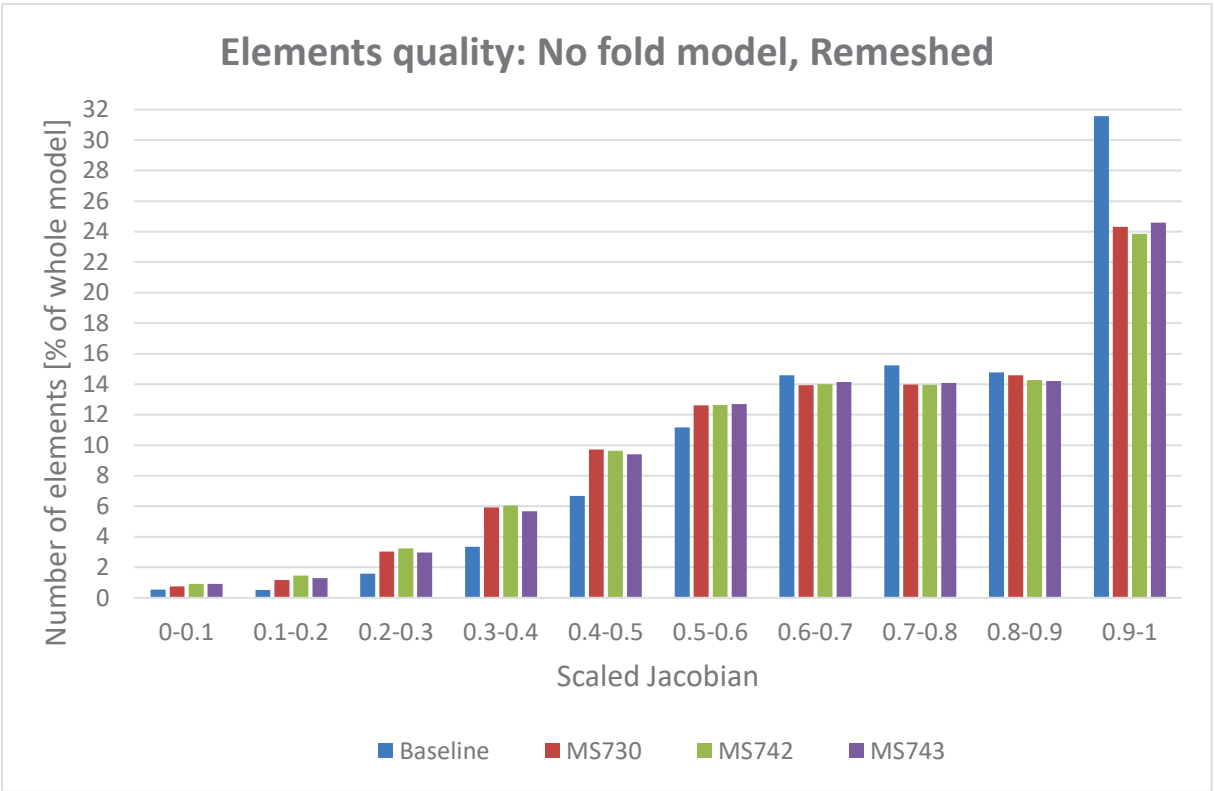


*Figure 86: Scaled Jacobian histogram for the noFold models. The baseline model is the same in both histograms. Negative SJ values not shown (see Table 7).*

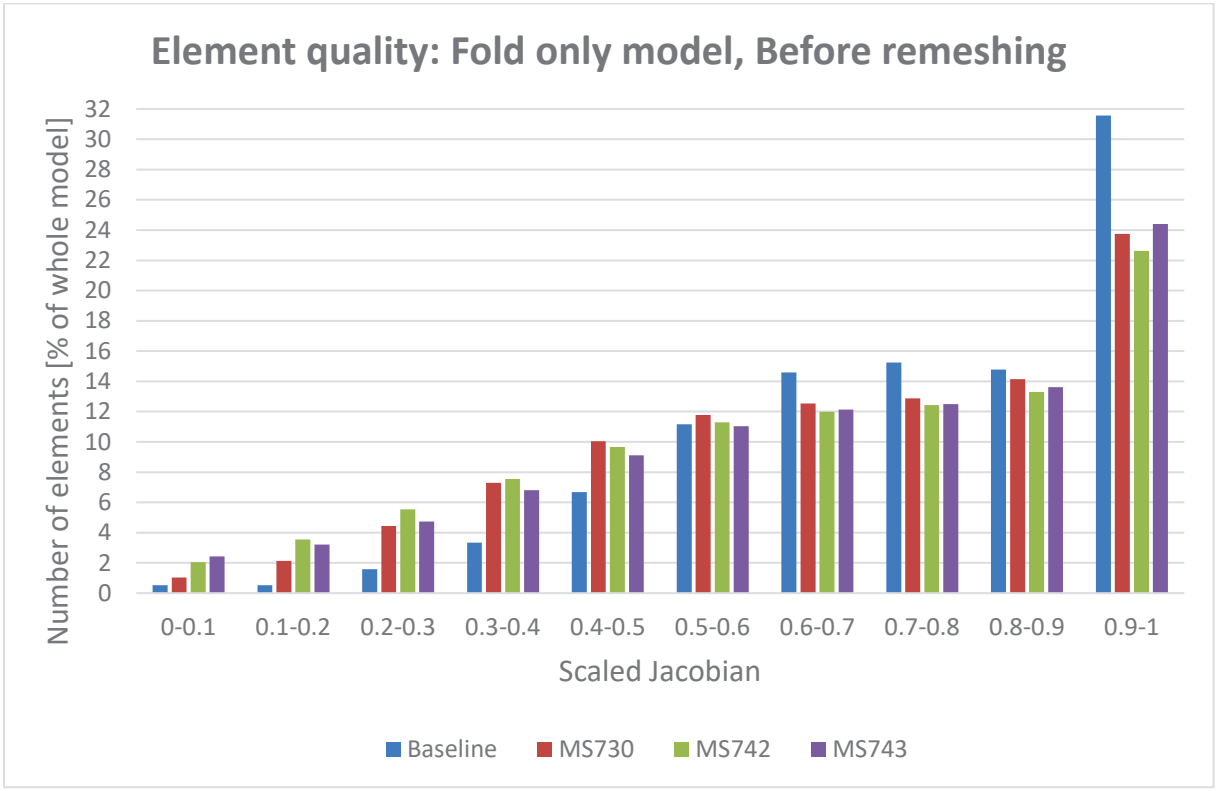


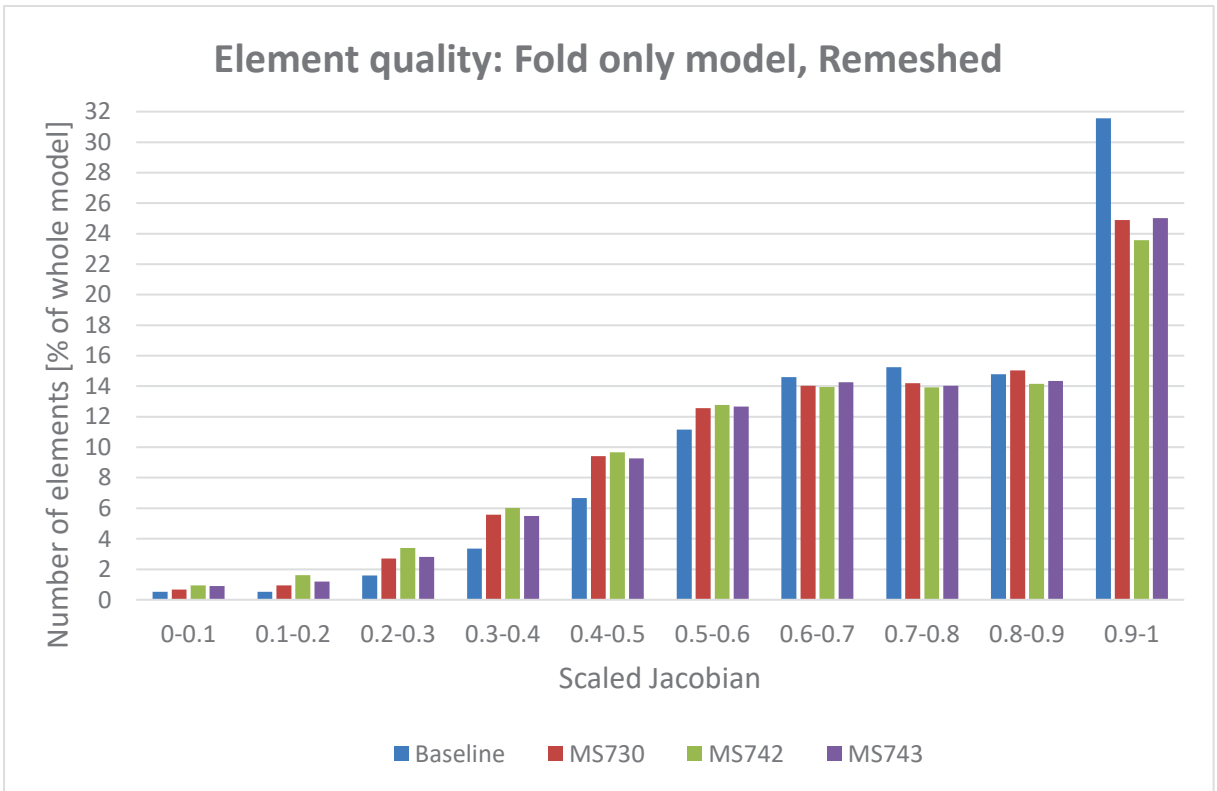


*Figure 87: Scaled Jacobian histogram for the foldOnly models. The baseline model is the same in both histograms. Negative SJ values not shown (see Table 7).*

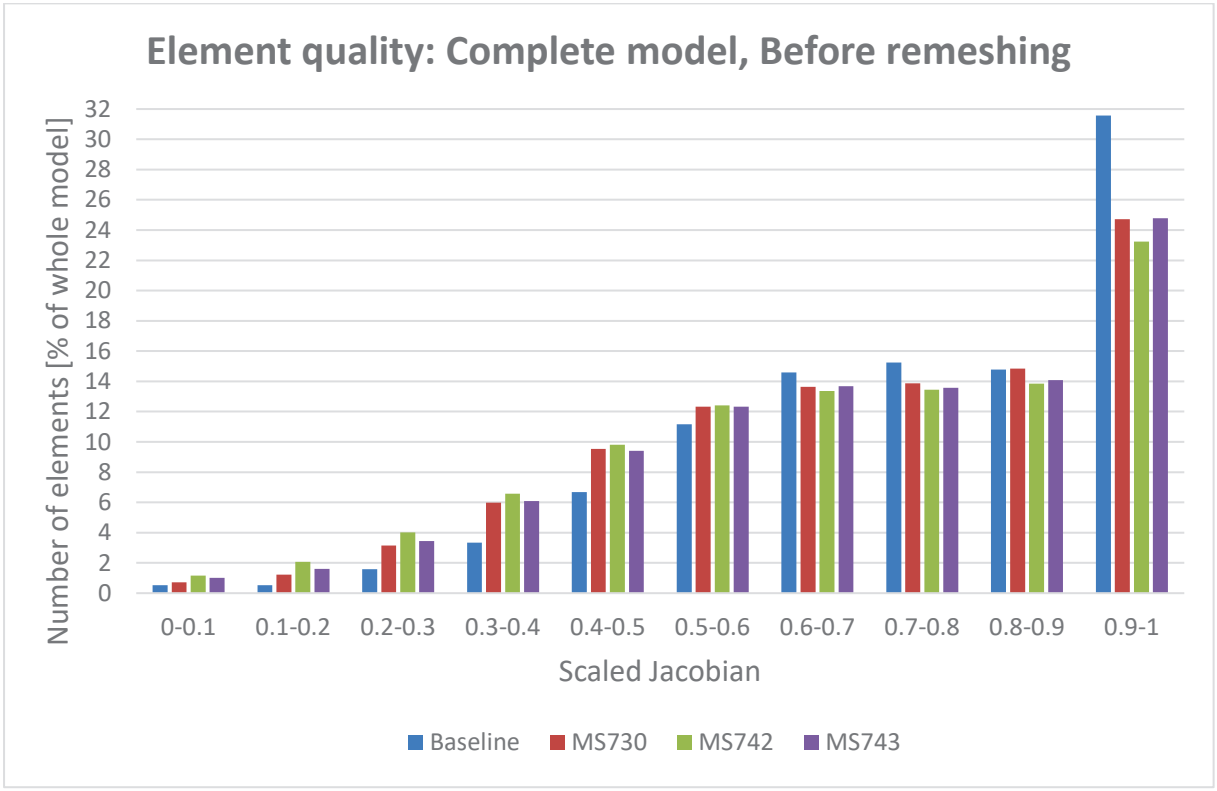


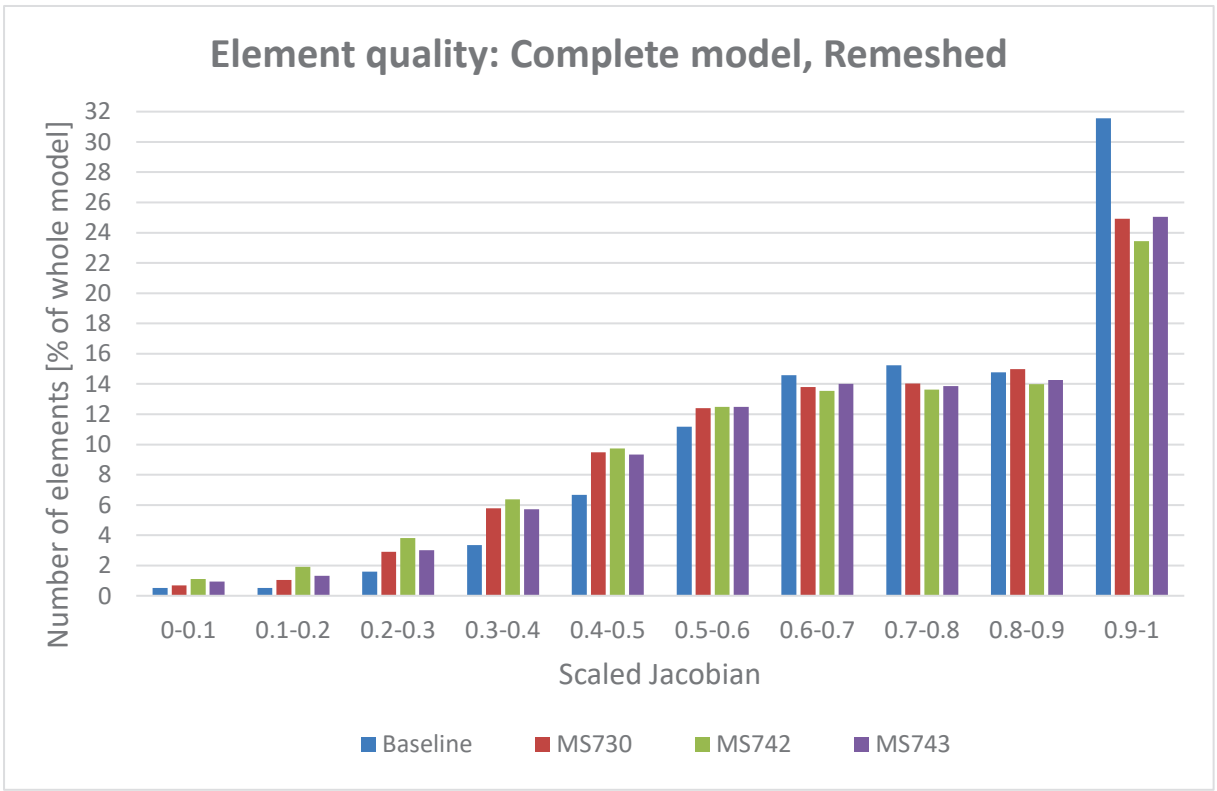


*Figure 88: Scaled Jacobian histogram for the complete models. The baseline model is the same in both histograms. Negative SJ values not shown (see Table 7).*

*Table 7: Number of solid elements with negative volume for the models before remeshing, negative SJ before remeshing and negative SJ after remeshing. The baseline model has 13 elements with negative SJ.*

| | MS730 | | | MS742 | | | MS743 | | |
|---|---|---|---|---|---|---|---|---|---|
| **Negative:** | Volume | SJ before remeshing | SJ remeshed | Volume | SJ before remeshing | SJ remeshed | Volume | SJ before remeshing | SJ remeshed |
| **noFold** | 208 | 429 | 221 | 99 | 197 | 103 | 49 | 290 | 241 |
| **foldOnly** | 121 | 163 | 42 | 174 | 274 | 100 | 223 | 316 | 93 |
| **complete** | 20 | 65 | 45 | 305 | 414 | 106 | 140 | 268 | 131 |

## 5.5. Discussion and Conclusions

Morphed models were generated to represent three of the obese PMHS used in the experimental studies. Compared to the test case from Section 4.3.6, the process to create these subject-specific models proved very challenging at each step.

The first step is the registration of the model skeleton to the PMHS skeleton based on the CT. In the absence of readily available software for this task, a first process using manual landmark definition in combination with the PIPER spine positioning was designed. It was time consuming and provided only limited accuracy for the resulting bone meshes. Skeleton registration with the experimental Anatoreg software was found more reliable. It allowed registering directly onto the CT images and seemed to be more user independent and accurate. Limitations are related to Anatoreg: the software is still in development, not commercially available, with missing features that could simplify and accelerate the process.

The creation of the skin targets by patching together surfaces from different sources also required significant manual effort with approximately 8-12 hours of work per target. Moreover, since the CT and laser surfaces are not exactly the same, it is required to make approximations to decide the surfaces respecting each part of the body. The laser scan was generally taken as the main source, especially in the abdominal area. Overall, many assumptions (engineering judgement) are required to create the target, likely limiting its reproducibility (which was not evaluated) and making it difficult to automatize. As in-position full body imaging on the testing site seems unlikely in the near future, the need to deal with the differences between data sources and postures will likely remain. Better workflows could be investigated, perhaps using realistic deformable models to help with postural adjustments based on limited measurements.

The creation of the subcutaneous target was completely manual and required guidance from the supine MRI. The data, along with the fixed markers on the skin to facilitate the registration, could be

used to investigate the transfer of fat thickness data from supine to seated postures. No other internal target were used but this could be refined in the future.

The Kriging workflow from Chapter 4 did not lead to runnable FE models, except for the least obese PMHS (MS730). However, although some of the issues observed could be formalized (e.g. mesh near the fold or target near the pelvic wings), no metric was developed during this project to try to assess a priori whether Kriging will be successful. The Kriging process for the M50-O model using the 3-pass iterative approach takes approximately 30 minutes and can be fully automatic using the batch mode of PIPER. Therefore, it might be acceptable to try to perform the morphing directly rather than trying to assess the feasibility beforehand based on the specificities of the target and the model. A workflow, in which the constraints or target registration could be adjusted automatically based on element quality after kriging in an iterative approach, seems feasible and could be investigated. A model specific method for enforcing the folding line by additional control points was tested as well, but it was abandoned due to the strong requirements it creates to specify the constraints (control points).

In the end, additional pre-processing of the M50-O was required to accommodate the large deformations near the abdominal fold. The way chosen for this work was to represent the abdominal soft tissues by a single part that can then be easily and automatically remeshed.

The remeshing approach led to runnable FE models for all the PMHS, including versions with and without the abdominal fold. The subcutaneous fat target was also applied, but with some limitations (anterior fat only, target violation near the pelvis, etc.). A different algorithm to simulate the subcutaneous fat growing (as in Saito et al. (2015)) may be more suitable but was not investigated within this study. Lastly, while the subcutaneous fat target provides realistic thickness for the subcutaneous fat, it also deforms the abdominal organs, often in a clearly unnatural way as can be seen on the liver in Figure 84. Targets for the abdominal organs would have to be provided in order to obtain a better result. However, as Section 2.6.3 showed, obtaining such target is problematic, as there seem to be many irregularities between sizes and shape of abdominal organs.

By comparing the element quality of the noFold and foldOnly models (see Figure 86 and Figure 87), one can see that although there are small differences in the 0.2-0.4 ranges, the general trend is the same. Interestingly, there is a large decrease of the highest quality elements (0.9-1) when compared to the baseline model, which almost does not change with remeshing. That suggests that either this decrease is happening in parts of the model that are not being remeshed, or that the remeshing algorithm is not tailored toward producing ideal tetrahedrons.

Overall, the mesh quality seems acceptable overall and it is the first time to our knowledge that some of these details targeted in the current study (fold, subcutaneous fat thickness) could be described in models for impact simulation. The next chapter will assess the effect of these details on the impact response.

# 6. Simulations

## 6.1. Introduction

The main objective of the simulations is to study the effect of modelling parameters on the response of an obese model. The geometrical parameters, including the description of the fold of the subcutaneous fat thickness are the primary focus. LS-Dyna was used to recreate the experiments presented in Section 3.2.3 as FE simulations using the HBMs presented in Section 5.4. Section 6.2 will first describe how the simulations were prepared. Specifically, Section 6.2.1 presents the rationale and process to select material properties for the adipose tissues. Sections 6.2.2 and 6.2.3 then shows the seatbelt positioning for the belt and sled experiments, respectively. Only the sled of MS743 was simulated. Finally, Section 6.3 shows the results of the simulation.

## 6.2. Methods

### 6.2.1. Candidate material properties for the new adipose tissues component

As seen in the previous chapter, some subcutaneous fat parts and muscles that are very thin in the PMHS (e.g. rectus and oblique) were merged into a new adipose part. While the study does not focus on adipose tissue material properties, material properties need to be selected for this new part.

The following text will first present an overview of materials used in the M50-O or proposed for use in morphed model (Section 6.2.1.1) followed by simulations results with the baseline M50-O (i.e. before morphing) and one of the belt tests to help select the candidate material properties (Section 6.2.1.2).

#### 6.2.1.1. Materials checked on the baseline and remeshed model

To reiterate findings from Section 2.2.2, experimental studies of adipose tissues indicate a very soft initial behaviour followed by a stiffening (prior to failure). However, the tests reported in literature focus on sub-failure strains, which are likely lower than those that can be reached during a vehicle impact scenario. Also, the mass of abdominal fat in obese occupants may introduce strains in the tissues that are not accounted for in the model initial position and that may not match in the initial state in sample tests.

Conversely, material properties used in the GHBMC models were extensively tested in the context of non-obese modelling, but their selection process is unclear and they do not always seem to account

for recent literature. Material properties of adipose tissues differ between body regions, perhaps due to choices and adjustments made by different modelling teams, sometimes close to 10 years ago. All regions use a MAT_SIMPLIFIED_RUBBER/FOAM material law (LSTC 2019). It is a tabular law using a uniaxial strain stress curve to specify the uniaxial response. It can be used either with a foam formulation (case of the thorax and pelvis) or with a nearly incompressible rubber formulation suggested to work similarly to an Ogden material law in the manual (case for the abdomen). Bulk moduli are input and vary between 2 GPa for the thorax and pelvis (likely based on water) and 5 MPa for the abdomen. For the abdomen – which was developed at LBMC – the value was selected to prevent shear locking and instability in tetra elements while maintaining the overall volume. Although it seems redundant for the foam, a Poisson ratio is used as well (0.3 for the thorax and pelvis). It was observed during the development at LBMC that, for the foam formulation, high bulk moduli did not prevent volume variations when a low Poisson ratio was used. The material also has damping parameters. The main one (called mu) varies between 0.4 (thorax and pelvis) and 0.1 (abdomen, which is the default value in Ls-Dyna). As part of the ongoing GHBMC efforts to reduce differences in material properties used for the same tissues in different body regions, a new set of parameters was recently proposed by Wake Forest University. It uses a rubber formulation, a 500MPa bulk modulus (mentioned in Comley and Fleck (2012) based on Saraf et al. (2007)) and a mu=0.1 for damping. Experimental curves digitized from Comley and Fleck (2012) were used in a rate dependent table to specify the uniaxial response.

In order to limit the extent of the investigation, a heuristic approach was used to select candidate material properties for the current study. First, numerical formulations were chose essentially based on previous modelling experiences (including the LBMC experience as the GHBMC Abdomen center of expertise):

- A MAT_SIMPLIFIED_RUBBER formulation was selected. While a true hyperelastic formulation may be preferable, its use may require work beyond the scope of the current study as it proved less numerically stable in past full body evaluations.
- For adipose hexahedral components, element type and hourglass control options were not changed. A formulation 13 (designed to limit shear locking and large strains) was used for the new tetrahedral component instead of a formulation 10.
- For the numerical parameters of the MAT_SIMPLIFIED_RUBBER law:
    - Because fat is generally considered as incompressible, the rubber formulation was selected. This is consistent with past choices for the abdomen and recent propositions by Wake Forest University. A bulk modulus of 0.5 GPa was selected based on the

proposition by Wake Forest (based on Comley and Fleck (2012) and Saraf et al. (2007)). Based on previous experiences, it was lowered to 5MPa for the tetrahedral elements to try to prevent shear locking. The sensitivity to this parameter will be checked.

- Based on previous experiences on the large effect of damping, the damping coefficient mu was reduced to its lowest value required for numerical stability. The value of 0.05 (i.e. the minimal value recommended for numerical stability in the Ls-Dyna manual) was used as a starting point. The effect of damping on the rate sensitivity was also assessed.

- For new strain stress uniaxial input curves:
  - No rate sensitivity was used as Comley and Fleck (2012) found the effects to be limited up to 10 $s^{-1}$ (which is believed to be relevant for impact but will be checked).
  - In order to minimize potential issues due to jumps in numerical derivative, the uniaxial response curve was finely discretized based on a numerical interpolation or a hyperelastic uniaxial response fit.
- In the model, skin and abdominal muscle/fascia are described using viscoelastic and elastic material laws, respectively. These are symmetric in tension and compression. However, compressive stresses are unlikely to occur *in situ* as membranes (and fibers within them) would fold. The properties were changed to an elastic fabric material cancelling the compressive stresses. The viscous response of the skin was neglected.

Then various uniaxial response curves were tested, including those already used in the model, curves from Comley and Fleck (2012), and new curves developed based on assumptions described below (the names that will be used further to denote each curve are in parenthesis):

1. (C670) the curve currently used in the GHBMC abdomen, thoracic and pelvic fat.
2. (C002) the curves based on Comley and Fleck (2012) proposed by Wake Forest University and input in a rate sensitive table. This proposition is still evolving and three versions were tested. The first one (C002, provided with the M50-0 version 5.0) uses curves that seem directly digitized from the article. The second (C002b, provided with version 5.1) uses idealized curves to approach them. The third (C002c) extends the idealized curves beyond the experimental range using an Ogden three term fit.
3. (NH) curves based on a NeoHookean material response (i.e. assuming linearity for the response). Elastic constants between 0.6 kPa (X1) and 16 kPa (X30) were tested. The lowest values corresponds approximately to the low strain static response of Comley and Fleck (2012).

4. (C23) A non-linear response curve based on a one-term Ogden formulation and the power coefficient proposed by Comley ($\alpha$=23). The modulus parameter was adjusted to match the initial experimental stiffness at low strain rate (μ=10 Pa).
5. (C315) A non-linear response curve based on a one-term Ogden formulation and a limit on the maximum tensile stress. This was achieved by using a plateau at 13.7 kPa in tension (subcutaneous fat strength in Lackey et al. (2014)) and a spline to ensure the continuity with the nonlinear term. As the plateau corresponds to damage, the MAT_SIMPLIFIED_RUBBER_WITH_DAMAGE variant of the material law was used. Several exponents were tested for the Ogden term but only the results with the exponent $\alpha$=15 (and μ=40 Pa) will be shown. Unloading was assumed to take the same form (i.e. one term Ogden) but with a higher exponent to allow for some dissipation. An exponent $\alpha$=20 was used.

Most of these curves have a similar initial stiffness (close to the experimental range) but can differ widely when the strain increases. Above 0.3 strain, which is a region where experimental results are missing, curves cover a very large range of stresses. In some cases, the tensile stresses seem irrelevant considering tissue failure limits. Also, for C23 and C002c, the high non-linearity leads to a very sharp stress increase, which may limit the strain that can be reached in a scenario where a limited energy is input. The new curves are represented in Figure 89 (the model curves were not plotted for confidentiality reasons).

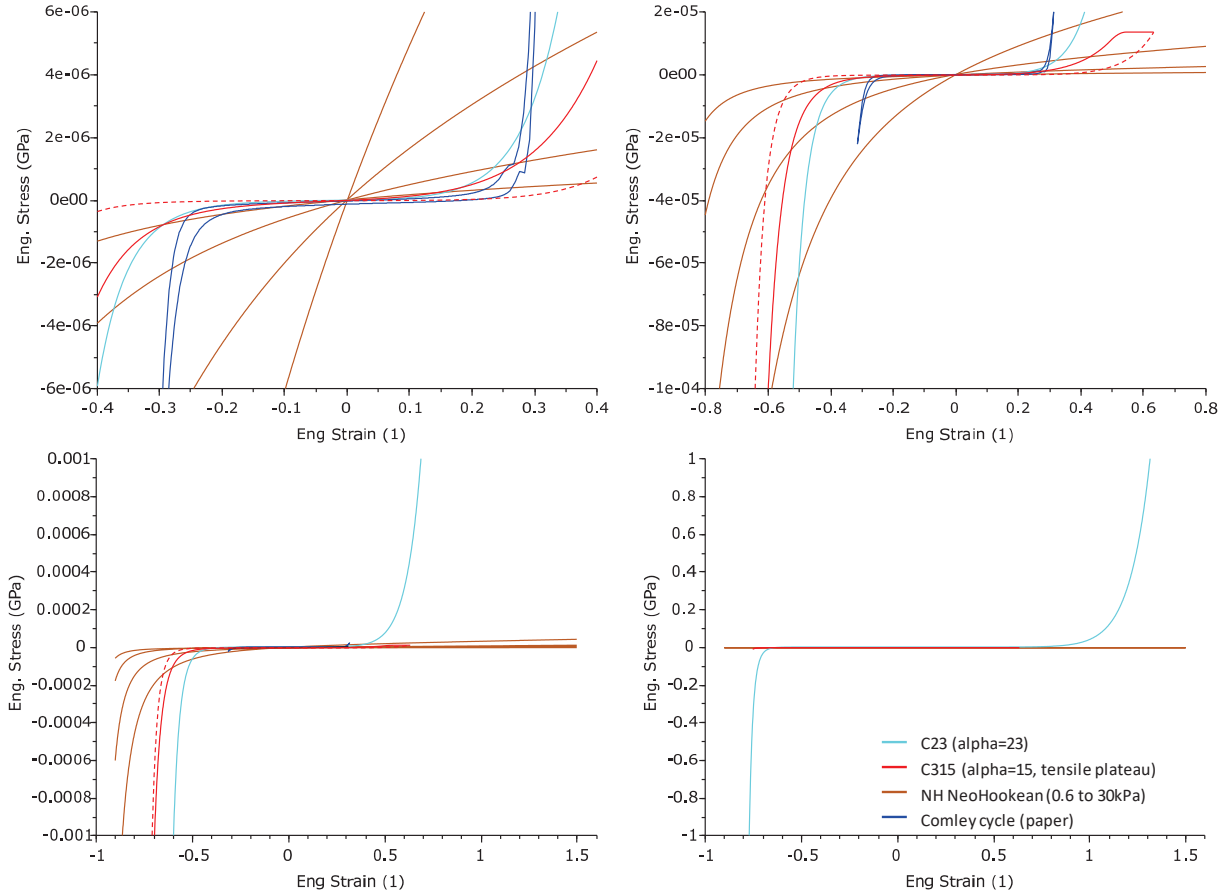


*Figure 89: Uniaxial strain stress curves tested with the MAT_SIMPLIFIED_RUBBER (except for Comley and Fleck (2012) cycle loading that is an experimental result shown in Figure 2). To facilitate the visualization, the four plots show the same curves over different ranges of strains and stresses. Legends: C23: using a one term Ogden $\alpha$=23 and $\mu$=10 Pa; C315: using a one term Ogden $\alpha$=15, $\mu$=40 Pa, a plateau in tension at 13.7 kPa and damage modelling (dashed: unloading); NH: NeoHookean with moduli between 0.6 and 30 kPa (X1 to X30), all plot with the same color.*

The effect of the parameter on the model response was assessed by comparing the standard M50-O (version 5.0) with the model including the new part and material parameters. The Lamielle et al. (2008) MHA belt loading condition was used because it is similar to the current study (mid abdomen belt compression performed on the same testing machine at relatively low speeds). It is an existing validation setup for the M50-O in which the force time history is applied to the belt. The same comparison was also done for the candidate material parameters in three additional GHBMC validation setups (names in the parenthesis will be used to reference the setups in further text):

- (Lamielle): Lamielle et al. (2008), "PRT" tests (as MHA but with a higher velocity)
- (Cavanaugh): A 32kg bar impacting the mid abdomen at 6m/s with free back condition (Cavanaugh et al. 1986).

(Hardy): A mid-abdomen belt loading with a free back condition (Hardy et al. 2001).

#### 6.2.1.2. Simulation results

First, the comparisons in the Lamielle et al. (2008) MHA configuration are shown in Figure 90. The baseline M50-O has a peak deflection that is on the low range of the experimental response. It is within the experimental variability for compression (deflection normalized by the depth) but still lower than for three of the four PMHS. C670 and C002c further reduced the penetration while C002b increased it (C002 terminated with error). The difference between C002b and C002c can be attributed to the extrapolation outside the experimental range: while a nonlinear extrapolation was used for C002c, a linear extrapolation is used for C002b (Ls-Dyna behaviour to extend curves). This highlights the importance of the definition of the curve outside the experimental range. When considering new curves, C23, which has as a high non-linearity as C002c, led to similar penetration reduction. The proposed curve C315 softened the response to the middle of the penetration range (close to the response of a PMHS with the same abdominal depth). It also matched the compression reached by three of the four PMHS. For that simulation, the damping parameter could be reduced to 0.01 (from 0.05) with limited effect on the response and no stability issues. When using the NeoHookean curves, the penetration of C315 could be achieved with a 6 kPa modulus (X10) and the penetration of the original model with an 18 kPa modulus (X30). A 0.6 kPa modulus lead to more penetration and compression than in the experimental range.

That soft response was selected to illustrate the potential effects of damping and bulk parameters (Figure 91). While the effect of bulk modulus on the tetrahedral part was marginal, the effect of damping was very large. Damping values lower than 0.05 softened the initial response and terminated with error. Values over 0.05 led to a significant stiffening: for 0.2, the penetration was reduced by almost 20 mm, leading to a response that is stiffer than with the curve C315 and closer to the original model. This suggests that the damping parameter can be predominant for low material stiffness. This is not a desired behavior as little control is available on that parameter.

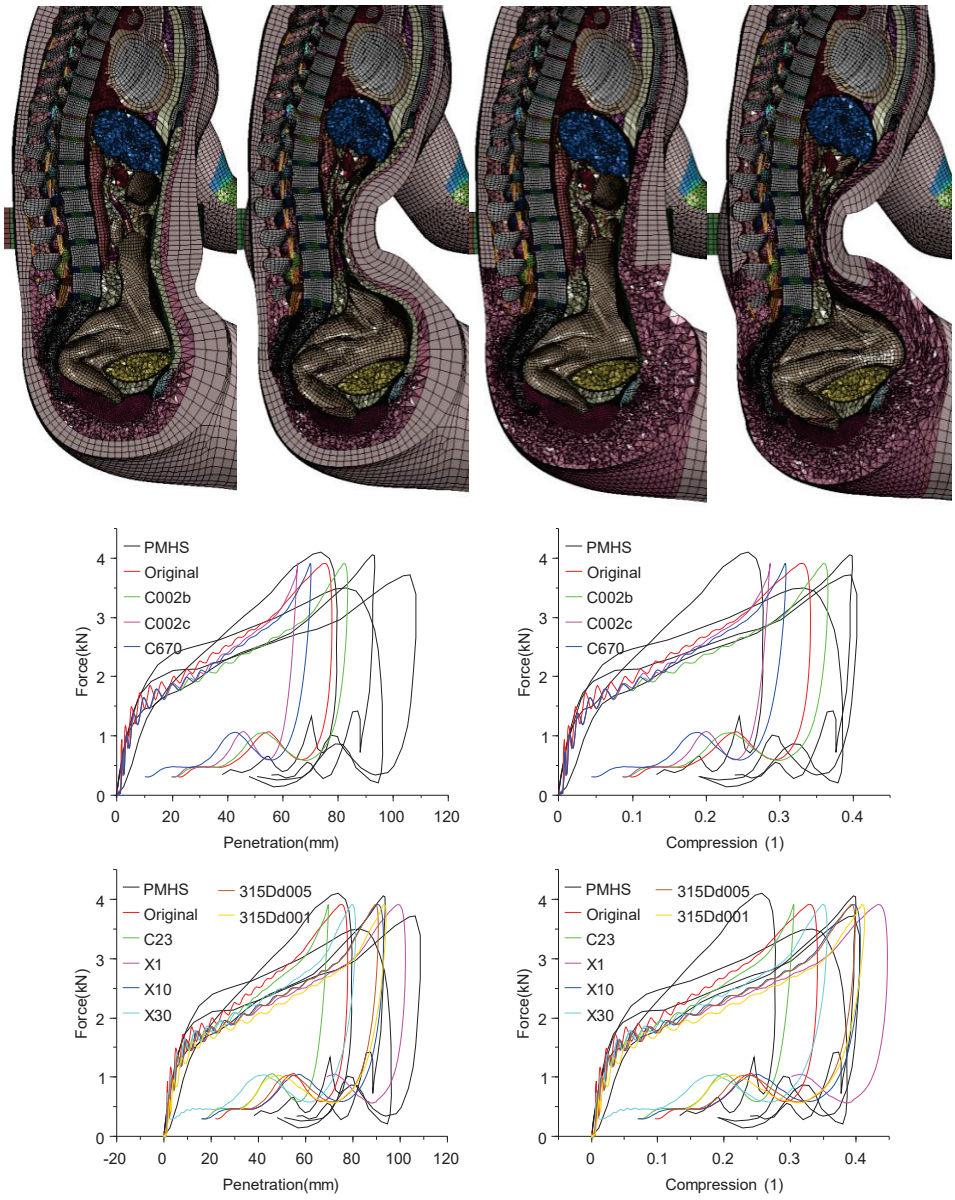


*Figure 90: Response of the M50 model in the Lamielle MHA condition and various input curves for the MAT_SIMPLIFIED_RUBBER. Top: mesh at the initial and peak deflection for the original (left) and modified (right) model using the properties C315 with damping 0.01. Centre: results using curves existing in the model. Bottom: results using new curves. Penetration is the belt penetration with respect to the back of the subject and compression the ratio of the penetration by the abdominal depth. Legends: PMHS: experimental data; Original = Baseline GHBMC model; C002b = idealized table derived from Comley and Fleck (2012) at strain rates from 0.2 and 2700 $s^{-1}$ (extended beyond the experimental range: c); C670 = curve used for the thorax and abdomen in the current model; C23 = based on an Ogden $\alpha$=23 and μ=10Pa; C315 = based on an Ogden $\alpha$=15, μ=40 Pa, a plateau in tension at 13.7 kPa and damage modelling (dashed: unloading); NH = NeoHookean with moduli between 0.6 and 30 kPa (X1 to X30), all plot with the same colour. All curves with damping 0.05 except C315Dd001 (damping 0.01).*

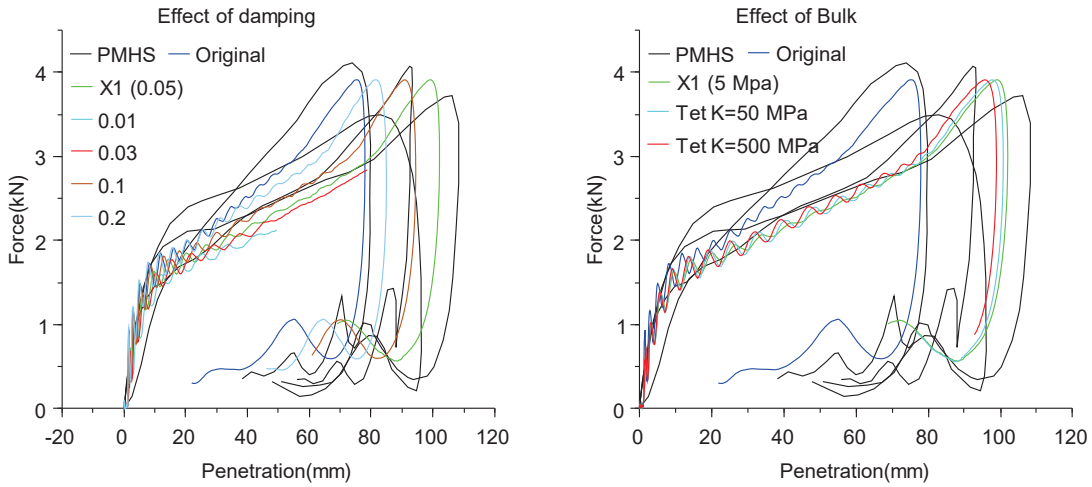


*Figure 91: Effect of damping and bulk modulus on the stability and response in the case of a soft material (here: NH 0.6 kPa, X1). Left: effect of damping parameters between 0.01 and 0.2. Right: effect of bulk between 5MPa and 500MPa for the new tetrahedral part.*

Considering that the original response was too stiff and that the fat in the modified replaced both subcutaneous fat and some muscles, the two softest responses, i.e. the input C315 with a damping 0.01 and the NH 0.6kPa with a damping 0.05 (X1) were used for further verification in three additional setups (Figure 92). Compared to the original model, C315 in the modified model increased the deflection in the belt tests, leading to a closer match with the PMHS results (Lamielle, Hardy). However, it degraded the shape of the response curves and reduced the initial stiffness (Hardy and Cavanaugh). For the properties NH 0.6kPa (X1), the simulations terminated with error (negative volumes), prior to the peak in two of the three cases but with most of the loading phase simulated. The X1 response was similar to C315 for the Cavanaugh and Hardy loading and led to less penetration in the Lamielle PRT case.

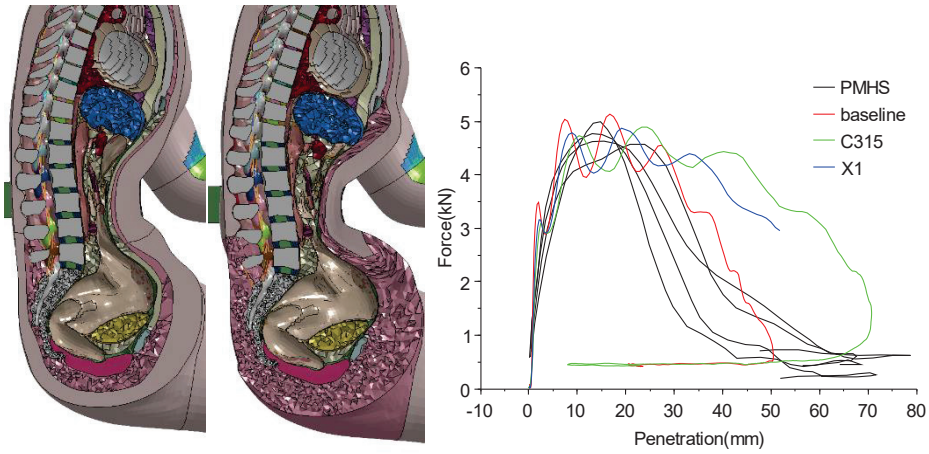


Lamielle mid abdomen fixed back PRT belt loading

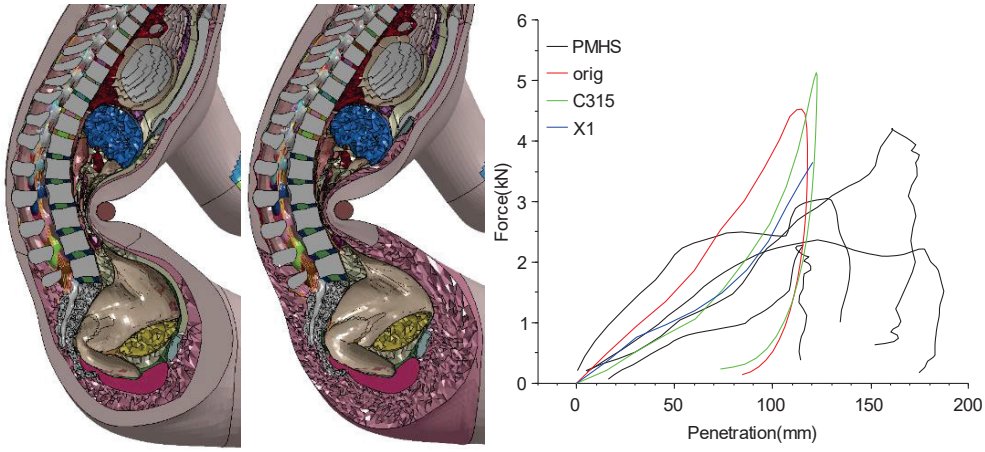


Cavanaugh free back 32kg 6m/s bar mid abdomen impact

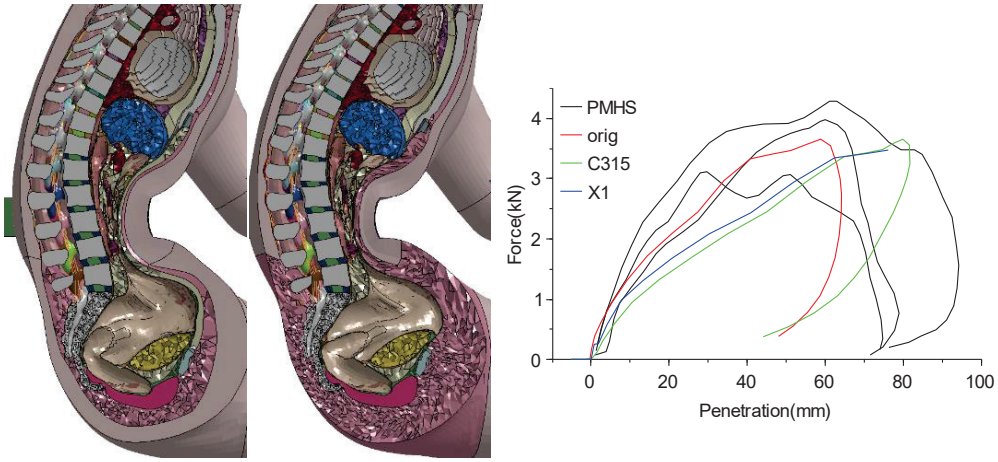


Hardy free back mid abdomen belt pull

*Figure 92: Additional setups used to compare the effect of remeshing and fat property change on the model response. All are part of the standard validation set for the M50-O. The baseline model (no remeshing) is compared with the remeshed model with curve C315 (damping 0.01) or NH 0.6 kPa (damping 0.05).*

#### 6.2.1.3. Summary

Different fat uniaxial responses and numerical parameters were tested with the MAT_SIMPLIFIED_RUBBER law in full body simulations. Results suggest that the material properties at ranges of strains for which experimental data is missing is essential for the full body response. Hence, assumptions made to extrapolate the material behaviour at large strains could largely determine the model response. In tension, limited results regarding tissue strength may already be usable to improve the model and prevent very high tensile stresses (e.g. implemented for now using a simple stress plateau with damage in C315). Using close to linear properties (NH 0.6 kPa, X1) also prevented stress from rising too much in tension. For compression, it was attempted to describe a wide range of behaviours through the exponent of the Ogden model used to generate the uniaxial response curves (e.g. between 2 and 15 for X1 and C315). Sample testing at high strains may be helpful to formulate better extrapolating assumptions. Regarding numerical parameters, damping seems very important, and even predominant over the uniaxial material properties in some cases. As damping is essentially a numerical parameter, its value was reduced as much as possible in the new curves. The higher damping value in X1 (0.05) compared to C315 (0.01) properties may explain that while X1 is softer in the Lamielle MHA loading, it appears stiffer at the higher speed Lamielle PRT.

Further improvements of the hypotheses may be possible by looking at the full body response curve shapes and considering additional experimental setups. However, this would be very time consuming considering the computational cost of the models and may lead to overfitting: other modelling assumptions may jointly contribute with the fat properties, and that one may compensate for the other one. In particular, the role of hollow organs modelling may be especially important for obese subjects and their modelling assumptions may need to be re-examined.

Considering the objectives of the current study, it was decided to move forward with the full body obese simulations. Some of the new properties tested (C315 and X1) may provide a softening of the model response that is likely desirable for obese modelling and comparisons will be shown in shown in Section 6.3.1.

### 6.2.2.Belt tests setup

#### 6.2.2.1. Belt definition

The models with the abdominal fold were used to place the belts. The general aim was to achieve the same relative position between the belt and pelvis and, if possible, the belt and the abdominal fold. The FaroArm measurements and videos from the experiments (Section 3.2.3) were used to place the

belt in a position that is close to the experiment while accounting for the slight shape changes between the time of CT scanning and the time of testing. First, the FaroArm points were imported in LS-Prepost and rigidly aligned using the belt attachment of the MP2D sensor as the reference point. Then small adjustments were made based on the videos and the belt was defined using “Belt Fitting” module in LS-Prepost.

For the tests with belt inside the abdominal fold, the central part of the belt is neither pointed with the FaroArm nor visible on the video. Therefore, the sides of the belt were used for reference and the central part was placed manually as deep as possible inside the fold while keeping it flat.

For the models without fold, the same belts were used and required only small manual corrections (less than 5 mm depenetration) to account for slight differences in the abdomen shape except for the configurations with belt inside the fold.

For that case, the positions of the pulleys and ends of the belt were kept but the belt itself was refitted to be flat on the thighs just below the abdomen. In order to check the effect of that belt placement, which would be the only possible if the fold was not defined, that belt placement was used in addition with the models with fold.

Figure 93, Figure 94 and Figure 95 contain the initial belt placements for all the tests with MS730, MS742 and MS743, respectively. For the belt inside configurations, the two positions corresponding to models with and without fold are shown.

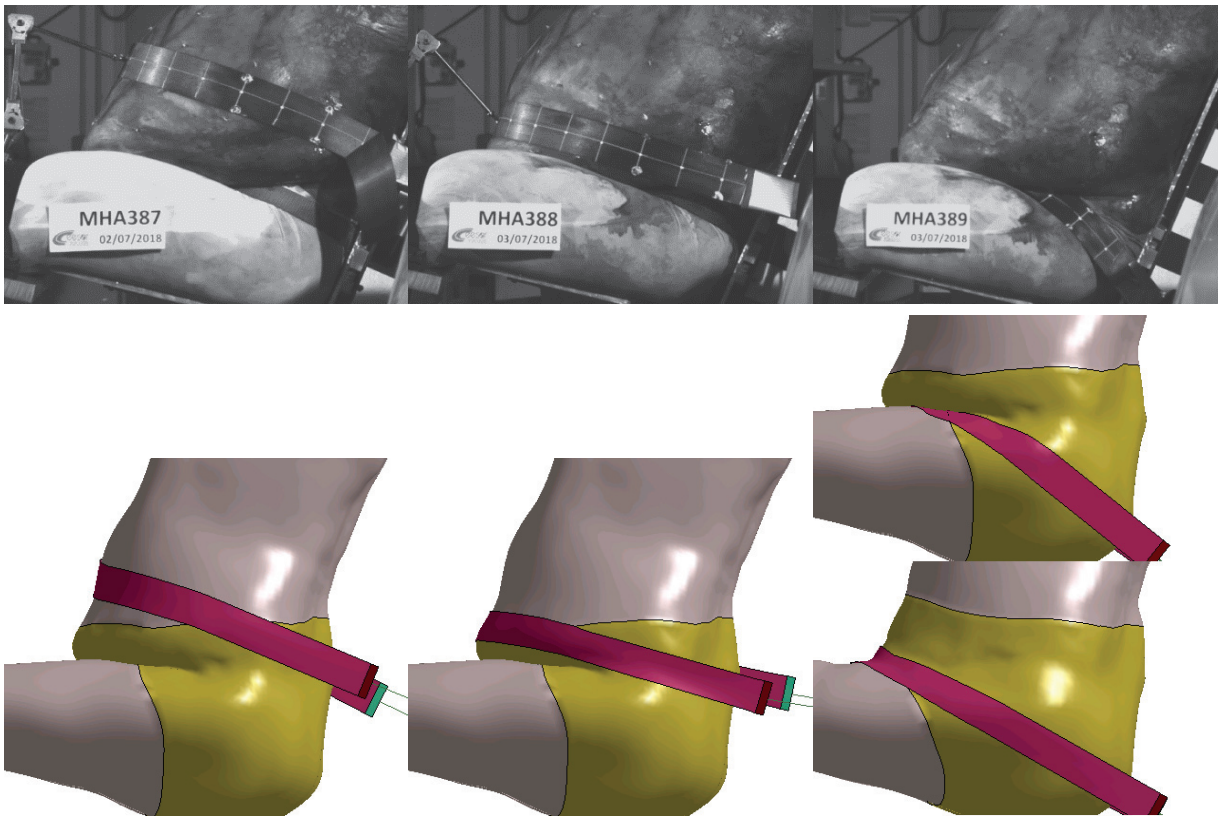


*Figure 93: Belt placement for the MS730 belt tests. Top: camera footage immediately before the experiment, bottom: model. The versions with and without fold are shown for the belt inside configuration.*

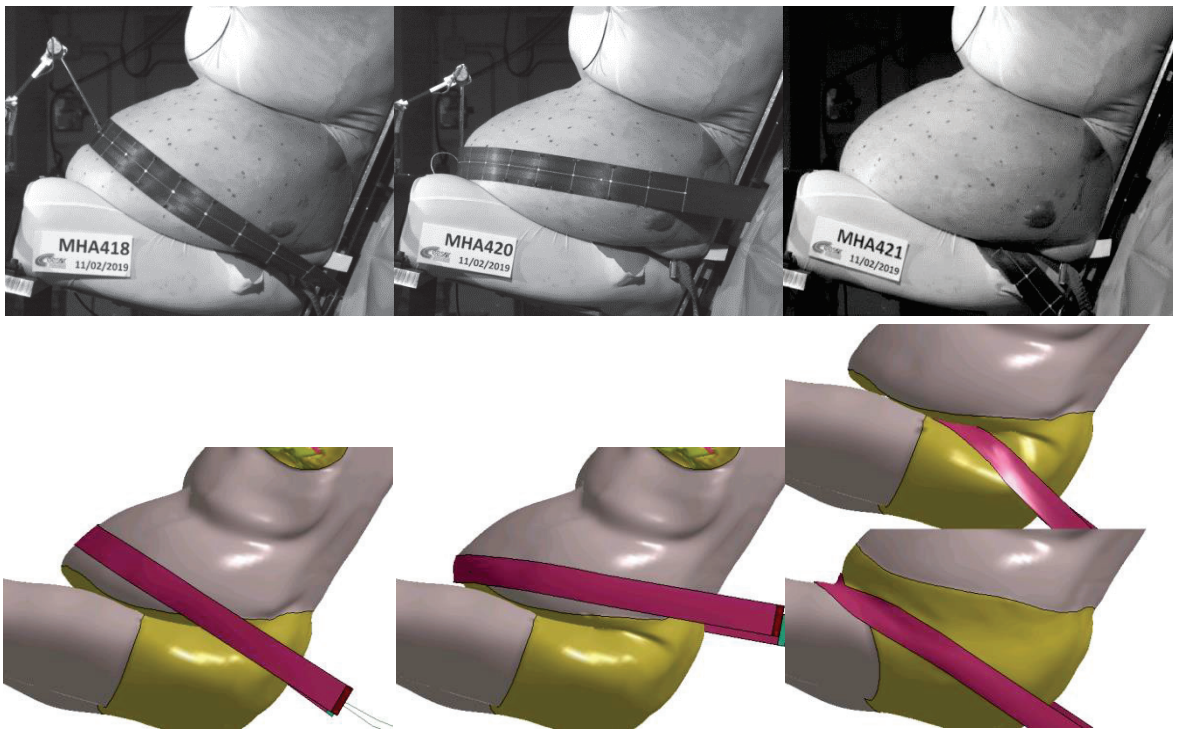


*Figure 94: Belt placement for the MS742 belt tests. Top: camera footage immediately before the experiment, bottom: model. The versions with and without fold are shown for the belt inside configuration.*

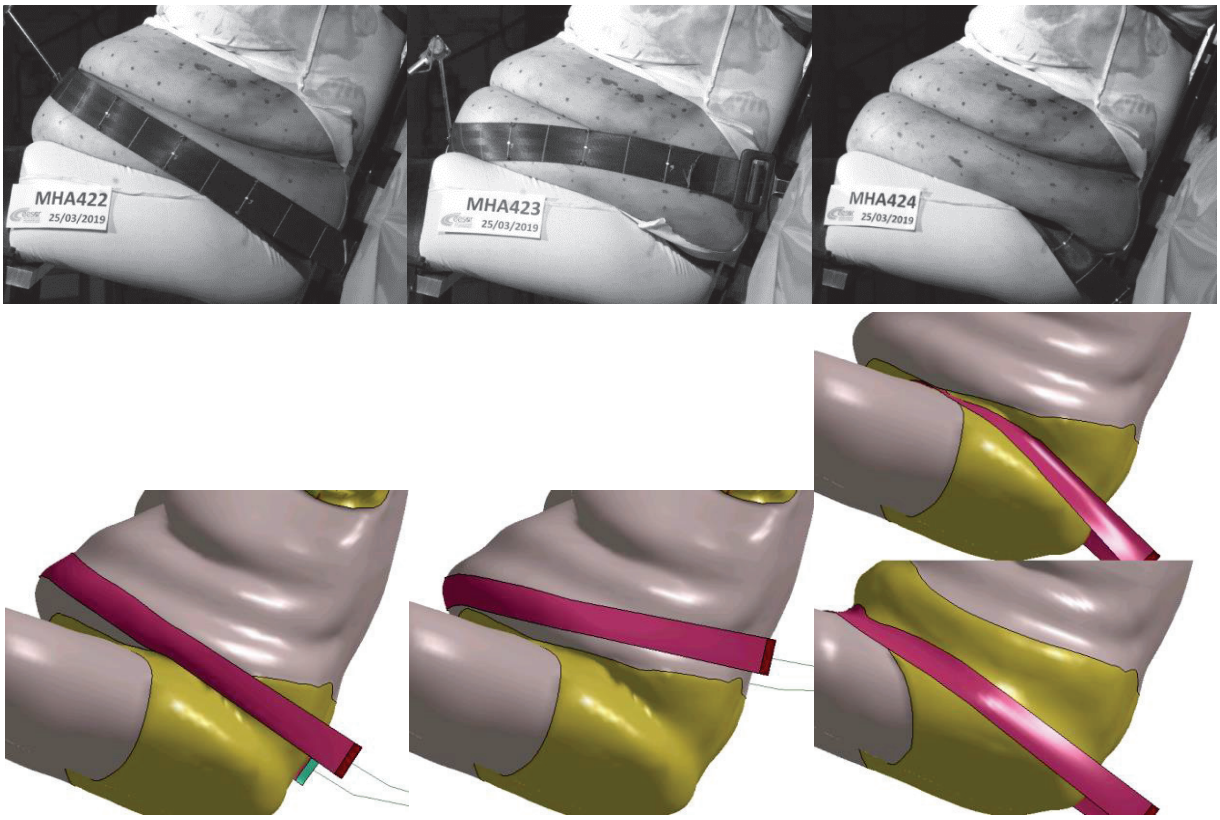


*Figure 95: Belt placement for the MS743 belt tests. Top: camera footage immediately before the experiment, bottom: model. The versions with and without fold are shown for the belt inside configuration.*

#### 6.2.2.2. Boundary conditions

A set of nodes on the back and bottom of the legs of the skin of the model was fixed in all directions to simulate the effect of the seat.

The steel cable connecting the belt to the pulling mechanism was represented by beam elements passing through a slip ring placed in the position of the pulley based on the FaroArm. The displacement of the cable measured by a string potentiometer during the experiment was prescribed to the end of the cable in the simulation. As it was missing for MHA418, the displacement of the left side of the belt tracked on the video was used instead. Figure 96 shows the displacements used for each test, grouped by the belt configuration. Notice that the displacement is maintained at the end of the test.

The velocity corresponding to the cable displacement shows minor oscillations for all tests with MS730 and for test MHA423. As these are not present on the belt, they may be damped by the buckle or the string potentiometer may be vibrating. To assess the transmission of these vibrations to the belt, the oscillations were filtered using low pass CFC filter designed according to the SAE J211 specification ($4^{th}$ order Butterworth). As an example, Figure 97 shows the cable velocity and belt forces for MHA423 and

various filtering frequencies. The relationship between the velocity and force vibrations are clear. As the results remain readable without filter, it was decided to not use the filtering in the end to avoid introducing an additional parameter in the simulation.

The results were analysed in terms total belt force of the lap belt, centre belt displacement (measured as centre node displacement and compared to the MP2D sensor) and left side belt displacement (measured as node displacement on the left side and compared to displacement of a point tracked on the video).

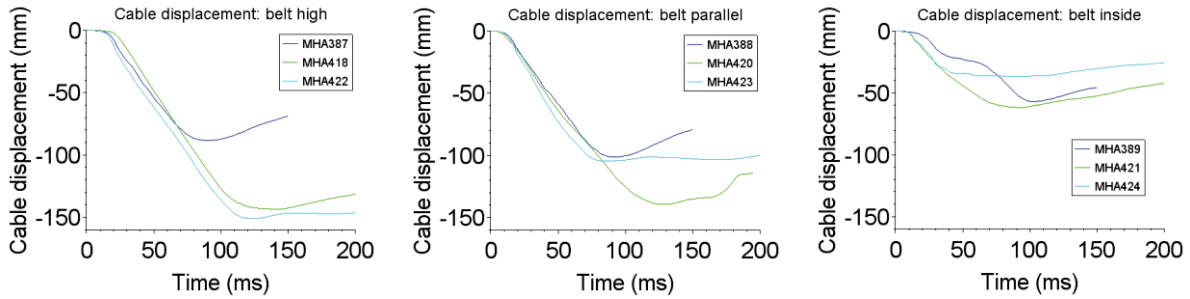


*Figure 96: The cable displacement used for loading of the belt tests. Left: belt high. Middle: belt parallel. Right: belt inside. Legend: blue curve is MS730, green MS742, cyan MS743.*

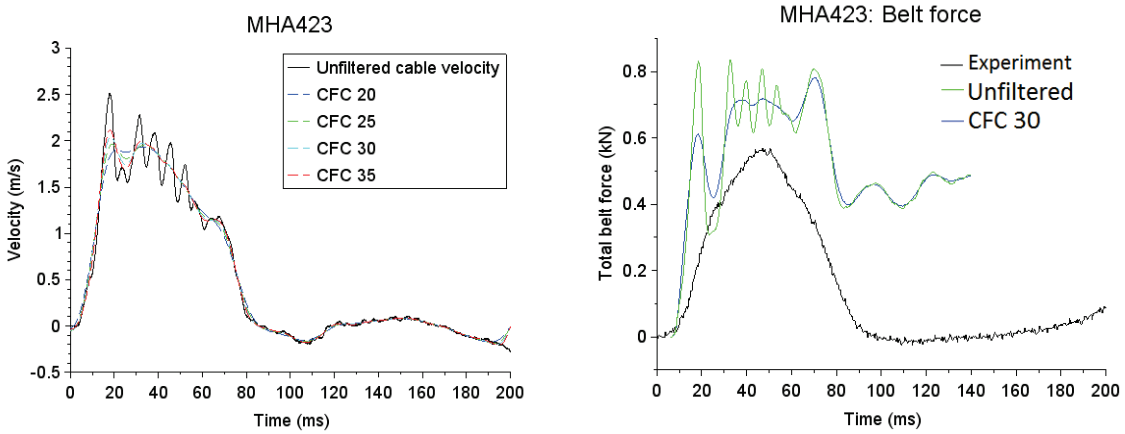


*Figure 97: Effect of CFC filter frequency on input curve and belt force for MHA423. Left: velocity of the cable unfiltered and filtered by 4$^{th}$ order Butterworth filters with four different frequency thresholds: 20, 25, 30 and 35 Hz (right: entire curve, left: detail between 10-70 ms). Right: belt force from a simulation with the "complete" model with unfiltered and filtered (CFC 30) input.*

#### 6.2.2.3. Belt modelling and friction

The material properties of the belt used in the experiments were provided by CEESAR. Simulations were initiated with Coulomb friction coefficients between the belt and the skin of 0.1 as these values were previously used by CEESAR and in GHBMC validation setups. However, when used in MHA418,

the belt slid above the abdomen. As this did not occur in any of the test, the coefficients were increased to 0.3 to keep the belt in position (Figure 98). Other belt tests were less prone to slipping but, to be consistent, 0.3 was used in all belt simulations. This seems in line with findings of Vilhena and Ramalho (2016), who measured friction of human skin and several different types of fabric. Although those did not include the seat belt fabric, their measurements varied between 0.2 and 0.4 for unlubricated skin, noting that the friction rises significantly up to 0.8 if the skin (or the fabric) is wet.

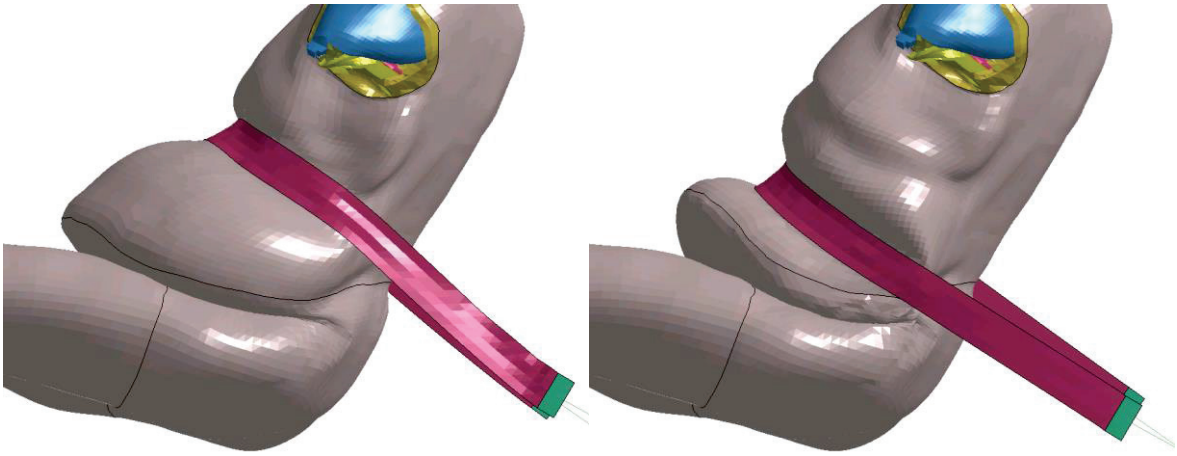

*Figure 98: Comparison of the MHA418 belt test with different belt friction at 112.5 ms using the C315 material. Left: friction 0.1. Right: friction 0.2. Arms are hidden in the figure for better visibility.*

### 6.2.3.MS743 sled tests setup

An Ls-Dyna FE model of the sled used during the experiments described in Section 3.2.3.2 was provided by LAB. The complete and noFold models were used for the experiments. After coarse positioning by rigid transformations, a simulation of gravity was applied to the model to settle it in the seat. The upper body (ribcage, upper limbs, head) was fixed during this simulation, only the lower body was subjected to the gravity. This serves two purposes: to close the gap in the abdominal fold (for the complete model) and to flatten the buttocks and bottom of thighs. Without the gravity positioning, the abdomen was too protruded and did not match the geometry captured by the measuring arm during the experiment (difference of 6-7 cm when using shoulder position as a reference point for aligning the arm data). By applying the gravity, besides closing the gap inside the fold, the abdomen stretched downwards, making the shape match the geometry captured by the arm closely (< 2cm differences) as shown on Figure 99 (middle).

Flattening the bottom of the body was important in order to establish contact with the seat. The kriging targets for legs were created with round legs, similar to how the legs are in the baseline GHBM-M50-

O. This was not an issue for the MHA belt tests as there is no need to simulate the seat, but it was necessary for the sled test.

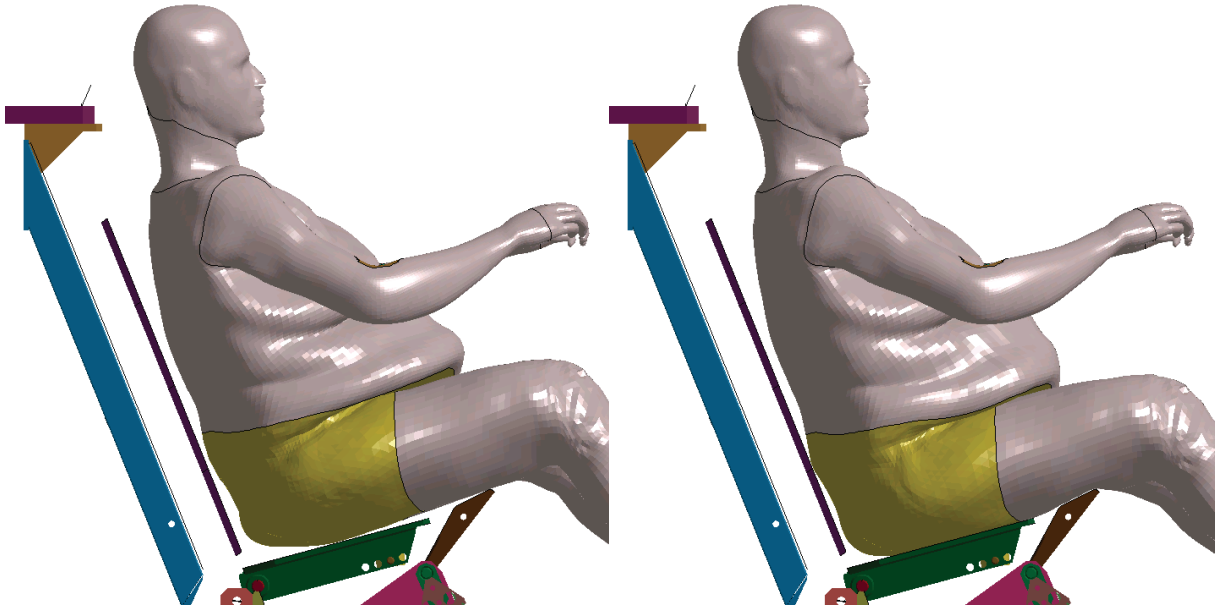

*Figure 99: Positioning of MS743 complete model in the sled. Left: only rigid transformations, before applying gravity. Right: after applying gravity.*

The belts were then fitted using the "Belt Fitting" module in LS-Prepost, with two separate straps for the shoulder and the lap belt. In the experiment, the strap is continuous: the belt passes through the buckle which allows for limited slippage of the belt to either the lap or the shoulder side. To simulate this behaviour in the FE model, a small plane of quadrilateral shape with rigid material is used to represent the solid part of the buckle. There are two slipring[7] nodes on the edges of this buckle through each of them passes a short string of beams (ELEMENT_SEATBELT) connecting the two belt straps. These two strings are allowed to slip in both directions, allowing for some motion of the belt while ensuring the relative position of the two straps remain close. Figure 100 shows a detail of the buckle of both the simulation and the experiment.

Pretensioners on both shoulder and lap belts were applied as well, using specification provided by LAB and times to fire of 18 and 25 ms, respectively. There was a 4kN load limiter on the shoulder belt. The belt was modelled as in the belt test. A friction of 0.3 was used as a starting point and the effect of

[7] ELEMENT_SEATBELT_SLIPRING, it is a special type of element that allows "*continuous sliding of a belt through a sharp change of angle*" (LSTC 2019), i.e. it acts as a pulley.

larger values (up to 0.8) will be shown in the results. A small load (20N) in the retractor was used to keep the contact and prevent any belt slack.

At the end of this positioning phase, it was found that the minimum distance between the pelvis (at the ischium) and the seat pan was still much higher in the model (60mm) than on the seated CT scan (about 15 mm). As this could be problematic for the interaction between the seat pan and the pelvis, this thickness was reduced to 20mm by applying a 6 g vertical acceleration to the model during 45ms while the upper body skin was made rigid. The simulation was run with the belts already in place.

The acceleration curve applied to the sled was presented in Section 3.2.3.2. The same curve is applied in the simulation after a delay of 30 ms during which gravity is apply to the model.

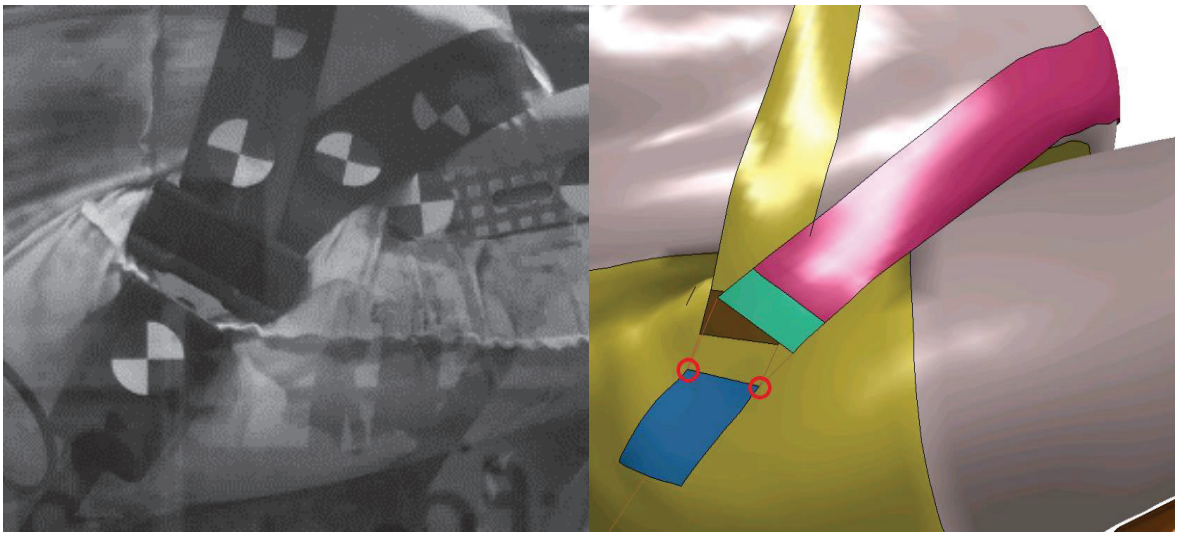

*Figure 100: Buckle of the seatbelt used in the sled test. Left: experiment. Right: simulation with the complete model. Location of the slipring nodes is marked by red circles.*

# 6.3. Simulation results

## 6.3.1. Belt tests

### 6.3.1.1. Fat material selection based on MHA420

A subset of fat properties (C002c, C23, NH 0.6kPa and 6kPa and C315) were compared to the experimental response of the test MHA420 (Figure 101). MHA420 was selected because it was a test with both large belt displacements and force.

As for the non-obese model, C23 and C002c led to a stiff response (force almost twice as high as the experiment), NH 0.6kPa (X1) was softer than the experimental result, and C315 and NH 6kPa (X10)

gave similar results (slightly over the experimental response in terms of force). When examining the curve shape, the initial force rise was captured using C315, which was attributed to the low damping value. However, the subsequent drop was not captured by any of the properties, except perhaps by the NH 0.6 kPa in which it is initiated. In order to check the strains and strain rates achieved in the simulations, the average of the principal first and third strain (rate) under the belt were computed in the tissues directly beneath the belt. Strain rates remained below 10 $s^{-1}$, which seems compatible with the assumptions on strain rate made up to this point.

Based on these results, the properties C315 and X1 were kept for further simulations.

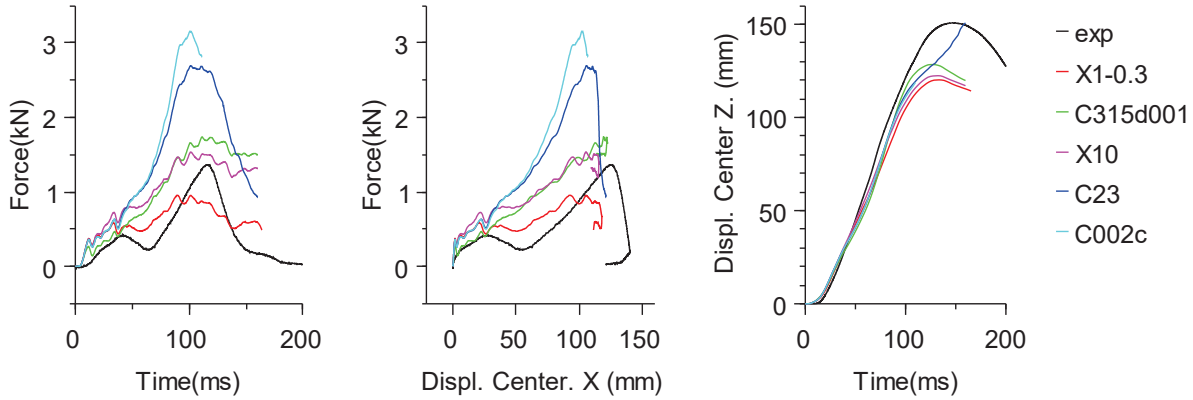


*Figure 101: Response comparison for the MHA 420 test and five input curves for the material model. Legends: exp: experimental data; X1-0.3 = NeoHookean with 0.6 kPa modulus. C315d001 = based on an Ogden $\alpha$=15, $\mu$=40Pa, a plateau in tension at 13.7 kPa and damage modelling; X10 = NeoHookean with 6 kPa modulus; C23=based on an Ogden $\alpha$=23 and $\mu$=10Pa; C002c= idealized table derived from Comley and Fleck (2012) at strain rates from 0.2 and 2700 $s^{-1}$ and extended beyond the experimental range; All curves with damping 0.05 except C315d001 (damping 0.01).*

#### 6.3.1.2. Responses for all MHA simulations

Figure 102 and Figure 103 show the models using the C315 material at the time of maximum centre displacement for the high and parallel belt configurations, respectively. Similarly, to the experiments (3.3), the abdominal gap opens up for models with fold. Two slightly different modes of the opening can be observed: in the high belt configuration (Figure 102), the belt divides the abdomen in two parts, compressing it in the middle. In the parallel configuration (Figure 103) for PMHS MS742 and MS743, the belt is positioned just above the fold and it "lifts" the entire abdomen rather than dividing it in two parts. Comparing this with the experiment footage (Figure 38 and Figure 39), the MS743 case looks similar to the experiment in this regard. However, in the MS742 case, the experiment is closer to the first mode. This might suggest that the used material is too stiff. However, as Figure 104 shows, there

are only minimal differences when the X1 material is used for these simulations. The belt can be seen penetrating deeper in the MHA420 case, but only slightly. Another factor that could be influencing this behaviour is the artificial gap in the fold that the models have.

Small differences can be observed between the abdomen shape between the foldOnly and complete models, e.g. in the belt parallel configuration the abdomen opens a bit more, but in general it shows the same behaviour.

The belt inside configuration is shown in Figure 105. The foldOnly models are not shown for the belt inside as they have almost the same response as the complete models for this configuration. Instead, the simulation with the complete model with the belt positioned as in the noFold model is shown. Similar to the experiment (Figure 40), the MS743 shows almost no visible abdomen deformation. The abdomen of MS742 deforms into a rounder shape, which is in line with the experiment footage. The MS730 shows deformation similar to the MS742 experiment, but in the simulation, the deformation is more subtle. The setup with the complete model, but with belt positioned as in the noFold model leads to no deformation. The belt is only pulled inside the abdominal fold, but the stroke is not large enough to make the belt engage the pelvis.

Figure 106 to Figure 114 summarise the main results of simulations of the belt tests. Appendix 2 contains plots with additional measurements. Each figure shows results of simulations with C315 (solid line), NH 0.6kPa (X1, dashed line). The X1 simulations were less stable and some of them terminated prematurely with negative volume errors (specifically: MHA387 complete after 77.5 ms, MHA389 complete after 75 ms, MHA421 foldOnly after 17.5 ms, MHA422 noFold and foldOnly after 107.5 ms, MHA424 foldOnly after 70 ms and MHA424 complete after 25ms). The belt inside configuration contains the results of two different belt placements for the complete model, one with belt inside the fold close to the abdomen and one with the belt placed in the same location as it is for the noFold model.

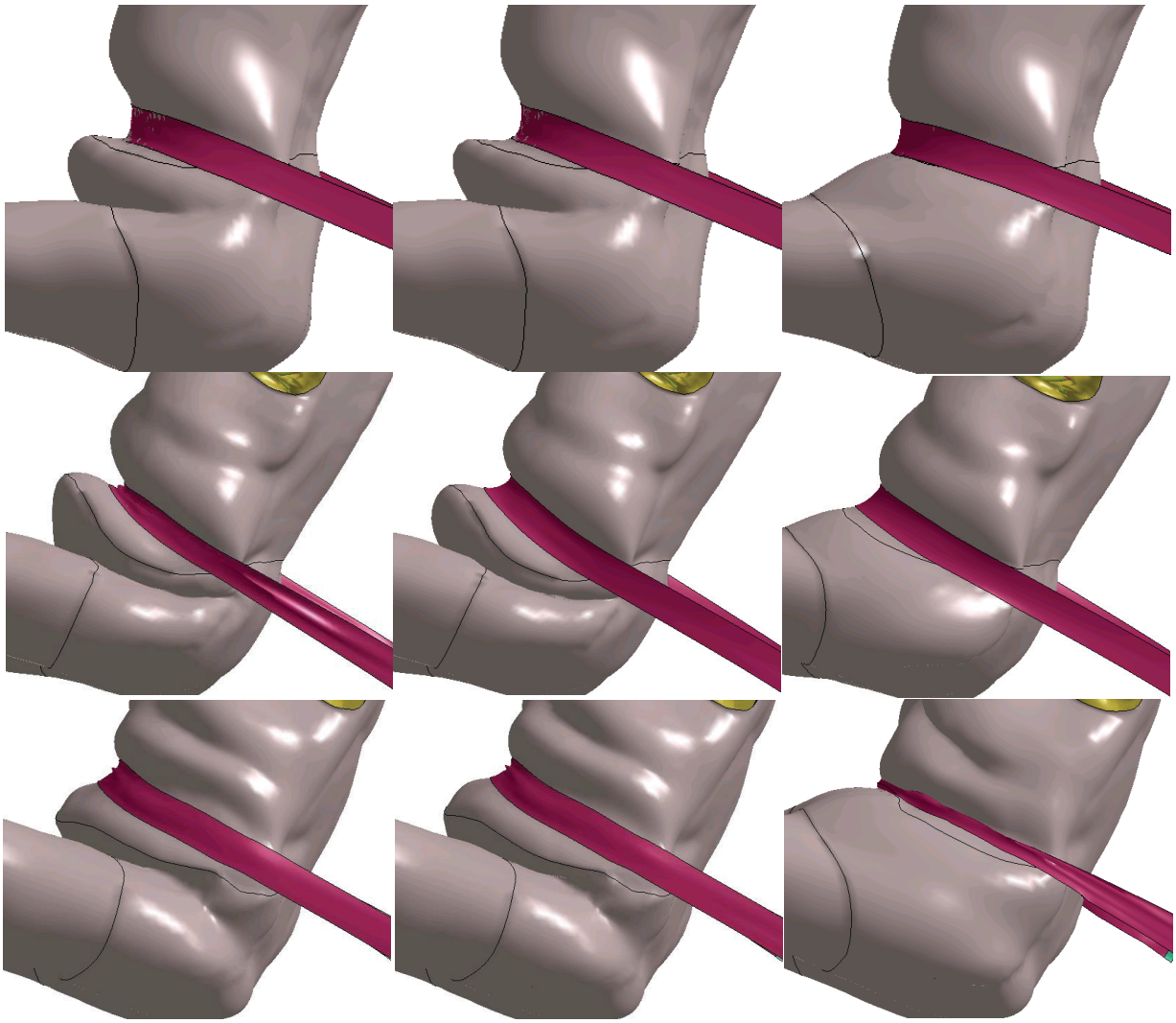

*Figure 102: Captures from simulations of the high belt configuration, C315 material, at the time close to the maximum centre displacement (which occurred at similar times for each model type). Top row: MHA387 (MS730) at 94.5 ms. Middle row: MHA418 (MS742) at 125 ms. Bottom row: MHA422 (MS743) at 128 ms. Left column has the complete, middle column the foldOnly and the right column the noFold models.*

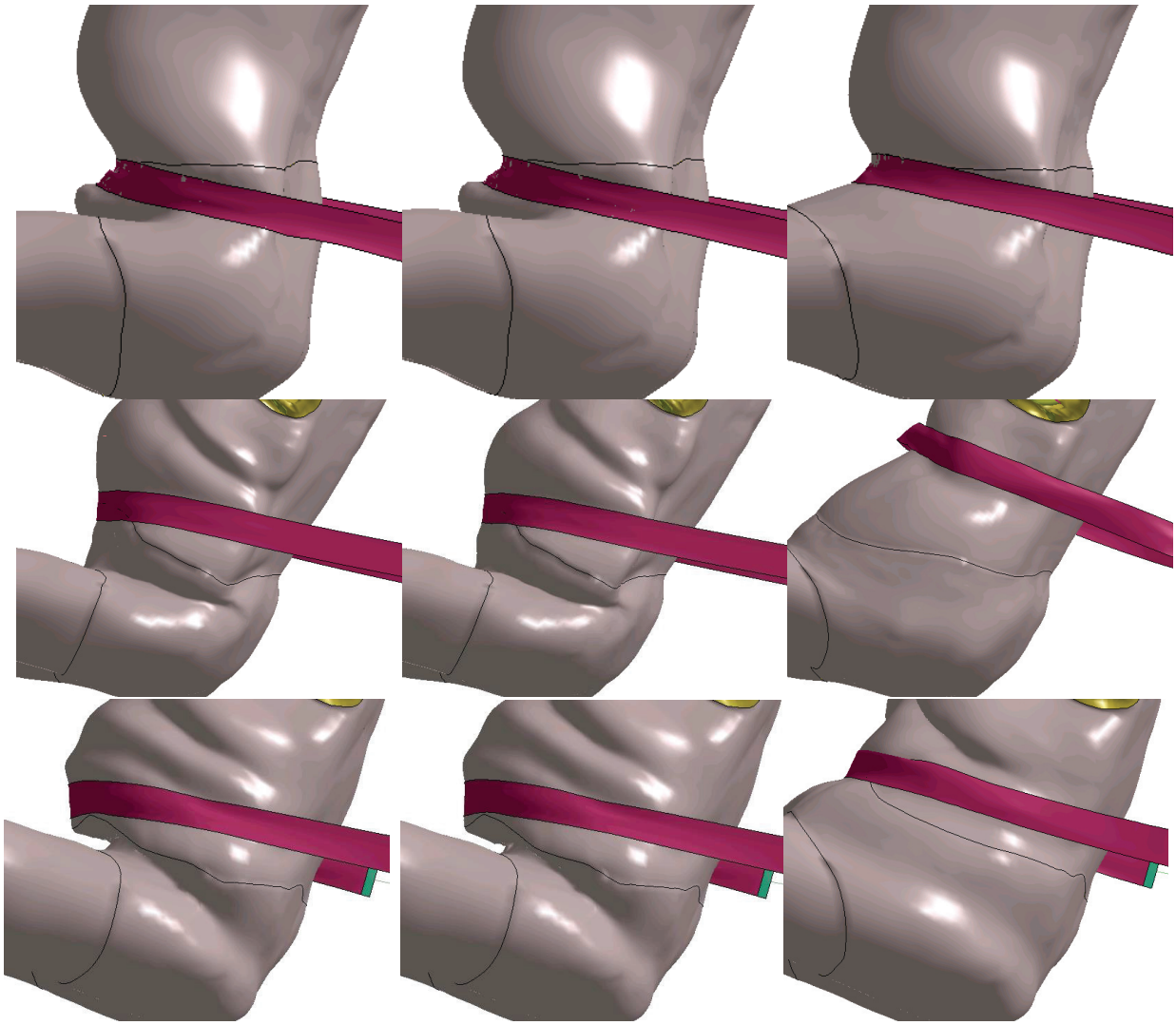

*Figure 103: Captures from simulations of the parallel belt configuration, C315 material, at the time close to the maximum centre displacement (which occurred at similar times for each model type). Top row: MHA388 (MS730) at 95 ms. Middle row: MHA420 (MS742) at 128 ms (the belt slipped in the noFold version). Bottom row: MHA423 (MS743) at 98 ms. Left column has the complete, middle column the foldOnly and the right column the noFold models.*

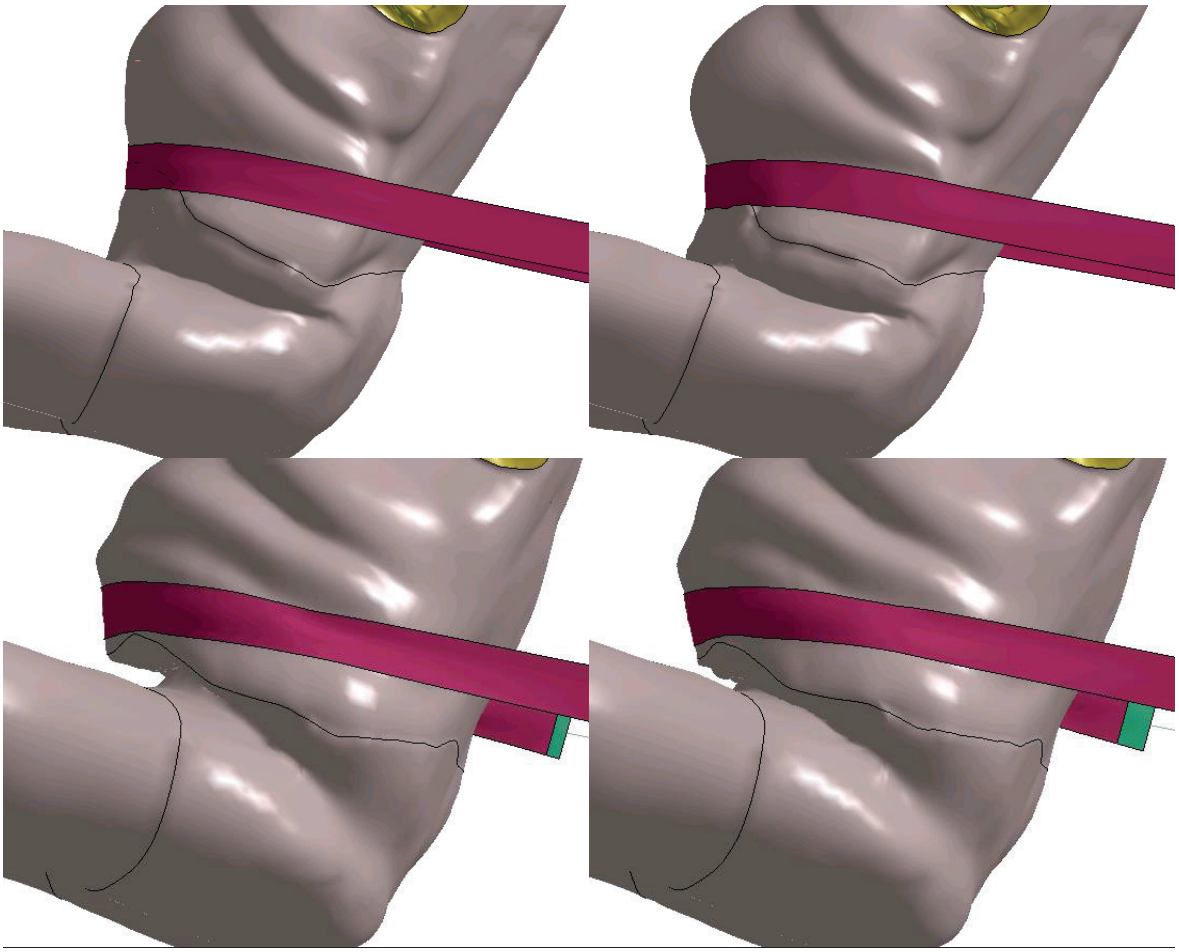

*Figure 104: Comparison of simulation with theC315 (left column) and X1 (right column) material. First row shows the MHA420 (MS742, belt parallel), second row the MHA423 (MS743, belt parallel).*

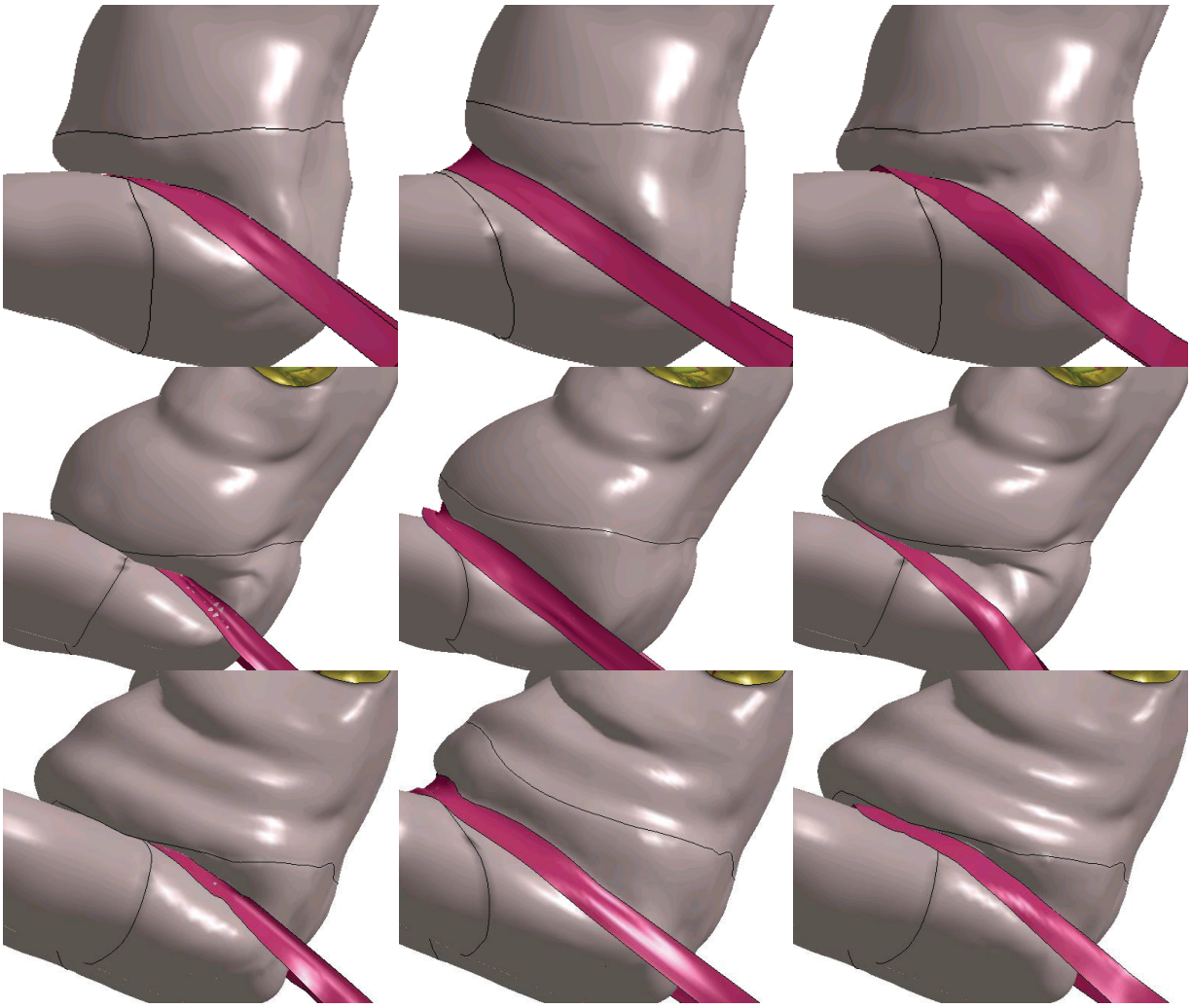

*Figure 105: Captures from simulations of the belt inside configuration, C315 material, at the time close to the maximum belt displacement (which occurred at similar times for each model type). Top row: MHA389 (MS730) at 97.5 ms. Middle row: MHA421 (MS742) at 89 ms (the belt slipped in the noFold version). Bottom row: MHA424 (MS743) at 70 ms. Left column has the complete, middle column the noFold and the right column the complete with belt in noFold position models.*

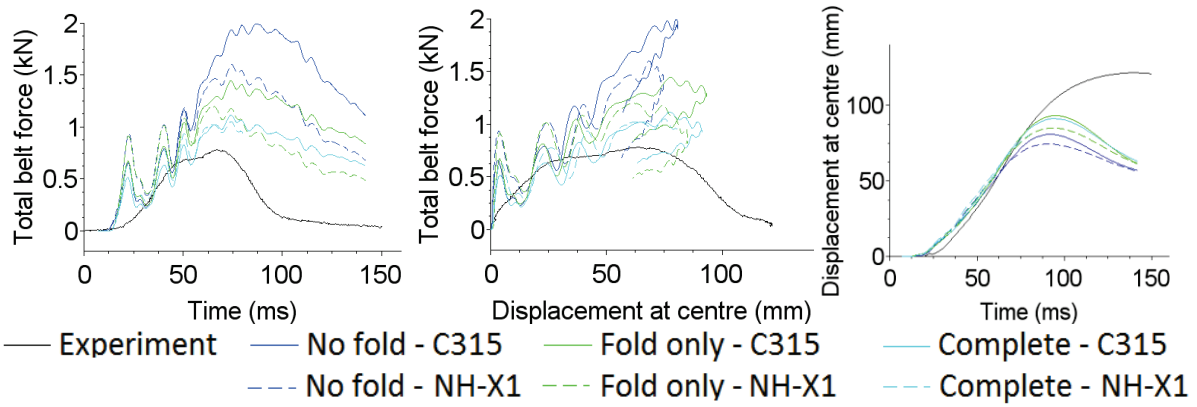


*Figure 106: MHA387 (MS730, high belt) simulation results.*

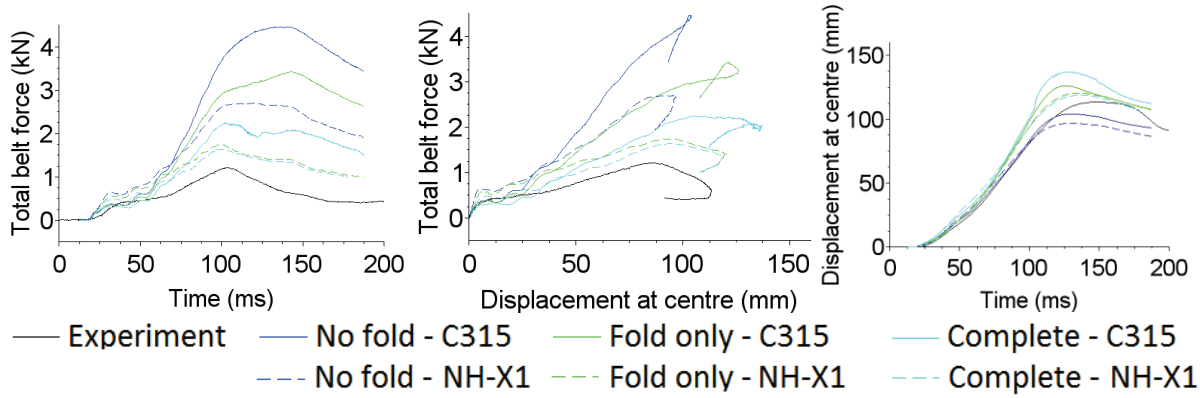


*Figure 107: MHA418 (MS742, high belt) simulation results.*

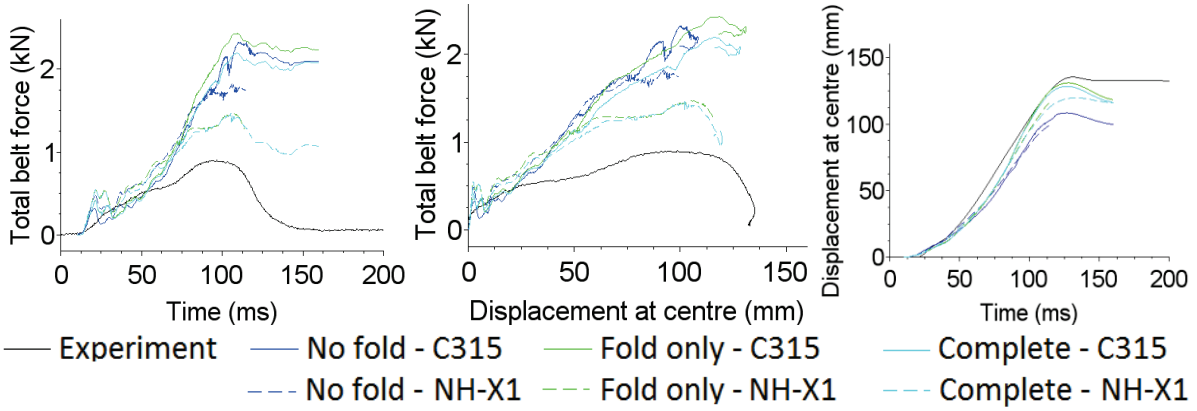


*Figure 108: MHA422 (MS743, high belt) simulation results.*

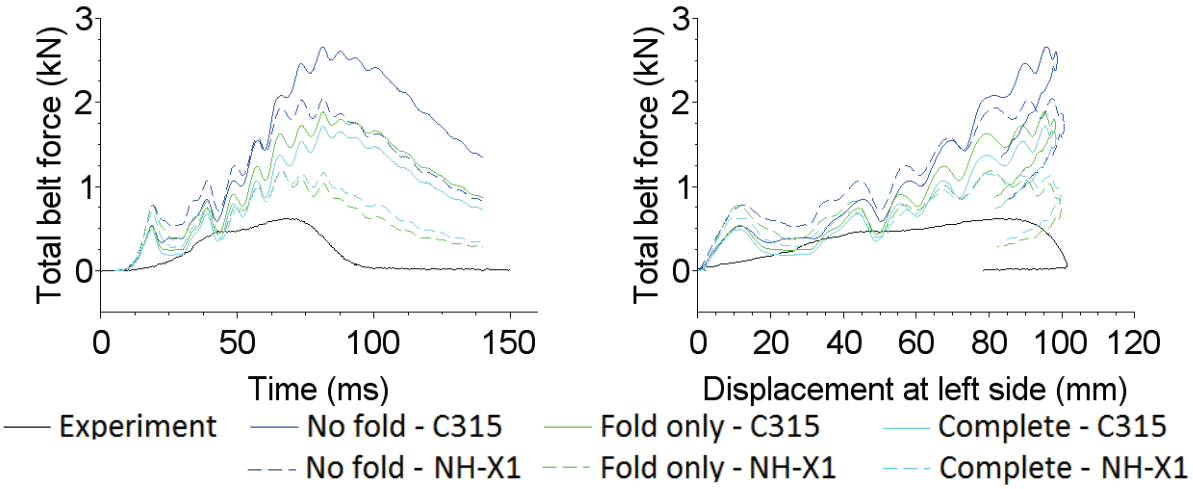


*Figure 109: MHA388 (MS730, parallel belt) simulation results.*

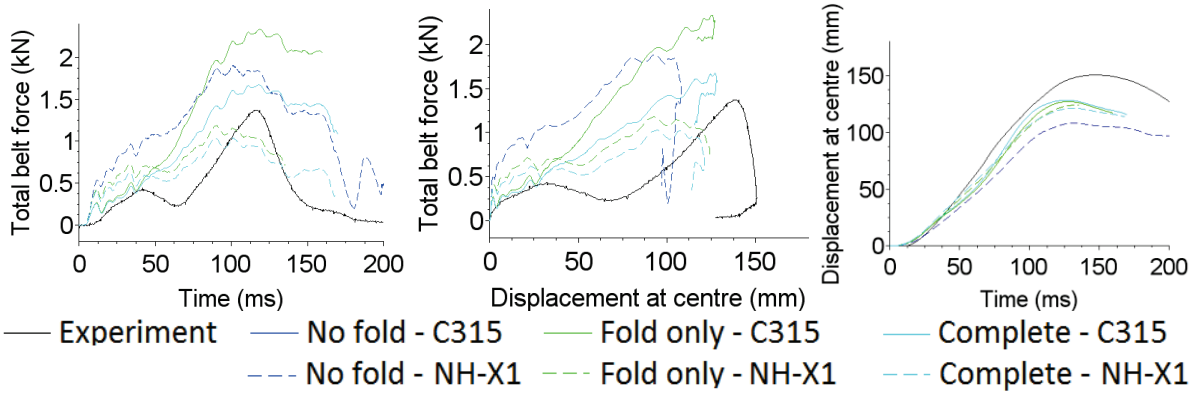


*Figure 110: MHA420 (MS742, parallel belt) simulation results. The noFold model with C315 is not shown as the belt slipped during the experiment.*

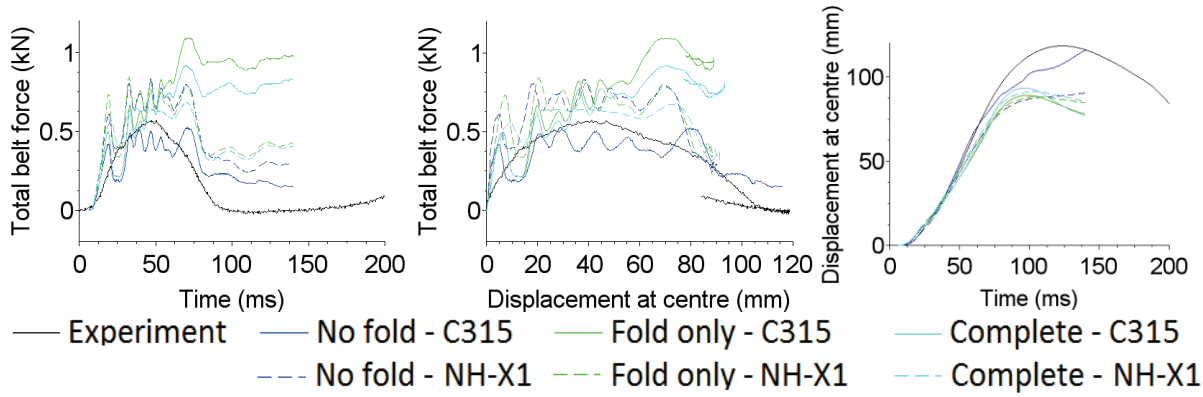


*Figure 111: MHA423 (MS743, parallel belt) simulation results.*

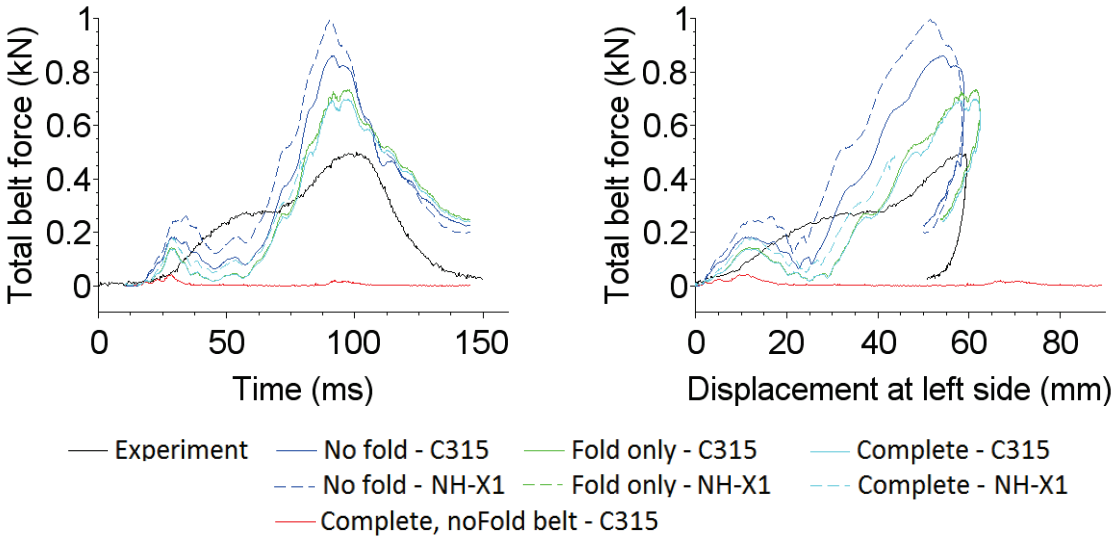


*Figure 112: MHA389 (MS730, belt inside) simulation results.*

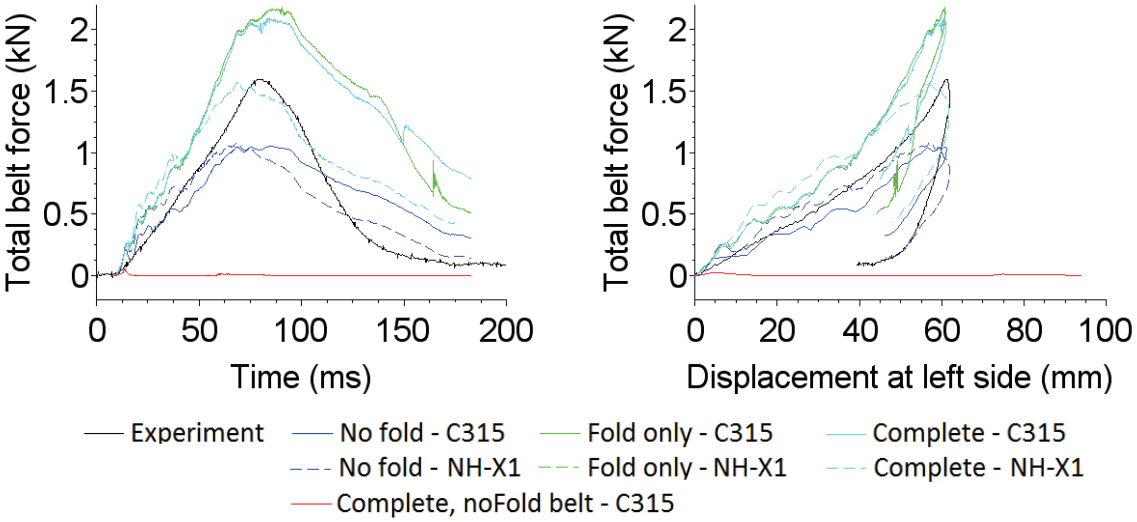


*Figure 113: MHA421 (MS742, belt inside) simulation results. The foldOnly model with NH-X1 is not shown as the simulation terminated after only 17.5 ms.*

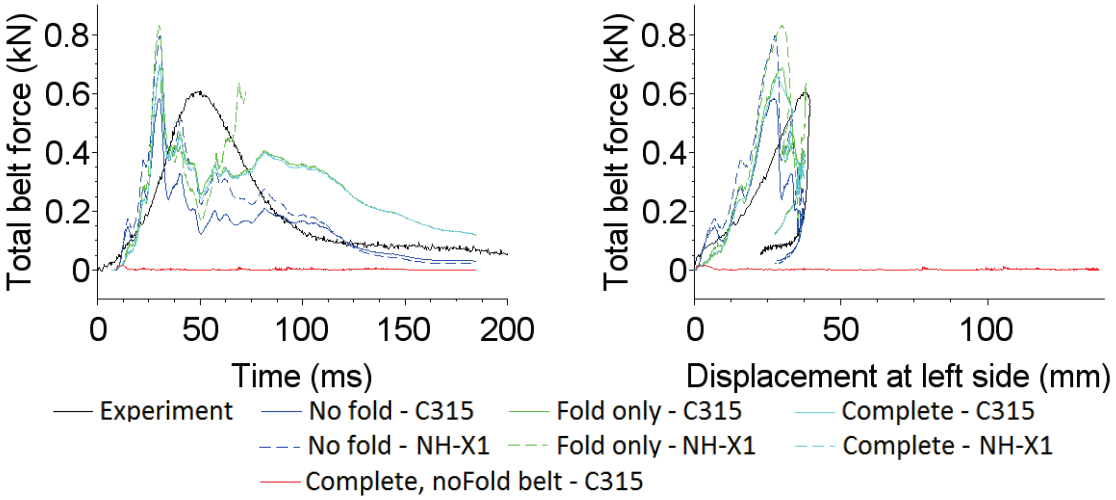


*Figure 114: MHA424 (MS743, belt inside) simulation results. The complete model with NH-X1 is not shown as the simulation terminated after only 25 ms.*

Vibrations on the forces related to the velocity variation previously observed is present in some test conditions but do not prevent relative comparisons as curves with different properties or conditions remain mostly parallel. Overall, most model responses were stiffer (higher forces) than the experimental results. The force drop at the end of the loading is also noticeably slower. It must be remembered that the belt remains in place (no unloading phase).

X1 properties led to lower forces than C315 in the high (Figure 106, Figure 107, Figure 108) and parallel (Figure 109, Figure 110, Figure 111) belt configurations, which are the one where large thickness of tissues are involved. This is consistent with the baseline model simulations.

The difference between the two was between 0.5-1 kN in most cases (except for MHA418 foldOnly, which led up to 1.7 kN difference, i.e. doubling the force). This made the X1 responses closer to the experimental results in all high and parallel belt cases. In the case of MHA420 (Figure 110) the force was even below the experimental value for X1. In the belt inside configuration, the results were contrasted. The X1 force were higher for MS730 (MHA389, Figure 111), lower for MS742 (MHA421, Figure 113), and could not be compared for MS743 (MHA424, Figure 114) as the simulation with the complete model crashed after 25 ms due to inverted elements. Simulation with the foldOnly model lasted 77.5 ms and the force is seen rising rapidly for the last 10 ms (Figure 114), which suggests that the result is problematic (reason unknown). The X1 simulations for the belt inside configurations were in general more unstable and most of them terminated before reaching the force peak.

Comparing the foldOnly and complete models, the foldOnly models had higher force response for the high and parallel belts, while it was inconsequential for the belt inside configuration in which the belt

loads the abdomen only in the lower part, which the subcutaneous target affects only minimally. The difference was up to 1 kN (50%) in the MHA418 (Figure 107) and MHA420 (Figure 110), i.e. for the MS742 PMHS. For the two other PMHS, the differences were smaller, within 0.3 kN. Beyond the material stiffness, this behaviour is consistent with a difference of deformation pattern for the parallel simulations, with the fold opening (when present) and leading to the upward belt motion.

With the X1 material, this difference was much less pronounced than with the C315. This might suggest that the properties of hollow organs and other tissues in the abdominal cavity play a higher role on the force response in the NH-X1 case.

The noFold model with C315 material was the stiffest (and furthest away from the experiment) for all tests but MHA423, where it instead had the lowest force response than any of the other configurations. As Figure 115 shows, this is due to partial slipping of the belt. Although the belt still provides some restraint, unlike MHA420 (Figure 103), slipping is noticeable. Another outlier was the MHA422 with the C315 material, in which the noFold model did not have significantly higher force than foldOnly or complete. Instead, all three models had similar responses, much higher than the experimental values. This was not the case for NH-X1. Here too, partial slipping of the belt was visible with the noFold. It was more prominent for C315 than X1 and no slippage was observed for the complete model.

Regarding the displacements at the centre, there are noticeable differences between the models with fold (foldOnly and complete being similar) and without it in the high and parallel belt configurations (Figure 106 to Figure 111). Particularly for the parallel belt (MHA420 and MHA423, Figure 110 and Figure 111), the belt is travelling downwards in the centre at the beginning before it starts rising, while in the experiment or in simulation with the noFold model, the trajectory is monotonously upward. This can be explained by the small gap between the abdomen and thighs due to the target preparation. This gap is closed by the belt pressure in the beginning of the simulation and only after that does the abdomen rise.

The choice of adipose tissue material did not have significant influence on most belt displacement curves. Although for the noFold models the models were more prone to upward belt slippage (especially for the C315 properties, cases MHA420, MHA422 and MHA423 (Figure 115)), upward belt motion was also visible with the fold models due to the fold opening.

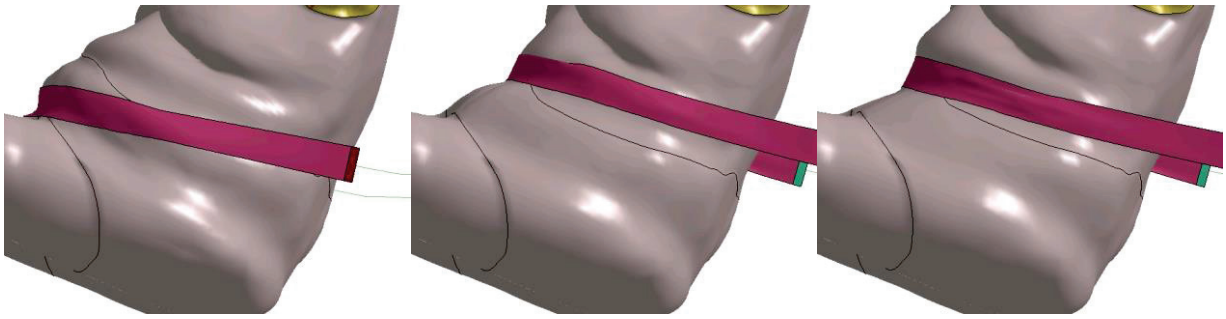

*Figure 115: Illustration of belt slippage on the noFold models of the belt parallel configuration using the MS743 model (MHA423). Left: initial position (0ms). Middle: C315 material, at 98 ms. Right: X1 material at 98 ms.*

## 6.3.2.Sled test MS743

Section 6.3.2.1 will present results of simulations with the complete model and Section 6.3.2.2 with the noFold model. The foldOnly model was not used for the sled simulation.

### 6.3.2.1. Complete model

Figure 116 and Figure 117 show snapshots of the simulation (front and side view, respectively) at several time points using three different friction coefficients: 0.3, 0.5 and 0.8 with the C315 material and 0.8 with the X1 material. As was shown in Section 3.3.2, the lap belt did not seem to slip inside the abdominal fold during the experiment. However, it does with the 0.3 friction. With 0.5 or higher, the central part of the abdomen stays below the belt for the entire time of the simulation. Furthermore, the shoulder belt tends to slip more over the trunk as well with friction 0.3. The forward excursion of the body is also significantly higher as can be observed by comparing the buttocks position in the rightmost series of images in Figure 117.

Simulations using the X1 material with friction 0.3 and 0.5 terminated due to negative volume elements after 60 ms and with friction 0.8 after 90 ms, which is shown on Figure 116 and Figure 117. Similarly to the parallel belt configuration in the belt tests, the X1 material allows for deeper penetration of the belt (Section 6.3.1.2), which reduced the belt tendency to slip into the fold.

The friction between the seat and the model also affects the behaviour significantly. The simulations in Figure 116 use the same friction coefficient for the seat and for the belt. Figure 118 shows a side view of two simulations with belt friction 0.8, but one with seat friction 0.8 (i.e. the same as in Figure 116) and one with seat friction 0.3. In the following text, the simulations will be denoted by their friction simply as “simulation X / Y”, where X is friction of the seatbelts and Y friction of the seat.

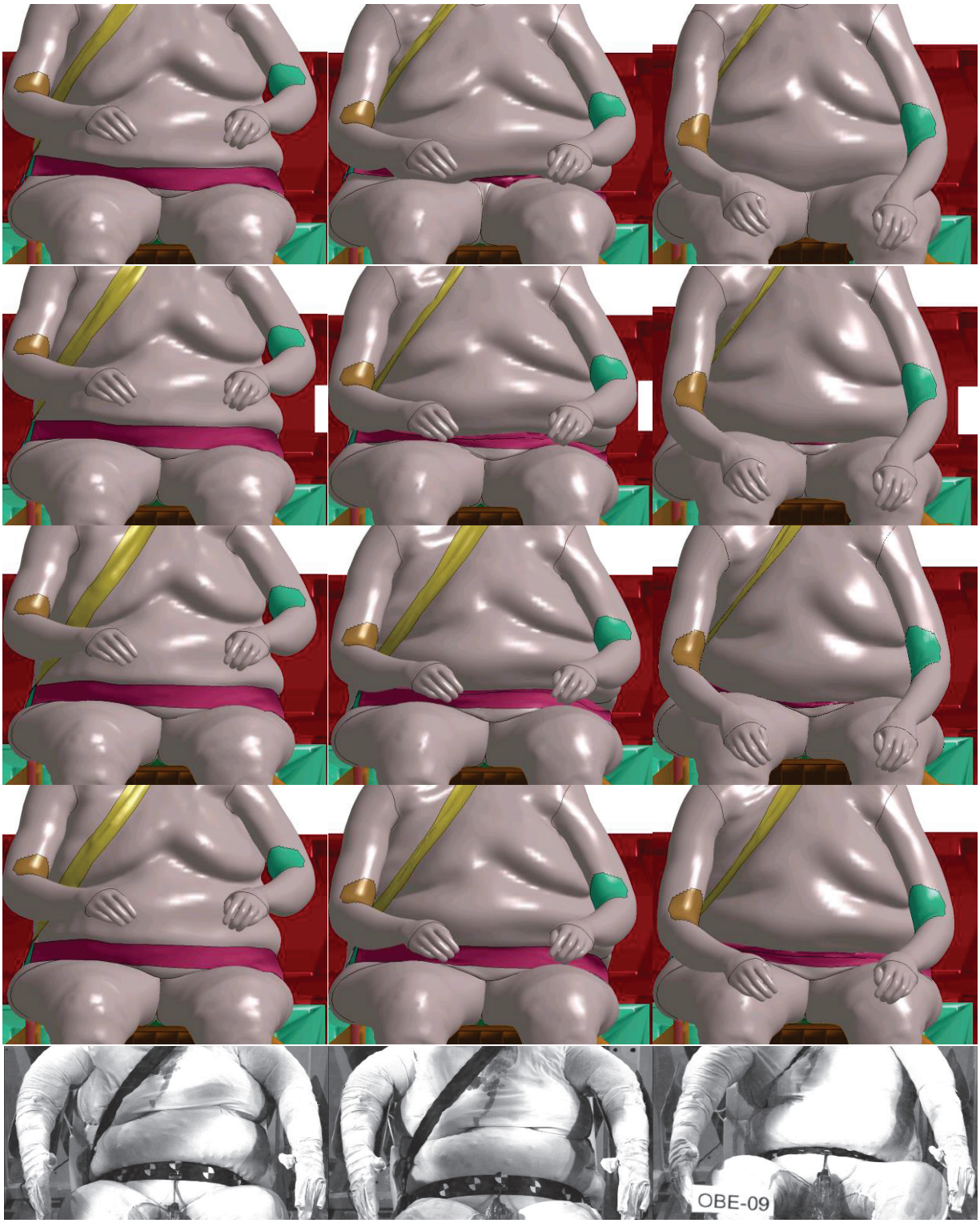


*Figure 116: Frontal view of the MS743 sled simulation at 30 ms (left), 60 ms (middle) and 90 ms (right). Each row shows a simulation with different friction, from top to bottom: 0.3, 0.5 and 0.8, all with the C315 material. Fourth row shows the simulation with friction 0.8 and the X1 material, although the third image is from time 79 ms as the simulation terminated afterwards due to negative volume elements. Last row shows the PMHS experiment.*

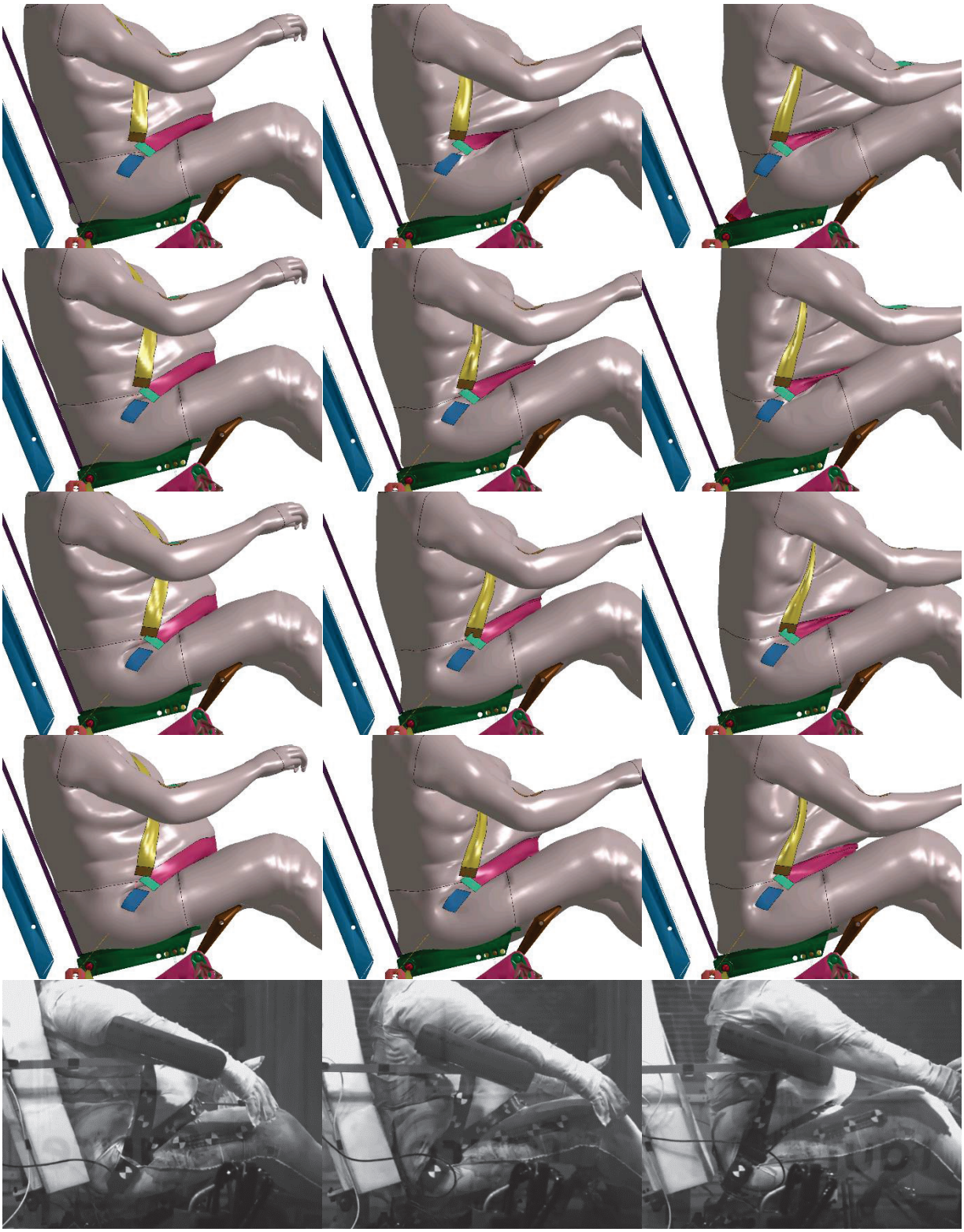

*Figure 117: Side view of the MS743 sled simulation at 30 ms (left), 60 ms (middle) and 90 ms (right). Each row shows a simulation with different friction, from top to bottom: 0.3, 0.5 and 0.8, all with the C315 material. The fourth row shows the simulation with friction 0.8 and the X1 material (the third image is from time 79 ms as the simulation terminated afterwards due to negative volume elements). The last row shows the PMHS experiment.*

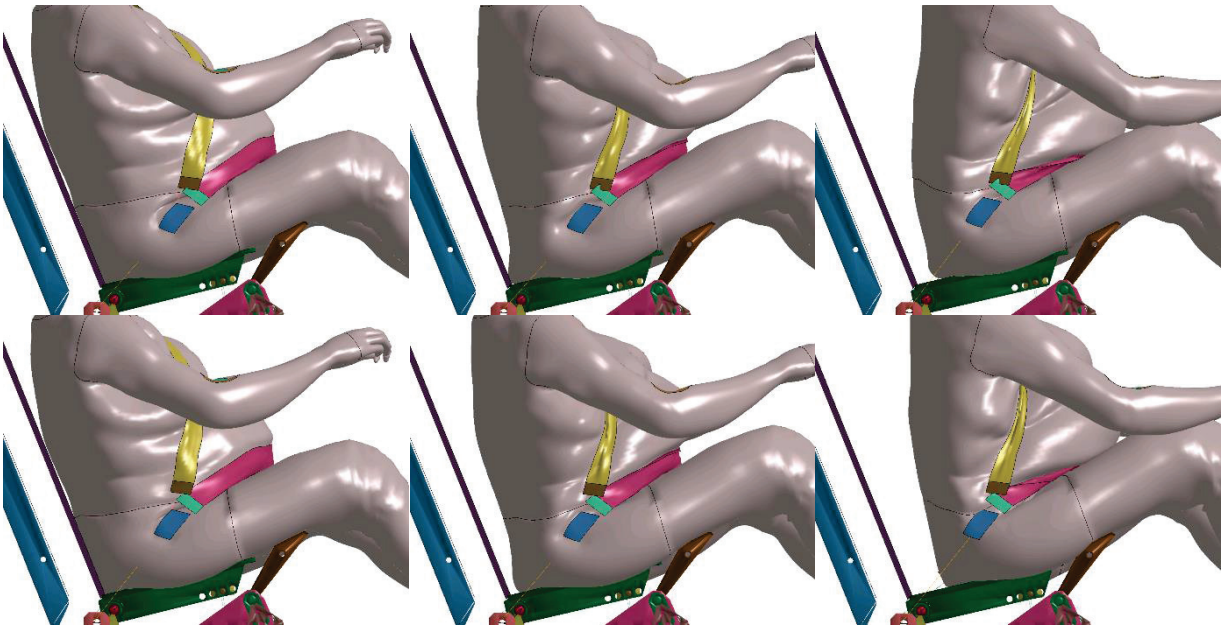

*Figure 118: Side view of the MS743 sled simulation at 30 ms (left), 60 ms (middle) and 90 ms (right). The first row shows a simulation with 0.8 friction on both the belts and the seat contact, while the second row uses 0.8 for the belts, but 0.3 for the seat. The C315 material is used in both cases.*

All shoulder belt forces were similar and close to the experimental result, i.e. reaching the load limiter (Figure 119). The effect of the belt slippage can be seen on the lap belt force (Figure 119, left): the 0.8 / 0.8 simulation is closest to the experimental value (peak within about 200 N), while for the 0.3 / 0.3, the peak lap belt force is 3 kN larger. As Figure 120 shows, in the 0.3 / 0.3 the seat belt slips close to the pelvis and loads it, which explains the higher force. The buckle force magnitude of the 0.3 / 0.3 (Figure 119, right) is closest to the experiment force but it associated with a different behaviour than the one observed in the experiment (i.e. limited belt slippage). All other buckle forces are lower than in the test results, as higher friction may reduce the belt force transmitted to the buckle side. The 0.5 / 0.5 simulation has similar lap belt force to the 0.8 / 0.8 for the first 100 ms of the simulation, but starts to diverge afterwards. It reaches up to 0.8 kN difference to the experimental values at 120 ms. Reducing the seat friction to 0.3 while keeping the belt friction at 0.8 (0.3 / 0.8) increased the lap belt force about half way between 0.3 / 0.3 and 0.8 / 0.8, i.e. by about 1.5 kN (still Figure 119), highlighting the combined effect of the seat and lap belt to restrain the pelvic area. Figure 120 shows the pelvis and belt for these three simulations: while the belt slipped close to the pelvis for 0.3 / 0.3, the differences are subtle between the two 0.8 belt friction cases, in which the belt did not slip. Using 0.8 / 0.8 as a reference, pelvis resultant excursion increased by 5.5 cm in 0.8 / 0.3 and 14.3 cm in 0.3 / 0.3.

To further quantify the behaviour of the model relative to the seat, the forces acting on the seat and the sacrum acceleration are compared with the experiment (Figure 121). In the experiment, there is

initially a sharp increase in the seat force and sacrum acceleration, followed by a steep drop after 40 ms. The force and acceleration rise again after 50ms. While the 0.3 / 0.3 simulation shows force in the X direction closest to the experiment at the beginning (until 50 ms), it becomes too low afterwards. This is in line with the larger pelvis excursion. The 0.8 / 0.8 simulation overestimates the peak force along X, which results in the force dropping too early. The first peak is even more pronounced on the Z force and the sacrum acceleration. This was not captured by any of the simulations and the reason is not clear.

Although the shoulder belt can be seen slipping more in the 0.3 friction case than the other cases (Figure 117, right column), the force at the anchor shows only small variations for all three friction settings (Figure 119, middle) as the 4 kN load limiter was reached in all cases.

Figure 122 shows the belt forces for simulations with the X1 material. Unfortunately, as stated above, the X1 simulations were more unstable and did not reach the peak force (of the experiment), allowing for only limited analysis. For all friction settings, the lap belt force is closer to the experiment than with the C315 materials: it is 0.3 to 0.5 kN higher in the X1 cases, 0.5 to 0.7 kN higher in the C315 cases at the 60 ms time. The shoulder belt shows the same behaviour regardless of material.

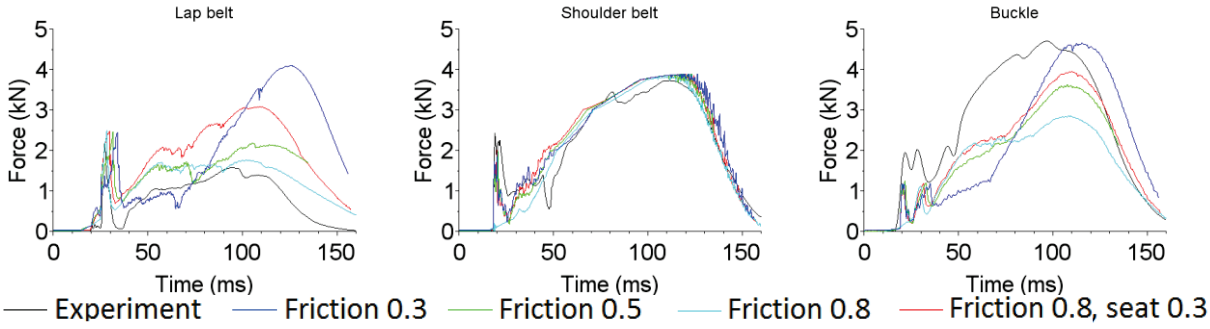


*Figure 119: Belt forces of the MS743 sled simulation with different friction for belt and seat, using the C315 material. Left: force at the left anchor of the lap belt. Middle: force at the shoulder belt anchor. Right: force at the belt buckle. Friction coefficient are the same for all belts and seat, except for the red curves, which use 0.8 for the belts and 0.3 for the seat.*

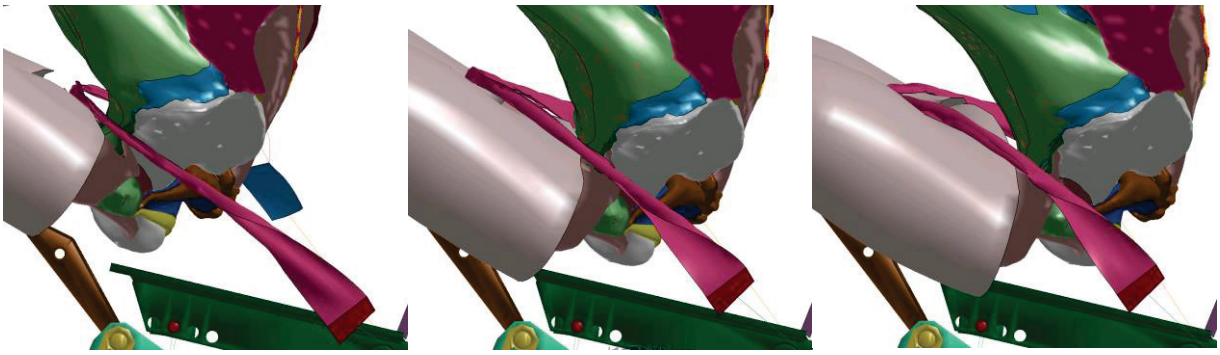

*Figure 120: Comparison of sled simulation with friction 0.3 belt / 0.3 seat (left), 0.8 belt / 0.3 seat (middle) and 0.8 belt / 0.8 seat (right), all with the C315 material at time 130 ms, i.e. time of peak force of the simulation with friction 0.3. Several parts of the models were removed to make pelvis visible (white surface).*

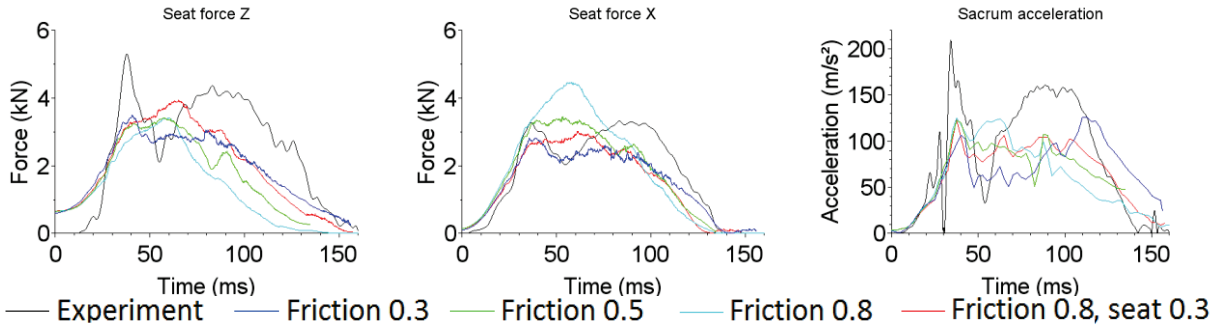


*Figure 121: Seat forces (X on the right, Z in the middle) and sacrum acceleration (right) during the MS743 sled simulation using the C315 material. The seat force is a summed over the seat pan and the anti-submarining guard. The simulation is preceded by a pre-load phase during which gravity acts on the model (Section 6.2.3) which is why the Z force is non-zero at time 0.*

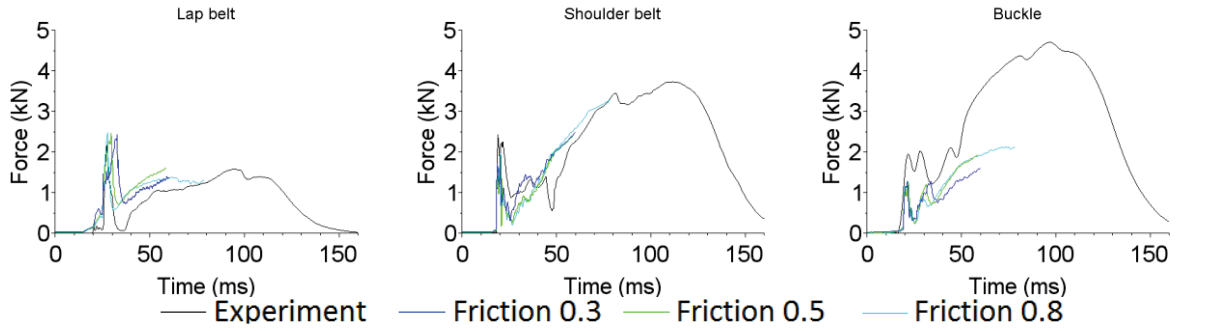


*Figure 122: Belt forces of the MS743 sled simulation with different friction for belt and seat, using the X1 material. Left: force at the left anchor of the lap belt. Middle: force at the shoulder belt anchor. Right: force at the belt buckle. All simulations terminated early due to negative volume elements.*

Finally, in order to see whether some of the effects of friction would still be present for a larger loading, the loading pulse used for the MS742 experiment was tested on the MS743 sled setup. Figure 123

shows the frontal view from two simulations with this pulse, 0.8 / 0.8 and 0.3 / 0.3 (both with the C315 material). Similarly to the lower pulse, the belt slips into the fold with the 0.3 friction, but does not with the 0.8.

The side view (Figure 124) reveals large excursion of the body. Footage from the MS742 experiment is added for comparison: while it is a different PMHS than the one used for personalizing the model and their stature different by 8 cm (153 cm and 161 cm), their mass was almost the same (100 kg and 101 kg), therefore some basic comparison can be made. While the excursion in the experiment was large as well, the PMHS stayed on the seat pan. The excursion in the 0.8 / 0.8 simulation seems similar to the one of the PMHS MS742, while in the 0.3 / 0.3 simulation the model slides off the seat pan completely. Details from the simulations with the pelvis shown is in Figure 125. Similarly to the lower pulse case, with the 0.3 friction the belt is close to the pelvis, while in the 0.8 case it can be seen compressing other soft tissues including the thighs as visible in the figure.

Finally, the corresponding belt forces are shown in Figure 126. Similarly to the pulse MS743, friction affected the lap belt force. The simulation with friction 0.3 terminated before reaching the peak, but at the time of termination it was already 1.5 kN higher than the peak for the 0.8 friction. This is similar to the differences observed in the simulations with the MS743 pulse in terms of absolute values, but this means it is smaller in terms of percentage as the magnitude is larger. Even higher difference (4 kN) is visible on the buckle force. The forces of the MS742 experiment are shown for reference. The belt force response of the 0.3 / 0.3 simulation is closer to the experiment in terms of timing and magnitude, although the premature termination prevents further analysis. The shoulder force is close to the experiment and unaffected by the friction.

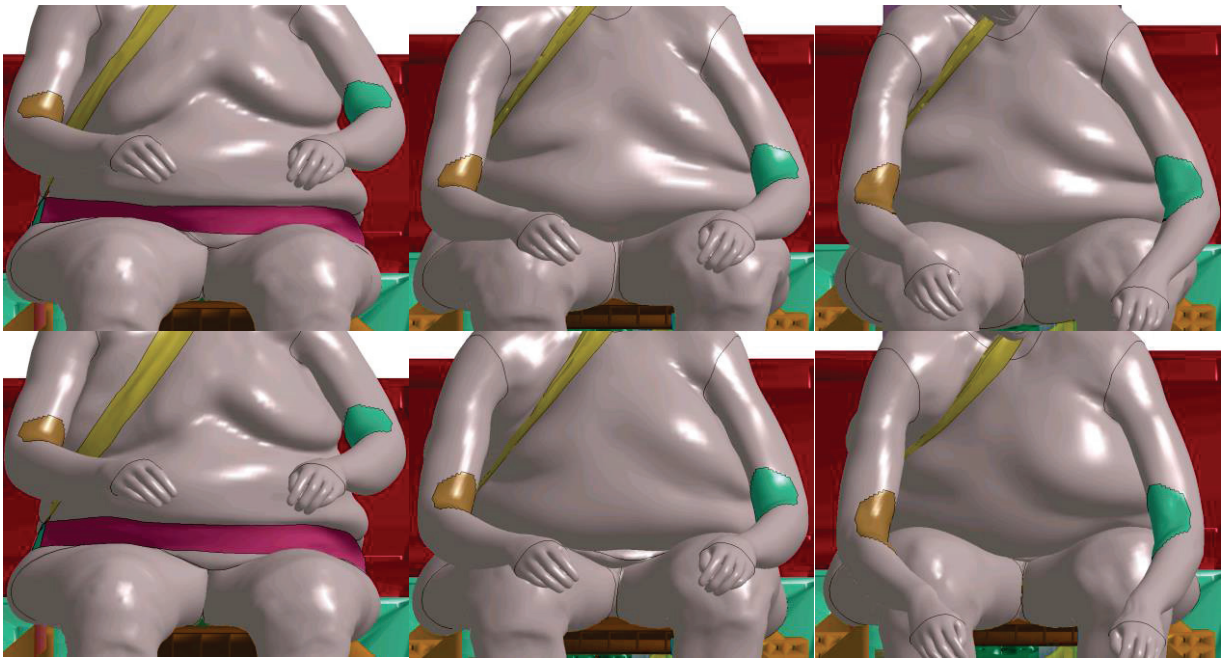

*Figure 123: Frontal view of the MS743 sled simulation using the faster loading pulse (from MS742 sled test) at 30 ms (left), 60 ms (middle) and 75 ms (right). First row: friction 0.3 / 0.3. Second row: friction 0.8 / 0.8 C315 material was used in both cases.*

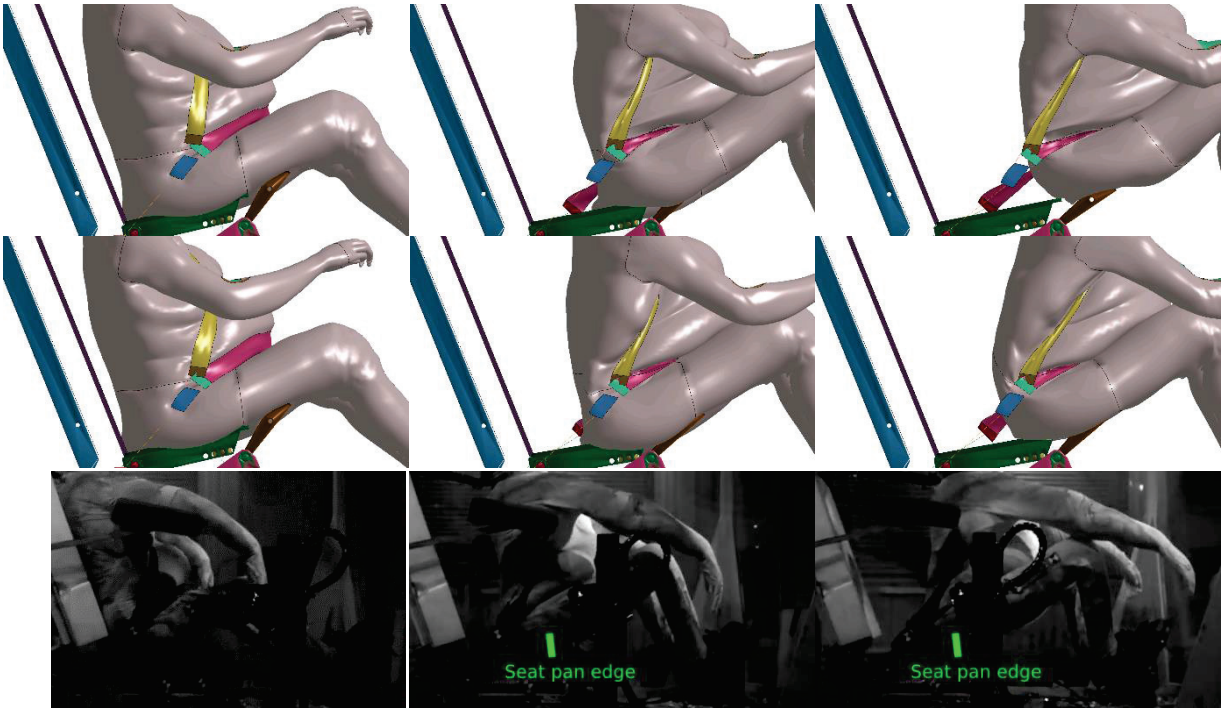


*Figure 124: Side view of the MS743 sled simulation using the faster loading pulse (from MS742 sled test) at 30 ms (left), 60 ms (middle) and 75 ms (right). First row: friction 0.3 / 0.3. Second row: friction 0.8 / 0.8 C315 material was used in both cases. Third row shows footage from the MS742 experiment. The edge of the seat pan is marked in green on the 60 ms and 75 ms images.*

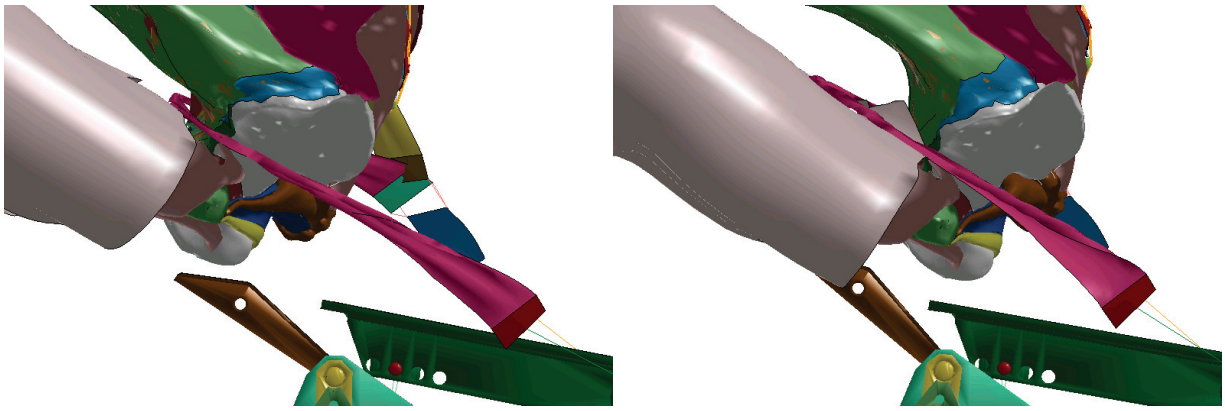

*Figure 125: Details of the MS743 sled simulation using the MS742 pulse. Left: friction 0.3 on seat and belt. Right: friction 0.8 on seat and belt. The C315 material was used in both cases. Captured at time 75 ms (the 0.3 simulation terminated afterwards due to negative volume elements). Several parts of the models were removed to make pelvis visible (white surface).*

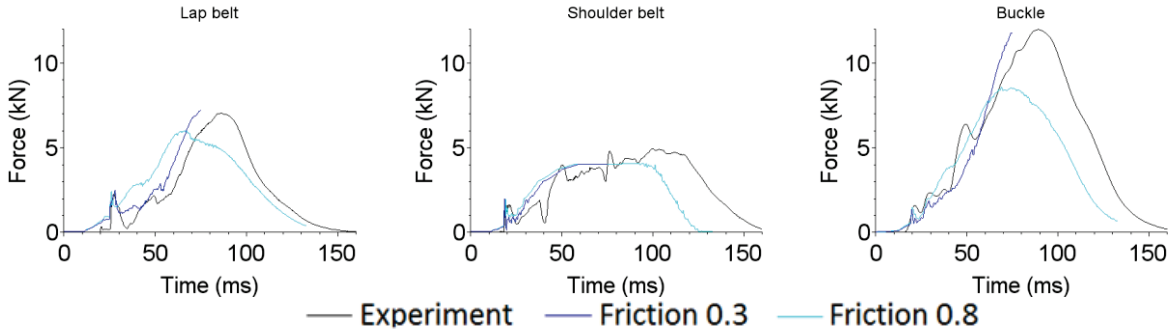


*Figure 126: Belt forces of the MS743 sled simulation using MS742 loading pulse, C315 material and friction 0.3 / 0.3 (belt / seat) and 0.8 / 0.8. The MS742 experiment is used as reference (black curves). Left: force at the left anchor of the lap belt. Middle: force at the shoulder belt anchor. Right: force at the belt buckle.*

#### 6.3.2.2. Model without fold

Three simulations were also performed with the noFold model. Figure 127 and Figure 128 show the side and frontal views, respectively, of the simulations with friction coefficients 0.3 / 0.3 and 0.8 / 0.8, both with the C315 material. The third simulation used the X1 (friction 0.8 / 0.8), but terminated after only 60 ms which is too early to analyse the response. Compared to the complete model, the frontal excursion of the pelvis is only 8 mm higher for the noFold model in the 0.8 / 0.8 case (at the 90 ms mark), but 57 mm lower in the 0.3 / 0.3 case. These excursions are illustrated on Figure 129.

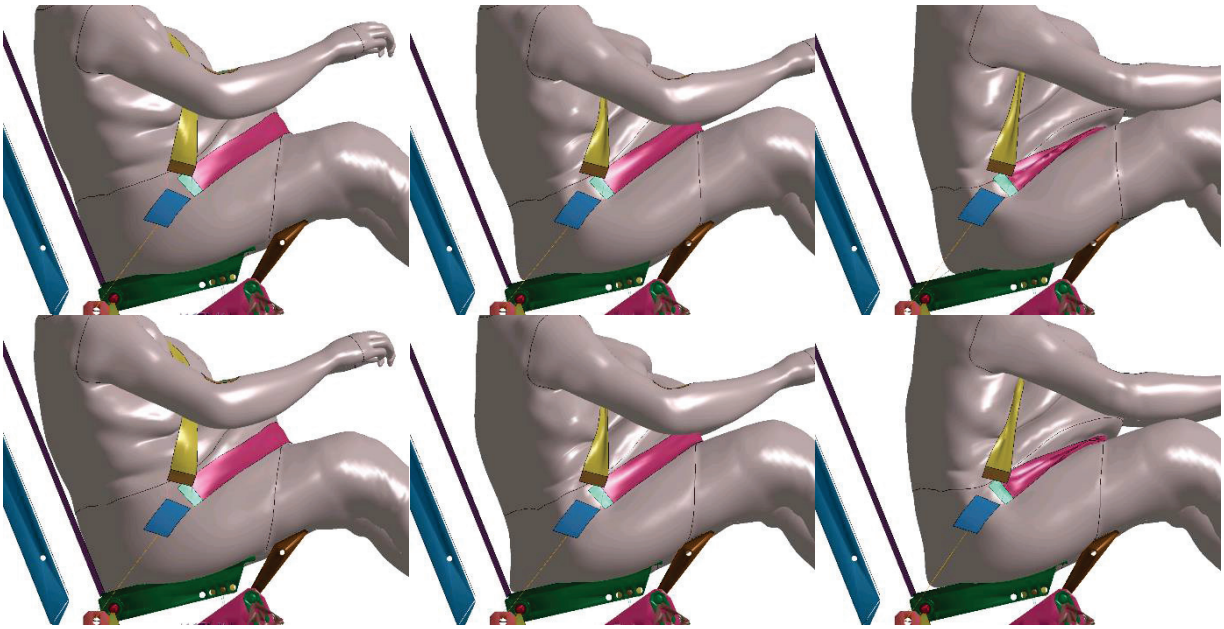

*Figure 127: Side view of the MS743 sled simulation at 30 ms (left), 60 ms (middle) and 90 ms (right) using the noFold model. First row shows a simulation with friction 0.3, second row with friction 0.8, both with the C315 material.*

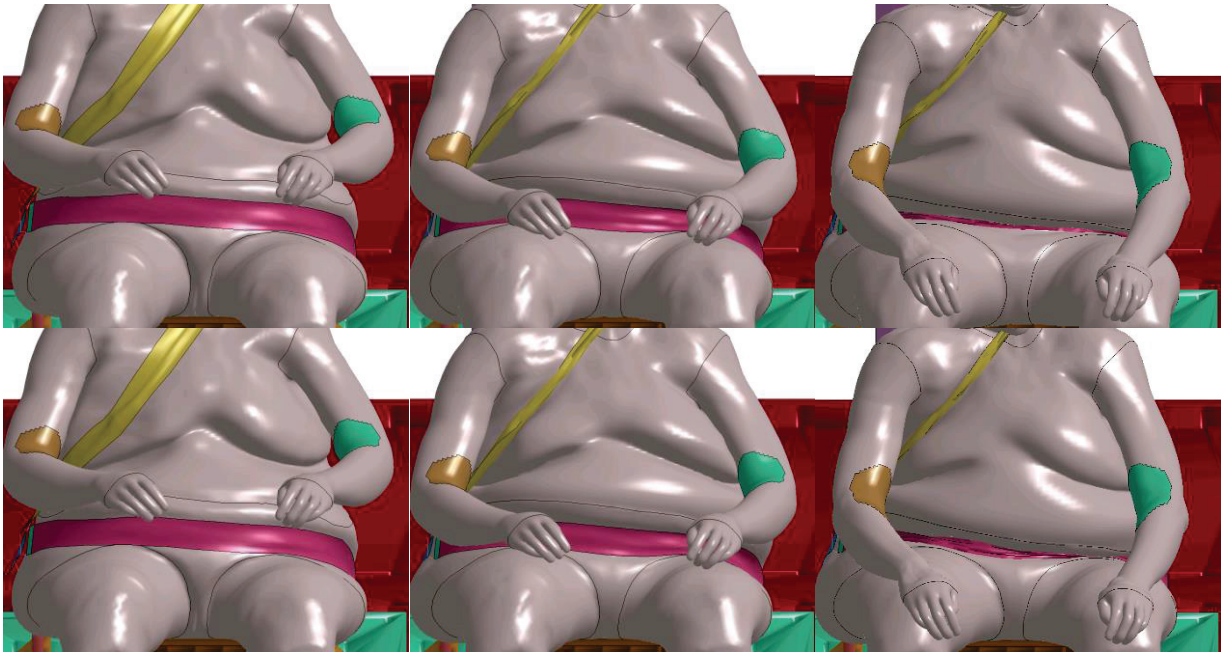

*Figure 128: Frontal view of the MS743 sled simulation at 30 ms (left), 60 ms (middle) and 90 ms (right) using the noFold model. First row shows a simulation with friction 0.3, second row with friction 0.8, both with the C315 material.*

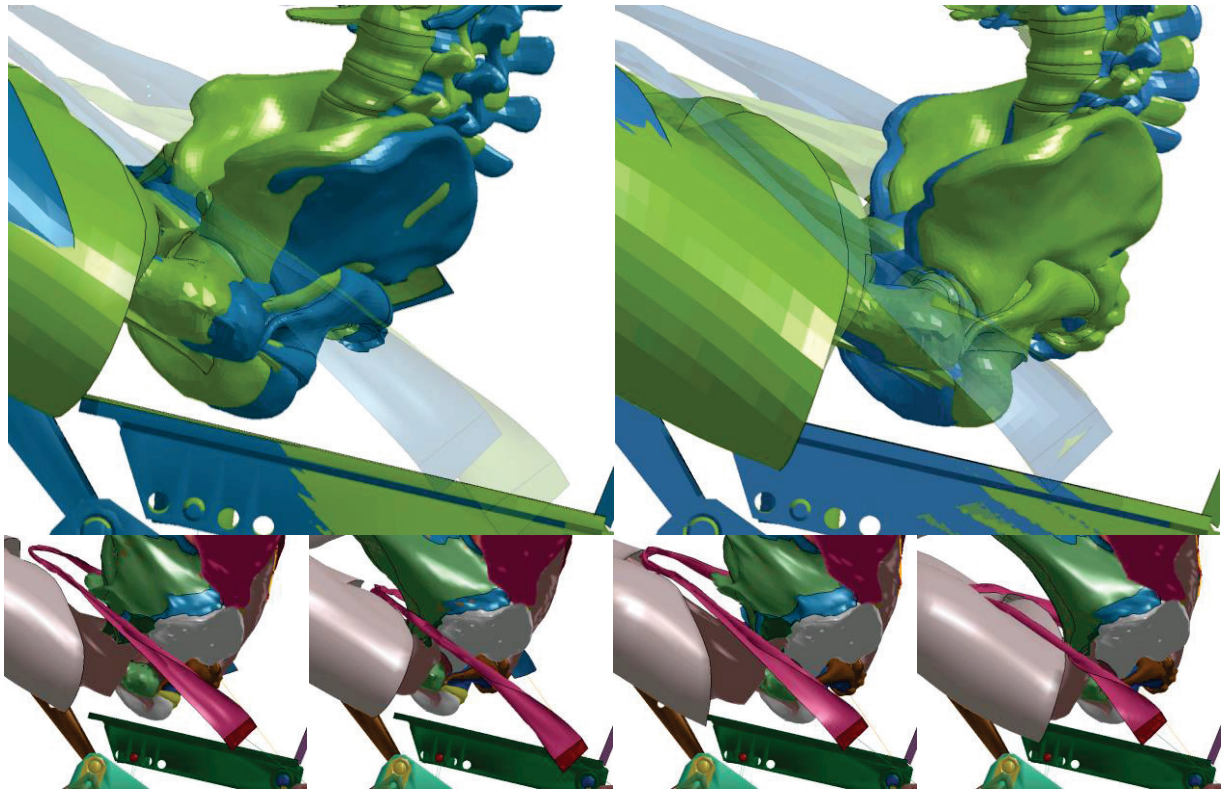

*Figure 129: Top: overlap of the simulation with complete (green) and noFold (blue) model of the MS743 sled at 90 ms. Left: friction 0.3 / 0.3. Right: friction 0.8 / 0.8. The lap belt is shown as partially transparent. Bottom: the same view but without overlapping to more clearly show the belt position, first two images show the 0.3 / 0.3 friction case (left: noFold, right: complete), the third and fourth image the 0.8 / 0.8 friction (left: noFold, right: complete).*

While, the pelvis excursion can be described as very similar for both model types (as it is constrained by the seat), the belt locations are very different for the two models: it is higher and more away from the pelvis for the noFold but it did not slip up the body. A minor rotation of the pelvis can also be observed in the 0.3 / 0.3 case (Figure 129), caused by the different belt positions. Compared to the complete models, the lap belt force in the 0.3 / 0.3 case has a lower peak and rises immediately after the pretensioning phase (Figure 130). This is due to the belt restraining the body immediately, without slipping into the abdominal fold as it does in the complete model. Still compared to the complete model, the force is higher in the 0.8 / 0.8 case at the beginning of the simulation (by approximately 0.5 kN) and further away from the experimental result, but later drops to a similar value just before the simulation terminated after 92.5 ms.

The simulation with the MS742 pulse was also attempted, but terminated after only 53 ms due to negative volume elements, which does not allow analysing the response.

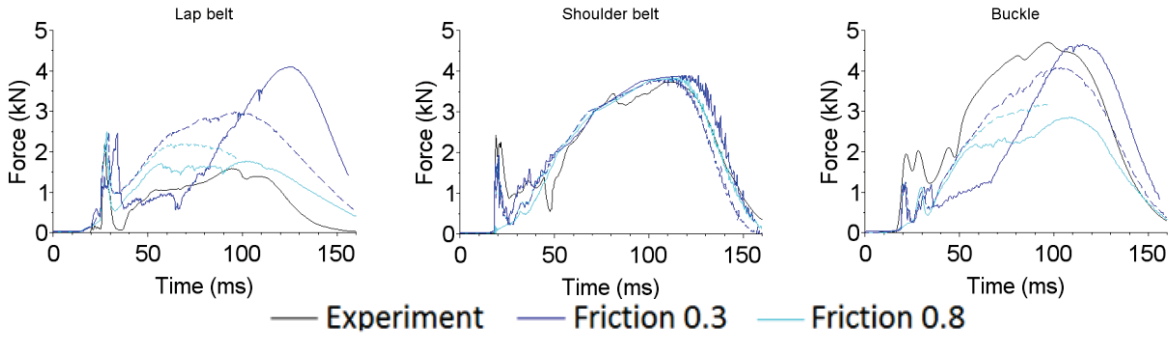


*Figure 130: Comparison of belt forces of the MS743 sled simulation with between the complete model (solid line) and the noFold model (dashed line). The C315 material was used for all simulations. Left: force at the left anchor of the lap belt. Middle: force at the shoulder belt anchor. Right: force at the belt buckle.*

## 6.4. Discussion and conclusions

The morphed models were subjected to a number of simulations, focusing mainly on the impact of a more precise representation the abdominal fold and the subcutaneous fat thickness as to our knowledge those were not accounted for in models used in previous work. To achieve that, three types of models with differing levels of detail (regarding use of those additional targets) were used and compared.

After a short study of material properties for representing adipose tissues, two were selected and compared in simulations. Both are significantly softer than the ones used in the original model, and they allowed approaching the PMHS response. The softer material (X1) was in most cases closest to the experimental values, but also more unstable in the simulations (negative volume). Softening them further may be challenging with the current modelling approach and would require further investigation. It is also possible that the adipose tissue material is already soft enough and that other components in the model need adjustments. Specifically, hollow organ modelling may need to be reconsidered as it may be adequate for a low volume of hollow organs as in the M50-O but not for the morphed models. In general, experimental data collected in full body tests (looking at abdominal wall thickness during compression), isolated abdominal wall testing or material sample testing at large compression would be useful.

The effect of the properties seemed less important during the sled. Although the softer X1 material showed slightly closer response in terms of lap belt force, the same deformation patterns were achieved with the C315. The instability of the X1 was even more pronounced in the sled test which prevented further comparison of the two materials.

Regarding deformation patterns of the abdomen, PMHS experiments showed that the abdominal fold tends to “open” when the belt is placed over the abdomen, whether in the “parallel belt” or “high belt” configurations. The simulations with those belt configurations showed a similar behaviour, which suggests the morphed models are suitable for capturing the mechanical behaviour of the abdomen.

With that in mind, the behaviour of the abdomen was analysed in more details using the belt test simulations. The presence of the fold led to very different kinematics interactions in belt tests. In most cases, the models without the fold led to significantly higher forces, compared to both the experiment and the models with fold. These may be due to tensile contributions of the tissues in the regions of the fold. In addition, the parallel belt configuration was more prone to slipping up the trunk of the model, which then turns into limited restraint, small forces and erroneous loading path. The noFold also imposes a belt position away from the pelvis, for which the forces would be very low if the fold was there as the belt would slide into it. This was apparent when comparing the noFold and complete models in the sled simulation using low belt friction (0.3): the belt slipped into the abdominal fold in the case of the complete model, leading to low force during the slipping phase and than large, steep peak once the belt engaged the pelvis. In the noFold case, the belt acted on the model from the beginning, leading to a significantly different force response. Altogether, this makes the models without fold less reliable.

Using the additional morphing target for subcutaneous fat affected the belt forces to a different degree in each configuration. Nevertheless, the force was consistently higher with the foldOnly models for all tests with the C315 material. With the X1, the differences were negligible, suggesting that with the softer material, other parts, such as hollow organs, have predominant effect on the response.

Friction was not quantified during the experiments, but it turned out to be more important than originally expected. With low friction (0.1), belt was prone to slipping in many configurations. After a brief literature review and testing in simulations, the value 0.3 was determined as minimal reliable value. Still, 0.3 was not sufficient for a few of the belt tests in which partial slippage occurred and for the sled test with MS743 in which the lap belt slipped inside the abdominal fold and the shoulder belt slipped to the side. A friction of 0.8 yielded more satisfactory results in terms of deformation patterns and belt forces (except at the buckle). The belt tests were performed with the belt in contact with dry skin, while during the sled tests the PMHS were clothed and may have been wet (as suggested by the stains on the photos). This could explain the need for different coefficients for the two setups and 0.8 could still be within the literature range for some skin conditions. However, the realism of the friction modelling using default contacts options for friction is unclear. Local deformation of the tissues at the

edge of the belt for example may increase the apparent friction by creating a small ridge. This cannot be easily captured due to the model element size. The fact that the softer properties seemed less prone to slippage, perhaps due to more deformation at the belt edge, could be consistent with that. This could be investigated numerically with a detailed model of the interaction. More generally, should similar experiments be repeated, measuring or estimating the friction would likely help.

Similarly, friction between the model and the seat was also an important parameter. In fact, the differences in lap belt force were higher between 0.8 / 0.3 and 0.8 / 0.8 simulation (belt friction / seat friction), than between 0.8 / 0.3 and 0.3 / 0.3. Although measuring it would be useful as well, some aspects of the interactions with the seat may not be related to friction and were not captured (e.g. vertical force peak). The reason, which is unclear at this time, should be investigated.

A minor limitation of how the fold was represented was the presence of an unnaturally large gap inside the fold in the belt test. This gap was created on purpose using foam on the CT to make sure it can be distinguished. The displacement of the centre of the belt was affected by this at the beginning of the simulations as the fold was first “closed” by the compression, but this was not considered a large issue as the overall behaviour was close to the experiment. This motivated the application of gravity to the model to close it for the sled test. In hindsight, the gravity could have also been applied to the models before performing the belt test simulations.

A related issue was the shape of the bottom of the model (buttocks and thighs). The targets were modelled to reflect the shape of the source M50-O model, i.e. with round legs, not flattened by a seat. This required another deformation by simulation to reduce that thickness as preliminary simulation showed that a large thickness was affecting the interaction with the seat.

More generally, the general issue of the initial state of such models applies, and may be even more important considering the amount of soft tissues: the morphing target was captured under gravity, but the strain and stress state of the tissues was unknown. Applying gravity again would deform the model and not applying gravity may reduce the coupling with the seat pan. Gravity was only applied for 30 ms to initiate the coupling but this could be further investigated.

In conclusion, the setup preparation requirements and the restraint mechanisms, including the balance between the seat and the lap belt, now seem better understood. The type of belt interaction (sliding or not, etc.) can lead to very different responses in the sled, almost like a bifurcation. While it was not possible due to time constraint, it would be interesting to verify these findings by simulating the sled with the MS742 PMHS as well as the sleds with the foldOnly and noFold models.

# 7. General discussion

## 7.1. Evaluation of the improved morphing methodology

A complete pipeline to generate obese HBM was presented: from the collection of PMHS to use as target, through their processing and registration of the geometry, up to the final morphing. In most previous studies, only a smoothed skin (without fold) and the skeleton were used as morphing targets. In this thesis, a refined skin and a subcutaneous target were used to further personalize the abdominal region.

A specific registration method was used for each of the morphing targets: a mesh-to-image registration for skeleton, mesh-to-mesh ICP-like non-rigid registration for skin and a manual mesh-to-mesh registration for the subcutaneous fat. A custom registration method was implemented in PIPER for the skin registration, while the other registrations were performed using third party software.

The registration of surfaces to use as morphing targets has proven to be a complex problem. The quality of the registration subsequently used to morph has a direct effect on the element quality of morphed FE models. Specifically, preferred correspondence is as perpendicular as possible to the source surface in order to avoid shearing of the FE elements degrading their quality. The manual registration provides a high quality by managing shearing through iterative manual corrections. However, it is very time consuming and impractical for all but very simple targets. The iterative method used for skin registration is based on surface descriptors and matches points with similar curvature and distance. However, the curvature around the abdominal fold is very different from the part of the source surface that is expected to be registered to it: the source is flat while the target is very curved. The curvature part of the descriptors then contributes little to the vertex matching in those areas, limiting the accuracy of the method. The implemented method used only a simple deformation model, but even with a more complex one, e.g. based on the as-rigid-as-possible models (Sorkine and Alexa 2007), the matching will remain less efficient. A mechanism for defining landmarks for the registration to force the matching of certain points was implemented as well: automatizing the requirement for “perpendicular” registration for the fold registration should alleviate the aforementioned problem. The registration method could enable sliding if underlying solid parts are connected by contacts and the transformation field from morphing can deal with discontinuous field as for extended FE.

The mesh-to-image registration used for skeleton led to satisfactory results. Improving the user interfaces of the current tools would increase work efficiency, but even the experimental Anatoreg software was a valuable tool. Note that using it for registration of the skin is theoretically possible

(although some adaptations of the software would be necessary). If such registration would have comparable quality to the mesh-to-mesh method, it would likely be preferable as having more homogenized workflows could lower the time needed for the registration.

However, in the end, none of these methods accounts for the element quality that will result from the morphing. This makes them lack robustness for the application (e.g. near the fold) and requires many correction steps. A different approach to improve both the efficiency and the quality of the registration would be to couple the registration and the morphing in a single automated iterative optimization process. As noted above, the "quality" of the registration affects the FE element quality of the morphing it is used for. That suggest that the FE element quality could be considered either as a constraint or as a quantity to optimize. A general draft of the algorithm could be as follows:

1. Set initial constraints for registration.
2. Register the source to the target surface using the non-rigid mesh-to-mesh registration under the specified constraints.
3. Perform morphing by kriging using the registered surfaces as source and target.
4. Measure and store element quality.
5. Compare the current element quality with element quality from previous iteration.
6. Modify the constraints based on the results of the comparison. For example, if the model was not improved by the last modification, return to the previous set of constraints, if it was, keep the current constraints and modify them in some way or add new ones.
7. Repeat 2-6 until the quality stops improving.

The constraints could for example be landmarks prescribing registration of several chosen vertices. The key issue to solve is the design of the step 6, i.e. how to modify the set of constraints such that the process will converge and will lead to optimal result. The experience gained from the semi-automated processes (looking at element quality issues and changing the registration) could be useful here to guide the constraint modification and limit the number of steps required. On the implementation side, the registration and morphing tools would have to be interconnected in order to allow fully automated processing. Since PIPER already has a library to compute FE element quality metrics, a fully functioning kriging module and the basic registration implementation created for this thesis, it would be a good platform for implementing the optimization process. Furthermore, to avoid excess computational time, the method should allow specifying an area of interest (e.g. abdomen) and let the optimization be performed only based on this area rather than the entire model.

Regarding the morphing itself, an improved spatial subdivision algorithm for kriging has been presented. It has been proven to allow using hundreds of thousands control points and theoretically is capable of even larger numbers. This is a significant improvement over previous methods that had practical limit of several tens of thousands control points because it allows introducing arbitrary details without limitation or need for planning. By smoothing the deformation field in overlapping regions of the subdivision, it can create FE models with satisfactory element quality. Further improvements to handle the overlaps more efficiently are likely possible, but even with the presented algorithms the computational time of tens of minutes is very low considering that the alternative is hours of FE simulation.

Limitation of both of the methods presented for maintaining continuity in the overlap regions is that all nodes in the overlapped region are treated equally. As a result, the boundary of the overlapping regions can still have minor discontinuities. An improvement could possibly be reached by introducing blending weights for each point in the overlap region, based on the distance of the point to the subdivision cell boundary, similarly to Auñón and Gómez-Hernández (2000). This should make the deformation field change more gradually and lead to smoother results.

However, the morphing towards severely obese targets has also revealed some limits of the morphing by kriging. While the M50-O model could be morphed towards the MS730, i.e. the least obese of the used PMHS, attempts to morph toward the MS742 and MS743 were not successful without partial remeshing. Deformation imposed by the abdominal fold was too large for those targets as the abdomen is flat in the source model. The elements around the folded area then always ended up warping, even with large nuggets. Model specific solutions for enforcing the fold during the morphing process could be designed, but the aim of the thesis was to create model agnostic methods and the resulting elements would be of poor quality in a region where large strains were expected. One can consider that the limits of the morphing approach are reached at that point. A more generic solution would be to create at least one model that already has the abdomen “foldable”. Morphing could then still be used on this model for a large variety of degrees of obesity. However, the magnitude of body shape changes that was attained is already very large considering possible variations of human anatomy. Improvements in different directions (e.g. introducing sliding between structures during morphing to break the continuity of the deformation on purpose) may be considered for future research over incremental improvements.

Similarly, for the subcutaneous fat target, the direct morphing failed due to large differences in the amount of fat between the source model and the target. The target could only be approached with

some violation near the pelvis. In general, algorithms simulating gradual fat growth around the skeleton may be more suitable for this type of changes. The introduction of automatic local remeshing with tetrahedral elements could also be considered to alleviate some of the issues at hand.

All these improvements could speed up the process, increase repeatability by decreasing the dependence on the user, make it accessible to less experienced users and further improve the element quality.

## 7.2. Model response vs. experimental results

The behaviour of the abdomen was studied by a series of belt loading tests. In belt configurations with the belt placed over the abdomen, i.e. the “parallel” and “high” position, a distinct opening of the gap between abdomen and thighs was observed in all tests. The simulation with models with abdominal fold successfully recreated this. Although this behaviour could be expected, it is the first time it was documented and reproduced, which served as a preparation step for the sled simulations.

Friction was found to have large impact on the kinematics. Even with a 0.3 friction value (plausible but larger than previously used in these simulations), belt slippage occurred in some tests with the models without abdominal fold. In the sled test with MS743, low friction led to the lap belt slipping inside the abdominal fold and the shoulder belt slipping off the side of the body, which was not observed in the experiment. Furthermore, friction between the seat and the body in the sled test had a similar importance for the forward excursion of the body. Increasing the friction (up to 0.8) led to kinematics closer to some of the experiments. This parameter should be further investigated both numerically (to understand if it is an artefact from the friction modelling, element size and local deformation pattern) and experimentally (to gather actual coefficient estimates and account for the effect of actual clothing that would be worn in vehicles). In the end, it may also be possible that friction plays a role that is different for obese, with large thickness of very soft tissues that can shear, compared to thinner subjects.

Material properties of adipose tissues were briefly investigated. While their use in thinner models where they likely contribute less to the response does not seem to be problematic, the material used in the current version (5.1) of the M50-O created issues for obese modelling. One of the specific issue of the current materials is that they are likely unrealistic for large strains, both in tension and in compression, partially due to the lack of experimental studies. Two new material curves were tested, created based on the available literature and different assumptions. Although they were deemed acceptable to move forward with the simulations and that they allowed approaching some of the

experimental responses, research dedicated to that problem and the simulation of the fat at large strains is much needed. The numerical stability of the response should be considered as well, as subjecting very soft material to very strenuous loading can lead to very large strains and numerical issues, as observed with the softest material properties tested (X1). While refinements could be considered (e.g. adaptive meshing), it is also to be remembered that the compressive response of fat is mainly of interest because it transfers loads to other structures, but it is not a structure of interest for injury in itself. The modelling of the hollow organs and intraperitoneal fat should also be investigated as their volume and mass increase in obese subjects is considerable. Modelling method approaches tested for ongoing development on the GHBMC baseline (e.g. using fluid modelling or smaller bags) could be tested. However, experimental data on this issue if very scarce, for both obese and non-obese.

As noted above, different behaviours were observed based on the belt placement and the friction settings. With some generalization, two types of loading can be distinguished: one where the belt compresses the abdomen (high and parallel belt tests, sled with high friction) and one where the belt is in the abdominal fold and loads predominantly the pelvis (belt inside tests, sled with slipping lap belt). Each could bring different injury risks.

In the first case, the important question is whether the load applied on the abdomen will be absorbed mostly by the fat tissues, or if it will load the abdominal organs. In the tested sled scenario, the belt remains on the lower abdomen and still seems to load the pelvis, while the internal organs do not seem to be under excess load. That is good from the safety perspective, but the excursion can still be large due to the softness of the tissues, leading to knee bolster contact or even a drop over the anterior edge of the seat pan.

In the “belt inside” configuration, the soft tissue compression is minimal and the load is quickly applied on the pelvis. This is an ideal scenario as it prevents both the possible abdominal organ injury as well as the excess forward excursion. If it slides in the gap (sled test MS742, simulations with low friction), the duration of the sliding phase is long for severely obese bodies as the MS743 and cannot be compensated by the standard belt pretensioners. The body is not restrained by the lap belt at all during this phase, which leads to large excursion followed by a steep rise of lap belt force once the belt finally reaches the pelvis. As the pelvic fractures in the MS742 sled experiment showed, this could on itself be critical considering the body mass to stop, at least for osteoporotic occupants. In a vehicle, the occupant is perhaps more likely to collide with the knee bolster or the instrument panel before the

belt reaches the pelvis in the front seat, although the edge of the seat might be reached on the rear seat (i.e. without knee bolsters).

Submarining was not observed in the tests or simulations. Although this was not quantified, in the cases where the belt is in or near the fold, the large amount of fat tissue above the belt might actually be helping in preventing the belt from travelling to upper regions of the abdomen (as friction would). However, the PMHS did not reach the edges of the seat as in Kent et al. (2010).

As one can see, most of the tested and simulated configurations increase the injury risk for the obese vehicle occupants in some way (compared to non-obese). The models presented in this thesis, or similar ones created using the developed methodology, can help in establishing what the correct belt placement configuration should be or improve the design of the restrain systems. Based on the simulations performed so far, configurations similar to the "belt inside" could be preferable as they limit the excursion and loading of the soft tissues and organs while quickly coupling the pelvis to the vehicle. However, as already stated, a following issue is that such configurations might currently not be commonly used in practice by the occupants. The volunteer study of Reed et al. (2012) showed that there was a strong correlation of volunteer BMI with distance of the lap belt from pelvis, which suggests the more common belt placement is one with belt over the abdomen. Comfort of the occupant might play a significant role in what placement they choose to use. Also, some types of clothing may prevent, or make it uncomfortable, to fit the belt tightly into the gap of the abdominal fold. A study of the comfort of various belt configurations with obese volunteers could perhaps help in designing modifications of the restraint systems to promote the correct belt placement. Regarding restraint systems, further investigations would be needed but, should the belt slide in the abdominal fold, as much slack as possible should be removed to load the pelvis as early as possible to minimize the excursion. Pretensioners with higher range of motion than those used in the current study may help for that.

Together, these observations suggest that representing the abdominal fold in obese HBM, which was new in the current study, is important to correctly simulate deformation modes that significantly affect the occupant restraint in vehicle. Further paired comparisons with the models without abdominal fold, which are examples of how the obese occupants were represented in obese models until now, could be done to illustrate this point. In the meantime, it is hoped that some of the results presented in this thesis can already be helpful to foster improvements in automotive safety.

# Bibliography


Adomeit, D., and A. Heger. 1975. “Motion Sequence Criteria and Design Proposals for Restraint Devices in Order to Avoid Unfavorable Biomechanic Conditions and Submarining.” In *SAE Technical Paper*. SAE International. https://doi.org/10.4271/751146.

Alkhouli, N., J. Mansfield, E. Green, J. Bell, B. Knight, N. Liversedge, J.C. Tham, et al. 2013. “The Mechanical Properties of Human Adipose Tissues and Their Relationships to the Structure and Composition of the Extracellular Matrix.” *American Journal of Physiology-Endocrinology and Metabolism* 305 (12): E1427–35. https://doi.org/10.1152/ajpendo.00111.2013.

Allen, B., B. Curless, and Z. Popovic. 2003. “The Space of Human Body Shapes: Reconstruction and Parameterization from Range Scans.” *ACM Trans. Graph.* 22 (July): 587–94. https://doi.org/10.1145/1201775.882311.

Arbabi, S., W.L. Wahl, M.R. Hemmila, C. Kohoyda-Inglis, P.A. Taheri, and S.C. Wang. 2003. “The Cushion Effect.” *Journal of Trauma and Acute Care Surgery* 54 (6): 1090–1093.

Arun, M.W., J.R. Humm, N. Yoganandan, and F.A. Pintar. 2015. “Biofidelity Evaluation of a Restrained Whole Body Finite Element Model under Frontal Impact Using Kinematics Data from PMHS Sled Tests.” In *Ircobi Conference Proceedings*. Vol. 15–69. Lyon, France.

Ashwell, M., P. Gunn, and S. Gibson. 2011. “Waist-to-Height Ratio Is a Better Screening Tool than Waist Circumference and BMI for Adult Cardiometabolic Risk Factors: Systematic Review and Meta-Analysis.” *Obesity Reviews : An Official Journal of the International Association for the Study of Obesity* 13: 275–86.

Auñón, J., and J.J. Gómez-Hernández. 2000. “Dual Kriging with Local Neighborhoods: Application to the Representation of Surfaces.” *Mathematical Geology* 32 (1): 69–85. https://doi.org/10.1023/A:1007554801750.

Baiker, M., J. Milles, A.M. Vossepoel, I. Que, E.L. Kaijzel, C.W.G.M. Lowik, J.H.C. Reiber, J. Dijkstra, and B.P.F. Lelieveldt. 2007. “FULLY AUTOMATED WHOLE-BODY REGISTRATION IN MICE USING AN ARTICULATED SKELETON ATLAS.” In *2007 4th IEEE International Symposium on Biomedical Imaging: From Nano to Macro*, 728–31.

Barker, J.B., D.S. Cronin, and R.W. Nightingale. 2017. “Lower Cervical Spine Motion Segment Computational Model Validation: Kinematic and Kinetic Response for Quasi-Static and Dynamic Loading.” *Journal of Biomechanical Engineering* 139 (6). https://doi.org/10.1115/1.4036464.

Baxter, B.J.C. 1992. *The Interpolation Theory of Radial Basis Functions*. University of Cambridge Department of Applied Mathematics and Theoretical Physics: University of Cambridge. https://arxiv.org/abs/1006.2443.

Beillas, P., and F. Berthet. 2017. “An Investigation of Human Body Model Morphing for the Assessment of Abdomen Responses to Impact against a Population of Test Subjects.” *Traffic Injury Prevention* 18 (sup1): S142–47. https://doi.org/10.1080/15389588.2017.1307971.

Beillas, P., and F. Berthet. 2018. “Effect of Contact Separation on the Abdominal Response to Impact of a Human Body Model.” In *Stapp Car Crash Conference, Short Communication 4*.

Bellal, J., S. Hadeed, A.A. Haider, M. Ditillo, A. Joseph, V. Pandit, N. Kulvatunyou, A. Tang, R. Latifi, and P. Rhee. 2017. “Obesity and Trauma Mortality: Sizing up the Risks in Motor Vehicle Crashes.” *Obesity Research & Clinical Practice* 11 (1): 72–78. https://doi.org/10.1016/j.orcp.2016.03.003.

Besl, P.J., and N.D. McKay. 1992. “A Method for Registration of 3-D Shapes.” *IEEE Transactions on Pattern Analysis and Machine Intelligence* 14 (2): 239–56. https://doi.org/10.1109/34.121791.

Bhatti, J.A., A.B. Nathens, and D.A. Redelmeier. 2016. “Driver’s Obesity and Road Crash Risks in the United States.” *Traffic Injury Prevention* 17 (6): 604–9. https://doi.org/10.1080/15389588.2015.1134793.

Bhoi, S.B., R.A. Kamle, S.K. Meshram, S.A. Waghmare, and K.B. Shirsat. 2017. “Study of Correlation of Organ and Body Weight during Autopsy with Regard to Age and Sex in Adult Population at Solapur Region.” *Indian Journal of Forensic and Community Medicine* 4 (2): 115–20.

Boulanger, B.R., D. Milzman, K. Mitchell, and A. Rodriguez. 1992. “Body Habitus as a Predictor of Injury Pattern after Blunt Trauma.” *The Journal of Trauma* 33 (2): 228–32.

Bradley, J.R., N. Cressie, and T. Shi. 2016. “A Comparison of Spatial Predictors When Datasets Could Be Very Large.” *Statist. Surv.* 10: 100–131. https://doi.org/10.1214/16-SS115.

Cavanaugh, J.M., G.W. Nyquist, S.J. Goldberg, and A.I. King. 1986. “Lower Abdominal Tolerance and Response.” In *SAE Technical Paper*. SAE International. https://doi.org/10.4271/861878.

Chirachariyavej, T., K. Ouyswat, S. Sanggarnjanavanich, M. Tiensuwan, V. Peonim, and V. Sirikulchayanonta. 2006. “Normal Internal Organ Weight of Thai Adults Correlated to Body Length and Body Weight.” *Journal of the Medical Association of Thailand = Chotmaihet Thangphaet* 89 (10): 1702–12.

Combest, J.J. 2018. “CURRENT STATUS AND FUTURE PLANS OF THE GHBMC.” Presented at the 7thInternational Symposium:Human Modeling and Simulation in Automotive Engineering, Berlin, Germany, October 18.

Comley, K., and N. Fleck. 2012. “The Compressive Response of Porcine Adipose Tissue from Low to High Strain Rate.” *International Journal of Impact Engineering* 46: 1–10. https://doi.org/10.1016/j.ijimpeng.2011.12.009.

Cressie, N., and G. Johannesson. 2008. “Fixed Rank Kriging for Very Large Spatial Data Sets.” *Journal of the Royal Statistical Society: Series B (Statistical Methodology)* 70 (1): 209–26. https://doi.org/10.1111/j.1467-9868.2007.00633.x.

Criminisi, A., J. Shotton, D. Robertson, and E. Konukoglu. 2011. “Regression Forests for Efficient Anatomy Detection and Localization in CT Studies.” In *Medical Computer Vision. Recognition Techniques and Applications in Medical Imaging*, edited by B. Menze, G. Langs, Z. Tu, and A. Criminisi, 106–17. Berlin, Heidelberg: Springer Berlin Heidelberg.

Cuingnet, R., R. Prevost, D. Lesage, L.D. Cohen, B. Mory, and R. Ardon. 2012. “Automatic Detection and Segmentation of Kidneys in 3D CT Images Using Random Forests.” In *Medical Image Computing and Computer-Assisted Intervention – MICCAI 2012: 15th International Conference, Nice, France, October 1-5, 2012, Proceedings, Part III*, edited by N. Ayache, H. Delingette, P. Golland, and K. Mori, 66–74. Berlin, Heidelberg: Springer Berlin Heidelberg. https://doi.org/10.1007/978-3-642-33454-2_9.

DeWit, J.A., and D.S. Cronin. 2012. “Cervical Spine Segment Finite Element Model for Traumatic Injury Prediction.” *Journal of the Mechanical Behavior of Biomedical Materials* 10: 138–50. https://doi.org/10.1016/j.jmbbm.2012.02.015.

“Eigen.” 2018. eigen.tuxfamily.org.

ERSO. 2018. “Vehicle Safety 2018.” European Road Safety Observation. https://ec.europa.eu/transport/road_safety/sites/roadsafety/files/pdf/ersosynthesis2018-vehiclesafety.pdf.

ERTRAC, 2019. “Safe Road Transport Roadmap. Towards Vision Zero: Roads without Victims.” European Road Transport Research Advisory Council (ERTRAC).

European Commision. 2020. “Next Steps towards ‘Vision Zero’: EU Road Safety Policy Framework 2021-2030.” https://op.europa.eu/en/publication-detail/-/publication/d7ee4b58-4bc5-11ea-8aa5-01aa75ed71a1.

Fehr, D., W. Beksi, D. Zermas, and N. Papanikolopoulos. 2014. *RGB-D Object Classification Using Covariance Descriptors*. *Proceedings - IEEE International Conference on Robotics and Automation*. https://doi.org/10.1109/ICRA.2014.6907663.

Fice, J.B., D.S. Cronin, and M.B. Panzer. 2011. “Cervical Spine Model to Predict Capsular Ligament Response in Rear Impact.” *Annals of Biomedical Engineering* 39 (8): 2152–62. https://doi.org/10.1007/s10439-011-0315-4.

Forman, J., F.J. Lopez-Valdes, D. Lessley, M. Kindig, R. Kent, and O. Bostrom. 2009. “The Effect of Obesity on the Restraint of Automobile Occupants.” *Annals of Advances in Automotive Medicine / Annual Scientific Conference* 53 (October): 25–40.

Fréchède, B., X. Wang, S. Kleiven, C. Giordano, V. Strömbäck Alvarez, E. Jolivet, M.T. Bah, and C. Lecomte. 2013. “Specifications for the Tool Describing Body Shape and Posture.” EC Project Deliverable. D2.2. PIPER - Position and Personalize Advanced Human Body Models for Injury Prediction.

Furrer, R., M.G. Genton, and D. Nychka. 2006. “Covariance Tapering for Interpolation of Large Spatial Datasets.” *Journal of Computational and Graphical Statistics* 15 (3): 502–23. https://doi.org/10.1198/106186006X132178.

Galea, G., C. Bollars, J. Breda, T. Kiaer, M. Kouzeh, L. McGale, I. Lanca de Morais, S. Whiting, and T. Wijnhoven. 2013. “Country Profiles on Nutrition, Physical Activity and Obesity in the 53 WHO European Region Member States. Methodolgy and Summary (2013).” World Health Organization, regional office for Europe.

Garby, L., O. Lammert, K.F. Kock, and B. Thobo-Carlsen. 1993. “Weights of Brain, Heart, Liver, Kidneys, and Spleen in Healthy and Apparently Healthy Adult Danish Subjects.” *American Journal of Human Biology* 5 (3): 291–296. https://doi.org/10.1002/ajhb.1310050307.

Gauriau, R., R. Cuingnet, D. Lesage, and I. Bloch. 2015. “Multi-Organ Localization with Cascaded Global-to-Local Regression and Shape Prior.” *Medical Image Analysis* 23 (1): 70–83. https://doi.org/10.1016/j.media.2015.04.007.

Gayzik, F.S., D.P. Moreno, K.A. Danelson, C. McNally, K.D. Klinich, and J.D. Stitzel. 2012. “External Landmark, Body Surface, and Volume Data of a Mid-Sized Male in Seated and Standing Postures.” *Annals of Biomedical Engineering* 40 (9): 2019–32. https://doi.org/10.1007/s10439-012-0546-z.

Gayzik, F.S., D.P. Moreno, C.P. Geer, S.D. Wuertzer, R.S. Martin, and J.D. Stitzel. 2011. “Development of a Full Body CAD Dataset for Computational Modeling: A Multi-Modality Approach.” *Annals of Biomedical Engineering* 39 (10): 2568. https://doi.org/10.1007/s10439-011-0359-5.

Gayzik, F.S., D.P. Moreno, N.A. Vavalle, A.C. Rhyne, and J.D. Stitzel. 2011. “Development of the Global Human Body Models Consortium Mid Sized Male Full Body Model.” In *Proceedings of the 39th International Workshop on Injury Biomechanics Research*. Vol. 39.

Geerligs, M., G.W.M. Peters, P.A.J. Ackermans, C.W.J. Oomens, and F.P.T. Baaijens. 2010. “Does Subcutaneous Adipose Tissue Behave as an (Anti-)Thixotropic Material?” *Journal of Biomechanics* 43 (6): 1153–59. https://doi.org/10.1016/j.jbiomech.2009.11.037.

Gelfand, N., N.J. Mitra, L.J. Guibas, and H. Pottmann. 2005. “Robust Global Registration.” In *Symposium on Geometry Processing*, 197–206.

Gepner, B.D., H. Joodaki, Z. Sun, M. Jayarhirtha, T. Kim, J.L. Forman, and J.R. Kerrigan. 2018. “Performance of the Obese GHBMC Models in the Sled and Belt Pull Test Conditions.” In *Ircobi Conference Proceedings*. Athens, Greece.

Gilles, B., L. Reveret, and D. Pai. 2010. “Creating and Animating Subject-Specific Anatomical Models.” *Comput. Graph. Forum* 29 (December): 2340–51. https://doi.org/10.1111/j.1467-8659.2010.01718.x.

Golub, G.H., and C.F. Van Loan. 1996. *Matrix Computations*. Johns Hopkins Studies in the Mathematical Sciences. Johns Hopkins University Press.

Grandmaison, G.L. de la, I. Clairand, and M. Durigon. 2001. “Organ Weight in 684 Adult Autopsies: New Tables for a Caucasoid Population.” *Forensic Science International* 119 (2): 149–54. https://doi.org/10.1016/S0379-0738(00)00401-1.

Grébonval, C., X. Trosseille, P. Petit, X. Wang, and P. Beillas. 2019. “Occupant Response in Frontal Crash, after Alterations of the Standard Driving Position.” In *Ircobi Conference Proceedings*. Vol. 19–57. Florence, Italy.

Gribov, A., and K. Krivoruchko. 2004. “Geostatistical Mapping with Continuous Moving Neighborhood.” *Mathematical Geology* 36 (2): 267–81. https://doi.org/10.1023/B:MATG.0000020473.63408.17.

Haas, T.C. 1990. “Lognormal and Moving Window Methods of Estimating Acid Deposition.” *Journal of the American Statistical Association* 85: 950–963.

Han, X.-F., J. Jin, J. Xie, M.-J. Wang, and W. Jiang. 2018. “A Comprehensive Review of 3D Point Cloud Descriptors.” *ArXiv Preprint ArXiv:1802.02297*.

Hardy, W.N., L.W. Schneider, and S.W. Rouhana. 2001. “Abdominal Impact Response to Rigid-Bar, Seatbelt, and Airbag Loading.” *Stapp Car Crash Journal* 45 (November): 1–32.

Hartman, L., and O. Hössjer. 2008. “Fast Kriging of Large Data Sets with Gaussian Markov Random Fields.” *Computational Statistics & Data Analysis* 52 (5): 2331–49. https://doi.org/10.1016/j.csda.2007.09.018.

Hassan, M.T.Z., and S.A. Meguid. 2018. “Effect of Seat Belt and Head Restraint on Occupant’s Response during Rear-End Collision.” *International Journal of Mechanics and Materials in Design* 14 (2): 231–42. https://doi.org/10.1007/s10999-017-9373-6.

Hayes, A.R., F.S. Gayzik, D.P. Moreno, R.S. Martin, and J.D. Stitzel. 2013. “Abdominal Organ Location, Morphology, and Rib Coverage for the 5(Th), 50(Th), and 95(Th) Percentile Males and Females in the Supine and Seated Posture Using Multi-Modality Imaging.” *Annals of Advances in Automotive Medicine* 57 (September): 111–22.

Heaton, M.J., A. Datta, A. Finley, R. Furrer, R. Guhaniyogi, F. Gerber, R.B. Gramacy, et al. 2017. “A Case Study Competition Among Methods for Analyzing Large Spatial Data.” *ArXiv E-Prints 1710.05013v2*, October.

Holcombe, S.A., and S.C. Wang. 2014. “Subcutaneous Fat Distribution in the Human Torso.” In *2014 IRCOBI Conference Proceedings - International Research Council on the Biomechanics of Injury*, 389–396. International Research Council on the Biomechanics of Injury.

Hu, J., A. Fanta, M.O. Neal, M.P. Reed, and J.-T. Wang. 2016. “Vehicle Crash Simulations with Morphed GHBMC Human Models of Different Stature, BMI, and Age.” In *Proceedings of the 4th International Digital Human Modeling Conference*. Montreal, Canada.

Hu, J., K. Zhang, A. Fanta, E. Hwang, and M.P. Reed. 2017. “Effects of Male Stature and Body Shape on Thoracic Impact Response Using Parametric Finite Element Human Modeling.” In *Proceedings of the 2017 IRCOBI Conference*. Antwerp, Belgium.

Huang, Q., B. Adams, M. Wicke, and L. Guibas. 2008. “Non-Rigid Registration Under Isometric Deformations.” In *Proc. of Eurographics Symposium on Geometry Processing 2008 (SGP)*, 1149–1458.

Hwang, E., J. Hallman, K. Klein, J. Rupp, M. Reed, and J. Hu. 2016. “Rapid Development of Diverse Human Body Models for Crash Simulations through Mesh Morphing.” In *SAE Technical Paper*. SAE International. https://doi.org/10.4271/2016-01-1491.

Ibrahim, M.M. 2010. “Subcutaneous and Visceral Adipose Tissue: Structural and Functional Differences.” *Obesity Reviews : An Official Journal of the International Association for the Study of Obesity* 11 (1): 11–18. https://doi.org/10.1111/j.1467-789X.2009.00623.x.

Janak, T., Y. Lafon, P. Petit, and P. Beillas. 2018. “Transformation Smoothing to Use after Positioning of Finite Element Human Body Models.” In *Proceedings of the 2018 IRCOBI Conference*. Athens, Greece.

Jehle, D., C. Doshi, J. Karagianis, J. Consiglio, and G. Jehle. 2014. “Obesity and Seatbelt Use: A Fatal Relationship.” *The American Journal of Emergency Medicine* 32 (7): 756–60. https://doi.org/10.1016/j.ajem.2014.01.010.

Jolivet, E., Y. Lafon, P. Petit, and P. Beillas. 2015. “Comparison of Kriging and Moving Least Square Methods to Change the Geometry of Human Body Models.” *Stapp Car Crash Journal* 59 (November): 337–57.

Joodaki, H., J. Forman, A. Forghani, B. Overby, R. Kent, J. Crandall, B. Beahlen, M. Beebe, and O. Bostrom. 2015. “Comparison of Kinematic Behaviour of a First Generation Obese Dummy and Obese PMHS in Frontal Sled Tests.” In *Ircobi Conference Proceedings*. Vol. 15–57. Lyon, France.

Kaess, B.M., A. Pedley, J.M. Massaro, J. Murabito, U. Hoffmann, and C.S. Fox. 2012. “The Ratio of Visceral to Subcutaneous Fat, a Metric of Body Fat Distribution, Is a Unique Correlate of Cardiometabolic Risk.” *Diabetologia* 55 (10): 2622–30. https://doi.org/10.1007/s00125-012-2639-5.

Katagiri, M., J. Zhao, J.R. Kerrigan, R.W. Kent, and J.L. Forman. 2016. “Comparison of Whole-Body Kinematic Behaviour of the GHBMC Occupant Model to PMHS in Far-Side Sled Tests.” In *Ircobi Conference Proceedings*. Vol. 16–88. Malaga, Spain.

Kent, R.W., J.L. Forman, and O. Bostrom. 2010. “Is There Really a ‘Cushion Effect’?: A Biomechanical Investigation of Crash Injury Mechanisms in the Obese.” *Obesity* 18 (4): 749–753. https://doi.org/10.1038/oby.2009.315.

Kim, Y., J.-E. Kim, and A. Eberhardt. 2012. “A New Cortical Thickness Mapping Method with Application to an in Vivo Finite Element Model.” *Computer Methods in Biomechanics and Biomedical Engineering* 17 (October). https://doi.org/10.1080/10255842.2012.731594.

Krige, D.G. 1951. “A Statistical Approach to Some Basic Mine Valuation Problems on the Witwatersrand.” *Journal of the Chemical, Metallurgical and Mining Society of South Africa* 52 (6): 119–139. https://doi.org/10.2307/3006914.

Kullberg, J., A. Hedström, J. Brandberg, R. Strand, L. Johansson, G. Bergström, and H. Ahlström. 2017. “Automated Analysis of Liver Fat, Muscle and Adipose Tissue Distribution from CT Suitable for Large-Scale Studies.” *Scientific Reports* 7 (1): 10425. https://doi.org/10.1038/s41598-017-08925-8.

Lackey, D.E., D.H. Burk, M.R. Ali, R. Mostaedi, W.H. Smith, J. Park, P.E. Scherer, et al. 2014. "Contributions of Adipose Tissue Architectural and Tensile Properties toward Defining Healthy and Unhealthy Obesity." *American Journal of Physiology-Endocrinology and Metabolism* 306 (3): E233–46. https://doi.org/10.1152/ajpendo.00476.2013.

Lafon, Y., F.W. Smith, and P. Beillas. 2010. "Combination of a Model-Deformation Method and a Positional MRI to Quantify the Effects of Posture on the Anatomical Structures of the Trunk." *Journal of Biomechanics* 43 (7): 1269–78. https://doi.org/10.1016/j.jbiomech.2010.01.013.

Lamielle, S., P. Vezin, J.-P. Verriest, P. Petit, X. Trosseille, and G. Vallancien. 2008. "3D Deformation and Dynamics of the Human Cadaver Abdomen under Seatbelt Loading." *Stapp Car Crash Journal* 52 (December): 267–94.

Li, M., K. Miller, G.R. Joldes, B. Doyle, R.R. Garlapati, R. Kikinis, and A. Wittek. 2015. "Patient-Specific Biomechanical Model as Whole-Body CT Image Registration Tool." *Medical Image Analysis* 22 (1): 22–34. https://doi.org/10.1016/j.media.2014.12.008.

Li, Z., M.W. Kindig, J.R. Kerrigan, C.D. Untaroiu, D. Subit, J.R. Crandall, and R.W. Kent. 2010. "Rib Fractures under Anterior–Posterior Dynamic Loads: Experimental and Finite-Element Study." *Journal of Biomechanics* 43 (2): 228–34. https://doi.org/10.1016/j.jbiomech.2009.08.040.

Li, Z., M.W. Kindig, D. Subit, and R.W. Kent. 2010. "Influence of Mesh Density, Cortical Thickness and Material Properties on Human Rib Fracture Prediction." *Medical Engineering & Physics* 32 (9): 998–1008. https://doi.org/10.1016/j.medengphy.2010.06.015.

Lloyd, B., E. Cherubini, S. Farcito, E. Neufeld, C. Baumgartner, and N. Kuster. 2016. *Covering Population Variability: Morphing of Computation Anatomical Models*. https://doi.org/10.1007/978-3-319-46630-9_2.

LSTC. 2019. "LS-DYNA Manual R11.0." LSTC. https://www.dynasupport.com/manuals.

Lu, Y.-C., A.R. Kemper, S. Gayzik, C.D. Untaroiu, and P. Beillas. 2013. "Statistical Modeling of Human Liver Incorporating the Variations in Shape, Size, and Material Properties." *Stapp Car Crash Journal* 57 (November): 285–311.

Machann, J., C. Thamer, B. Schnoedt, M. Haap, H.-U. Haring, C.D. Claussen, M. Stumvoll, A. Fritsche, and F. Schick. 2005. "Standardized Assessment of Whole Body Adipose Tissue Topography by MRI." *Journal of Magnetic Resonance Imaging : JMRI* 21 (4): 455–62. https://doi.org/10.1002/jmri.20292.

Mao, H., L. Zhang, B. Jiang, V.V. Genthikatti, X. Jin, F. Zhu, R. Makwana, et al. 2013. "Development of a Finite Element Human Head Model Partially Validated With Thirty Five Experimental Cases." *Journal of Biomechanical Engineering* 135 (111002). https://doi.org/10.1115/1.4025101.

Mattucci, S.F.E., J.A. Moulton, N. Chandrashekar, and D.S. Cronin. 2012. "Strain Rate Dependent Properties of Younger Human Cervical Spine Ligaments." *Journal of the Mechanical Behavior of Biomedical Materials* 10 (June): 216–26. https://doi.org/10.1016/j.jmbbm.2012.02.004.

Mattucci, S.F.E., J.A. Moulton, N. Chandrashekar, and D.S. Cronin. 2013. "Strain Rate Dependent Properties of Human Craniovertebral Ligaments." *Journal of the Mechanical Behavior of Biomedical Materials* 23 (July): 71–79. https://doi.org/10.1016/j.jmbbm.2013.04.005.

Maurovich-Horvat, P., J. Massaro, C.S. Fox, F. Moselewski, C.J. O'Donnell, and U. Hoffmann. 2006. "Comparison of Anthropometric, Area- and Volume-Based Assessment of Abdominal Subcutaneous and Visceral Adipose Tissue Volumes Using Multi-Detector Computed Tomography." *International Journal Of Obesity* 31 (September): 500.

Mayer, Ch., J. Dobberstein, U. Nagel, S. Pandharkar, H.G. Kumar, and S. Kulkarni. 2017. “Reconstruction of a Side Impact Accident with Far-Side Occupant Using HBM (Human Body Model) - Discussion of Injury Risk Evaluation by HBM Morphed to Individual Occupant Body Dimensions.” Presented at the International VDI Conference, Human Body Modelling in Automotive Safety, Berlin, November 28.

Mock, C.N., D.C. Grossman, R.P. Kaufman, C.D. Mack, and F.P. Rivara. 2002. “The Relationship between Body Weight and Risk of Death and Serious Injury in Motor Vehicle Crashes.” *Accident Analysis & Prevention* 34 (2): 221–28. https://doi.org/10.1016/S0001-4575(01)00017-3.

Naseri, H., H. Johansson, and K. Brolin. 2018. “A Nonlinear Viscoelastic Model for Adipose Tissue Representing Tissue Response at a Wide Range of Strain Rates and High Strain Levels.” *Journal of Biomechanical Engineering* 140 (4). https://doi.org/10.1115/1.4038200.

NHTSA. 2020. “Fatality Analysis Reporting System (FARS).” https://www.nhtsa.gov/research-data/fatality-analysis-reporting-system-fars.

NIH. 1998. “Clinical Guidelines on the Identification, Evaluation, and Treatment of Overweight and Obesity in Adults--The Evidence Report. National Institutes of Health.” *Obesity Research* 6 Suppl 2 (September): 51S-209S.

NTDB. 2020. “National Trauma Data Bank.” https://www.facs.org/quality-programs/trauma/ntdb.

Ogden, C.L., and K.M. Flegal. 2010. “Changes in Terminology for Childhood Overweight and Obesity.” *National Health Statistics Reports*, no. 25 (June): 1–5.

Okada, T., M.G. Linguraru, M. Hori, R.M. Summers, N. Tomiyama, and Y. Sato. 2015. “Abdominal Multi-Organ Segmentation from CT Images Using Conditional Shape-Location and Unsupervised Intensity Priors.” *Medical Image Analysis* 26 (1): 1–18. https://doi.org/10.1016/j.media.2015.06.009.

Orphanidou, C., L. McCargar, C.L. Birmingham, J. Mathieson, and E. Goldner. 1994. “Accuracy of Subcutaneous Fat Measurement: Comparison of Skinfold Calipers, Ultrasound, and Computed Tomography.” *Journal of the American Dietetic Association* 94 (8): 855–58.

Park, B.-K., J. Bae, B.-Y. Koo, and J.J. Kim. 2014. “Function-Based Morphing Methodology for Parameterizing Patient-Specific Models of Human Proximal Femurs.” *Computer-Aided Design* 51 (Supplement C): 31–38. https://doi.org/10.1016/j.cad.2014.02.003.

Park, G., T. Kim, J.R. Crandall, C. Arregui-Dalmases, and B.J. Luzón Narro. 2013. “Comparison of Kinematics of GHBMC to PMHS on the Side Impact Condition.” In *Ircobi Conference Proceedings*. Vol. 13–41. Gothenburg, Sweden.

Pepper, M.R., J.H. Freeland-Graves, W. Yu, P.R. Stanforth, and B. Xu. 2010. “Evaluation of a Rotary Laser Body Scanner for Body Volume and Fat Assessment.” *Journal of Testing and Evaluation* 39 (1): 1–6. https://doi.org/10.1520/JTE102871.

PIPER. 2020. “PIPER Project.” www.piper-project.org.

Pishchulin, L., S. Wuhrer, T. Helten, C. Theobalt, and B. Schiele. 2017. “Building Statistical Shape Spaces for 3D Human Modeling.” *Pattern Recognition*.

Potier, P. 2010. “Contribution Méthodologique à La Thanatomécanique et à La Thanatométrologie.” PhD Thesis. http://www.theses.fr/2010VALE0017/document.

Poulard, D., R.W. Kent, M. Kindig, Z. Li, and D. Subit. 2015. “Thoracic Response Targets for a Computational Model: A Hierarchical Approach to Assess the Biofidelity of a 50th-Percentile Occupant Male Finite Element Model.” *Journal of the Mechanical Behavior of Biomedical Materials* 45 (May): 45–64. https://doi.org/10.1016/j.jmbbm.2015.01.017.

Reed, M.P., S.M. Ebert-Hamilton, and J.D. Rupp. 2012. “Effects of Obesity on Seat Belt Fit.” *Traffic Injury Prevention* 13 (4): 364–72. https://doi.org/10.1080/15389588.2012.659363.

Reed, M.P., U. Raschke, R. Tirumali, and M.B. Parkinson. 2014. “Developing and Implementing Parametric Human Body Shape Models in Ergonomics Software.” In *Proceedings of the 3rd International Digital Human Modeling Symposium*. Tokyo, Japan.

Rice, T.M., and M. Zhu. 2013. “Driver Obesity and the Risk of Fatal Injury during Traffic Collisions.” *Emergency Medicine Journal* 31 (1): 9–12. https://doi.org/10.1136/emermed-2012-201859.

Rivoirard, J., and T. Romary. 2011. “Continuity for Kriging with Moving Neighborhood.” *Mathematical Geosciences* 43 (4): 469–81. https://doi.org/10.1007/s11004-011-9330-0.

Robinette, K.M., H. Daanen, and E. Paquet. 1999. “The CAESAR Project: A 3-D Surface Anthropometry Survey.” In *Second International Conference on 3-D Digital Imaging and Modeling (Cat. No.PR00062)*, 380–86. https://doi.org/10.1109/IM.1999.805368.

Saito, S., Z.-Y. Zhou, and L. Kavan. 2015. “Computational Bodybuilding: Anatomically-Based Modeling of Human Bodies.” *ACM Trans. Graph.* 34 (4).

Sang, H., M. Jun, and J.Z. Huang. 2011. “Covariance Approximation for Large Multivariate Spatial Data Sets with an Application to Multiple Climate Model Errors.” *Ann. Appl. Stat.* 5 (4): 2519–48. https://doi.org/10.1214/11-AOAS478.

Saraf, H., K.T. Ramesh, A.M. Lennon, A.C. Merkle, and J.C. Roberts. 2007. “Mechanical Properties of Soft Human Tissues under Dynamic Loading.” *Journal of Biomechanics* 40 (9): 1960–67. https://doi.org/10.1016/j.jbiomech.2006.09.021.

Sarkalkan, N., H. Weinans, and A.A. Zadpoor. 2014. “Statistical Shape and Appearance Models of Bones.” *Bone* 60 (Supplement C): 129–40. https://doi.org/10.1016/j.bone.2013.12.006.

Scafoglieri, A., J.P. Clarys, E. Cattrysse, and I. Bautmans. 2014. “Use of Anthropometry for the Prediction of Regional Body Tissue Distribution in Adults: Benefits and Limitations in Clinical Practice.” *Aging and Disease* 5 (6): 373–93. https://doi.org/10.14366/AD.2014.0500373.

Schneider, H.J., N. Friedrich, J. Klotsche, L. Pieper, M. Nauck, U. John, M. Dörr, et al. 2010. “The Predictive Value of Different Measures of Obesity for Incident Cardiovascular Events and Mortality.” *The Journal of Clinical Endocrinology & Metabolism* 95 (4): 1777–85. https://doi.org/10.1210/jc.2009-1584.

Seidell, J., A. Oosterlee, M.A.O. Thijssen, J. Burema, P. Deurenberg, J.G.A.J. Hautvast, and J.H.J. Ruijs. 1987. “Assessment of Intra-Abdominal and Subcutaneous Abdominal Fat: Relation between Anthropometry and Computed Tomography.” *Am. J. Clin. Nutr. 45 (1987) 7-13.*

Shen, W., Z. Wang, M. Punyanita, J. Lei, A. Sinav, J.G. Kral, C. Imielinska, R. Ross, and S.B. Heymsfield. 2003. “Adipose Tissue Quantification by Imaging Methods: A Proposed Classification.” *Obesity Research* 11 (1): 5–16. https://doi.org/10.1038/oby.2003.3.

Shi, X., L. Cao, M.P. Reed, J.D. Rupp, and J. Hu. 2015. “Effects of Obesity on Occupant Responses in Frontal Crashes: A Simulation Analysis Using Human Body Models.” *Computer Methods in Biomechanics and Biomedical Engineering* 18 (12): 1280–92. https://doi.org/10.1080/10255842.2014.900544.

Shigeta, K., Y. Kitagawa, and T. Yasuki. 2009. “Development of next Generation Human FE Model Capable of Organ Injury Prediction.” *Proceedings of the 21st Annual Enhanced Safety of Vehicles*.

Shin, J., and C.D. Untaroiu. 2013. “Biomechanical and Injury Response of Human Foot and Ankle under Complex Loading.” *Journal of Biomechanical Engineering* 135 (10): 101008. https://doi.org/10.1115/1.4025108.

Sigal, I.A., H. Yang, M.D. Roberts, and J.C. Downs. 2010. “Morphing Methods to Parameterize Specimen-Specific Finite Element Model Geometries.” *Journal of Biomechanics* 43 (2): 254. https://doi.org/10.1016/j.jbiomech.2009.08.036.

Smith Choban, P., L.J.JR. Weireter, and C. Maynes. 1991. *Obesity and Increased Mortality in Blunt Trauma*. Vol. 31. https://doi.org/10.1097/00005373-199109000-00009.

Sommer, G., M. Eder, L. Kovacs, H. Pathak, L. Bonitz, C. Mueller, P. Regitnig, and G.A. Holzapfel. 2013. “Multiaxial Mechanical Properties and Constitutive Modeling of Human Adipose Tissue: A Basis for Preoperative Simulations in Plastic and Reconstructive Surgery.” *Acta Biomaterialia* 9 (11): 9036–48. https://doi.org/10.1016/j.actbio.2013.06.011.

Soni, A., and P. Beillas. 2015. “Modelling Hollow Organs for Impact Conditions: A Simplified Case Study.” *Computer Methods in Biomechanics and Biomedical Engineering* 18 (7): 730–39. https://doi.org/10.1080/10255842.2013.843677.

Sorkine, O. 2006. “Differential Representations for Mesh Processing.” *Comput. Graph. Forum* 25 (December): 789–807. https://doi.org/10.1111/j.1467-8659.2006.00999.x.

Sorkine, O., and M. Alexa. 2007. “As-Rigid-As-Possible Surface Modeling.” In *Geometry Processing*, edited by A. Belyaev and M. Garland. The Eurographics Association. https://doi.org/10.2312/SGP/SGP07/109-116.

Stein, M.L. 2014. “Limitations on Low Rank Approximations for Covariance Matrices of Spatial Data.” *Spatial Statistics Miami* 8 (May): 1–19. https://doi.org/10.1016/j.spasta.2013.06.003.

Stevens-Simon, C., P. Thureen, E. Stamm, and A. Scherzinger. 2001. “A Comparison of Four Techniques for Measuring Central Adiposity in Postpartum Adolescents.” *The Journal of Maternal-Fetal Medicine* 10 (3): 209–13.

Stimpson, C., C. Ernst, P. Knupp, P. Pébay, and D. Thompson. 2007. “The Verdict Library Reference Manual,” April.

Sun, Y., B. Li, and M.G. Genton. 2012. “Geostatistics for Large Datasets.” In *Advances and Challenges in Space-Time Modelling of Natural Events*, edited by E. Porcu, J. Montero, and M. Schlather, 55–77. Springer Berlin Heidelberg.

Swainson, M. (Michelle), A.M. (Alan) Batterham, C. (Costas) Tsakirides, Z.H. (Zoe) Rutherford, and K. (Karen) Hind. 2017. “Prediction of Whole-Body Fat Percentage and Visceral Adipose Tissue Mass from Five Anthropometric Variables.” *PLOS One* 12 (5). http://hdl.handle.net/10149/621092.

Takhounts, E.G., M.J. Craig, K. Moorhouse, J. McFadden, and V. Hasija. 2013. “Development of Brain Injury Criteria (BrIC).” In *57th Stapp Car Crash Conference*. The Stapp Association. https://doi.org/10.4271/2013-22-0010.

Thorbole, C.K. 2015. “Seatbelt Submarining Injury and Its Prevention Countermeasures: How a Cantilever Seat Pan Structure Exacerbate Submarining.” *Journal of Family Medicine and Primary Care* 4 (4): 587–90. https://doi.org/10.4103/2249-4863.174299.

Tournier, M., M. Nesme, B. Gilles, and F. Faure. 2015. “Stable Constrained Dynamics.” *ACM Trans. Graph.* 34 (4): 132:1–132:10. https://doi.org/10.1145/2766969.

Trochu, F. 1993. “A Contouring Program Based on Dual Kriging Interpolation.” *Engineering with Computers* 9 (3): 160–177. https://doi.org/10.1007/BF01206346.

Untaroiu, C.D., N. Yue, and J. Shin. 2013. “A Finite Element Model of the Lower Limb for Simulating Automotive Impacts.” *Annals of Biomedical Engineering* 41 (3): 513–26. https://doi.org/10.1007/s10439-012-0687-0.

Uriot, J., P. Potier, P. Baudrit, X. Trosseille, P. Petit, O. Richard, S. Compigne, M. Masuda, and R. Douard. 2015. “Reference PMHS Sled Tests to Assess Submarining.” *Stapp Car Crash Journal* 59: 203–23.

V. R. Brown, C., A. L. Neville, P. Rhee, A. Salim, G. C. Velmahos, and D. Demetriades. 2005. “The Impact of Obesity on the Outcomes of 1,153 Critically Injured Blunt Trauma Patients.” *The Journal of Trauma* 59: 1048–51; discussion 1051.

Vadgama, D.K., M.M. Trangadia, R.A. Mehta, and B. Gupta. 2014. “Autopsy Study of Organ Weights in Relation to Body Weight and Body Length of Adult Cases in Jamnagar Region.” *Journal of Indian Academy of Forensic Medicine* 36 (3): 238–241.

Vavalle, N.A., S.L. Schoell, A.A. Weaver, J.D. Stitzel, and F.S. Gayzik. 2014. “Application of Radial Basis Function Methods in the Development of a 95th Percentile Male Seated FEA Model.” *Stapp Car Crash Journal* 58 (November): 361–84.

Viergever, M.A., J.B.A. Maintz, S. Klein, K. Murphy, M. Staring, and J.P.W. Pluim. 2016. “A Survey of Medical Image Registration – under Review.” *20th Anniversary of the Medical Image Analysis Journal (MedIA)* 33 (October): 140–44. https://doi.org/10.1016/j.media.2016.06.030.

Vilhena, L., and A. Ramalho. 2016. “Friction of Human Skin against Different Fabrics for Medical Use.” *Lubricants* 4 (1). https://doi.org/10.3390/lubricants4010006.

Wang, Y., L. Cao, Z. Bai, M.P. Reed, J.D. Rupp, C.N. Hoff, and J. Hu. 2016. “A Parametric Ribcage Geometry Model Accounting for Variations among the Adult Population.” *Journal of Biomechanics* 49 (13): 2791–98. https://doi.org/10.1016/j.jbiomech.2016.06.020.

World Health Organization. 2000. *Obesity: Preventing and Managing the Global Epidemic*. 894. World Health Organization.

World Health Organization. 2020. “Obesity and Overweight.” https://www.who.int/news-room/fact-sheets/detail/obesity-and-overweight.

Xu, B., W. Yu, M. Yao, M.R. Pepper, and J.H. Freeland-Graves. 2009. “Three-Dimensional Surface Imaging System for Assessing Human Obesity.” *Optical Engineering (Redondo Beach, Calif.)* 48 (10): nihpa156427–nihpa156427. https://doi.org/10.1117/1.3250191.

Yamazaki, S., M. Kouchi, and M. Mochimaru. 2013. “Markerless Landmark Localization on Body Shape Scans by Non-Rigid Model Fitting.” In *2nd Digital Human Modeling Symposium*.

Yanaoka, T., and Y. Dokko. 2013. “A Parametric Study of Age-Related Factors AffectingIntracranial Responses under Impact Loading Using a Human Head/Brain FE Model.” In *Ircobi Conference Proceedings*. Vol. 13–50. Gothenburg, Sweden.

Yang, J., Z.-G. Cao, and Q. Zhang. 2016. “A Fast and Robust Local Descriptor for 3D Point Cloud Registration.” *Information Sciences* 346 (February): 163–79. https://doi.org/10.1016/j.ins.2016.01.095.

Yue, N., and C. Untaroiu. 2014. “A Numerical Investigation on the Variation in Hip Injury Tolerance With Occupant Posture During Frontal Collisions.” *Traffic Injury Prevention* 15 (March): 513–22. https://doi.org/10.1080/15389588.2013.840884.

Zhang, K., L. Cao, A. Fanta, M.P. Reed, M. Neal, J.-T. Wang, C.-H. Lin, and J. Hu. 2017. “An Automated Method to Morph Finite Element Whole-Body Human Models with a Wide Range of Stature

and Body Shape for Both Men and Women." *Journal of Biomechanics* 60 (July): 253–60. https://doi.org/10.1016/j.jbiomech.2017.06.015.

Zhou, K., J. Huang, J. Snyder, X. Liu, H. Bao, B. Guo, and H.-Y. Shum. 2005. "Large Mesh Deformation Using the Volumetric Graph Laplacian." *ACM Trans. Graph.* 24 (July): 496–503. https://doi.org/10.1145/1186822.1073219.

Zhu, Z., and G. Li. 2011. "Construction of 3D Human Distal Femoral Surface Models Using a 3D Statistical Deformable Model." *Journal of Biomechanics* 44 (13): 2362–68. https://doi.org/10.1016/j.jbiomech.2011.07.006.

Zimmet, P., and S. Inoue. 2000. *The Asia-Pacific Perspective: Redefining Obesity and Its Treatment*. Health Communications Australia.

# Appendix 1

The test case simulates a change of skin surface while keeping all bones unchanged. This could be understood as a simplified representation of a rapid weight gain or loss for an individual. It was designed to evaluate the morphing method but does not attempt to account for all factors that could be associated with weight changes in reality.

The GHBMC M50-O model (Gayzik, Moreno, Geer, et al. 2011) version 4.1 was used in all tests. The model is composed of 1 255 225 nodes and 2 313 366 elements organized in parts describing various anatomical structures. The model stature and weights are 174.9 cm and 77.53 Kg, for a corresponding Body Mass Index (BMI) of 25.34 kg/m².

Four skin surfaces were generated using a publicly available statistical shape model (SSM) ((Reed et al. 2014), available at *http://humanshape.org)*. One skin surface was generated for anthropometric parameters similar to those of the GHBMC M50-O (BMI 25.34 kg/m²) and it was defined as the baseline mesh (source). Three other surfaces were generated with the same anthropometric parameters except the BMI to be used as targets: one of an obese model (BMI 35) and two with a lower weight (BMI 20 and 22.7). The surface meshes had several quality issues that required changes before using them as targets: areas around armpits and crotch were smoothed, and the hand surface meshes were manually replaced by those of the GHBMC M50-O.

Since the GHBMC M50-O and *humanshape.org* postures are different (arms are in a different position, see Figure 131), the GHBMC M50-O was first morphed to the baseline skin surface as follows: the baseline skin surface mesh was resampled to obtain a more homogenous distribution of 17 282 vertices. Then, it was aligned with the GHBMC M50-0 using Iterative Closest Point in Meshlab (ISTI – CNR, Italy) to minimize rigid transformations needed to register the surfaces. After the alignment, the skin of GHBMC M50-O was registered to it using the *mHBM* registration software (Yamazaki et al. 2013). The registration was guided by landmarks on the hands, elbows, heels, toes, knees and nose. The GHBMC M50-O was morphed by standard kriging using the registered vertices as source CPs and the baseline vertices as target CPs. This morphed model, referred to as $GHBMC_{25.3}$ in the following text, was subsequently used as the source model for the actual morphing tests. Note that despite targeting BMI 25.34, the actual BMI achieved was 26.58 (81.31 kg of mass).

The *mHBM* software was also used to register the (resampled) target surfaces to the $GHBMC_{25.3}$ mesh, although it required less landmarks thanks to the now more similar posture (typically only shoulders, knees and in the BMI 35 case also sternum, elbows and thighs). After registration, small adjustment of

the target skin surfaces were required as the BMI 20 and BMI 22.7 skin surfaces intersected the bones of the $GHBMC_{25.3}$ around the ribcage and pelvis. To correct this issue, the surfaces were locally adjusted by manual cage morphing followed by smoothing in Ls-Prepost (LSTC, CA), enforcing about a 10 mm gap between skin and bones in the thoracic region and pelvis. It was also assumed that the BMI 35 surface should be outside the $GHBMC_{25.3}$ skin, which was not the case everywhere. This was also solved by manual morphing in LS-Prepost, mainly on arms and legs. Finally, the resampled baseline skin was registered onto these adjusted skin surfaces using the mHBM software.

All the 17 282 vertices of the registered baseline skin surface were used as control points to morph the $GHBMC_{25.3}$ onto the various BMI SSM skin surfaces. In addition, to avoid any deformation of the bones, all 217 495 nodes on the surface of bones of the $GHBMC_{25.3}$ were used as fixed CPs (i.e. CPs with identical source and target positions). This led to a total of 234 777 CPs. Illustrations of three of the resulting surfaces created to serve as targets for full model morphing are provided in Figure 131, as well as the original $GHBMC_{25.3}$ skin surface.

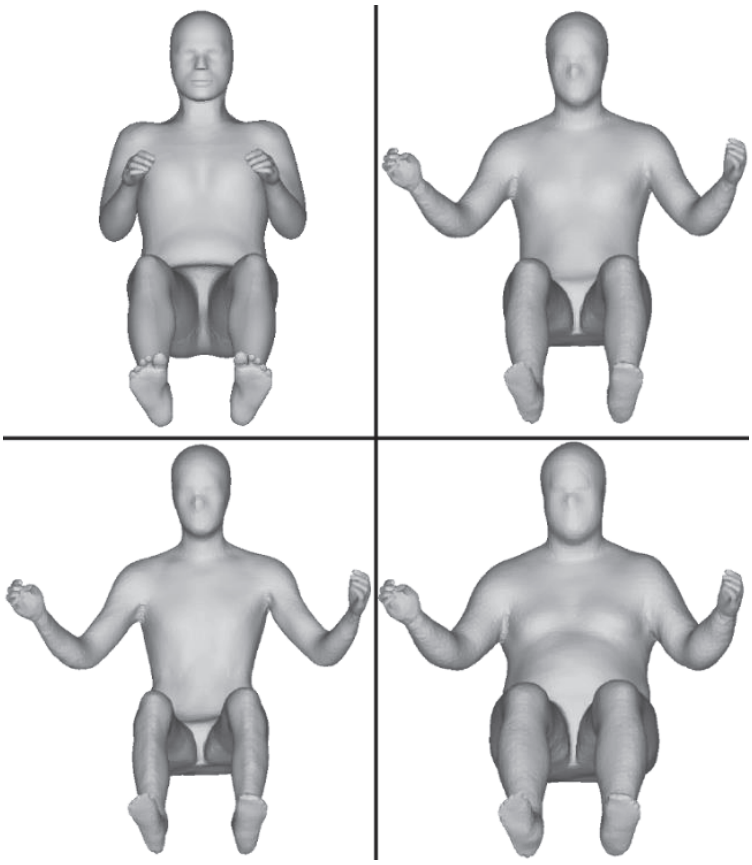

*Figure 131: Overview of the targets shapes after smoothing and local adjustments used for the current study: top right is the "baseline" surface (same BMI as the GHBMC M50-O); bottom left BMI 20 and bottom right the BMI 35 surface. The original $GHBM_{25.3}$ skin surface is shown in top left for comparison.*

# Appendix 2

The following figures show all results of the MHA belt tests presented in Section 6.3.1.2, i.e. belt displacements of centre and left side of the belt both as time histories as well as trajectories, force time history and force / displacement plots.

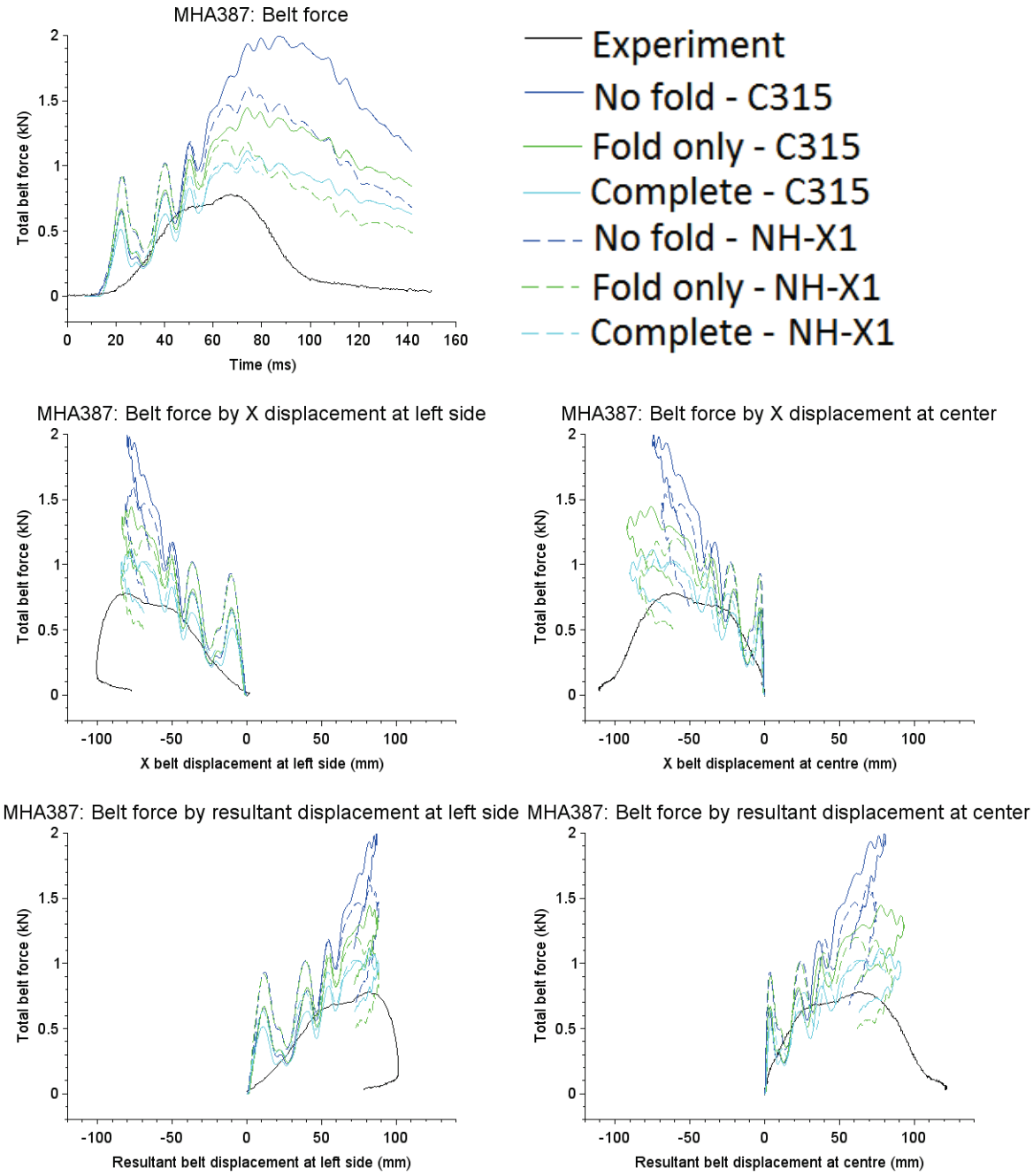


*Figure 132: MHA387.*

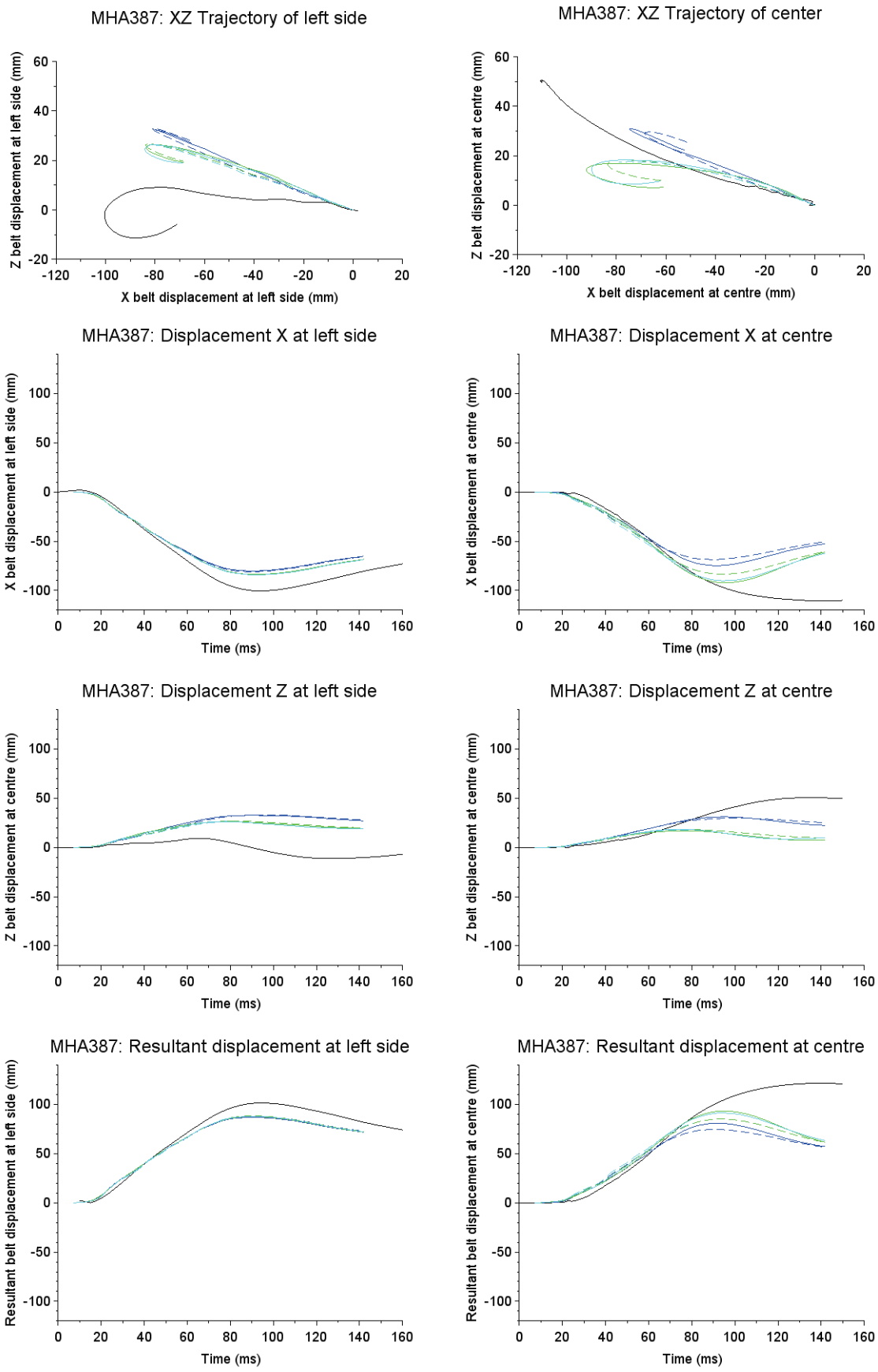


*Figure 133: MHA387, displacements.*

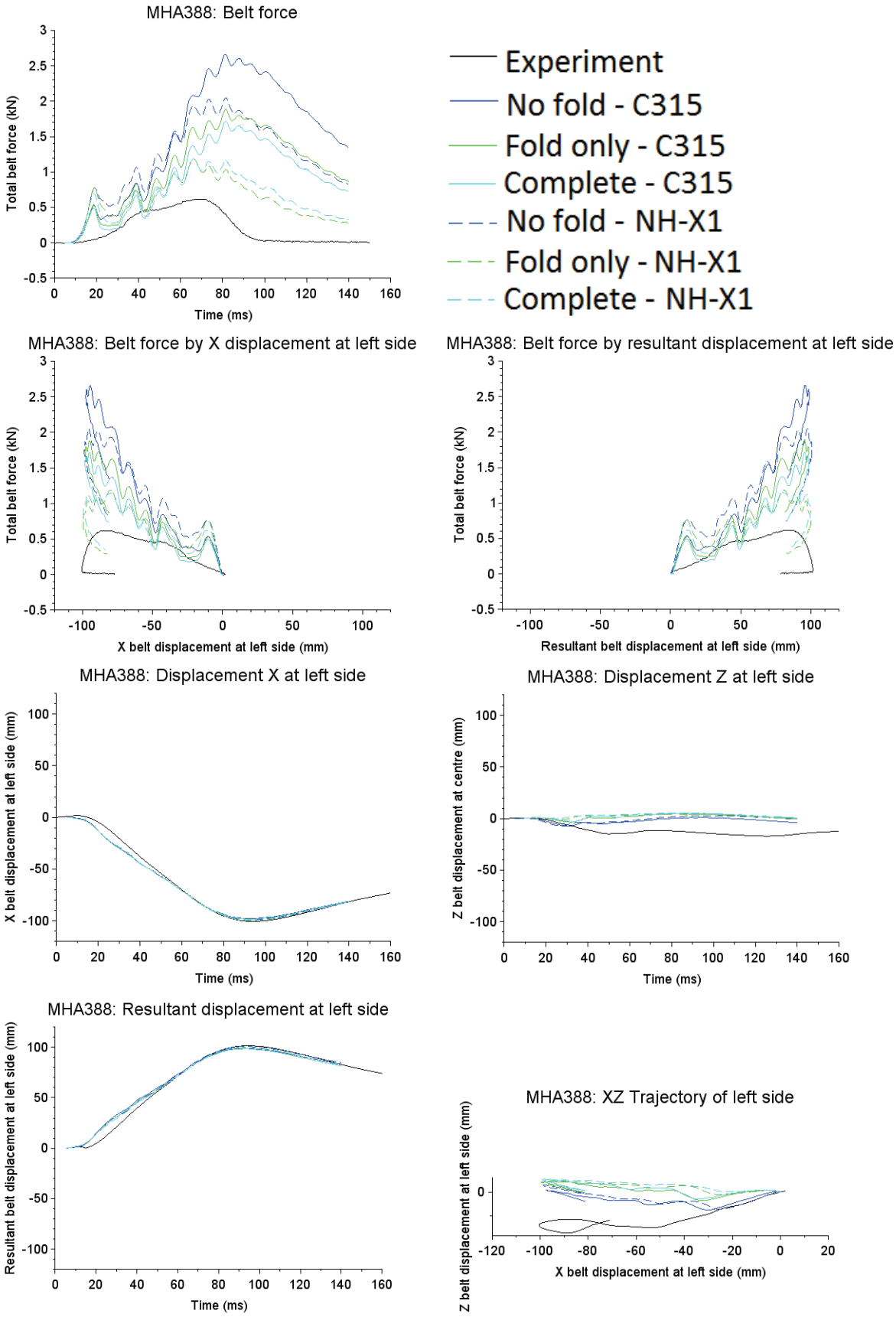


*Figure 134: MHA388.*

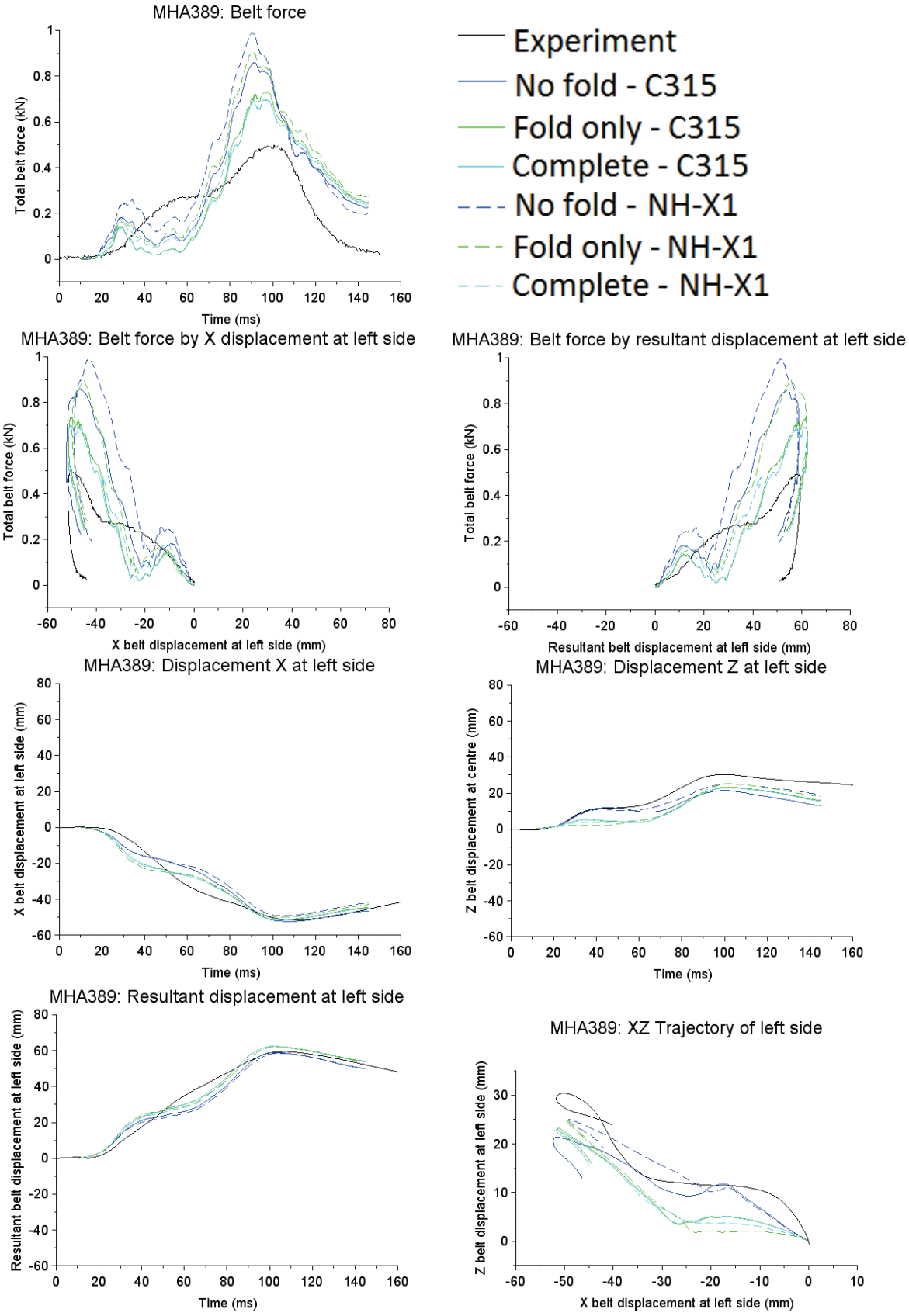


*Figure 135: MHA389.*

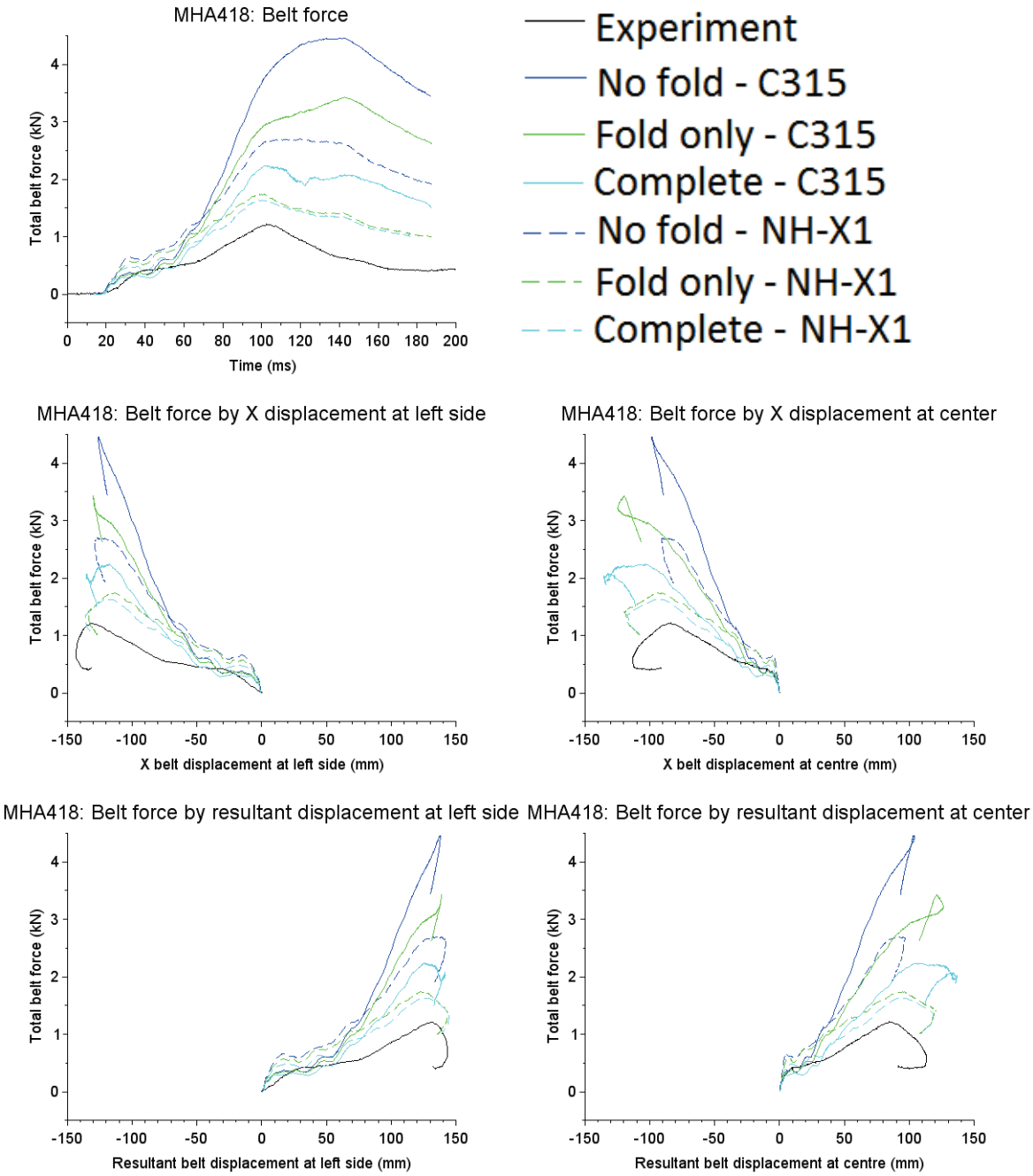


*Figure 136: MHA418.*

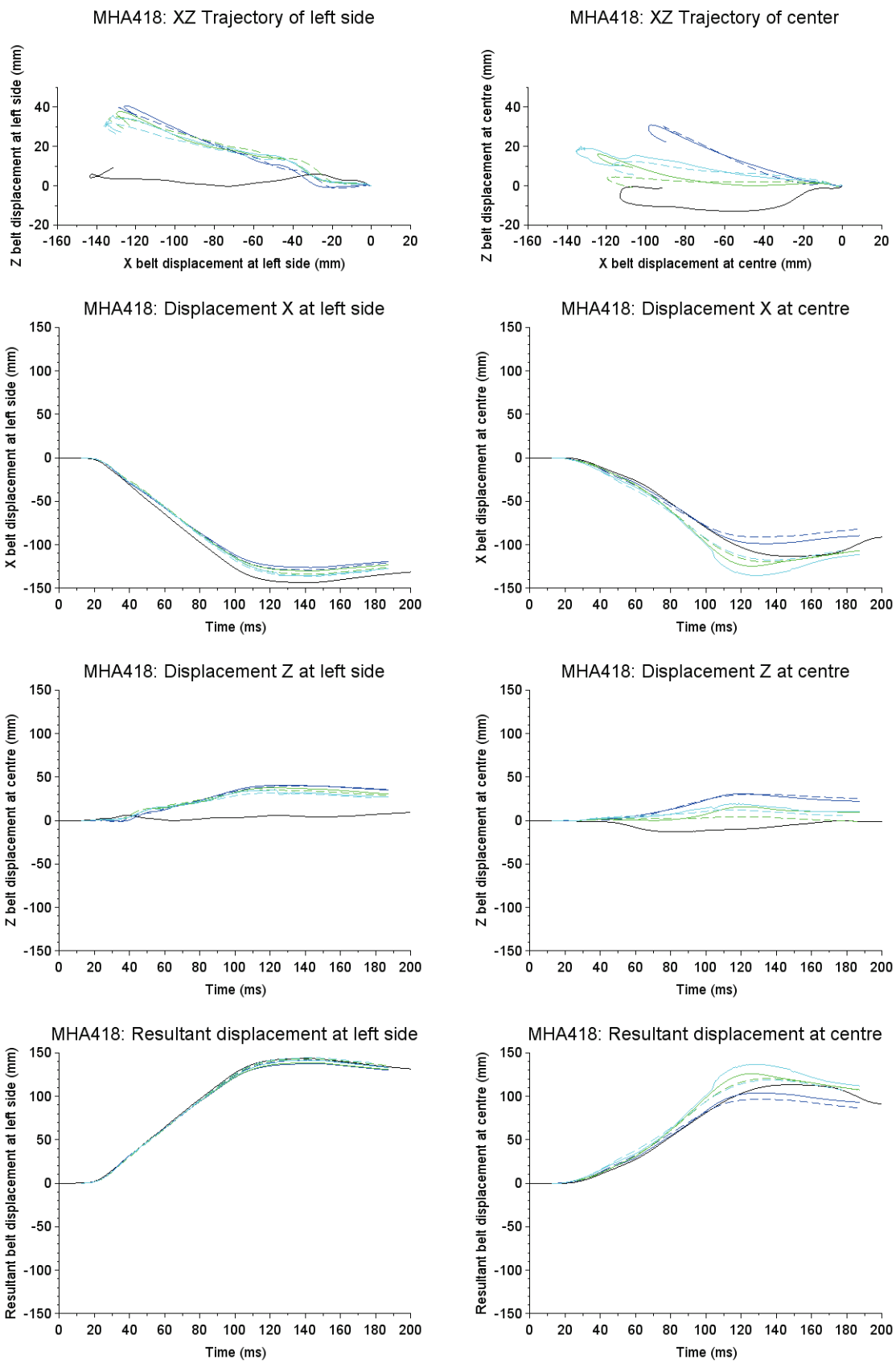


*Figure 137: MHA418.*

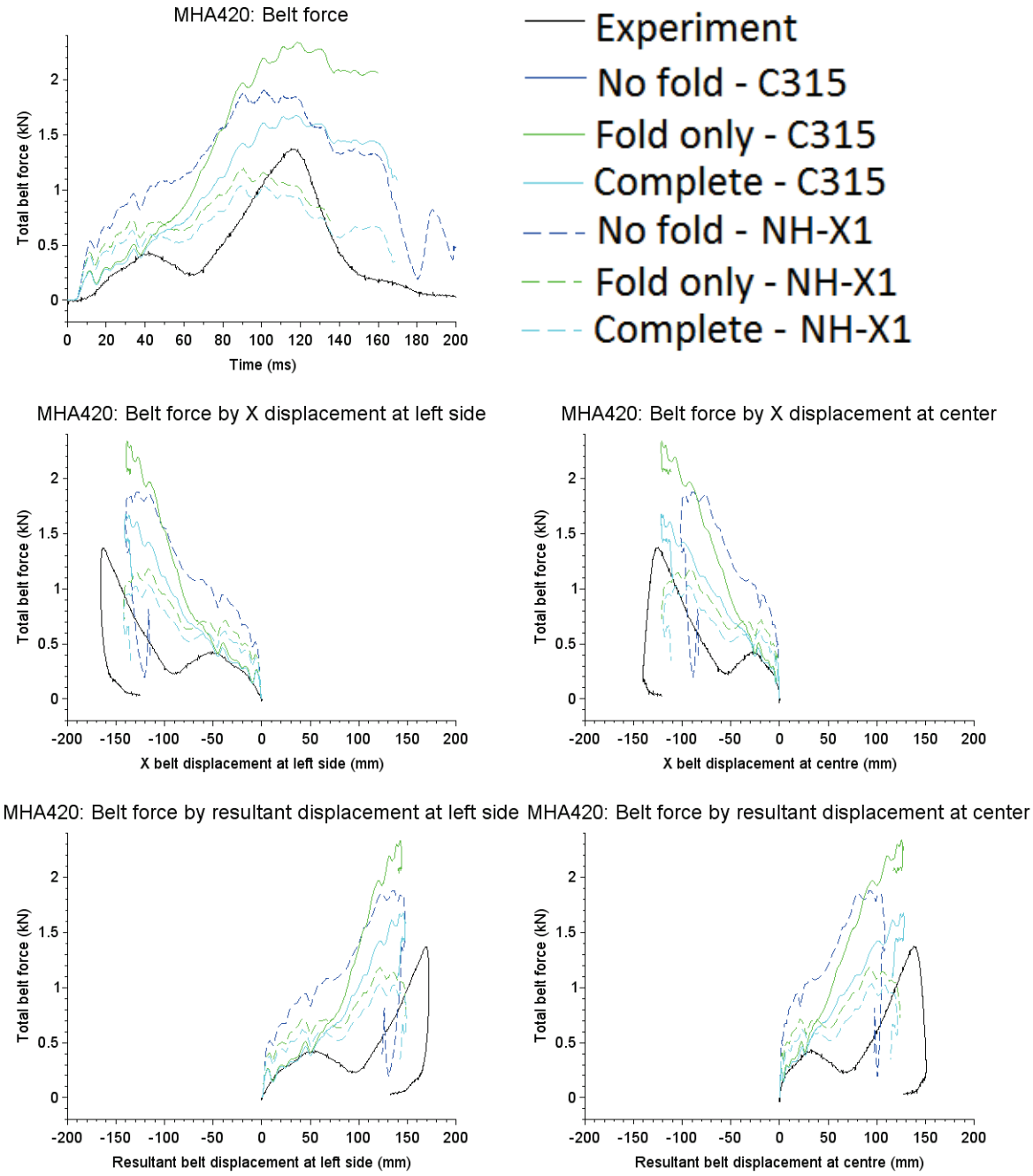


*Figure 138: MHA420. Belt slipped in the noFold version of C315, curve is not included.*

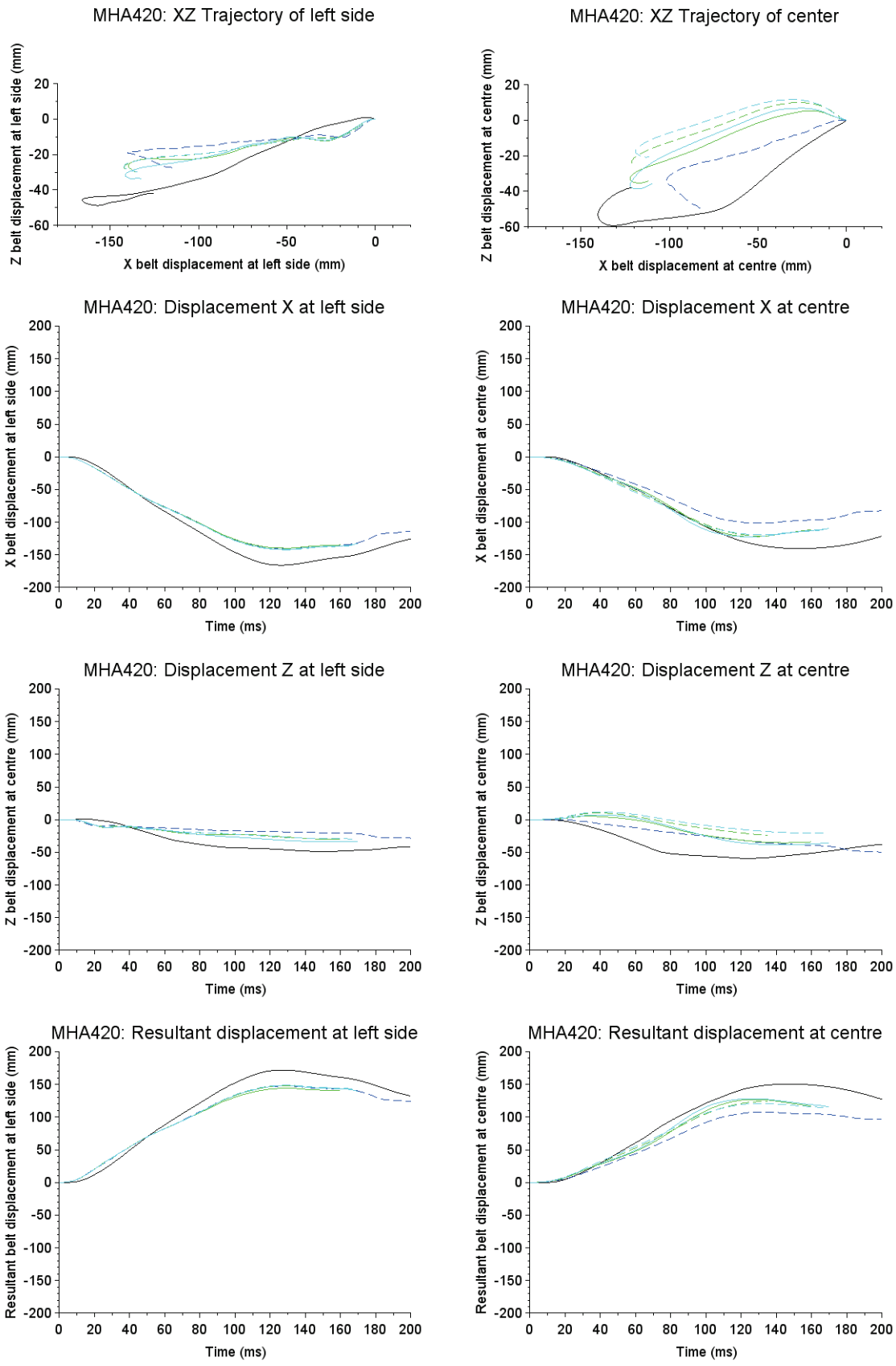


*Figure 139: MHA420, displacements.*

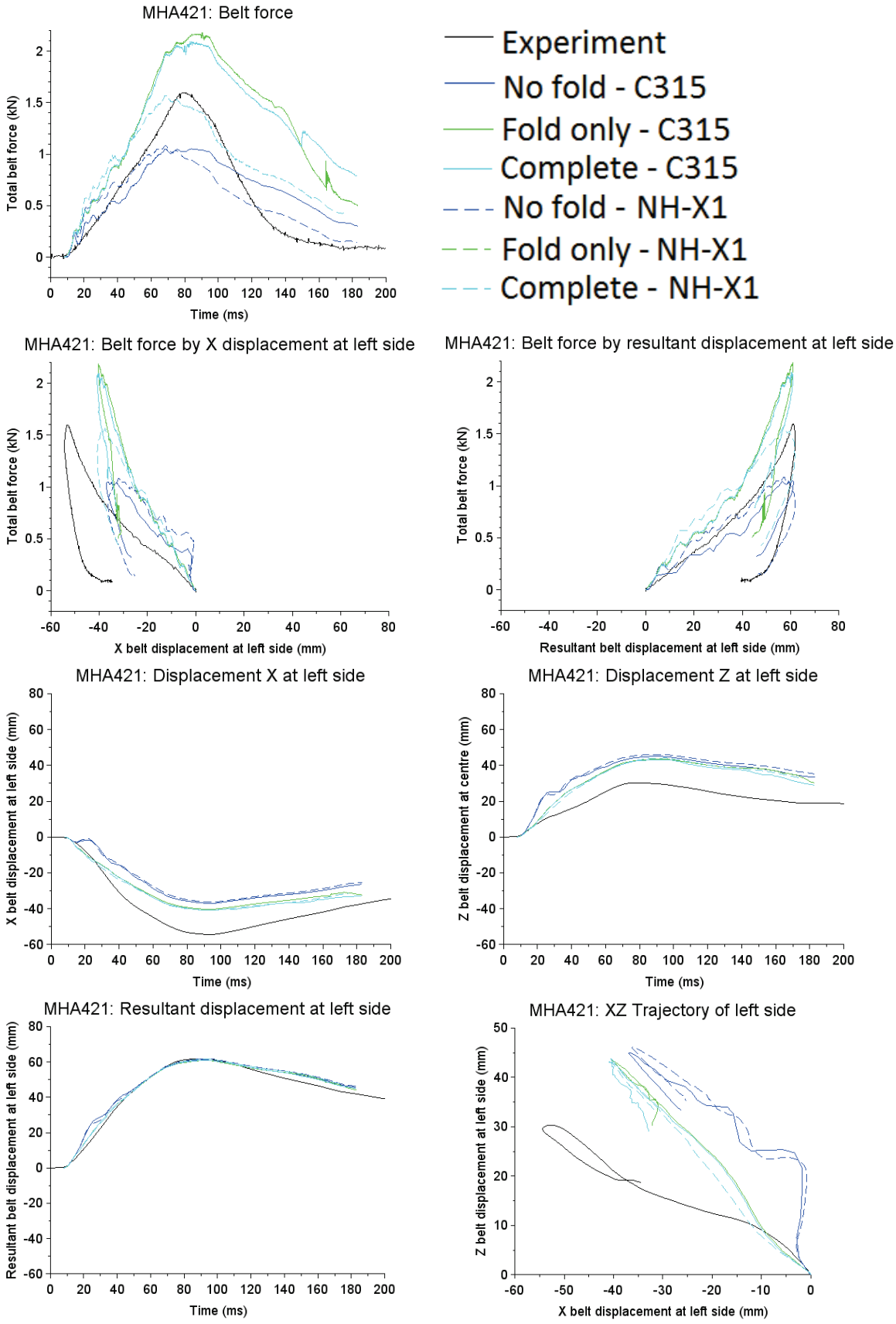


*Figure 140: MHA421. The foldOnly version of X1 crashed after 22.5 ms – not included.*

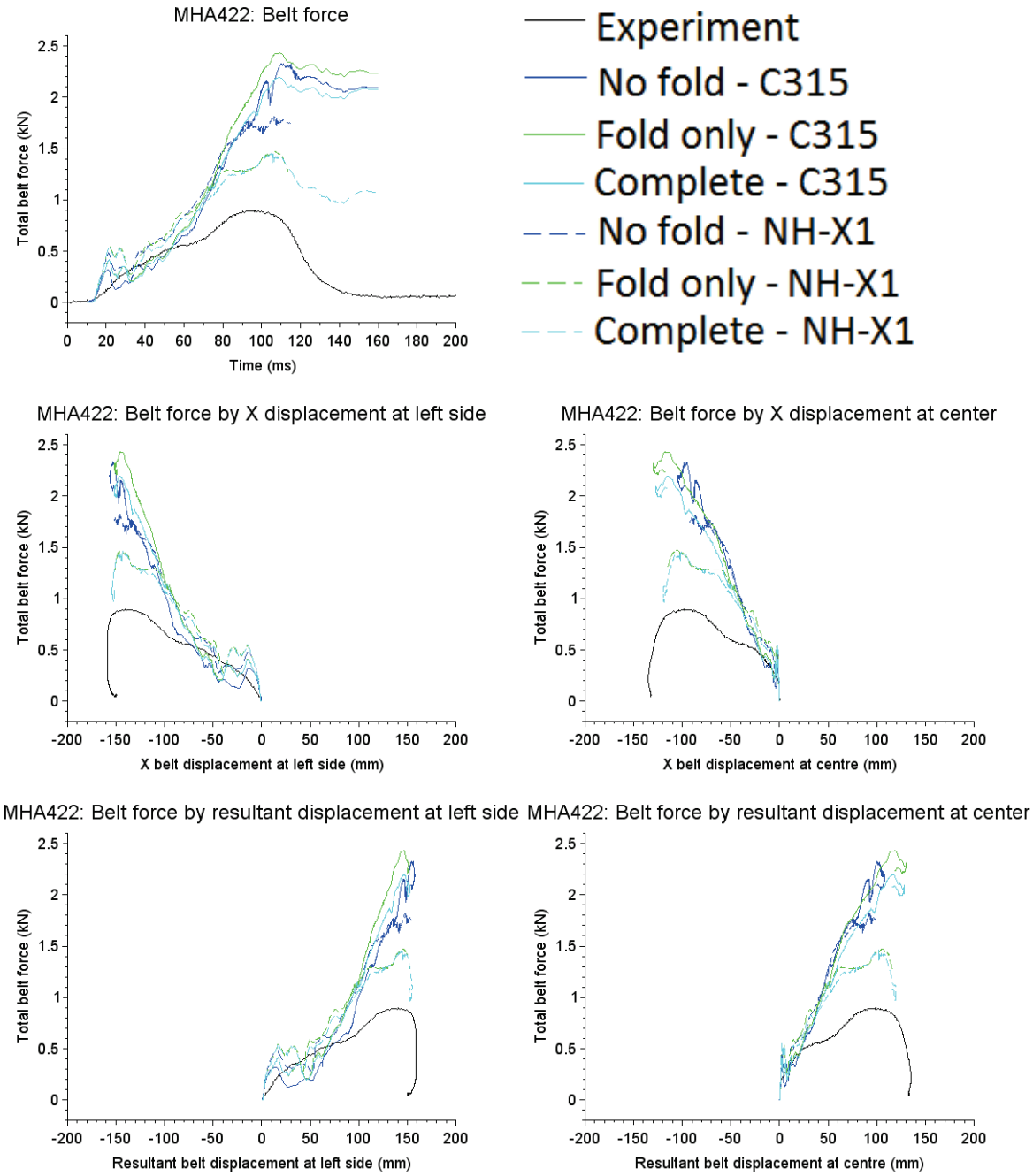


*Figure 141: MHA422 forces.*

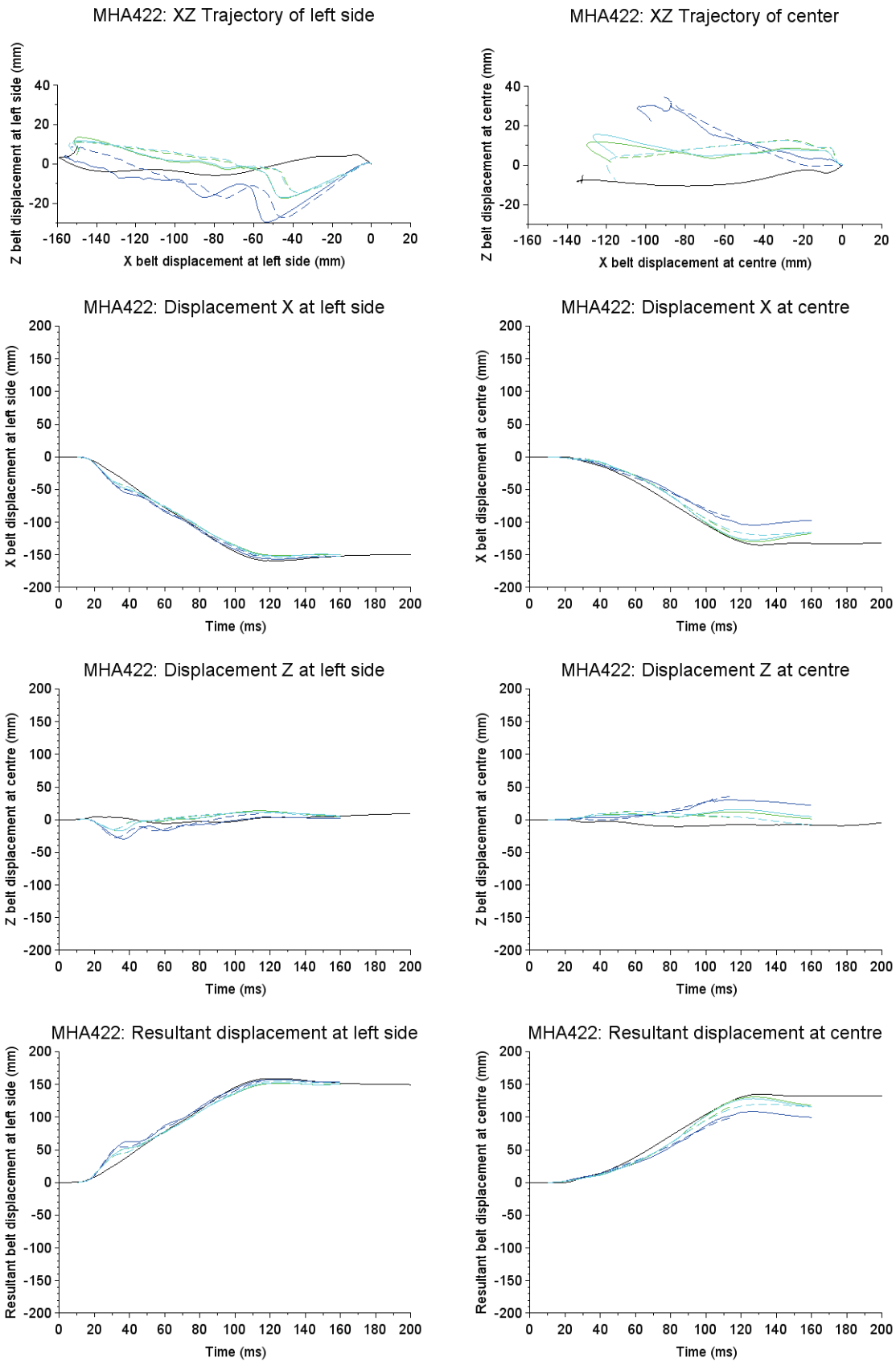


*Figure 142: MHA422 displacements.*

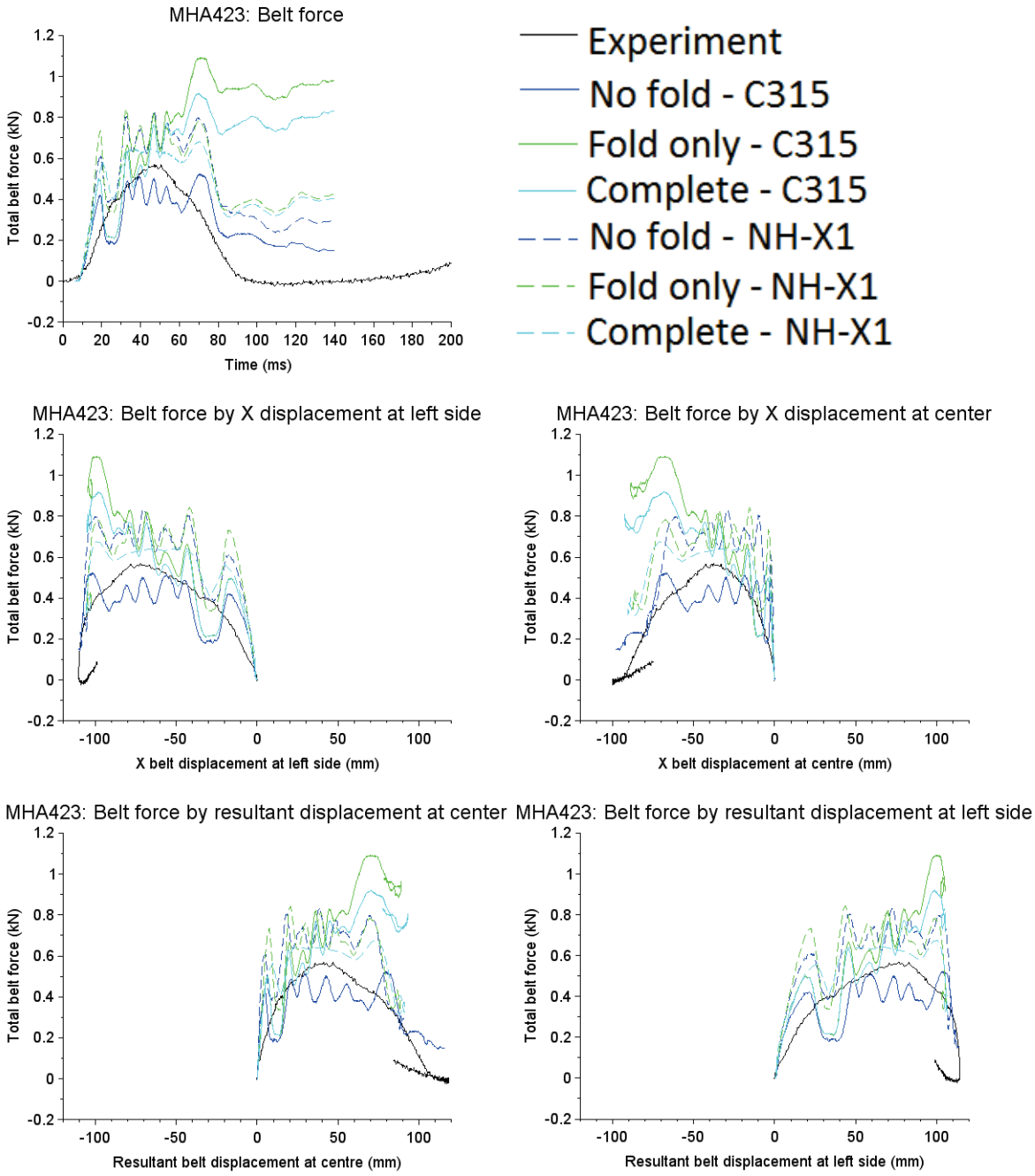


*Figure 143: MHA423 forces.*

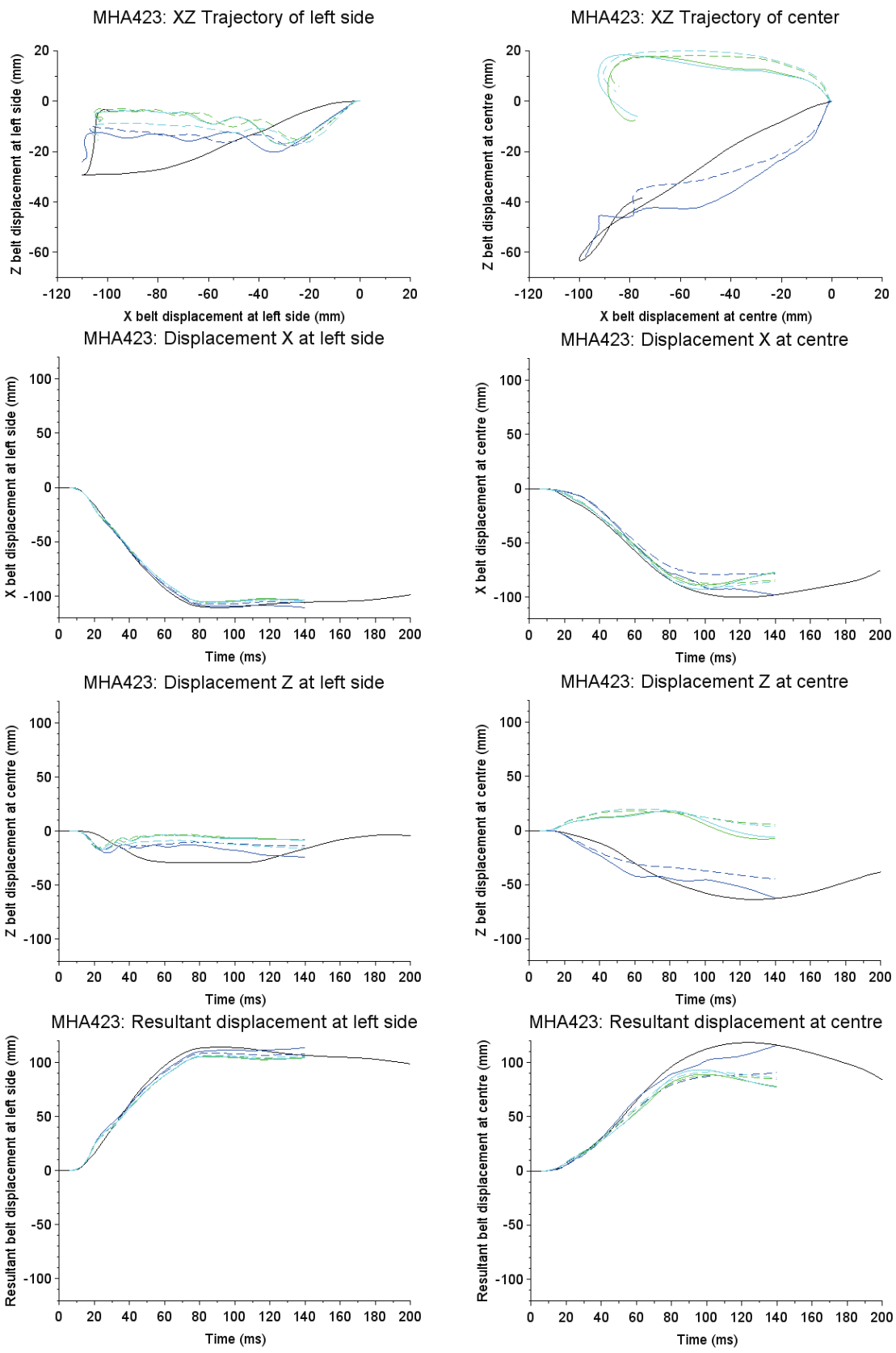


*Figure 144: MHA423 displacements.*

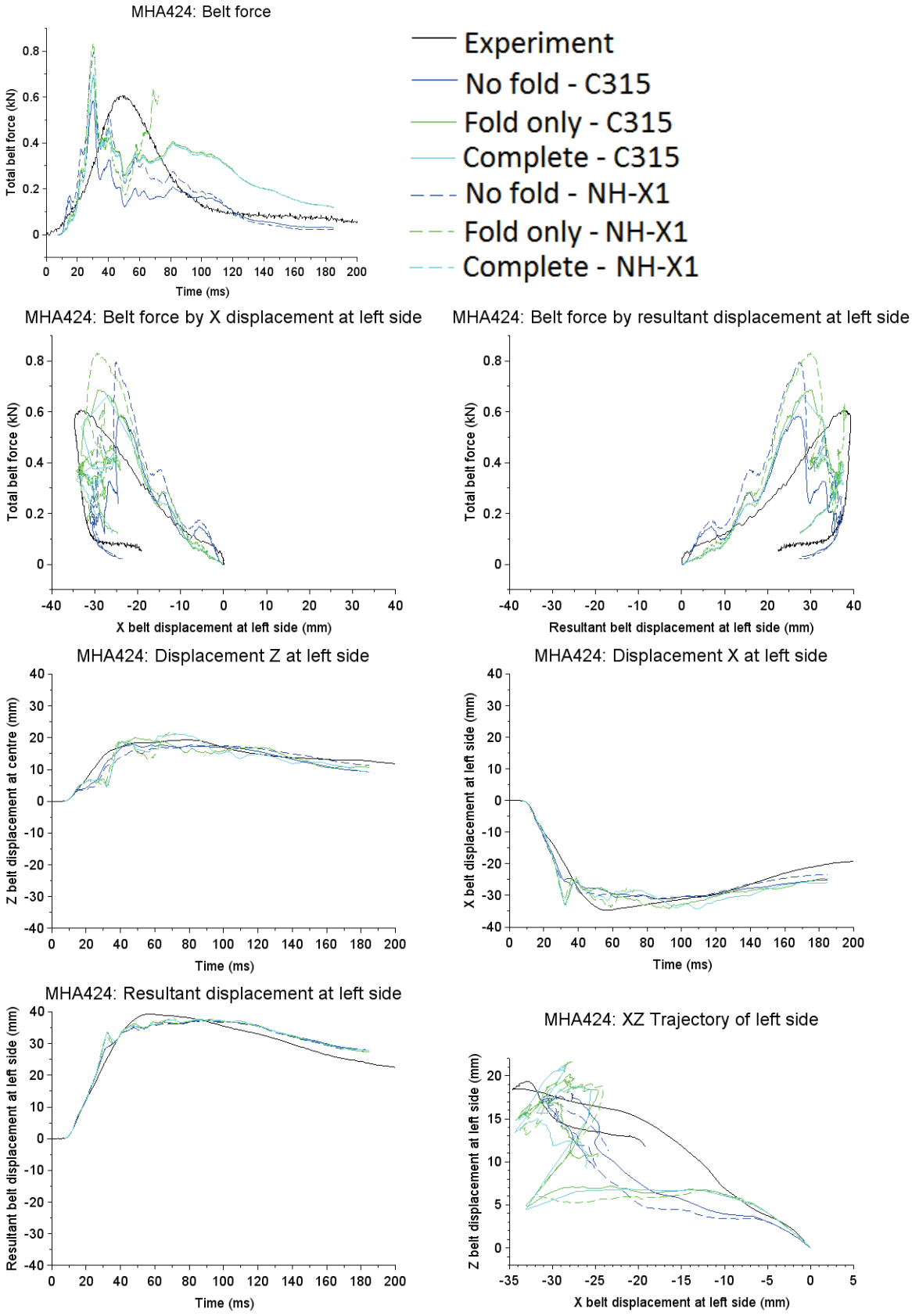


*Figure 145: MHA424. Complete with X1 did not finish (not included).*

# Résumé

L'obésité augmente depuis plusieurs décennies et on estime maintenant qu'elle touche près de 30% de la population mondiale. La masse de tissus adipeux des occupants de véhicule obèses peut affecter négativement le risque et la gravité des blessures subies lors d'un accident. Les modèles du corps humain (HBM) sont utiles pour étudier les scénarios d'accident afin de concevoir de meilleurs systèmes de sécurité, mais ils ciblent principalement la population non obèse. Cependant, le morphing a été suggéré comme une alternative au coûteux développement de nouveaux modèles. Cette thèse présente des améliorations aux méthodes de morphing existantes qui permettent d'utiliser des cibles de morphing très détaillées pour personnaliser non seulement la forme externe du corps, mais aussi l'intérieur. Les méthodes ont été implémentées dans le logiciel open source PIPER. Elles ont ensuite été appliquées pour créer des HBM personnalisés et détaillés, décrivant à la fois la graisse sous-cutanée et le pli abdominal de trois sujets d'anatomie obèses (PMHS). Des tests effectués sur les mêmes PMHS pour caractériser l'interaction d'un abdomen obèse avec la ceinture de sécurité ont ensuite été simulés à l'aide des modèles correspondants. Les résultats montrent l'importance du pli abdominal, qui n'était pas pris en compte dans les études précédentes, pour capturer correctement le comportement de l'abdomen.

Globalement, ces résultats apportent de nouvelles connaissances et méthodes permettant de mieux comprendre et simuler les conditions de retenue des sujets obèses en choc automobile. Ceux-ci devraient aider à l'avenir à concevoir des systèmes de retenue plus efficaces.

**Mots clés:** obésité, modèle du corps humain, morphing, krigeage, recalage, ceinture de sécurité

# Résumé substantiel

Le taux de mortalité routière à l'échelle de l'UE stagne depuis plus de cinq ans (European Commission, 2020). Bien que les systèmes de sécurité s'améliorent régulièrement dans les véhicules, leur conception est principalement évaluée pour une population moyenne en termes d'anthropométrie. L'Observatoire Européen de la Sécurité Routière recommande de « mieux prendre en compte les besoins de la variabilité des êtres humains » et encourage l'utilisation de simulations physiques et numériques car « les tests virtuels (…) peuvent tenir compte des variations naturelles biomécaniques entre les individus » (ERSO 2018). Or les personnes obèses représentent l'un des plus grands groupes avec une vulnérabilité accrue. En 2013, 40 des 53 régions européennes de l'Organisation Mondiale de la santé rapportait 20% d'obèses parmi leur population adulte (Galea et al. 2013), et les taux d'obésité dans le monde continuent d'augmenter chaque année (OMS 2020). Dans le même temps, les occupants obèses de véhicules sont exposés à des risques accrus de blessures liés à une retenue incorrecte par la ceinture abdominale en raison de l'augmentation du volume de gras dans la région abdominale (Kent et al. 2010; Thorbole 2015).

Les substituts aux humains sont un outil précieux pour aider à concevoir des systèmes de retenue dans les véhicules. Les mannequins de crash test sont utilisés par l'industrie pour les tests de sécurité depuis des décennies et les modèles de corps humains (HBM) utilisant la méthode des éléments finis (EF) font partie des nouvelles façons de « *fournir des informations pour la conception et l'évaluation des futurs systèmes de protection avancés* » (ERTRAC 2019). Leur utilisation est en augmentation car ces modèles numériques offrent plus de flexibilité que les scénarios de test avec mannequins, ainsi qu'une biofidélité plus élevée pour les HBM évolués. Cependant, ces modèles sont créés pour ne représenter qu'une partie restreinte de la population, souvent les hommes du 50$^{ème}$ centile et les femmes du 5$^{ème}$ centile. Étant donné que le développement d'un nouveau modèle est coûteux et prend du temps, le morphing (i.e. personnalisation géométrique) a récemment été utilisé en recherche pour représenter différents groupes de population sur la base de HBM existants. Notamment, le projet open source PIPER, initialement cofinancé par l'Union européenne, fournit des outils pour aider au positionnement et à la personnalisation de HBM pour la sécurité routière (PIPER 2020).

Cette thèse vise à étudier comment de telles méthodologies de morphing peuvent être utilisées pour créer des modèles de corps humain qui représenteraient de manière réaliste la population obèse pour l'évaluation de la sécurité routière. Les travaux abordés dans cette thèse couvrent plusieurs aspects, dont la méthode de morphing elle-même, la description géométrique des sujets obèses, leur

caractérisation mécanique et l'utilisation de modèles ainsi personnalisés pour évaluer leur pertinence et étudier l'interaction avec la ceinture de sécurité.

Tout d'abord, bien que le morphing soit une pratique courante avec les modèles surfaciques en infographie, le morphing de modèles en éléments finis pose des défis spécifiques. Ces HBM sont constitués de millions d'éléments groupés en milliers de parties connectées qui décrivent le volume entier d'un corps humain. La stabilité du modèle lors de de simulations est, entre autres, affectée par la forme de chaque élément ainsi que par les contacts entre les parties. La méthode de morphing doit donc maintenir la qualité des éléments et les contacts pour que le HBM soit utilisable après son morphing.

Il faut ensuite définir des « cibles » de morphing, c'est-à-dire les formes vers lesquelles le HBM doit être déformé. Les contraintes spécifiques à l'obésité incluent la distribution spatiale des tissus adipeux (intra-abdominale vs. sous-cutanée) ainsi que la présence d'un jeu entre les cuisses et l'abdomen dû à l'abdomen proéminent qui se replie. Ce pli abdominal pourrait affecter les interactions avec la ceinture de bassin lors d'un accident, mais cela n'a pas été étudié jusqu'à présent.

Enfin, une fois les HBM créés par morphing, leur pertinence peut être évaluée en comparant leur réponse après simulation aux données issues des tests mécaniques sur sujets d'anatomie (PMHS). Seul un petit nombre de ces tests avec PMHS obèses ont été rapportés dans la littérature. Des tests supplémentaires portant spécifiquement sur le pli abdominal sont donc nécessaires.

Le deuxième chapitre passe en revue la littérature sur l'obésité, son rôle dans la sécurité des véhicules, les modèles EF et leur morphing. Tout d'abord, les tissus adipeux sont définis et leurs propriétés mécaniques sont illustrées. L'obésité est ensuite brièvement présentée, principalement dans ses relations avec l'anthropométrie, car la forme du corps est plus pertinente pour la sécurité automobile que les risques pour la santé traditionnellement liés à l'obésité (c'est-à-dire les problèmes cardiaques et métaboliques). L'impact de l'obésité sur les modèles de blessures dans les véhicules est ensuite résumé, suivi par une revue des tests mécaniques effectués pour étudier le comportement des occupants obèses dans les véhicules. Dans l'ensemble, bien que divers mécanismes de blessure soient discutés, aucun consensus ne semble se dégager.

Les parties ultérieures du deuxième chapitre se concentrent sur les HBM et leur morphing. Le modèle détaillé d'un homme du 50$^{ème}$ centile (M50-O) du Global Human Body Model Consortium (GHBMC) utilisé pour cette étude est décrit plus en détail. En ce qui concerne la géométrie cible pour le morphing, les sources pertinentes de géométrie de sujets obèses sont rares car la plupart des données

d'imagerie médicale sont en position couchée et ne représentent pas la forme de l'abdomen pour un sujet assis dans un véhicule.

Cela a conduit à fixer des objectifs supplémentaires à la thèse : collecter des données d'imagerie de PMHS obèses en position assise afin de pouvoir créer des cibles de morphing personnalisées. Ces PMHS ont également été utilisés pour des tests mécaniques afin de caractériser leur comportement et de permettre des comparaisons avec les modèles personnalisés.

Le troisième chapitre présente les expérimentations sur PMHS qui ont été menées au CEESAR en coordination avec cette étude. Quatre PMHS obèses ont été testés, bien que seulement trois aient été utilisés pour le morphing et la simulation. Pour préparer des cibles de morphing pour chaque PMHS, des tomodensitogrammes et des scanners laser de surface ont été réalisés en position assise et sur le dos, ainsi que des clichés IRM partiels de l'abdomen. Afin de caractériser l'interaction de l'abdomen avec la ceinture de sécurité, un chargement de ceinture non lésionnel a été effectué dans trois positions de ceinture. Enfin, des tests de type charriot ont été menés sur deux des PMHS.

Le quatrième chapitre présente les efforts visant à améliorer les méthodes numériques de morphing des modèles EF. Avant la thèse, l'auteur était impliqué dans le projet PIPER en tant que développeur. Bien que la méthode de déformation par krigeage ait déjà été implémentée dans le logiciel open source PIPER, des défis subsistaient, notamment des coûts de calcul prohibitifs pour des cibles détaillées. Ce problème a été résolu durant la thèse en développant une méthodologie basée sur la subdivision de l'espace occupé par le modèle EF et en résolvant la déformation de chaque partie séparément. Le principal défi d'une telle approche réside dans la continuité entre chacune des parties afin d'éviter les éléments inversés dans le modèle EF déformé. La thèse présente plusieurs solutions à ce problème ainsi qu'une étude de validation utilisant le morphing vers des cibles génériques obèses et maigres. La méthodologie a été soumise pour publication dans un journal.

De plus, un algorithme de recalage de maillage surfacique basé sur la littérature a été implémenté afin d'établir une correspondance entre le modèle à personnaliser et la géométrie cible. Conformément à l'approche « open science » de PIPER, toutes les méthodes développées dans le cadre de cette étude sont généralement applicables à tout HBM et mises en œuvre en tant que modules dans le cadre de l'outil open source PIPER.

Le cinquième chapitre décrit en détail les processus utilisés pour construire des cibles de morphing décrivant le squelette, la peau et la graisse sous-cutanée de trois des PMHS, ainsi que leur utilisation pour transformer le HBM.

La génération de cibles squelettiques du corps entier était particulièrement difficile et les premières tentatives utilisant uniquement des changements généraux d'anthropométrie (par exemple la hauteur, la longueur des membres, etc.) n'étaient pas satisfaisantes. Ce problème a été résolu à l'aide du logiciel *Anatoreg*, qui fournit des outils pour le recalage déformable de modèles sur des images tomodensitométriques (Gilles et al. 2010).

Les cibles correspondant à la peau ont été créées sur la base de la tomodensitométrie et du scanner laser de surface. Le principal défi a porté sur l'assemblage des différentes données, toutes partielles, pour construire une description complète de la peau. Le morphing d'un modèle non obèse vers cette cible était également difficile, car le pli abdominal a imposé de grandes déformations locales. Au final, un remaillage partiel des parties sous-cutanées abdominales du M50-O a été nécessaire en raison des deux PMHS les plus obèses. En général, bien que le morphing puisse être utilisé pour créer des modèles obèses, il y a clairement une limite à l'ampleur des déformations locales réalisables sans préparation spécifique du modèle.

Enfin, la cible correspondant au gras sous-cutané a été créée en extrayant manuellement la limite du gras sur les tomodensitométries. Pour cette cible, le morphing direct près du bassin a échoué en raison de grandes différences dans la quantité de gras entre le modèle et la cible autour du bassin. Les algorithmes simulant la croissance progressive des graisses autour du squelette pourraient être plus adaptés à ce type de changements.

Trois modèles ont été créés pour chaque PMHS: un modèle détaillant à la fois le gras sous-cutané et le pli abdominal, un modèle avec le pli abdominal mais sans le gras sous-cutané, et un modèle sans pli ni gras sous-cutané (en utilisant uniquement une forme de peau simplifiée avec le pli abdominal lissé, qui correspondrait à l'état de l'art dans la littérature). Outre les modèles créés, les processus utilisés et les suggestions pour leur amélioration pourraient servir de guide pour des études supplémentaires.

Enfin, le chapitre 6 décrit la simulation des expérimentations PMHS avec le HBM personnalisé. Les propriétés de matériau utilisées pour modéliser le tissu adipeux dans le M50-O ont été jugées inadéquates pour l'application actuelle et deux autres propriétés des matériaux ont été testées. L'importance du pli abdominal et de l'épaisseur de gras sous-cutané a été évaluée en comparant le comportement mécanique des trois types de modèles aux tests avec ceinture (figure 5). Le pli abdominal a un impact important : les modèles sans pli ont conduit à des efforts ceinture beaucoup plus élevés et à des glissements irréalistes. L'utilisation de la cible sous-cutanée a eu moins d'impact. Dans l'ensemble, le modèle le plus détaillé, avec à la fois le pli et la cible sous-cutanée, et les propriétés des matériaux les plus souples se sont les mieux approchés des observations expérimentales. Un

examen plus approfondi des propriétés du modèle, non seulement pour les tissus adipeux mais aussi pour les organes abdominaux internes, serait utile.

Seul l'un des tests charriot a été simulé, car l'autre PMHS a subi des lésions pelviennes graves qui seraient difficiles à représenter. Cette configuration est plus complexe à simuler que les tests ceinture et les forces sont plus importantes : cela conduit à des difficultés de convergence, en particulier pour l'ensemble de propriétés des matériaux plus souples. Néanmoins, de nombreuses simulations ont été réalisées avec succès (figure 6). Le frottement a été identifié comme un paramètre important qui peut changer considérablement le comportement cinématique : de faibles valeurs des coefficients de frottement ont conduit à une retenue limitée du bassin par le siège qui s'est accompagné d'un glissement de la ceinture à l'intérieur du pli abdominal et d'un effort ceinture faible. Ceci a engendré à une plus grande excursion frontale du corps. Des valeurs de coefficient de frottement plus élevées sur la ceinture et le siège ont permis d'approcher les forces observées expérimentalement dans les brins de la ceinture. La ceinture n'a jamais glissé sur le bassin ou sur l'abdomen mou, mais un effort important a été atteint et transmis au bassin lorsque la ceinture ventrale a glissé dans le pli abdominal. Il est à noter que sur la base de la vidéo de l'essai sur PMHS, ce glissement dans le pli semble s'être produit pour l'un des deux tests (celui avec fracture pelvienne). Il semble donc important de disposer de modèles avec pli abdominal pour modéliser et étudier correctement les interactions de la ceinture abdominale avec l'abdomen.

Pour résumer, l'étude présente plusieurs nouvelles connaissances et méthodologies dont :

- Une méthodologie efficace pour le morphing des modèles de corps humain EF en utilisant des cibles détaillées, ainsi que sa mise en œuvre dans un logiciel open source,
- Des processus pour créer des cibles de morphing détaillées à partir de PMHS obèses,
- Une caractérisation de l'interaction entre des abdomens obèses et les ceintures de sécurité, avec de nouvelles informations sur le rôle du pli abdominal et de l'épaisseur de la graisse sous-cutanée.

Ensemble, ces résultats apportent de nouvelles connaissances et méthodes permettant de mieux comprendre et simuler les conditions de retenue des sujets obèses en environnement automobile, ce qui devrait aider à l'avenir à concevoir des systèmes de retenue plus efficaces.

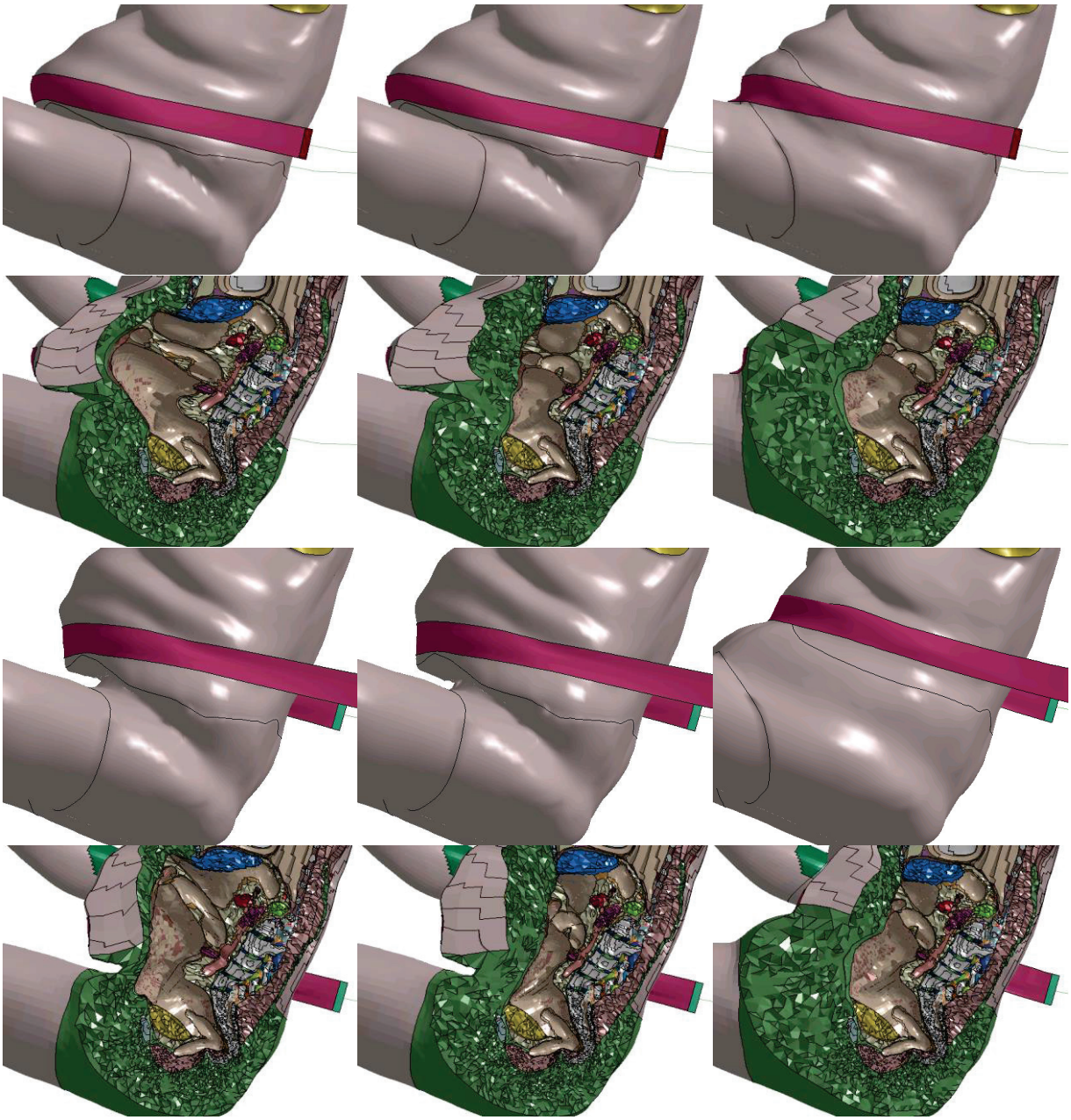

*Figure 146: Exemple de déplacement de la ceinture ventrale en utilisant différents types de modèles pour la configuration de ceinture « parallèle ». Gauche : modèle avec à la fois la cible de gras sous-cutané et le pli abdominal. Milieu : modèle avec pli abdominal uniquement. À droite : modèle sans pli abdominal. Les deux premières lignes montrent l'état initial, les deux lignes suivantes montrent le temps de force maximale.*

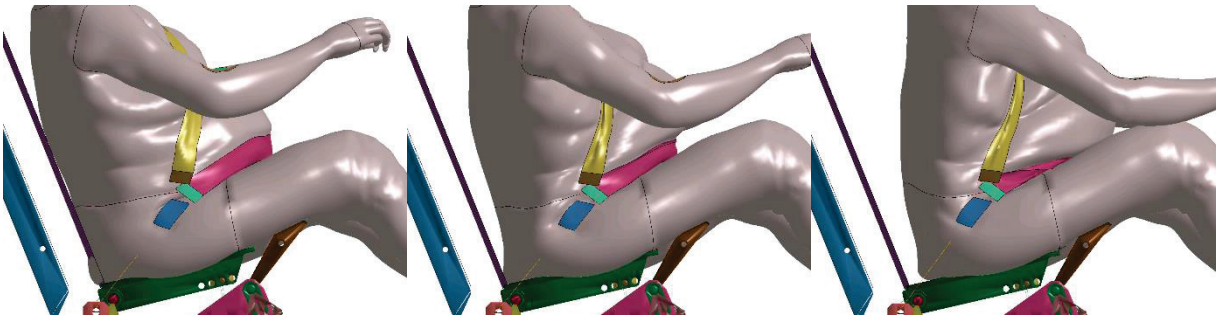

*Figure 147: Exemple de test charriot à différents temps de la simulation (gauche : 30 ms, milieu : 60 ms, droite : 90 ms).*

# Abstract

The prevalence of obesity has been increasing for several decades and it is now estimated to affect close to 30% of population worldwide. The increased mass of adipose tissues of obese vehicle occupants can negatively affect the risk and severity of injuries sustained during a car crash. Human Body Models (HBM) are a useful tool for studying crash scenarios in order to design better safety systems, but they mainly target non-obese population. However, morphing has been suggested as an alternative to the costly development of new model. This thesis presents enhancements to existing morphing methods which allow using very detailed morphing targets to personalize not only the external shape of the body, but also the inside. The methods were implemented as open source software in the PIPER framework. They were then applied to create a detailed personalized HBM that describe both the subcutaneous fat and abdominal fold of three obese Post Mortem Human Surrogates (PMHS). Tests performed on the same PMHS to characterize the interaction of an obese abdomen with the safety belt were then simulated using the morphed models. The results show the importance of the abdominal fold, which was not accounted for in previous studies, to correctly capture the behaviour of the abdomen.

Overall, these results bring new knowledge and methods allowing to better understand and simulate the restrains conditions of obese subjects in automotive environment. These should help in the future to design more efficient restrain systems.

**Keywords:** obesity, human body model, morphing, kriging, registration, safety belt